Matthias Bösing

Acoustic Modeling of Electrical Drives

Noise and Vibration Synthesis based on Force Response Superposition

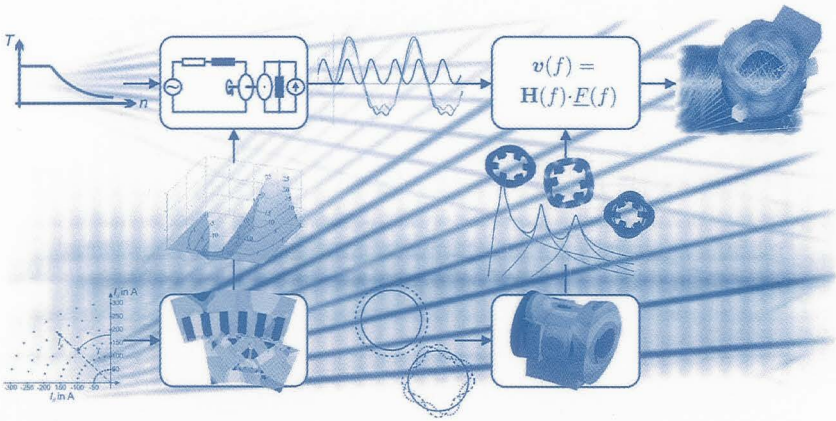

Aachener Beiträge des ISEA Band 71

Acoustic Modeling of Electrical Drives

—

Noise and Vibration Synthesis based on Force Response Superposition

Von der Fakultät für Elektrotechnik und Informationstechnik der Rheinisch-Westfälischen Technischen Hochschule Aachen zur Erlangung des akademischen Grades eines Doktors der Ingenieurwissenschaften genehmigte Dissertation

vorgelegt von
Diplom-Ingenieur
Matthias Bösing
aus Duisburg

Berichter:
Univ.-Prof. Dr. Ir . Dr. h. c. Rik W. De Doncker
Univ.-Prof. Dr.-Ing. habil. Dr. h. c. Kay Hameyer

Tag der mündlichen Prüfung: 12. September 2013

Matthias Bösing

Acoustic Modeling of Electrical Drives

Noise and Vibration Synthesis based on Force Response Superposition

Bibliographic information published by the Deutsche Nationalbibliothek
The Deutsche Nationalbibliothek lists this publication in the Deutsche Nationalbibliografie; detailed bibliographic data are available in the Internet at http://dnb.d-nb.de.

Zugl.: D 82 (Diss. RWTH Aachen University, 2013)

AACHENER BEITRÄGE DES ISEA

Herausgeber:

Univ.-Prof. Dr. ir. Dr. h.c. Rik W. De Doncker
Leiter des Instituts für Stromrichtertechnik und
Elektrische Antriebe der RWTH Aachen (ISEA)
52056 Aachen

Printed in Germany.

ISBN 978-3-8440-2752-5
ISSN 1437-675X

Shaker Verlag GmbH • P.O. BOX 101818 • D-52018 Aachen
Phone: 0049/2407/9596-0 • Telefax: 0049/2407/9596-9
Internet: www.shaker.de • e-mail: info@shaker.de

Danksagung

Das Themenfeld Antriebsakustik erreichte das Institut für Stromrichtertechnik und Elektrische Antriebe (ISEA) der RWTH Aachen durch die diesbezüglich notorische Geschaltete Reluktanzmaschine. Jens Fiedler und Knut Kasper gilt mein Dank, da sie mit ihren Arbeiten hier den Boden bereitet haben. Industriepartner aus dem Automobilbereich schenkten dem Institut nun ihr Vertrauen, sie auch bei akustischen Fragestellungen zu Permanentmagnet-Synchronmaschinen zu unterstützen. Dies ermöglichte mir, während meiner Zeit als wissenschaftlicher Mitarbeiter von 2007 bis 2012 die vorliegende Arbeit zu verfassen. Ich danke Herrn Professor De Doncker für die Betreuung dieser Arbeit und die großen Freiräume für eigenständige wissenschaftliche Arbeit. Herrn Professor Hameyer gilt mein Dank für die Übernahme des Koreferats. Die inspirierende Atmosphäre des ISEA und der vielfältige Austausch mit Arbeitskollegen und Studenten aller im Haus vertretenen Teildisziplinen hat wesentlich zum Gelingen der Arbeit beigetragen. Besten Dank euch allen! Meine Heimat im ISEA war die Antriebsgruppe. Christian Carstensen ermunterte mich früh zu dieser Arbeit und Helge Brauer war mir in den Anfangsjahren ein treuer Bürokollege. Martin Hennen unterstützt von Claude Weiss und Raphael Wegmann danke ich für das schöne Bahnrad, dessen Modellierung mir viel Freude bereitete. Für die Schaltfrequenzen war die Diplomarbeit von Markus Nießen sehr wertvoll, für die Schrägung jene von Thomas Schniedertöns. Dass Timo Schoenen eine sehr harmonische Maschine unterkam, inspirierte mich zum entsprechenden Maschinemodell. Mit Daniel van Treek verbrachte ich etliche Zeit mit Fachbuchlektorat und Elektroautobau. Bei letzterem danke ich Michael Ritter für die Brücke, die seine Diplomarbeit baute. Mit großer Unterstützung der Werkstätten brachten Tobias Lange, Stephan Koschik, Martin Christoph, Martin Rosekeit und Silvano Taraborrelli den Wagen auf die Straße, während ich mich wieder der vorliegenden Arbeit widmete. Andreas Hofmann fühlte jeder Theorie auf den Zahn und Mareike Schenk unterstütze mich durch ihre Diplomarbeit. Beiden gilt zudem mein Dank für das Korrekturlesen der Arbeit. Über das ISEA hinaus gilt mein Dank all jenen Kollegen und Wissenschaftlern, die ich im Laufe der Jahre im In- und Ausland traf, für den fachlichen und persönlichen Austausch und die stets neuen Impulse für meine Arbeit. Schließlich danke ich Familie und Freunden für steten Rückhalt und Ermunterung.

Ludwigsburg, im Dezember 2013 *Matthias Bösing*

Deutsche Kurzfassung

In der Arbeit wird eine universelle Modellierungsmethodik für das akustische Verhalten elektrischer Antriebe vorgestellt. Ziel ist es, die Qualität der akustischen Modellierung elektrischer Antriebe zu verbessern und gleichzeitig ihre Anwendung zu vereinfachen und einer breiten Anwendergruppe zugänglich zu machen. Die Methodik basiert auf einem Systemsimulations- und einem Schwingungssyntheseansatz. Mittels des vorgestellten Verfahrens kann eine umfassende und realitätsnahe Modellierung und Auralisation der elektromagnetischen Geräuschanregung routinemäßig bei der Auslegung von elektrischen Antriebssystemen erfolgen.

Zum Einsatz kommt ein zweistufiger Prozess. Zunächst werden offline automatisiert Kraftanregungskennfelder sowie Strukturschwingungsantworten berechnet. Hieran schließt sich als interaktiver Teil eine benutzergesteuerte Systemsimulation mit Kraftinterpolation und anschließender Schwingungssynthese an. Dieser Prozess erlaubt die Nutzung komplexer numerischer 3-D-Strukturmodelle bei gleichzeitig recheneffizienter Simulation beliebiger Betriebspunkte. Dabei lassen sich zudem Regelungseinflüsse, Raumharmonische und Schaltfrequenzkomponenten berücksichtigen. Kern der effizienten Synthese ist ein Superpositionsansatz. Für die maschineninhärenten Kraftanregungsformen werden Strukturschwingungsformen und -antworten vorherberechnet. Diese werden bei der Synthese mit den aus der Systemsimulation gewonnenen Kraftanregungsverläufen als Skalierungsfaktoren überlagert. Besonderes Augenmerk gilt der räumlichen Kraftzerlegung, so dass die zugrundeliegenden Basisfunktionen für die Aufbringung in strukturdynamischen Modellen der elektrischen Maschine geeignet sind. Der Schwingungssyntheseprozess ist für alle Maschinentypen und Bauformen geeignet, einschließlich geschrägter, Axialfluss-, Transversalfluss- oder Außenläufermaschinen. Maschinen- und Luftspaltkraftmodelle werden für permanenterregte Synchron- und Geschaltete Reluktanzmaschinen erarbeitet und in die Systemsimulation eingebettet.

Veranschaulicht und verifiziert wird die Methodik anhand verschiedener Beispielantriebe. Dabei handelt es sich um permanenterregte Synchronmaschinen für Elektro- und Hybridfahrzeuge und um eine Geschaltete Reluktanzmaschine (GRM) für Industrieanwendungen. Zur Demonstration der Anwendbarkeit der eingeführten Methodik auch auf spezielle Maschinen und Betriebszustände wird abschließend das akustische Verhalten eines Außenläufer-GRM-Traktionsantriebs mit verteiltem Umrichter in verschiedenen Fehlerzuständen synthetisiert.

Contents

1 Introduction

In product engineering, the primary challenge often lies less in realizing the product's functionality itself but in meeting the constraints which the product and its development face. The functionality of an electrical drive is to provide a certain torque over a certain speed range. These requirements by themselves are in many cases not hard to meet. However, electric vehicle drives, for example, face strong requirements regarding size, cost, efficiency, weight, and, among others, acoustic noise.

Drive acoustics as multi-disciplinary problem

The acoustic characteristics of an electrical drive system are influenced by a number of factors. The system requirements and project background often lead to the selection of a certain machine type at an early stage of the design process. This choice of machine type defines the fundamental acoustic characteristics in terms of the machine inherent noise components. These are the most prominent noise components for many traction drives in (hybrid) electric vehicles. Further machine parameters like pole count, winding configuration, air-gap length, and lamination geometry are determined by the machine designer and refine the acoustic characteristics. The power electronics engineer's choice of inverter topology, type of semiconductor switches, and voltage level, sets the constraints for voltages, currents, and switching frequency for feeding the machine. The switching frequency related harmonics can become the dominant noise components when the frequency lies within the audible range. This is frequently the case for large industrial drives or traction drives in trains. The control engineer determines within these limits the operation strategy for the machine. Where the drive is located in the system, what kind of housing is used, and how it is attached to the system are decisions made by the mechanical design engineer and the system integrator. The size of the drive predetermines the frequency range in which the drive becomes noisy as the resonance frequencies are predominantly size-dependent. Its location and fixation influences sound radiation and transmission. All of the above disciplines influence the acoustic characteristics of a drive system and can contribute to its low noise design. Simulations are common in all of the above fields, some also focus on acoustics. A comprehensive and generic approach for modeling the acoustic characteristics of electrical drive systems is desired.

Requirements for an acoustic modeling process

Numerical simulations have been established in many fields of engineering. They facilitate multi-objective development tasks and reduce the need for building prototypes. Insight is gained into the system behavior and into quantities not available for measurements. In terms of acoustics, the most relevant source quantity is the air-gap force, which cannot be measured directly but can be obtained from simulations.

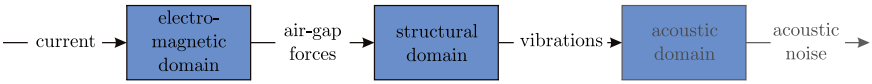

Figure 1.1: Causal path from current excitation via air-gap forces and structural vibrations to audible acoustic noise

Acoustic modeling should not be performed isolated from other models but integrated into a system simulation environment. It needs to be readily and routinely applicable in practice and to provide insight into the noise and vibration characteristics of a drive. It must keep modeling overhead low and has to build on data available in the individual domains. The modeling environment is not an end in itself. It needs to be accessible for the individual domains and enable them to analyze and optimize the system acoustics with respect to those aspects that are under their influence.

The subdomains need to be linked with clear and well-structured interfaces. This enables the applicability to a broad range of drive systems and to cope with a heterogeneous simulation software and measurement hardware environment. Initial invest in a modeling environment is required but will pay back when being reused. Modeling is an iterative process and clear interfaces allow for refining and exchanging parts of the model without altering the remainder of the simulation environment. For example, analytical models can be replaced by numerical ones and eventually be refined through measurement updates.

Electrical drives are nowadays predominantly variable speed drives. The modeling process must allow for efficient simulation of arbitrary torque-speed trajectories rather than being limited to single fixed-speed operating points. The user should have the opportunity to perform 'what-if' studies allowing to investigate relationships between parameters. The results must qualitatively and quantitatively match those obtained by measurements. If measured vibrations are displayed in spectrograms, so must be the simulated ones. If sound is auralized from simulation results, not only the spectral composition must agree but also modulation and roughness effects to match the acoustic impression. Not just those with a broad background in acoustic but all users must be able to judge the quality of the results and to make decision based on the simulations.

Causal path from air-gap force to acoustic noise

Figure 1.1 depicts the causal path of electromagnetically excited acoustic noise generation. It goes from electromagnetic excitation (currents, magnets) via structure borne sound (vibrations) towards airborne sound (sound pressure). This three-domain approach is common ground in machine acoustics since Jordan's work [Jor50]. A drawing similar to figure 1.1 is nowadays found at the beginning of most monographs on acoustic noise of electrical drives, for example, [GWL06; Le 08; Kas10; vGie11]. [VB94] is the earliest example the author was able to identify. There is typically no significant feedback from the mechanical domain to the electromagnetic and also none from the acoustic to the mechanical. It is explained in [Gar+97], in terms well-suited for the electrical engineer, that there is an impedance mismatch between the three modeling regimes. In the numerical modeling world, the term weakly-coupled is used.

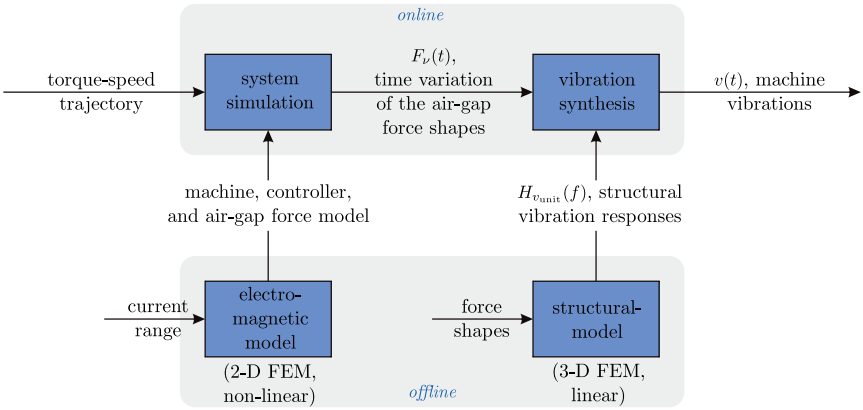

Figure 1.2: Simulation path for efficient acoustic modeling

Models in these three domains, the electromagnetic domain, the mechanical domain, and the acoustic domain are generally used to model the acoustic behavior. Typically, the modeling path is identical with the causal path. First, the air-gap forces are calculated for a specific operating point. These are then applied to a structural model which provides the vibrations for this respective operating point. Likewise, the radiated sound is obtained via an acoustic model for this operating point or frequency. This procedure is efficient only if all these models are computationally cheap analytical models. In many practical cases, however, computationally expensive numerical models are required.

Efficient simulation through separation of causal path and simulation steps

The vibration synthesis process for acoustic modeling of electrical drives, which is presented in this thesis, unbundles these simulations. The computationally expensive numerical simulations for the electromagnetic and the structural model are performed offline and independently from one another. The vibrations themselves are then obtained online. The structure of these simulations is shown in figure 1.2.

The basic concept is that from the air-gap force of the machine, only a limited number of spatial force shapes is structurally and thus acoustically relevant. For these, the normalized structural responses are pre-calculated in structural dynamics finite element (FE) simulations. A system simulation model of the machine including an air-gap force model is parametrized via electromagnetic FE simulations. Those are the two offline simulation steps. The two online and user-interactive steps are the system simulation in which the drive is operated along an arbitrary torque-speed trajectory. Via the pre-parametrized force model, the time variations of the air-gap force shapes are obtained. These are used in the subsequent vibration synthesis for scaling and superposing the normalized air-gap force responses. As a result, the

machine vibrations under arbitrary operating conditions are obtained.

Aim of this work

The aim of this thesis is to provide a universal acoustic modeling framework for electrical drives based on a system simulation and vibration synthesis process. This process was designed to fulfill the above discussed requirements for an acoustic modeling process. The vibration synthesis process is universal and can readily cope with any machine type and geometry, including, for example, skewed machines, axial and transversal flux machines, and outer rotor machines. Particular effort is spent on decomposing the air-gap forces in a manner suitable for the use with structural models. Machine and air-gap force models integrated into a system simulation environment are provided for permanent magnet synchronous machines (PMSMs) and switched reluctance machines (SRMs). Analyzing induction machines (IMs) and DC machines (DCMs) requires adding a corresponding force model. This work deals with noise of electromagnetic origin and the vibrations of the machine assembly. Transmission or radiation of these vibrations are outside the scope of this thesis.

Examples for noise mitigation via rotor skew or injection of current harmonics are given, but this work does not specifically aim at machine design or acoustic optimization, neither electromagnetically nor structurally. The modeling process, however, aims to serve as a valuable tool for this purpose. Likewise, providing 'best-in-class' structural models is not a goal. Due to the modular approach, however, these can be incorporated. The vibration synthesis process scales well for more complex models.

The acoustic characteristics of drives are becoming relevant for more and more applications. This thesis' aim is to improve the quality of acoustic modeling while at the same time making acoustic modeling more accessible and affordable. The objective is that realistic and comprehensive acoustic modeling can routinely be performed in drive system design. The data is available. It just needs to be linked.

Outline

Chapter 2 – Fundamentals

Chapter 2 deals with basic aspects which either motivate the chosen approach or lay down fundamentals on which the modeling approach builds. Automotive acoustics and noise sources in electrical machines and drives are discussed. The basic acoustic terms sound power, radiation efficiency, and mean-square surface normal velocity are introduced. Fourier series based signal descriptions will be frequently used and are therefore defined. At last, an overview over the machines used in the numerical examples and measurements is provided.

Chapter 3 – Modeling electrical machines

Chapter 3 introduces the system simulation. Fundamental machine equations for PMSMs and SRMs are introduced in a unified manner. Based on these, machine models for use in the system simulation are introduced. The ideal rotating transformer (IRTF) based PMSM model with spatial harmonics has been developed for this thesis and is introduced. After this,

control and operation of PMSMs and SRMs is discussed. The chapter closes by describing the electromagnetic FE simulations which parametrize machine model, controller, and force model in an offline process.

Chapter 4 – Air-gap force decomposition and analysis

Chapter 4 is dedicated to temporal and spatial decomposition as well as analysis of air-gap forces in electrical machines. Formulas are given which allow to determine the general acoustic characteristics of PMSMs and SRMs based on their configuration. The vibration synthesis process decouples the determination of force excitation and structural vibration responses based on a force response superposition approach. For this approach to be applicable, the force excitation needs to be decomposed in a manner which is on the one hand an as-close-as-possible approximation of the real force distribution in the machine and on the other hand allows to determine the structural responses for the individual force shapes. Three different approaches are presented and analyzed and their advantages and limitations are discussed. The chapter closes with a combined analytical-numerical application example analyzing the effectiveness of skew in a PMSM on reducing the shape 0 force excitation.

Chapter 5 – Force models for time domain simulations

Chapter 5 develops force models for use in time domain simulations. Permanent magnet and switched reluctance machines are considered including skewed PMSMs, stacked SRMs, and outer rotor machines. The models are lookup-table based and parametrized with the coefficients of the spatially decomposed air-gap force. The force models complete the system simulation. The vibration synthesis will be performed in the frequency domain based on the time domain force signals from the system simulation force models.

Chapter 6 – Structural response calculation and vibration synthesis

Chapter 6 focuses on calculating the structural responses and on the vibration synthesis. Structural response calculation (offline, no user-interaction) and vibration synthesis (online, user-interactive) are separate steps but share the same formalism. Parts of the structural response superposition are furthermore performed online in the vibration synthesis process. Structural response calculation and vibration synthesis are therefore combined in this chapter. The formalism of modal and harmonics analyses is presented to the degree required for understanding and implementing response calculation and vibration synthesis. Of particular importance is the representation of vibrations by a scaled superposition of eigenshapes. Exemplary force response results on test bodies are given for the three different force decomposition options.

Chapter 7 – Application of the acoustic modeling process

The acoustic modeling process has been developed with the goal to be readily and routinely applicable in practice, to provide insight into the vibration characteristics of a drive, and to deliver real-life results. The application examples in chapter 7 underline that this goal is met. Numerical examples are validated against measurements for PMSMs and SRMs including PMSM traction drives and an outer rotor SRM with integrated distributed inverter

operating under various fault conditions. Different PMSM skew setups are analyzed and their effectiveness on the acoustic characteristics is analyzed. Two application studies of the vibration synthesis process for noise mitigation via the feeding currents and for the acoustic assessment of different switching frequencies and modulation strategies are performed.

Chapter 8 – Summary and conclusions

Chapter 8 summarizes and discusses the contributions of this work and lays down remaining questions and further steps.

2 Fundamentals

Several basic aspects are introduced in this chapter before starting the modeling process in chapter 3. An overview of noise in electrical machines is given in section 2.1. The vibration synthesis process provides surface vibrations. How these relate to audible sound is described in section 2.2. Various quantities, foremost the air-gap force, are decomposed in space and time. The formal representation of the resulting Fourier series is given in section 2.3. Section 2.4 provides an overview over the permanent magnet and switched reluctance machines used in the numerical examples and measurements.

2.1 Noise in electrical machines

The acoustics of electric traction drives in vehicles are discussed in section 2.1.1. Section 2.1.2 summarizes the various noise sources in electrical machines and further motivates this thesis' focus on electromagnetically excited noise.

2.1.1 Electric traction drives in vehicles

Research and development of electric vehicles (EVs) and hybrid electric vehicles (HEVs) has picked up speed in recent years. The electric traction drive is becoming an additional element with the potential for being a new source of acoustic noise in a vehicle. This has created demand from automobile manufacturers and component suppliers for providing means for modeling, assessing, and mitigating noise of electrical machines. The interior permanent magnet synchronous machine (IPMSM) is currently the quasi-standard traction drive and/or generator in HEVs. Most PMSM related topics in this work have been developed against this background.

Not loud enough

Electric vehicles are not renowned for being noisy but rather for being particularly quiet – too quiet. Pedestrians are used to hear cars approaching due to the omnipresent sound of the combustion engines. Electric vehicles have at low speeds a very low exterior noise level. This helps to keep traffic noise down but makes it more difficult for pedestrians to hear them. This has even triggered newspaper articles labeling electric vehicles as "silent killers" [Hol12]. Legislation in both the European Union (EU) and the United States (US) is taking measures to ensure that all motor vehicles provide a certain minimum exterior noise level. The European commission decided in December 2011 on a proposal titled "On the sound level of motor vehicles" [Eur11]. It aims "at ensuring road and occupational safety by introducing requirements regarding the minimum noise for electric and electric-hybrid vehicles". As a consequence, electric cars are being equipped with sound generators adding to the exterior noise at low speeds. The National Highway Traffic Safety Administration (NHTSA) of the US Department of Transportation has examined the incidence rates of pedestrian and

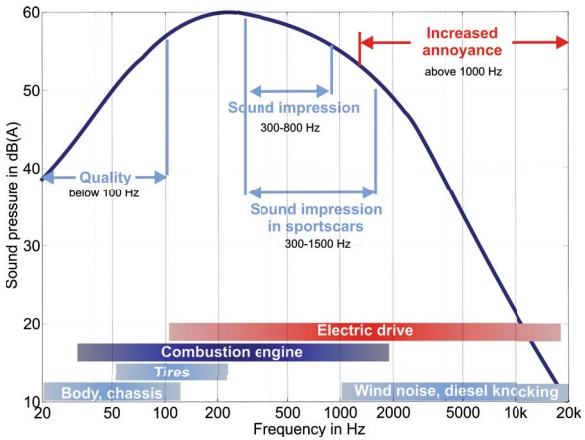

Figure 2.1: Noise sources and sound perception in automobiles (based on [Kön07])

bicyclist crashes that involved HEVs and compared the results to internal combustion engine (ICE) vehicles under similar circumstances in [Han09]. The US Congress' Pedestrian Safety Enhancement Act of 2010 [One10] "directs the Secretary of Transportation to study and report to Congress on the minimum level of sound that is necessary to be emitted from a motor vehicle, or some other method, to alert blind and other pedestrians of the presence of operating motor vehicles while traveling".

At this point, the conclusion should be not to make electrical drives less but more noisy.

Not necessarily loud but annoying

Electrical drives are not generally loud but have the potential to be noisy under certain circumstances. In particular, their sound has the potential to be annoying. Electrical machines tend to produce tonal noise at high frequencies. Combustion engines have a more broadband noise in the lower frequency range. Figure 2.1 is based on an illustration by the German car magazine AutoBild [Kön07]. It shows the envelope of the sound pressure in passenger cars over frequency. Horizontal bars mark in what frequency range certain sound components (combustion engine, tires, etc.) lie. The bar for the electrical drive has been added.

Sound in the low-frequency range can give the impression of quality. A car related example is the sound a car door makes when being closed. A solid, "heavy" sound with a significant low-frequency content is preferred over a sound with a stronger high-frequency content, e.g., resembling the sound a soda can makes when being squished. In the mid-frequency range, the sound impression of the car is formed. This is also the range where the sound pressure level is highest. High-frequency sounds are generally considered to be annoying, even when their level is low. The envelope shows that the overall level in cars decreases towards higher frequencies. The acoustic noise from electrical machines therefore tends to be audible also in the presence of a combustion engine and even more so in electric vehicles.

The general design rule for electrical machines and drives therefore is to make them as quiet as possible.

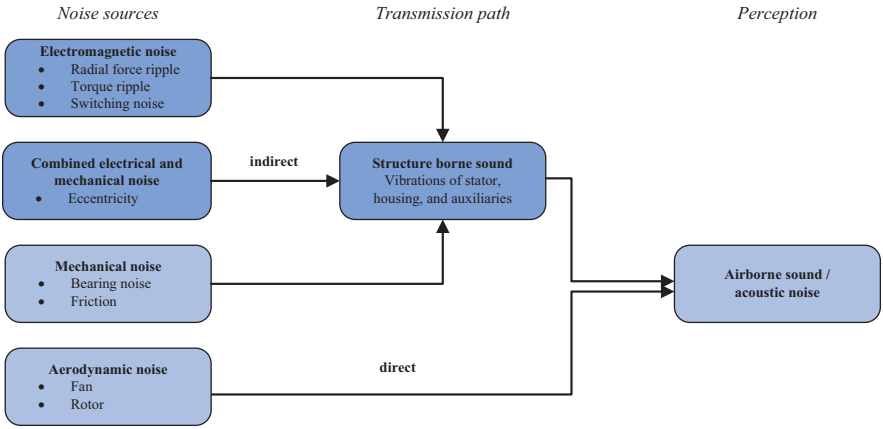

Figure 2.2: Noise sources in electrical machines and drives

2.1.2 Noise sources in electrical machines

Figure 2.2 gives an overview of noise sources in electrical machines and their transmission towards airborne sound. This classification is introduced by Timar et al. in [Tim+89]. Noise can be of electromagnetic, mechanical, combined electrical and mechanical, or aerodynamic origin. Noise of the first three groups is transmitted indirectly. A force is created which excites vibrations in a body. The vibrations of the body (stator, housing, auxiliaries) then give rise to airborne sound. Aerodynamic noise is caused when rotating parts of the machine lead to perturbations in air.

For large air-cooled drives, Garvey et al. explain in [Gar+97] that fan efficiency and cooling improvement have reduced ventilation noise and that the thermal gain has been exploited by increasing the electromagnetic loading. This has led to an increase in magnetic sourced noise levels. They state that "it was only a matter of time before the reducing vibration noise levels and the increasing electromagnetic noise levels would cross over" and that "[this] time was the nineties". Electric traction drives are typically liquid-cooled and highly utilized and so are the PMSMs investigated in this work. There is no fan noise. The magnetic loading is particularly high and so is the potential for electromagnetically excited acoustic noise. The SRMs in this work are convection cooled. Fiedler et al. have shown in [FKD05] for SRMs that also there the acoustic noise is of electromagnetic and not of aerodynamic origin if the rotor is not both open and spinning at very high speeds.

Aerodynamic noise is not further considered here. Likewise, mechanical noise is left out. Mechanical noise is to a certain degree present for the drives investigated, with frequencies usually lower than those of the electromagnetically excited noise. However, its level is neither very high nor is this noise within the scope of this thesis. It was found that for auralizing the sound, mechanical noise can at times help to provide a more realistic sound impression. This should be considered where auralization is a stronger focus. This work deals with noise of electromagnetic origin and the vibrations of the machine assembly. Combined electrical

and mechanical noise can also be treated with the presented vibration synthesis process. Electromagnetic noise is caused by force fluctuations in the air-gap of an machine. For inner-rotor machines, the stator assembly including the housing is the most important part of the machine structure with respect to its acoustic characteristic. For outer-rotor machines, this is consequently the rotor. Measurements presented in chapter 7 will eventually confirm that electromagnetically excited acoustic noise is the dominant noise component for the drives treated in this thesis. This comprises PMSMs for (hybrid) electric vehicles, a switched reluctance (SR) auxiliary drive, and an SR direct drive for trains.

2.2 Basic acoustic terms and definitions

Acoustic noise is generally understood as audible sound which is unwanted or considered to be unpleasant. Vibrations may be perceived directly where they are transmitted to the body through, for example, floor, seat, or a handle. For most parts, however, not this direct path but the sound radiated from a vibrating body is of interest in terms of acoustic noise, as was shown in figure 2.2. Thus, sound power or pressure and not vibration is what eventually matters. This thesis now claims to deal with acoustic noise, yet will hardly ever deal with sound power or pressure. The reason for this is twofold. First, the vibration synthesis process described in this thesis can be readily extended to the calculation of radiated sound. Possible options are discussed in section 6.4.5. Second, the vibrations or more precisely the mean-square surface normal velocity are a measure for the radiated sound power. Below, expressions for the basic acoustic terms radiated sound power, radiation efficiency, and mean-square surface normal velocity are given.

2.2.1 Radiated sound power

The radiated sound power P of a vibrating body is calculated as

$$P = \oiint_{\partial\Omega} \boldsymbol{I}\,\mathrm{d}\boldsymbol{S} = \oiint_{\partial\Omega} p\,\boldsymbol{v}\,\mathrm{d}\boldsymbol{S}, \tag{2.1}$$

where I is the intensity, p the sound pressure and v the vibration velocity. $\partial\Omega$ is any surface enclosing the body Ω and in particular the surface of the body itself. $\boldsymbol{n}$ is a normal vector pointing outwards from $\partial\Omega$. Defining the surface normal velocity v_n as

$$v_\mathrm{n} = \boldsymbol{v} \perp \boldsymbol{S} \quad \Leftrightarrow \quad v_\mathrm{n} = \boldsymbol{v}\,\boldsymbol{n}, \tag{2.2}$$

the expression for the radiated sound power becomes

$$P = \oiint_{\partial\Omega} \overline{p\,v_\mathrm{n}}\,\mathrm{d}S. \tag{2.3}$$

From structural dynamics simulations, we obtain v_n. The radiation would need to be calculated explicitly in order to obtain p.

If the impedance of the vibrating body is matched to the wave impedance of the ambient medium, the relationship between sound pressure and velocity is defined by the free-field impedance $Z_0 = \rho_0 c$ as $p = Z_0\,v$. The density of air ρ_0 equals $1.205\,\mathrm{kg/m^3}$ under standard

conditions and the speed of sound c in air then equals 343.7 m/s. The free-field sound power P_0 can therefore be written as

$$P_0 = Z_0 \oiint_{\partial\Omega} v_\mathrm{n} v_\mathrm{n}^* \,\mathrm{d}S = Z_0 \, S \, \overline{|v_\mathrm{n}|^2}, \tag{2.4}$$

with $\partial\Omega = S$. The sound pressure p can cancels out leaving the surface velocity v_n as the only variable.

2.2.2 Radiation efficiency

From equation (2.4), we see that with matched impedances, the mean-square surface normal velocity of a vibrating body is proportional to the radiated sound power. The question remains in how far this holds for arbitrary vibrating bodies or, more precisely, electric machines. The radiation efficiency σ [CHP10] is the relationship between the radiated sound power P and the free-field sound power P_0.

$$\sigma = \frac{P}{P_0} \tag{2.5}$$

If σ equals 1, the radiated sound power can be determined directly from the mean-square surface normal velocity. Next to the shape of the vibration, the radiation efficiency depends on the relationship between the wavelength of sound $\lambda = {}^{c}/_{f}$ in the medium into which the body radiates and the size of the body. This is expressed by the product $k\,a$, where $k = {}^{2\pi}/_{\lambda}$ is the wavenumber and a the radius of the body[(i)]. For large $k\,a$ products, σ approaches unity,

$$\sigma \underset{k\,a \gg 1}{\to} 1. \tag{2.6}$$

An example illustrates this. Figure 2.3 shows the analytically determined radiation efficiencies for two basic acoustic radiators, the radiating sphere and the piston radiator [CHP10]. In addition, a numerical example calculated using the boundary element method (BEM) for machine PM-C (PM-N60p5) sitting in a test-bench housing and excited by a shape 0 force excitation [BKD08] is shown. Shape 0 forces will be explained in chapter 4. For now, we can work with the information that for the machine investigated in the example, shape 0 is the acoustically most relevant part of the force excitation. The machine housing has an approximate radius of $r = 15\,\mathrm{cm}$. The frequency axis on top of figure 2.3 is based on these $k\,a$. The machine's radiation efficiency shows an overshoot similar to the piston radiator.

From a few hundred Hertz onwards, the radiation efficiency is close to 1. Approximating a value between 0.8 and 1.2 with 1.0 results in an error lower than 1 dB, which is well within the approximation error of the overall acoustic calculations. For the given example, the mean-square surface normal velocity is proportional to the radiated sound power and can therefore be used a measure for radiated sound. We will see in the application examples in chapter 7 that most acoustic noise phenomena are found in the kilohertz range. Without further proof, the assumption is that for freely radiating electric traction drive sized electrical machines, the expression

[(i)] assuming more or less spherical bodies

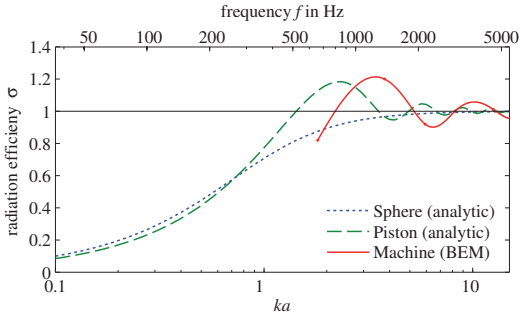

Figure 2.3: Radiation efficiency for two basic acoustic radiators, the radiating sphere and the piston radiator and a machine under shape 0 force excitation

$$P \propto \overline{|v_\mathrm{n}|^2} \tag{2.7}$$

is a valid approximation and that the mean-square surface normal velocity can consequently be used as a measure for acoustic noise.

2.2.3 Mean-square surface normal velocity

Equation (2.4) already defines the mean-square surface normal velocity $\overline{|v_\mathrm{n}|^2}$ implicitly. We will use this quantity repeatedly so that it is defined explicitly for later reference. Furthermore, when analyzing the machine vibrations, we will not always look at the entire outside surface S, but treat surface segments S_j individually.

$$S = \sum_{j=1}^{J} S_j, \tag{2.8}$$

where S_j is one of the J surfaces into which the outside surface is segmented. For a finite surface S, the mean-square surface normal velocity is then defined as:

$$\overline{|v_\mathrm{n}|^2} = \frac{1}{S} \iint_S |\boldsymbol{v}\,\boldsymbol{n}|^2 \mathrm{d}S = \frac{1}{S} \iint_S v_\mathrm{n} v_\mathrm{n}^* \,\mathrm{d}S. \tag{2.9}$$

2.3 Signal description

The acoustic modeling uses and transforms various types of signals in time and space. General signal characteristics as well as various forms of Fourier series used throughout this thesis are therefore introduced in the following.

2.3.1 Signal characteristics

This work considers functions in time t and space α with the following characteristics:

Periodicity
Signals in the time domain are assumed to be stationary. Even under transient operation we assume that these transients (speed run-ups) occur slowly in comparison with the acoustically relevant frequencies. Quantities in the air-gap of rotating machines are always periodic.

Discrete signals
Time domain signals are either sampled with a constant sampling rate or taken from analytic descriptions directly as Fourier series. Quantities in the air-gap (forces, flux densities) are sampled at equally distant points.

Fourier transform (FT) variables
For time domain signals in t, the frequency domain variable is the angular frequency ω or frequency f with $\omega = 2\pi f$,

$$f(t) \circ\!\!-\!\!\bullet\ F(\omega). \tag{2.10}$$

For spatial domain signals in α, the (spatial) frequency domain variable is u,

$$f(\alpha) \circ\!\!-\!\!\bullet\ F(u). \tag{2.11}$$

Fourier series approximation
Fourier series representations are used frequently. They are summarized below.

Conventions
Frequency domain values can by definition be complex. They are mostly not underlined. Fourier series coefficients describe peak values, i.e., amplitudes rather than root mean square (RMS) values.

2.3.2 Fourier series

Fourier series are used to analyze forces and vibrations in space and time.

Positive-negative sequence Fourier series
A function $\underline{f}(\alpha)$ shall be periodic with $\underline{f}(\alpha) = \underline{f}(\alpha + 2\pi)$ and discrete with $\alpha \in \{0,\ 1{\cdot}2\pi/N,\ 2{\cdot}2\pi/N,\ \dots\}$. Due to periodicity, $\underline{f}(\alpha)$ is fully defined by N elements in the interval $\alpha \in [0,2\pi)$. The Fourier series for this function can be written as

$$\underline{f}(\alpha) = \sum_{\nu=0}^{N_\mathrm{p}} \underline{c}_{\mathrm{p},\nu} \mathrm{e}^{\mathrm{j}\nu\alpha} + \sum_{\nu=0}^{N_\mathrm{n}} \underline{c}_{\mathrm{n},\nu} \mathrm{e}^{-\mathrm{j}\nu\alpha} \tag{2.12}$$

where

$$N_\mathrm{p} = \begin{cases} 1/2(N-2) & N \text{ even} \\ 1/2(N-1) & N \text{ odd} \end{cases} \tag{2.13a}$$

$$N_\mathrm{n} = \begin{cases} 1/2(N) & N \text{ even} \\ 1/2(N-1) & N \text{ odd} \end{cases} . \tag{2.13b}$$

and

$$N = N_\mathrm{p} + N_\mathrm{n} + 1 \quad (1 \text{ for the } \nu = 1 \text{ coefficient}) \quad . \tag{2.14}$$

Accounting for even and odd length Fourier series is important because we will frequently have Fourier series approximations with a relatively low number of elements. For example, the structural vibration response tends to decrease with increasing spatial order of the excitation shape [Jor50] so that only few shapes are taken into account. Furthermore, some Fourier series are very short even if completely developed. For the forces per stator tooth in a 6/4 SRM, for example, one pole with $6/2 = 3$ stator teeth forces forms the periodic function.

Cosine-sine sequence Fourier series

Besides the above positive-negative series description, signals can be described in a cosine-sine series as

$$\underline{f}(\alpha) = \sum_{\nu=0}^{N_\mathrm{n}} \underline{a}_\nu \cos(\nu\alpha) + \sum_{\nu=0}^{N_\mathrm{n}} \underline{b}_\nu \sin(\nu\alpha) , \tag{2.15}$$

where

$$\begin{aligned} \underline{a}_\nu &= (\underline{c}_{\mathrm{p},\nu} + \underline{c}_{\mathrm{n},\nu}) & \qquad \underline{c}_{\mathrm{p},\nu} &= 1/2\,(\underline{a}_\nu - \mathrm{j}\underline{b}_\nu) \\ \underline{b}_\nu &= \mathrm{j}(\underline{c}_{\mathrm{p},\nu} - \underline{c}_{\mathrm{n},\nu}) & \qquad \underline{c}_{\mathrm{n},\nu} &= 1/2\,(\underline{a}_\nu + \mathrm{j}\underline{b}_\nu). \end{aligned} \tag{2.16}$$

Amplitude-phase Fourier series

A third representation of the Fourier series is the amplitude-phase notation.

$$\underline{f}(\alpha) = \sum_{\nu=0}^{N_\mathrm{n}} \underline{A}_\nu \cos(\nu\alpha - \varphi_\nu) , \tag{2.17}$$

where

$$\underline{A}_\nu = \sqrt{\underline{a}_\nu^2 + \underline{b}_\nu^2} \quad \text{and} \quad \varphi_\nu = \mathrm{atan2}(\underline{b}_\nu, \underline{a}_\nu)^{(\mathrm{ii})}. \tag{2.18}$$

All of these representations are used at some point in this work.

Fourier series and discrete Fourier transform

The coefficients $\underline{c}_{\mathrm{p},\nu}$ and $\underline{c}_{\mathrm{n},\nu}$ of the above positive-negative sequence Fourier series also form the discrete Fourier transform $F(u)$ of the periodic function $f(\alpha)$. With $F(u) \bullet\!\!-\!\!\circ\, f(\alpha)$ and

(ii) atan2 is the two-argument version of the arc-tangent function. atan2(y,x) is the angle in radians between the positive x-axis and a point with the coordinates (x,y).

$u = \nu$,

$$F(u > 0) = \underline{c}_{\mathrm{p},\nu}, \tag{2.19}$$
$$F(u < 0) = \underline{c}_{\mathrm{n},\nu}, \tag{2.20}$$
$$F(u = 0) = 2\left(\underline{c}_{\mathrm{p},0} + \underline{c}_{\mathrm{n},0}\right). \tag{2.21}$$

Symmetry for real-valued signals

If $\underline{f}(\alpha)$ is real, i.e., $\underline{f}(\alpha) = f(\alpha)$, the spectrum $F(u)$ is symmetric with $F(u > 0) = F(u < 0)^*$ [(iii)]. Then

$$\underline{c}_{\mathrm{p},\nu} = \underline{c}^*_{\mathrm{n},\nu} \tag{2.22}$$

and

$$\underline{a}_\nu = \Re\left\{\underline{a}_\nu\right\} = a_\nu, \quad \underline{b}_\nu = \Re\left\{\underline{b}_\nu\right\} = b_\nu. \tag{2.23}$$

Wherever we deal with real signal (e.g., the radial air-gap force), we often use Fourier coefficients $\underline{c} = a_\nu + \mathrm{j}b_\nu$ which are, for example, stored in the lookup tables of the force models.

2-D Fourier series

Fourier series or the discrete Fourier transform are also defined in 2 or N dimensions. Within this work, quantities are dependent on time and space and 2-dimensional (2-D) Fourier series occur. As 1-dimensional (1-D) Fourier series decomposition is a linear operation, a 2-D Fourier series can generally be obtained by applying the 1-D transforms one after another to the respective dimension and this is the way it is done here. For example, the air-gap force will be first decomposed into spatial frequencies, referred to as force shapes, in the u domain. Then, (a subset of) these force shapes are decomposed in time into their (temporal) frequency components in the f domain.

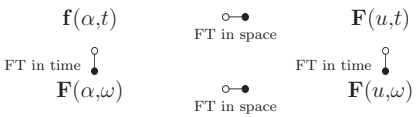

$\mathbf{f}$ and $\mathbf{F}$ are $\mathbb{C}^{N_{\mathrm{elem}} \times N_{\mathrm{steps}}}$ matrices where N_{elem} is the number of elements or sampling points in the air-gap (space) and N_{steps} the number of simulated rotor positions (time).

2.4 Machines considered in this work

The simulation and measurement examples in this work are based on several machines. These are either real machines or, for some simulation studies, derived from or similar to real machines. The results presented aim to be general. Either in the sense of characterizing the acoustic modeling process presented or in the sense of being valid for or applicable to a class of drives rather one specific sample. Eventually, it is the machine configuration and size that determines most of the acoustics characteristics. All machines but one are drives for traction applications. Among the traction drives, one is for a railway application while the rest is

[(iii)] Similar analogies also hold for imaginary time signals or real/imaginary spectra.

designed for EV or HEV applications. Characteristic machine parameters are summarized in tables in section A.1.

PMSMs

Machine PM-A (PM-N24p10) is an IPMSM for a hybrid electric vehicle. It has a large diameter, short stack length, and a high pole count. It is designed to be placed inside the gearbox and on the crankshaft. Machine PM-B (PM-N12p4) is an IPMSM for an HEV in a more conventional configuration. On the EV side, there are the machines PM-C (PM-N60p5) and PM-D (PM-N72p6). With respect to the acoustic modeling process, they are comparable and mainly differ in pole count.

SRMs

On the SRM side, two machines are analyzed. Machine SR-X (SR-8/6) is an auxiliary drive for a weaving machine[(iv)]. It is the only non-traction machine and the only machine without an output power in the double-digit kW-range. Machine SR-Y (SR-20/16or) is an outer rotor switched reluctance machine developed by Hennen in [Hen11]. Its intended application as direct drive for railway traction application requires a low-speed, high-torque drive.

[(iv)] This machine has been investigated extensively in recent publications. Fiedler and Kasper used it for acoustic measurements, modeling, and transfer function analyses in [Fie06] and [Kas10]. Fingerhuth performed psycho-acoustic analyses of its acoustic noise in [Fin09]. V. Treek implemented PWM-DITC based sensorless control with auto-parametrization on this machine in [vTre11].

3 Modeling electrical machines

The vibration synthesis process incorporates a system simulation of the drive system. The structure of the system simulation is introduced in section 3.1. While acoustic noise in electrical machines is at the heart of this thesis, the purpose of an electrical machine is to produce torque. Fundamental machine equations are therefore introduced in section 3.2. Focus is laid on PMSMs and SRMs. From these fundamental equations, machine models for use in system simulations are derived in section 3.3 including a novel PMSM model with spatial harmonics. Control of PMSMs and SRMs is discussed in section 3.4. Section 3.5 discusses the quantities that need to be determined in electromagnetic FE simulations for parametrizing the content of the system simulation model, i.e., controller, machine model, and force model.

3.1 System simulation of electrical drives

Origin of the electromagnetically excited acoustic noise is the air-gap force. In this work, the goal of the system simulation therefore is to model the electromagnetic air-gap forces of PMSMs, also those fed with non-sinusoidal currents and including spatial harmonics, as well as the forces of SRMs. The objective is to do this efficiently under arbitrary operating conditions based on a time-domain force interpolation approach. Precision is to be combined with speed. Figure 3.1 shows the block diagram of a system simulation model for electrical drives.

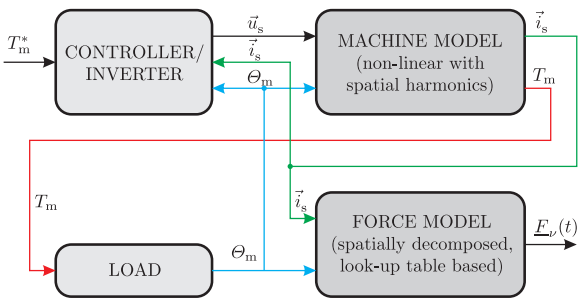

Figure 3.1: System simulation model for electrical drives with air-gap forces for acoustic analyses

The blocks controller/inverter, machine model, and load are commonly used in time domain simulations of electrical machines. The load model is not further discussed here. The blocks machine model and controller/inverter are discussed within this chapter. The fourth block in figure 3.1 is the air-gap force model, which is added for acoustic modeling. This block

delivers the forces which excite the acoustically relevant vibrations. The coefficients for the spatially decomposed force are derived in chapter 4 while the force model itself is developed in chapter 5.

3.2 Fundamental machine equations

Electrical machines are electromechanical energy converters. They convert electrical energy into mechanical energy (and vice versa) via magnetic energy. To model an electrical machine in terms of its feeding voltages and currents (electrical part), its inner flux linkage (magnetic part), and its mechanical torque (mechanical part), we need three basic "ingredients": the general stator voltage equation, the characteristic flux linkage relationship, and the general torque expression. From these three basic expressions, both the models and the control are derived. Where reasonable the conventions from [DPV11] are followed. Section A.2 lists conventions for mathematical operations on space vectors used in this work.

3.2.1 Stator voltage equation

The stator voltage equation links the stator voltage $\vec{u}_\mathrm{s}$ to the stator current $\vec{i}_\mathrm{s}$ and the stator flux linkage $\vec{\psi}_\mathrm{s}$,

$$\vec{u}_\mathrm{s} = R_\mathrm{s}\,\vec{i}_\mathrm{s} + \frac{\mathrm{d}\vec{\psi}_\mathrm{s}}{\mathrm{d}t}. \tag{3.1}$$

R_s is the stator resistance. The voltage equation can be understood as describing the electric behavior.

3.2.2 Flux linkage relationship

The flux linkage relationship describes the magnetic behavior. It is machine dependent and characterizes the operating principle of a particular type of machine.

3.2.2.1 Permanent magnet synchronous machines

The flux linkage in a permanent magnet (PM) synchronous machine is in principle described by the PM flux linkage ψ_PM along with the d- and q-axis current components i_sd and $i_\mathrm{sq}$weighted by the inductances L_d and L_q, respectively,

$$\vec{\psi}_\mathrm{s}^{\,\mathrm{dq}} = \psi_\mathrm{PM} + L_\mathrm{d} i_\mathrm{sd} + \mathrm{j} L_\mathrm{q} i_\mathrm{sq}. \tag{3.2}$$

We will see in section 3.3.1 that in a general non-linear and position dependent dq-model, this analytic expression is replaced by a lookup table (LUT) with

$$\vec{\psi}^{\mathrm{dq}} = \vec{\psi}^{\mathrm{dq}}(\vec{i}_\mathrm{s}^{\,\mathrm{dq}}, \theta_\mathrm{m}). \tag{3.3}$$

Nevertheless, many real life problems can be taken care of with a lumped parameter model as in equation (3.2).

3.2.2.2 Switched reluctance machines

Switched reluctance machines are operated in saturation. In addition to the rotor position θ_m dependence due to the saliency of stator and rotor, the phase flux linkage ψ is also a function of the current i,

$$\psi = \psi(i,\theta_\mathrm{m}). \tag{3.4}$$

In machine models, the machine characteristics are typically taken from LUTs. In SRMs, saturation is essential for a high energy conversion ratio (i.e., the ratio of active power to apparent power per magnetization cycle).

The SRM's basic working principle, the torque generation in the next section, is better understood when starting from a magnetically linear example where the flux linkage is only a function of position, allowing to write

$$\psi_\mathrm{s} = L(\theta_\mathrm{m})\, i, \tag{3.5}$$

with the position dependent inductance $L(\theta_\mathrm{m})$. For an introduction to SRMs see [DPV11].

3.2.3 Torque production and energy conversion

Despite the different working principle, i.e., torque production, of switched reluctance machines versus rotating field machines and direct current (DC) machines, a general compact torque expression valid for all electrical machines can be derived. This expression is subsequently further analyzed for SRMs and PMSMs.

We start with the energy balance equation,

$$\mathrm{d}W_\mathrm{in} = \mathrm{d}W_\mathrm{mag} + \underbrace{\mathrm{d}W_\mathrm{m}}_{=T_\mathrm{el}\,\mathrm{d}\theta_\mathrm{m}}\,. \tag{3.6}$$

The electrical input energy W_in is either stored in the machine as magnetic energy W_mag or transmitted via the shaft as mechanical energy W_m. The inertia of the shaft is here seen as part of the load so that no mechanical but only magnetic energy can be stored in the machine. The energy conversion is ideal and all losses occur externally. All quantities (W_in, W_mag, W_m, T_el, etc.) are functions of i and θ_m, which for conciseness is not explicitly written in the following.

On the electrical supply side, $\mathrm{d}W_\mathrm{in}$ depends on the product of voltage and current,

$$\mathrm{d}W_\mathrm{in} = (\vec{u})^\mathrm{T}\ \vec{i}\ \mathrm{d}t. \tag{3.7}$$

$\vec{u} = \vec{u}^{\,\alpha\beta}$ is transformed via

$$\vec{u} = \vec{u}^{\,\mathrm{dq}}\,\mathrm{e}^{\mathrm{j}\theta} \tag{3.8}$$

into a field-oriented dq-coordinate system. The voltage-to-flux-linkage relationship in the dq coordinate system is,

$$\vec{u}^{\,\mathrm{dq}} = \frac{\mathrm{d}\vec{\psi}^{\,\mathrm{dq}}}{\mathrm{d}t} + \mathrm{j}\,\frac{\mathrm{d}\theta}{\mathrm{d}t}\vec{\psi}^{\,\mathrm{dq}}. \tag{3.9}$$

For PMSMs, the dq coordinate system is the rotor-fixed xy coordinate system with $\theta = \theta_\mathrm{m}$, so that ${\mathrm{d}\theta}/{\mathrm{d}t} = \omega_\mathrm{m}$[(i)]. For SRMs, the dq system is the stator-fixed $\alpha\beta$ system with $\theta = 0$. The second term in equation (3.9) therefore disappears. We use space vectors for obtaining an expression which is valid for both rotating field machines (for which space-vectors are introduced), as well as for switched reluctance machines (for which, based on a single-phase equivalent circuit, all vectors lie in the same axis, which here is the α-axis. Due to the doubly salient nature, a two-axis transform is not possible.).

The differential magnetic energy $\mathrm{d}W_\mathrm{mag}$ is split in its i- and its θ_m-dependent parts,

$$\mathrm{d}W_\mathrm{mag} = \frac{\partial W_\mathrm{mag}}{\partial i}\mathrm{d}i + \frac{\partial W_\mathrm{mag}}{\partial \theta_\mathrm{m}}\mathrm{d}\theta_\mathrm{m}. \tag{3.10}$$

Likewise, we split the flux linkage derivative in its i- and its θ_m-dependent parts,

$$\frac{\mathrm{d}\psi}{\mathrm{d}t} = \underbrace{\frac{\partial \psi}{\partial i}}_{=:l}\frac{\mathrm{d}i}{\mathrm{d}t} + \underbrace{\frac{\partial \psi}{\partial \theta_\mathrm{m}}}_{=:e}\underbrace{\frac{\mathrm{d}\theta_\mathrm{m}}{\mathrm{d}t}}_{=\omega_\mathrm{m}} \quad \Leftrightarrow \quad \frac{\mathrm{d}\psi}{\mathrm{d}t} = \underbrace{l\frac{\mathrm{d}i}{\mathrm{d}t}}_{=:u_\mathrm{l}} + \underbrace{e\,\omega_\mathrm{m}}_{=:u_\mathrm{el}} \tag{3.11}$$

l is the incremental inductance, u_el the motional electromotive force (EMF) and e the normalized motional EMF.

If equation (3.7) and equations (3.9)-(3.11) are now recursively inserted into equation (3.6), we can group the $\mathrm{d}i$- and $\mathrm{d}\theta_\mathrm{m}$-dependent parts and obtain expressions for W_mag and T_el.

The magnetic energy W_mag becomes,

$$W_\mathrm{mag} = \int_0^{\vec{i}^{\,\mathrm{dq}}} \left(\mathbf{l}^\mathrm{dq}\vec{i}^{\,\mathrm{dq}}\right)\mathrm{d}\,\vec{i}^{\,\mathrm{dq}} \quad \Leftrightarrow \quad W_\mathrm{mag} = \int_0^{\vec{\psi}^{\,\mathrm{dq}}} \vec{i}^{\,\mathrm{dq}}\,\mathrm{d}\vec{\psi}^{\,\mathrm{dq}}, \tag{3.12}$$

with

$$\mathbf{l}^\mathrm{dq} = \begin{pmatrix} l_\mathrm{dd} & l_\mathrm{dq} \\ l_\mathrm{qd} & l_\mathrm{qq} \end{pmatrix}.$$

For the torque T_el we find,

$$T_\mathrm{el} = \underbrace{\left(\mathrm{j}\vec{\psi}^{\,\mathrm{dq}}\right)^\mathrm{T}\vec{i}^{\,\mathrm{dq}}}_{=\vec{\psi}^{\,\mathrm{dq}}\times\vec{i}^{\,\mathrm{dq}}} + \underbrace{\left(\vec{e}^{\,\mathrm{dq}}\right)^\mathrm{T}\vec{i}^{\,\mathrm{dq}} - \frac{\partial W_\mathrm{mag}}{\partial \theta_\mathrm{m}}}_{=:\frac{\partial W'_\mathrm{mag}}{\partial \theta_\mathrm{m}}}, \tag{3.13}$$

where W'_mag is the magnetic co-energy. In a compact, coordinate-system-independent form, this becomes the general torque expression valid for all types of electrical machines (keeping

(i) In the general case, the rotor-fixed coordinate system is labeled xy; dq is an (arbitrary) field-oriented coordinate system. For synchronous machines, however, the dq coordinate system is usually aligned with the xy system. For simplicity, only the dq coordinate system as both PM field-oriented and rotor-fixed coordinate system is used in this work.

in mind that for SRMs it is an per-phase expression),

$$T_{\mathrm{el}} = \left(\vec{\psi} \times \vec{i}\right) + \frac{\partial W'_{\mathrm{mag}}}{\partial \theta_{\mathrm{m}}}. \tag{3.14}$$

While applicable to all types of electrical machines, the above expression is equal to the machine shaft torque T_{m} only for a machine with a pole pair number $p = 1$ and when using power invariant space vectors. In case of amplitude invariant space vectors (which are used throughout this work), p pole pairs, and $m = 3$ phases, we obtain the torque expression,

$$T_{\mathrm{m}} = \frac{3}{2} p \left(\vec{\psi} \times \vec{i}\right) + \frac{\partial W'_{\mathrm{mag}}}{\partial \Theta_{\mathrm{m}}}, \tag{3.15}$$

with $\Theta_{\mathrm{m}} = {}^{1}/_{p}\,\theta_{\mathrm{m}}$. We will see in the following that while this expression can be simplified to the first or second term in most cases, the entire term needs to be taken into account if spatial harmonics for rotating-field machines are taken into account.

Equation (3.15) is derived using a two-axis model, which has no effect for the single-axis SRM model. If for the rotating field machines all phases are treated separately, the per-phase expression is the same as for the SRM. Only the co-energy term remains in expression (3.15), which now describes the entire torque and not only the fluctuating component. This is exploited in [SSM95] for synchronous reluctance motors (SYNCHRELs) and SRMs and is in [Sta+96] extended to PMSMs and IMs. The first quadrant co-energy loop $\psi(i)$ of an SRM (whose area is equal to the converted mechanical energy) is there compared to the co-energy ellipses of the other machine types.

3.2.3.1 Flux-linkage current loop

Similar to [SSM95] and [Sta+96], the flux-linkage current loop for a PMSM and an SRM is shown in figure 3.2. The area enclosed is equivalent to the mechanical energy converted per phase per electrical period. The four-quadrant ellipse nature for PMSMs is seen in figure 3.2a. The deviation from an ideal ellipse is due to the presence of spatial harmonics. The pulse-width-modulated (PWM) influence can be seen only marginally for the 1000 r/min curve. Figure 3.2b shows the first quadrant flux-linkage current loop for an SRM (SR-X (SR-8/6)). At 800 r/min and to a lesser extend at 1300 r/min, the tolerance band is seen. Beyond that the machine is in single-pulse operation. For both PMSMs and SRMs, the ratio of current per flux-linkage increases at high speeds.

3.2.3.2 Rotating field machines

Machine models aiming at the control of synchronous machines typically neglect spatial harmonics (including cogging torque), so that ${}^{\partial W'_{\mathrm{mag}}}/_{\partial \Theta_{\mathrm{m}}} = 0$ is assumed. The torque expression from equation (3.15) then becomes,

$$T_{\mathrm{m}} = \frac{3}{2} p \left(\vec{\psi} \times \vec{i}\right). \tag{3.16}$$

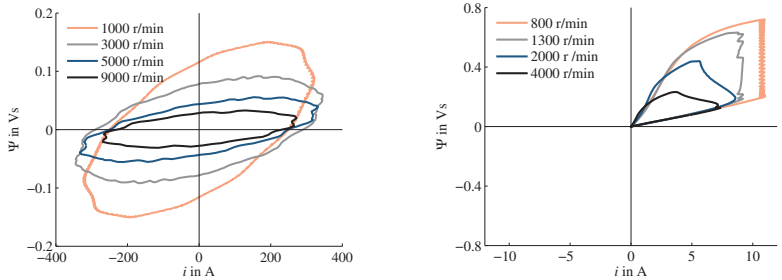

(a) PMSM PM-C (b) SRM SR-X

Figure 3.2: Co-energy loops of a PMSM and an SRM at different speeds

The area spanned by the vectors $\vec{\psi}$ and $\vec{i}$ is proportional to the torque.

The cross-product expression is furthermore equally valid for the DC machine. Where the field flux linkage ψ_f (often written as $k\Phi_\mathrm{f}$) is in the d- and the armature current i_a is in the q-axis.

If spatial harmonics are taken into account, the torque expression from equation (3.15) cannot be simplified but must be evaluated in its entirety as we will see in section 3.3.1.5 .

3.2.3.3 Salient synchronous machines

With the help of equation (3.2) and the simplification above, the basic torque expression for a salient synchronous machine becomes,

$$T_\mathrm{m} = \frac{3}{2} p \left(\psi_\mathrm{f}\, i_\mathrm{q} + (L_\mathrm{d} - L_\mathrm{q}) i_\mathrm{d} i_\mathrm{q}\right). \tag{3.17}$$

3.2.3.4 Switched reluctance machines

The torque expression for a SRM is obtained when recalling that the single-phase equivalent circuit is assumed to lie in the α-axis. The cross product from equation (3.15) is then zero and the torque expression reduces to,

$$T_\mathrm{m} = \frac{\partial W'_\mathrm{mag}}{\partial \Theta_\mathrm{m}}. \tag{3.18}$$

Phase coupling is usually neglectable and the torque is the sum of the torques of the individual phases [PP98],

$$T_\mathrm{m} = \sum_{n=1}^{N_\mathrm{phase}} \frac{\partial W'_{\mathrm{mag},n}}{\partial \Theta_\mathrm{m}}. \tag{3.19}$$

For a magnetically linear machine, we can write using equation (3.5):

$$T_{\mathrm{m,lin}} = \frac{1}{2} N_{\mathrm{r}} \frac{\mathrm{d}L(\theta_{\mathrm{m}})}{\mathrm{d}\theta_{\mathrm{m}}} i^2, \tag{3.20}$$

with $\theta_{\mathrm{m}} = N_{\mathrm{r}} \Theta_{\mathrm{m}}$. We see that for an SRM, torque depends on the derivative of the inductance with respect to position and that the torque is independent of the sign of the current.

3.3 Machine models for the system simulation

This section introduces the machine models for PMSMs and SRMs used in the system simulations. The models have a voltage input as the machines are fed from voltage source inverters. Within the context of this work, the aim is to determine torque and machine currents under arbitrary operating conditions. The electromagnetic force excitation as origin of the electromagnetic noise is subsequently determined from machine currents and rotor position.

3.3.1 Permanent magnet machine models

The electromagnetic air-gap forces are modeled in dependence of stator currents and rotor position as will be shown in chapter 4. It is therefore necessary to model the stator currents including all relevant harmonics. The fundamental currents in PMSMs with sinusoidal back-EMF are sinusoidal. The initial version of the vibration synthesis process [Boe+09; Boe+10] also assumes sinusoidal currents. The developed time-domain simulation model now allows arbitrary currents.

The model has been developed by the author for the acoustic modeling process described in this work. It has been presented in [Boe+12] on which this section builds. The spatial harmonic machine model itself is applicable beyond modeling the acoustic behavior of electrical drives wherever the effect of spatial harmonics and the respective torque fluctuations are of interest.

Switching frequency components stem from the inverter where they are generated with common modulators. The modulators are contained in the controller/inverter block in figure 3.1 and are not further discussed. Spatial harmonic current components, however, stem from the machine itself. To account for spatial harmonics in the stator currents, a generic non-linear PMSM model including spatial harmonics is introduced. It differs from a general, fundamental wave model by including the effects of air-gap harmonics on voltages, currents, flux-linkage, and torque.

3.3.1.1 Machine modeling concept

The PMSM machine models are based on the ideal rotating transformer (IRTF) modeling concept introduced by Veltman et al. in [VvB91]. Independent of their degree of detail, all models share the general structure of a generic IRTF-based PMSM model shown in figure 3.3. Only the inverse magnetization $\vec{i}_{\mathrm{s}}^{\,\mathrm{dq}}(\vec{\psi}_{\mathrm{s}}^{\,\mathrm{dq}}, \theta_{\mathrm{m}})$-block – linking current to flux linkage and eventually rotor position – changes depending on the degree of detail that is desired. Three different implementations are derived below, finally leading to the desired non-linear model with spatial harmonics.

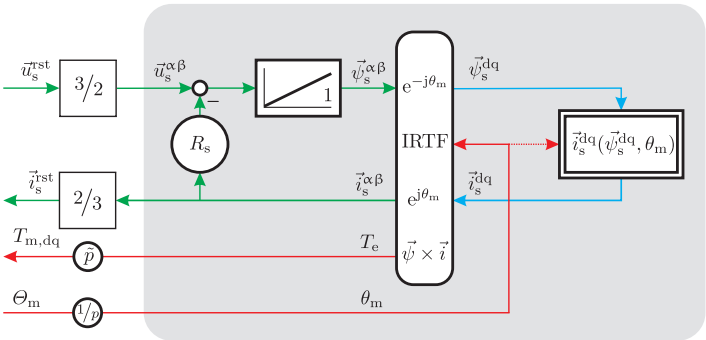

Figure 3.3: Generic structure of an IRTF based machine model for a PMSM. The $\vec{i}_s^{dq}(\vec{\psi}_s^{dq},\theta_m)$-block changes with the degree of model detail that is desired. Three representations (linear, non-linear, and non-linear with spatial harmonics) are derived.

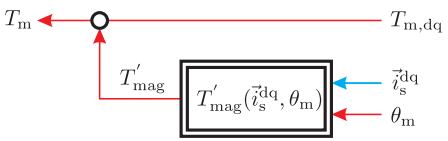

Figure 3.4: Lookup table added to the machine model in figure 3.3 for the fluctuating torque component T'_{mag} that depends on the derivative of the co-energy (see section 3.3.1.5).

The models have a voltage input as they are to be driven by a voltage-source inverter. The electrical quantities voltage, current, and flux linkage are represented by space vectors. A star connection is assumed and the zero-sequence component is left out. It can be easily integrated when needed. Electrical quantities on the left-hand side of the IRTF are in the stationary (stator-fixed) αβ-coordinate system, while quantities on the right hand side are in rotating (rotor-fixed) dq-coordinates. The IRTF itself is a three-port with two electrical and one mechanical port. It is defined by the equations

$$\vec{\psi}_s^{dq} = \vec{\psi}_s^{\alpha\beta}\, e^{-j\theta_m} \tag{3.21}$$

$$\vec{i}_s^{\alpha\beta} = \vec{i}_s^{dq}\, e^{j\theta_m} \tag{3.22}$$

$$T_{el} = \vec{\psi}_s \times \vec{i}_s, \tag{3.23}$$

where $\vec{\psi}_s$ is the stator flux linkage, $\vec{i}_s$ the stator current, and θ_m the shaft angle in electrical degrees. The 'electrical' torque T_{el} is linked to the mechanical torque at the shaft by the expression $T_{m,dq} = \tilde{p}\, T_{el}$ with $\tilde{p}$ accounting for the pole-pair number p and the Park transform factor (e.g., 3/2 in case of the amplitude invariant Park transform). The mechanical shaft angle Θ_m equals $1/p\,\theta_m$.

3.3.1.2 Linear model

Starting with a simple linear model of a salient permanent magnet machine, the $\vec{i}_{\mathrm{s}}^{\,\mathrm{dq}}(\vec{\psi}_{\mathrm{s}}^{\,\mathrm{dq}},\theta_{\mathrm{m}})$-block from figure 3.3 is only flux linkage dependent and represented by

$$i_{\mathrm{sd}} = \frac{1}{L_{\mathrm{d}}}\left(\psi_{\mathrm{sd}} - \psi_{\mathrm{PM}}\right) \tag{3.24}$$

$$i_{\mathrm{sq}} = \frac{1}{L_{\mathrm{q}}}\psi_{\mathrm{sq}} \tag{3.25}$$

as shown in figure 3.5. L_{d} and L_{q} are the d- and q-axis inductances. ψ_{PM} is the PM flux linkage in the d-axis. There is no rotor position θ_{m} dependency and the coefficients (inductances and PM flux linkage) are constant. Furthermore, cross-coupling is neglected. This model is particularly useful for didactic purposes and can be found in [DPV11].

3.3.1.3 Non-linear model

A non-linear PMSM model, which takes into account the saturation dependent change of the model parameters, is developed next. The model coefficients are no longer constant and do not follow simple analytical expressions. The general $\vec{i}_{\mathrm{s}}^{\,\mathrm{dq}}(\vec{\psi}_{\mathrm{s}}^{\,\mathrm{dq}},\theta_{\mathrm{m}})$-block from figure 3.3 is therefore represented by a lookup table (LUT). There is still no position dependency so that $\vec{i}_{\mathrm{s}}^{\,\mathrm{dq}}(\vec{\psi}_{\mathrm{s}}^{\,\mathrm{dq}},\theta_{\mathrm{m}})$ is only $\vec{i}_{\mathrm{s}}^{\,\mathrm{dq}}(\vec{\psi}_{\mathrm{s}}^{\,\mathrm{dq}})$. The two 2-D lookup tables are

$$i_{\mathrm{sd}} = i_{\mathrm{sd}}(\vec{\psi}_{\mathrm{s}}^{\,\mathrm{dq}}) \tag{3.26}$$

$$i_{\mathrm{sq}} = i_{\mathrm{sq}}(\vec{\psi}_{\mathrm{s}}^{\,\mathrm{dq}}). \tag{3.27}$$

The structure is shown in figure 3.6. We use this model as the general model for a permanent magnet machine. In particular in case of buried magnets strong changes in saturation occur. Parameters stem from either FE simulations or measurements and are also used to configure the controller.

The model does not use PM flux linkages or inductances explicitly but only the total stator flux linkage. This approach results in less elements, is computationally more efficient, and the parameters are easier to measure. However, the model can be easily modified to treat PM flux linkage and inductances separately, so that the structure from figure 3.6 becomes that of figure 3.5, with the exemption that the constant parameters for $1/L_{\mathrm{sd}}$, $1/L_{\mathrm{sq}}$, and $\vec{\psi}_{\mathrm{PM}}$ are replaced by lookup tables. Cross-coupling is taken into account by determining $L_{\mathrm{sd}}(\vec{i}_{\mathrm{s}}^{\,\mathrm{dq}})$ and $L_{\mathrm{sq}}(\vec{i}_{\mathrm{s}}^{\,\mathrm{dq}})$ according to

$$L_{\mathrm{sd}}(\vec{i}_{\mathrm{s}}^{\,\mathrm{dq}}) = L_{\mathrm{sdd}}(\vec{i}_{\mathrm{s}}^{\,\mathrm{dq}}) + L_{\mathrm{sdq}}(\vec{i}_{\mathrm{s}}^{\,\mathrm{dq}})\frac{i_{\mathrm{sq}}}{i_{\mathrm{sd}}} \tag{3.28}$$

$$L_{\mathrm{sq}}(\vec{i}_{\mathrm{s}}^{\,\mathrm{dq}}) = L_{\mathrm{sqq}}(\vec{i}_{\mathrm{s}}^{\,\mathrm{dq}}) + L_{\mathrm{sqd}}(\vec{i}_{\mathrm{s}}^{\,\mathrm{dq}})\frac{i_{\mathrm{sd}}}{i_{\mathrm{sq}}}, \tag{3.29}$$

where L_{sdd} and L_{sqq} are the self inductances and L_{sdq} and L_{sqd} the mutual inductances [Daj06].

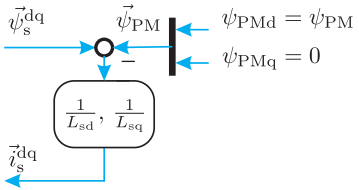

Figure 3.5: $\vec{i}_\mathrm{s}^\mathrm{dq}(\vec{\psi}_\mathrm{s}^\mathrm{dq},\theta_\mathrm{m})$-block for the generic machine model from figure 3.3 for the simplified linear model. No θ_m dependency, no cross coupling, and only constant coefficients.

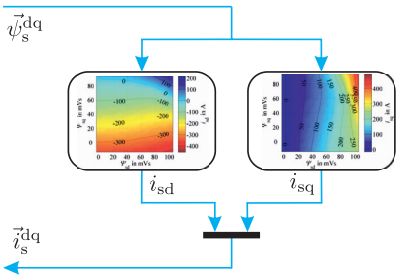

Figure 3.6: $\vec{i}_\mathrm{s}^\mathrm{dq}(\vec{\psi}_\mathrm{s}^\mathrm{dq},\theta_\mathrm{m})$-block in the non-linear model. Still no θ_m dependency. Cross coupling and saturation taken into account, $\vec{i}_\mathrm{s}^\mathrm{dq}$ currents determined by $\vec{\psi}_\mathrm{s}^\mathrm{dq}$-dependent LUT.

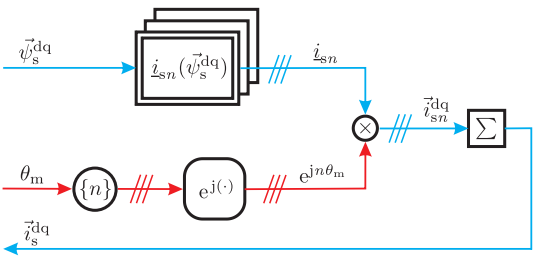

Figure 3.7: $\vec{i}_\mathrm{s}^\mathrm{dq}(\vec{\psi}_\mathrm{s}^\mathrm{dq},\theta_\mathrm{m})$-block in the spatial harmonics machine model. Explicit θ_m dependency. One complex-valued LUT for each current harmonic n.

3.3.1.4 Non-linear model with spatial harmonics

In a last step, a non-linear model with spatial harmonics is derived. In the following, this model will be referred to as *spatial IRTF model*. This model accounts for magnetomotive force (MMF) harmonics, which depend on the winding configuration, and slotting harmonics, which describe a position dependence of the air-gap permeance. The $\vec{i}_\mathrm{s}^\mathrm{dq}(\vec{\psi}_\mathrm{s}^\mathrm{dq},\theta_\mathrm{m})$-block now entails

the θ_m dependency. Each spatial harmonic $\pm n$ in the model is treated individually here. This allows for better insight into the harmonics content, to 'turn on' each harmonic individually, and provides analytic expressions for spatial-harmonics as, for example, in [BD02]. In the model, $\vec{i}_\mathrm{s}^{\,\mathrm{dq}}(\vec{\psi}_\mathrm{s}^{\,\mathrm{dq}},\theta_\mathrm{m})$ is represented by a Fourier series as

$$\vec{i}_\mathrm{s}^{\,\mathrm{dq}} = \sum_{n=-N,\ldots,-12,-6,0,6,12,\ldots,N} \underline{i}_{\mathrm{s},n}(\vec{\psi}_\mathrm{s}^{\,\mathrm{dq}})\,\mathrm{e}^{\mathrm{j}n\theta_\mathrm{m}}, \tag{3.30}$$

where the coefficient $\underline{i}_{\mathrm{s},n}(\vec{\psi}_\mathrm{s}^{\,\mathrm{dq}})$ for each harmonic n is represented as a lookup table. The sign of n describes the direction in which a harmonic rotates in the dq-system. The $\vec{i}_\mathrm{s}^{\,\mathrm{dq}}(\vec{\psi}_\mathrm{s}^{\,\mathrm{dq}},\theta_\mathrm{m})$-block for the spatial IRTF model is shown in figure 3.7. This model reduces to the non-linear model from section 3.3.1.3 in case $n = 0$.

Model parametrization

The parametrization of the model is performed as follows. The lookup table parameters are determined by (2-D static) FE simulations as will be further discussed in section 3.5.2. For a set of $\vec{i}_\mathrm{s}^{\,\mathrm{dq}}$ points in the dq-current plane (typically filling the second quadrant), the flux linkage $\vec{\psi}_\mathrm{s}$ is calculated at a number of rotor positions to obtain its rotor position dependent characteristics. The magnetization characteristic $\vec{\psi}_\mathrm{s}^{\,\mathrm{dq}}(\vec{i}_\mathrm{s}^{\,\mathrm{dq}},\theta_\mathrm{m})$ is then inverted to $\vec{i}_\mathrm{s}^{\,\mathrm{dq}}(\vec{\psi}_\mathrm{s}^{\,\mathrm{dq}},\theta_\mathrm{m})$ and interpolated onto a ψ_sd-ψ_sq grid so that the lookup tables have equally spaced supporting points. The current $\vec{i}_\mathrm{s}^{\,\mathrm{dq}}(\vec{\psi}_\mathrm{s}^{\,\mathrm{dq}},\theta_\mathrm{m})$ is now decomposed into its positive and negative sequence Fourier series elements $\underline{i}_{\mathrm{s},n}(\vec{\psi}_\mathrm{s}^{\,\mathrm{dq}})$ from equation (3.30).

The transformation steps, decomposition, interpolation, and re-mapping, need to be performed carefully. From the authors' experience the maps $\underline{i}_{\mathrm{s},n}(\vec{\psi}_\mathrm{s}^{\,\mathrm{dq}})$ become (numerically) noisy for higher harmonics. The Fourier series is therefore typically limited to 2 or 3 spatial harmonics. The results presented here take into account the two spatial harmonics of order 6 and 12.

The parameters for the non-linear model from section 3.3.1.3 are determined in the same way, except that the average over the rotor position is formed. Linearization then delivers the parameters for a linear model as described in section 3.3.1.2.

3.3.1.5 Fluctuating torque component from position dependent change in co-energy

Even though the model from figure 3.3 now includes spatial-harmonics and as such is a spatial-harmonics model in terms of the electrical quantities voltage, current, and flux linkage, it does not yet deliver the correct fluctuating torque. This becomes clear when looking at the general torque expression (3.15) from section 3.2.3. A spatial model requires to also consider the position dependence of the co-energy W'_mag to account for the resulting torque component $T'_\mathrm{mag} = \partial W'_\mathrm{mag}/\partial\Theta_\mathrm{m}$. While T'_mag delivers the working torque in SRMs, it is a fluctuating component in PMSMs. The torque T_m is expressed by

$$T_\mathrm{m} = T_\mathrm{m,dq} + T'_\mathrm{mag}. \tag{3.31}$$

A simple example why the total torque T_m is not fully described by $T_\mathrm{m,dq} = \tilde{p}\,\vec{\psi}_\mathrm{s} \times \vec{i}_\mathrm{s}$ is cogging torque, which also occurs when there is no current but still PM flux in the machine. A detailed analysis of the torque components can be found in [BA10]. Equation (3.31) can be

derived based on the incremental energy balance between electrical, mechanical, and magnetic energy. The co-energy $W'_{\mathrm{mag}}(\vec{i}_{\mathrm{s}}^{\,\mathrm{dq}},\theta_{\mathrm{m}})$ is determined by FE simulations. Figure 3.4 shows the resulting lookup table which is integrated into the machine model. On a side note, equation (3.31) contains the derivative of the machine's total co-energy. This is unlike the general instantaneous per-phase torque expression of an electrical machine where $T'_{\mathrm{mag,phase}} = \partial W'_{\mathrm{mag,phase}}/\partial\Theta_{\mathrm{m}}$ [Sta+96].

3.3.1.6 Time domain evaluation of the spatial model

Simulation results in the time domain for a stationary operating point give an insight into the variables of the model. The simulations shown are based on the PM-B (PM-N12p4) machine, which is a 3-phase, 12-slot/4-pole-pair interior permanent magnet synchronous machine for a hybrid electric vehicle. Peak torque is 150 Nm and the maximum speed is 10 000 r/min (see table A.2). The machine is fed from a 400 V dc link. In figure 3.8, speed is set to $n = 2000\,\mathrm{r/min}$ and the mean torque T_{m} equals 118 Nm. The currents are proportional-integral (PI) controlled and the voltage is space-vector modulated. The switching frequency f_{switch} is set to 10 kHz.

Figure 3.8a observes the stator currents $i_{\mathrm{s}\alpha}$ and $i_{\mathrm{s}\beta}$ on the left-hand side of the IRTF in the stationary (stator-fixed) $\alpha\beta$-system. Frequency components related to spatial harmonics and switching frequency components are noticeable.

The stator flux linkage ψ_{sd} and ψ_{sq} in figure 3.8b is taken from the right-hand side of the IRTF in the rotating (rotor-fixed) dq-system. It can be easily seen that the main ripple component is the 6^{th} multiple of the electrical frequency f_{el} stemming from the fundamental spatial harmonic.

Two different ways for obtaining the torque are compared in figure 3.8c. First, the torque $T_{\mathrm{m}} = T_{\mathrm{m,dq}} + T'_{\mathrm{mag}}$ from the machine model (figure 3.3 with figure 3.4) is shown. Second, we jump ahead and compare T_{m} against the torque T_{LUT} from the tangential shape 0 force of the force model. The latter will be introduced in section 5.1, figure 5.2. At 180°el, the plot order is flipped so that T_{m} is shown on top of T_{LUT}. T_{m} is based on integral quantities (flux linkage, current, co-energy), while T_{LUT} is formed from the local tangential force density in the air-gap, which is multiplied by the air-gap radius and then integrated to form torque. Both torque curves agree well and help to validate the accuracy of the model as they are determined differently. While the switching frequency ripple – given its high frequency and considering the inertia of the shaft – cannot be observed outside the machine, the torque ripple related to spatial-harmonics is of interest for most applications.

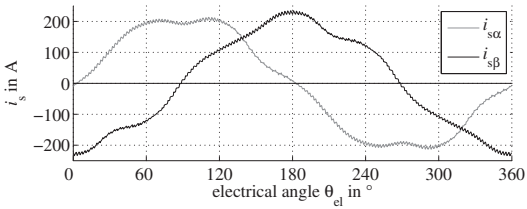

(a) Stator currents $i_{s\alpha}$ and $i_{s\beta}$ in the stationary (stator-fixed) $\alpha\beta$-system. Frequency components related to spatial harmonics and switching frequency components are noticeable.

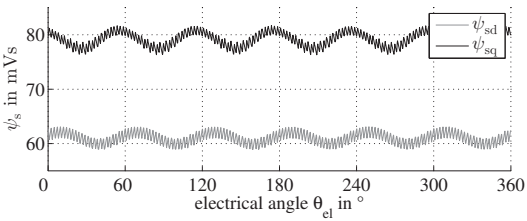

(b) Stator flux linkage ψ_{sd} and ψ_{sq} in the rotating (rotor-fixed) dq-system. The fundamental fluctuating component is the 6^{th}multiple of the electrical frequency f_{el} from the fundamental spatial harmonic.

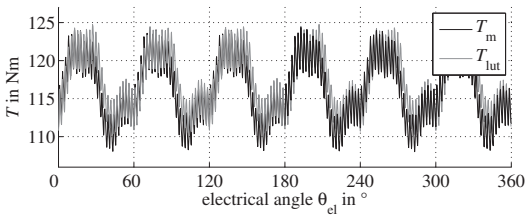

(c) Torque $T_m = T_{m,dq} + T'_{mag}$ from the spatial harmonic machine model (figure 3.3 with figure 3.4) vs. the torque T_{LUT} from the tangential shape 0 force of the force model (figure 5.2)

Figure 3.8: Characteristic variables of the non-linear spatial-harmonic machine model under stationary operation at $n = 2000\,\mathrm{r/min}$ and $T_m = 118\,\mathrm{Nm}$ with switching frequency $f_{switch} = 10\,\mathrm{kHz}$.

3.3.1.7 Frequency domain evaluation of the spatial model

Acoustic characteristics of time signals are often better seen when observed in the frequency domain. The analysis of air-gap forces and surface normal vibrations is therefore mostly performed in the frequency domain in the applications chapter 7. This is now done here for

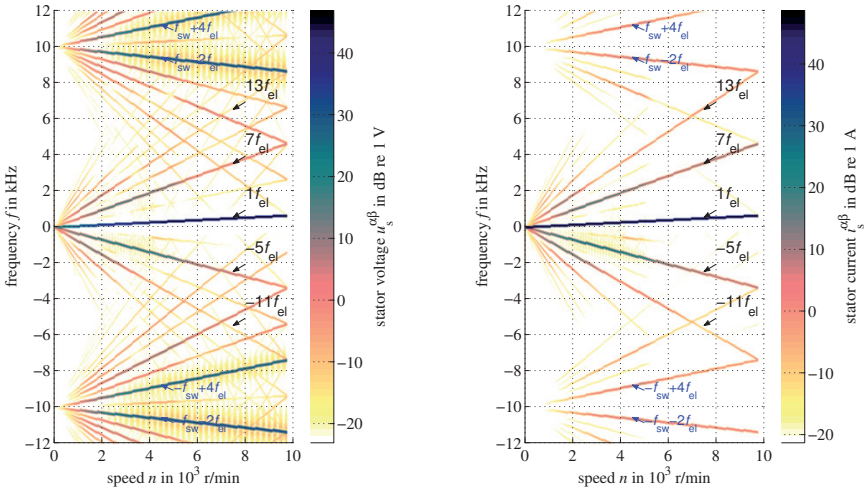

(a) Voltage (b) Current

Figure 3.9: Spectrograms of stator voltage and current during run-up including spatial-harmonic and SVM-related current harmonics (machine PM-B)

the stator voltage $\vec{u}_s^{\alpha\beta}$ and the stator current $\vec{i}_s^{\alpha\beta}$. The results shown are based on a 10 s run-up from 0 to 10 000 r/min at full-load.

Since the zero-sequence component was omitted, the space vectors are 2-dimensional and can therefore be expressed by complex time signals as $\underline{u}_s^{\alpha\beta}(t)$ and $\underline{i}_s^{\alpha\beta}(t)$. Figure 3.9 shows the two-sided spectrogram (i.e., the positive and negative sequence frequency components), which was motivated by [Vel+03]. Both, the spatial harmonics related frequency components {-5, +7, -11, +13...}$\cdot f_{\mathrm{el}}$, as well as the space-vector modulation (SVM) related switching frequency side bands ($\pm f_{\mathrm{switch}} - 2f_{\mathrm{el}}, \pm f_{\mathrm{switch}} + 4f_{\mathrm{el}}, \ldots$) [BH90] can be observed in voltage and current. Due to the low pass characteristic of an electrical machine ($i \propto {}^{u}/_{(R+sL)}$), the magnitudes of the switching frequency components generated by the voltage source inverter are lower in the current than they are in the voltage waveforms. The spatial harmonics, however, are generated inside the machine and are therefore stronger in the current than they are in the voltage waveforms. They are visibly stronger in the voltage waveforms when controller tries to compensate them, which is when the harmonics are within the PI regulator bandwidth and when there is still voltage headroom. Once the end of the base-speed range (and thus the voltage limit) is reached, i.e., at approximately 5000 r/min, they abruptly decrease in the voltage even though the dq-current set point only changes slowly.

3.3.1.8 Remarks on the spatial model

The spatial model has almost the same accuracy as the finite element results that are used to parametrize it. Alongside the $\vec{i}_s^{\mathrm{dq}}(\vec{\psi}_s^{\mathrm{dq}}, \theta_m)$-block for the spatial model from equation (3.30)

and figure 3.7, the corresponding $\vec{\psi}_\mathrm{s}^\mathrm{dq}(\vec{i}_\mathrm{s}^\mathrm{dq},\theta_\mathrm{m})$-block has been created. If constant dq-currents (as in the FE simulations) are fed to this $\vec{\psi}_\mathrm{s}^\mathrm{dq}(\vec{i}_\mathrm{s}^\mathrm{dq},\theta_\mathrm{m})$-block, the same fluctuating flux linkage as in the FE results is obtained. This then – let aside very minor fluctuations – leads to the original constant dq-currents if fed to the $\vec{i}_\mathrm{s}^\mathrm{dq}(\vec{\psi}_\mathrm{s}^\mathrm{dq},\theta_\mathrm{m})$-block. Very good agreement between measured and FE-calculated flux linkages and currents is reached in [Mil+05] so that this is also to be expected from this model. Measured and simulated currents for machine PM-A (PM-N24p10) based on this model are shown in figure 7.4. As long as transient effects (eddy-current) on the flux linkage and stator current can be neglected, circuit coupled FE simulations can therefore be replaced by this significantly faster model.

3.3.1.9 Comparing the spatial IRTF model with spatial models from literature

A comparison is now drawn between the above introduced spatial IRTF model and spatial-harmonics machine models from literature [SLT09; Her+11; Moh+12]. All models are system-simulation models and aim to achieve accuracies which converge against the underlying FE model. They all use static FE simulations at the front-end for creating lookup-table-based models. The inverse-magnetization representation and in particular the individual treatment of the spatial harmonics are unique features of the model presented above.

Individual treatment of spatial harmonics

Spatial harmonic PMSM models usually add the θ_m dimension to the lookup table [SLT09; Her+11; Moh+12]. As mentioned above, better insight into the machine is obtained due to the harmonics' individual treatment in the spatial IRTF model. In addition, model size is reduced, stability is increased, and the simulation is sped up. The number of lookup tables is increased by the number of harmonics taken into account, but they stay 2-D rather than obtaining a 3-dimensional (3-D) $\vec{i}_\mathrm{s}^\mathrm{dq}(\vec{\psi}_\mathrm{s}^\mathrm{dq},\theta_\mathrm{m})$ table when adding the θ_m dimension. The number of harmonics, usually 2 to 3, is lower than the θ_m steps in the position dimension for which 60 is usually a good starting point. Section 7.1.2 compares simulated and measured currents and shows for the respective machine that two pairs of harmonics are sufficient.

Inverse magnetization vs. direct form

Owing to its IRTF based nature, the spatial IRTF model can maintain the simple, physically-based structure shown in figure 3.3. The spatial IRTF model is an *inverse magnetization model*. Current is obtained as a function of flux linkage (cf. figure 3.3). The system simulation model contains no differentiator but only an integrator. The FE data, which delivers flux linkage as function of current, is inverted when parametrizing the model. While this structure is routinely used for SRM models (cf. section 3.3.2), it is not common place for PMSM models. The models from [SLT09; Her+11; Moh+12] all use what [CM89] calls the *direct form*. [SC79] points out that models using an inverse magnetization $i(\psi,\theta_\mathrm{m})$ representation are more accurate, require less input data and furthermore avoid differential coefficients, which occur in the direct models. Within this work the direct models are called *incremental inductance models*. An implementation for the SRM is discussed in section 3.3.2.

For the spatial IRTF model, as well as [SLT09] and [Moh+12], separation of current- and permanent-magnet-excitation related flux linkage or the evaluation of inductances is not required. It is, however, required for the direct-form dq-reference-frame model from [Her+11], which uses a larger number of 3-D look-up tables as a result of splitting up the total flux linkage.

The model in [SLT09] uses a 3-D lookup table which outputs three-phase flux linkages as function of dq-current and rotor position. It then uses a differentiator in the system simulation to determine the three phase voltages.

The αβ-reference frame model from [Moh+12] uses lookup tables for the flux linkages only but requires an interpolation method which supports interpolation operator for the first partial derivatives.

Interpolation

The spatial IRTF model has been implemented using linear interpolation for the table lookup whereas [Her+11; Moh+12] use spline interpolation. Mohr et al. point out in [Moh+12] that spline interpolation allows working with a coarser subdivision and is well-suited for evaluation of the first partial derivatives. Derivatives do not occur in the spatial IRTF model. The decomposition and reduction of the θ_m-domain furthermore reduce the data, so that the for the remaining 2-D tables size is not a issue. For the spatial IRTF model, spline interpolation is used for obtaining the lookup table parameters. FE data for arbitrarily distributed points in the dq-current plane is mapped onto a rectangular grid in the dq-flux-linkage plane. Linear interpolation then leads to high simulation speeds.

Torque representation

The models in [SLT09; Moh+12] use a lookup table for the total torque. In the spatial IRTF model as wells as in the model from [Her+11], torque is represented as in equation (3.15) so that the $\vec{\psi} \times \vec{i}$ term from analytic models is maintained. Only here, the data for $T'_\mathrm{mag} = {}^{\partial W'_\mathrm{mag}}/_{\partial \Theta_\mathrm{m}}$ is determined explicitly. In [Her+11], $T'_\mathrm{mag} = T_\mathrm{FEM} - T_\mathrm{m,dq}$ is used, which here serves for validation.

FE simulation rotor stepping angle

An interesting side note is that both [SLT09] and [Moh+12] stress that for the FE input simulating 60°el is sufficient. I mentioned this in [BKD08]. It appears that, despite being rather obvious, this simplification is often left out in electromagnetic simulations of three-phase machines and that 180°el (if not 360°el) are simulated.

Commercial software

PMSM machine models with saturation effects and spatial harmonics have in recent years also been implemented in commercial electrical machine modeling and design software. The model from [SLT09] is implemented in the Maxwell/ Simplorer software by ANSOFT (now a subsidiary of ANSYS). The software JMAG by JSOL allows extracting models with spatial harmonics called JMAG-RT (where RT supposedly stands for real-time) according to [JSO10]. Implementation details, however, appear to be undisclosed.

3.3.2 Switched reluctance machine models

For PMSMs, the above discussed model representation using lookup tables rather than (constant) lumped parameters can still be seen as somewhat off-standard. The model representation of SRMs has been using machine characteristic lookup tables for decades as standard model due to the non-linear nature of the SRM. Early publications in the field are [SC79] and [CM89].

The general SRM model structure is shown in figure 3.10. Recalling that in section 3.2.3 a

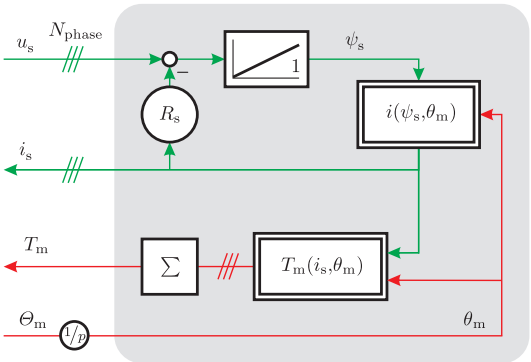

Figure 3.10: Generic structure of an SR machine model

unified torque expression was derived for PMSMs and SRMs, it does not come as a surprise, that PMSM and SRM model also share many characteristics and can be unified. The SRM model in figure 3.10, for example, is found, when in the PMSM model in figure 3.3, the phase currents are fed directly to the model. θ_m in the IRTF is set to zero and can then be omitted. Due to the single-axis nature of the SRM, $T_{m,dq} = \vec{\psi} \times \vec{i}$ equals zero and in terms of torque only the co-energy derivative related term from figure 3.4 remains leading to the structure shown in figure 3.10.

In the PMSM model, only the fluctuating torque component is taken from a lookup table. The average torque is determined by $T_{m,dq} = \vec{\psi} \times \vec{i}$ so that the overall electrical-to-mechanical energy balance is guaranteed. For SRMs, the torque is entirely read from a lookup table and no direct link between electrical and mechanical side exists. Erroneous parametrization can here easily lead to unphysical results. An energy balance can prevent this.

For modeling SRMs, two different types of models presented in literature are used in this work. First, single-phase lookup table models and second, a reluctance network model.

3.3.2.1 Single-phase lookup model

The single-phase lookup model can be seen as the standard model for SRMs. Two different core implementations are shown, *inverse magnetization* or *incremental inductance*.

Inverse magnetization model

In the *inverse magnetization model*, the $i(\psi_s,\theta_m)$ block from figure 3.10 is implemented as a lookup table,

$$i = i(\psi_s,\theta_m). \tag{3.32}$$

From the singe-phase lookup models, this is the model chosen for all simulation results presented in the following. Figure 3.11 shows an inverse magnetization table $i(\psi_s,\theta_m)$ and a torque lookup table $T_m(i_s,\theta_m)$.

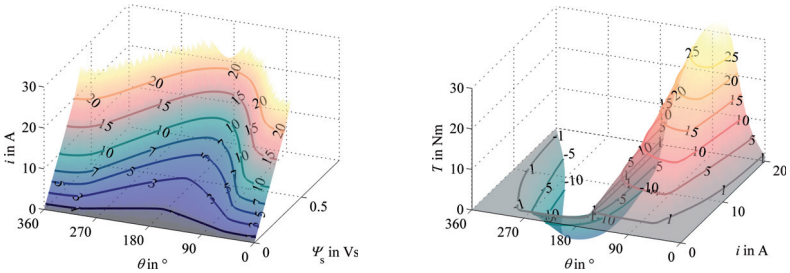

(a) inverse magnetization table $i_\mathrm{s}(\psi_\mathrm{s},\theta_\mathrm{m})$ (b) torque lookup table $T_\mathrm{m}(i_\mathrm{s},\theta_\mathrm{m})$

Figure 3.11: SRM lookup table examples

Incremental inductance model

In the spatial PMSM model review in section 3.3.1.9, an *incremental inductance model* for a PMSM was discussed. For an SRM, such a model takes the form

$$\frac{\mathrm{d}i_\mathrm{s}}{\mathrm{d}t} = \frac{\frac{\mathrm{d}\psi_\mathrm{s}}{\mathrm{d}t} - e}{\frac{\partial\psi_\mathrm{s}}{\partial i_\mathrm{s}}}, \tag{3.33}$$

with

$$e = \frac{\partial L}{\partial\theta_\mathrm{m}}\, i_\mathrm{s}\, \omega_\mathrm{m} \quad \text{and} \quad \frac{\partial\psi_\mathrm{s}}{\partial i} = L + \frac{\partial L}{\partial i_\mathrm{s}}\, i_\mathrm{s}. \tag{3.34}$$

The back-EMF term e and the torque-relevant position dependence of the inductance (cf. - equation (3.20) for torque in a linear SRM) can be observed directly. The model size increases, but this is not too grave. Due to the single-phase nature of the SRM, coupling terms can be ignored. The number of lookup tables increases from one to two or three (depending on whether or not $\partial\psi_\mathrm{s}/\partial i_\mathrm{s}$ is split up). These tables are $\partial L/\partial\theta_\mathrm{m}(i_\mathrm{s},\theta_\mathrm{m})$, $L(i_\mathrm{s},\theta_\mathrm{m})$, and $\partial L/\partial i_\mathrm{s}(i_\mathrm{s},\theta_\mathrm{m})$. Due to additional operations and the differential coefficients, the model is less accurate than the inverse magnetization model. Given that $\mathrm{d}i/\mathrm{d}t$ and not $\mathrm{d}\psi/\mathrm{d}t$ is integrated, the incremental inductance model does not fit exactly into the model structure in figure 3.10.

3.3.2.2 Reluctance network model

When faults and unbalances are investigated, phase coupling can no longer be neglected, preventing the use of single-phase models. If the direct lookup based approach is then continued, the order of FE solutions required for model parametrization increases with the number of phases. Furthermore, the reduction of the FE domain to one pole of the machine is no longer possible.

To cope with this, a reluctance network model [PL91; Mil95] has been developed in [Hen11]. For surface PMSMs, a reluctance network model is presented in [Ram+09]. A reluctance network is a representation of the magnetic circuit of the machine as a lumped parameter model. The air-gap reluctances are non-linear elements in the model. Its nature is quite different compared to the above $i(\psi,\theta_\mathrm{m})$ lookup table. The generic model shown in figure 3.10,

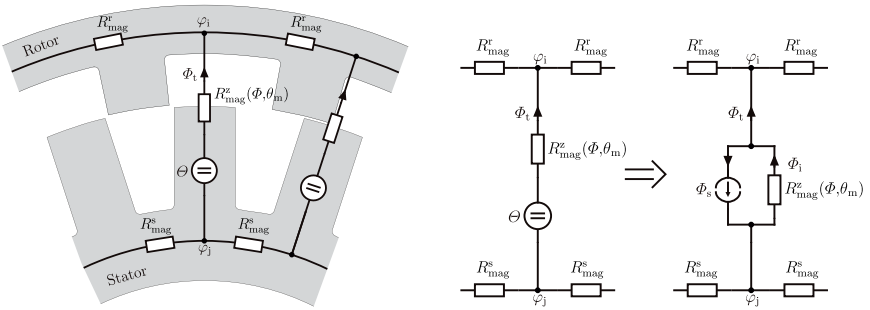

(a) Segment of the model

(b) Conversion from MMF source to flux source

Figure 3.12: Reluctance network model [Hen11]

however, remains unaltered. The reluctance network is also a representation of the $i(\psi,\theta_m)$ block.

A segment of the reluctance network is shown in figure 3.12a. It is first transformed from a MMF-source to a flux-source model as shown in figure 3.12b. In matrix notation, the model is then defined as

$$\mathbf{G}_{mag}\boldsymbol{\varphi} = \boldsymbol{\Phi}, \tag{3.35}$$

where $\mathbf{G}_{mag}$ is the magnetic conductance matrix, $\boldsymbol{\varphi}$ are the magnetic potentials, and $\boldsymbol{\Phi}$ is the source flux. $\mathbf{G}_{mag}$ contains the inverses of the magnetic reluctances $R_{mag}(\psi,\theta_m)$. For each model time step, equation (3.35) is solved recursively.

The link to the electric circuit is formed at the input of the reluctance network, where the source flux $\boldsymbol{\Phi}$ is a function of the flux linkage ψ,

$$\boldsymbol{\Phi} = f(\psi), \tag{3.36}$$

and at the output, where the current i is a function of the magnetic potentials $\boldsymbol{\varphi}$,

$$i = f(\boldsymbol{\varphi}), \tag{3.37}$$

with the model matrix $\mathbf{G}_{mag} = \mathbf{G}_{mag}(\psi,\theta_m)$. As such it can be used as another implementation of the $i(\psi,\theta_m)$ block in figure 3.10. All stator coils, however, are treated individually so that in figure 3.10, N_{phase} becomes N_s.

To parametrize the model, the same number of FE simulations is required as for the single-phase lookup model. Due to the required iterations and the N_s instead of N_{phase} signals (the machine for which this is used has 4 poles) system simulation models are about one order slower than the direct lookup models. This is still orders of magnitudes faster than solving the non-linear FE model at each time step.

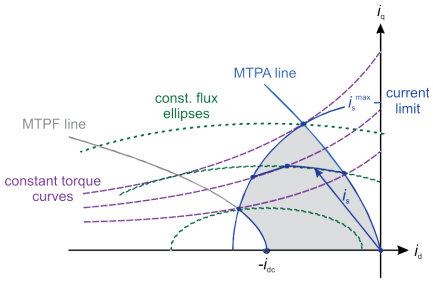

Figure 3.13: IPMSM dq-current limits

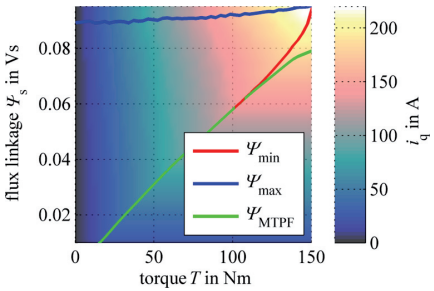

Figure 3.14: Exemplary lookup table for i_q as function of T and ψ_s

3.4 Machine operation

In section 3.2, the fundamental machine equations were introduced, section 3.3 showed how simulation models are built from them. Machine operation and control is discussed in the following.

3.4.1 Operation of permanent magnet synchronous machines

In this work, PMSMs are operated with field-oriented current control. Figure 3.13 shows the dq-current limits for an IPMSM for operation with positive torque. In this example, the maximum current i_s^{max} is larger than the short-circuit current i_{sc}. This is the usual design for PMSMs operated in deep field-weakening as in automotive traction applications. The save state is short-circuiting the machine terminals preventing over-voltages on the DC-link side in case of faults at speeds higher than the base speed.

The shaded area in figure 3.13 encompasses the dq-currents used during normal operation and positive torque. Four boundaries limit this area. First, i_q must be larger than zero to deliver positive torque. Second, maximum torque per ampere (MTPA) is generally loss-optimal operation. This line is followed in the base speed range. Third, the current limit is taken into account by the maximum current (MA) line. The voltage limit is reached when the voltage ellipse, whose radii decrease with speed, intersects with the MTPA line and current limit in a single point. The voltage limit then drives the chosen operating point away from the MTPA line into the shaded area, either along a constant power line or eventually along the current limit. At very high speeds, torque is only limited by the maximum achievable flux which occurs along the maximum torque per flux (MTPF) line. For the derivation of the trajectories, it is referred to [DPV11]. How the lumped machine parameters and the electromagnetic forces are determined for the operating range is shown section 3.5.

Controller implementation

The controller itself does not know about any of the above limits explicitly. It reads the current set points from a lookup table,

$$\vec{i}_{\mathrm{s}}^{\,\mathrm{dq*}} = \vec{i}_{\mathrm{s}}^{\,\mathrm{dq*}}(T_{\mathrm{m}}^{*},\hat{\psi}) \quad \text{with} \quad \hat{\psi} = \hat{\psi}(u_{\mathrm{dc}},n), \tag{3.38}$$

where T_{m}^{*} is the torque set point and $\hat{\psi}$ the maximum achievable flux linkage amplitude depending on DC-link voltage u_{dc} modulation, and machine speed n. The q-axis current of the LUT for the machine PM-B is exemplarily shown in figure 3.14. The implementation is based on [Bae+03]. The lookup table is found by inverting the expression used for figure 3.13 where torque and flux are shown as a function of dq-current. An important advantage of this maximum flux linkage based implementation is that a variable DC-link voltage is automatically accounted for. The DC-link voltage can vary with the state of charge (SOC) of the battery or when operated on a controlled DC link [vHoe+10]. For the results shown in this work, the DC-link voltage is set to a constant value so that the dq-current becomes a function of torque and speed. PI d- and q-axis current-controllers regulate the currents according to the set point.

3.4.2 Operation of switched reluctance machines

For switched reluctance machines, two control concepts, a low-level and a high-level one, are used in this work.

Hysteresis bang-bang current control (HBCC)

First, analog hysteresis bang-bang current control (HBCC) is described. Its principle is that within a certain rotor position range, a phase is active and its current is kept near a usually constant value within a tolerance band. There are only five operating point dependent parameters (upper and lower current amplitude i^{max} and i^{min}, turn-on angle θ_{on}, free-wheeling angle θ_{free}, and turn-off angle θ_{off}). Passing of any of these limits leads to a logic operation. The curve on the left-hand side of figure 3.15 shows a typical current HBCC current waveform. Despite being simple, HBCC can still be the method of choice for very high-speed machines where sampled system are not fast enough.

HBCC control originated from analog implementations. However, the ease of determining the control parameters and the low computational effort is the reason why HBCC is also regularly used in sampled system for low performance drives or initial tests. Sampled systems can only react at discrete instants in time and for HBCC, the sampling time is usually not negligibly small. If a limit is passed, the controller only sees this at the next sampling time. The curve on the right hand side of figure 3.15 shows this. The current can only be maintained near but not inside the tolerance band. A digital implementation of hysteresis bang-bang control is used in section 7.4 where measured and synthesized vibrations are compared for a two-pole switched reluctance machine.

Predictive direct instantaneous torque control (PWM-DITC)

The second control technique is PWM based predictive DITC, or short PWM-DITC [Fue07]. With the earlier DITC [Ind02; ID03], it shares the characteristic that it allows to control – hence its name – the instantaneous torque. DITC is analog and observer-based while PWM-DITC is digital and model-based.

There is an invertible relationship between current and flux linkage so that torque can also be expressed as $T_{\mathrm{m}} = T_{\mathrm{m}}(\psi,\theta_{\mathrm{m}})$. Thus, if at a given position, a certain torque is required, the

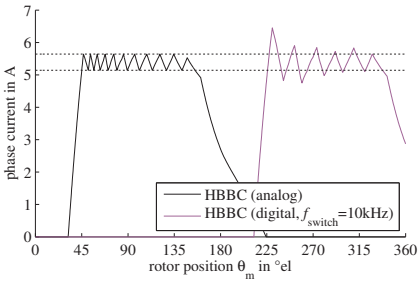

Figure 3.15: Hysteresis bang-bang control currents ($n = 1000\,\mathrm{r/min}$, $T = 5\,\mathrm{Nm}$)

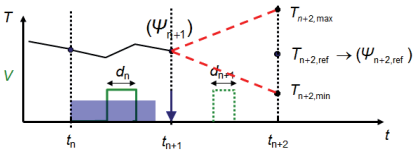

Figure 3.16: Flux linkage and torque prediction in PWM-direct instantaneous torque control (DITC) [Bra07]

respective flux has to be linked with the phase. Flux linkage is chosen over current because with a voltage source inverter, the flux linkage increment is directly determined by the duty cycle. The working principle is shown in figure 3.16. There is a two-sample prediction horizon because at time t_n, the duty cycle for time t_{n+1} can be set, which then leads to the desired flux linkage and torque at t_{n+2}. For this example, we assume only one active phase. In the overlap region, torque sharing algorithms are overlaid [BHD12]. The outer rotor switched reluctance machine analyzed in section 7.5 is operated with PWM-DITC.

Comparison

Tolerance band current control allows within limits to influence the machine behavior in terms of torque ripple, losses, or acoustic noise by varying the control parameters. With focus on acoustics, this has been exploited in [Kas10] under the name early single-pulse strategy (ESPS). Model-based control allows full control over the machine states and can thus optimally control certain characteristics which is torque in PWM-DITC but can also be the radial force. Work in this field is currently underway at the Institute for Power Electronics and Electrical Drives (ISEA).

In terms of switching harmonics, PWM-DITC and sampled HBCC have a defined spectrum due to the PWM frequency while DITC and analog HBCC have a wide quasi-random spectrum where the switching frequency is defined by current rise- and fall-time and tolerance-band width.

3.5 Electromagnetic FE simulations

This section lists the result quantities that are obtained in the FE simulations and explains how these simulations are conducted for PMSMs and SRMs.

3.5.1 Result quantities

From the electromagnetic FE simulations, two groups of results are obtained. First, the magnetic forces in the air-gap as local quantities and second, flux linkages, inductances, and

magnetic energies as global quantities.

3.5.1.1 Magnetic forces

Magnetic air-gap forces are calculated in two ways, by the virtual work method (vw) and by means of the Maxwell stress tensor (mx).

Virtual work forces

In section 3.2.3, we have derived the torque expression from the energy balance equation (3.6). The expression for the global magnetic co-energy W'_{mag} in equation (3.13) is based on the integral quantities flux linkage ψ and current i which are observable from the terminals of the machine. The local magnetic forces can be derived from the local magnetic co-energy. The co-energy is now represented by the local field quantities magnetic flux density B and magnetic field strength H, whose integral representations can be understood as ψ and i.

The energy stored in the region Ω (which in the FE domain represents an element) is given by

$$W'_{\mathrm{mag}} = \int_{\Omega} \int_{0}^{\boldsymbol{H}} \boldsymbol{B}^{\mathrm{T}} \mathrm{d}\boldsymbol{H}\, \mathrm{d}\Omega. \tag{3.39}$$

The virtual work force $F_{\mathrm{vw},s}$ acting in the direction s ($s = x,y,z$) is given by the derivative of the co-energy with respect to the direction s

$$F_{\mathrm{vw},s} = \left.\frac{\partial W'_{\mathrm{mag}}}{\partial s}\right|_{i=\mathrm{const}}. \tag{3.40}$$

Combining the above two expressions for force and co-energy, we obtain the expression for the *virtual work forces* [CM84],

$$F_{\mathrm{vw},s} = \int_{\Omega} \boldsymbol{B}^{\mathrm{T}} \frac{\partial \boldsymbol{H}}{\partial s}\, \mathrm{d}\Omega + \int_{\Omega} \int_{0}^{\boldsymbol{H}} \boldsymbol{B}^{\mathrm{T}} \mathrm{d}\boldsymbol{H}\, \frac{\partial}{\partial s} \mathrm{d}\Omega. \tag{3.41}$$

This expression is valid and evaluated in a layer of air-elements surrounding a movable part. For the air-gap forces here, it is evaluated in the layers of air-gap elements adjacent to the stator and to the rotor. In section 4.3.4 (figure 4.6), we will further analyze the choice of the boundary region. To obtain the torque, the tangential force density is integrated over the layer of air-gap elements [ANS11]

$$T_{\mathrm{vw}} = l_{\mathrm{stk}} \frac{1}{\mu_0} \int_{\Omega} \boldsymbol{r} \times \left(\frac{1}{2} (\boldsymbol{B}\boldsymbol{B}) \nabla s - (\boldsymbol{B} \nabla s) \boldsymbol{B} \right) \mathrm{d}\Omega, \tag{3.42}$$

where l_{stk} is the stack length of the machine and $B = \mu_0 H$ in the air-gap.

Maxwell forces

As an alternative to the above virtual work forces, *Maxwell forces* are another way for calculating the magnetic forces [CED89]. The Maxwell force vector $\boldsymbol{F}_{\mathrm{mx}}$ in 2-D in the global

Cartesian coordinate system is given by

$$\boldsymbol{F}_{\mathrm{mx}}^{\mathrm{cart}} = \begin{pmatrix} F_{\mathrm{mx},x} \\ F_{\mathrm{mx},y} \end{pmatrix} = \frac{1}{\mu_0} \int\limits_{\partial\Omega} \underbrace{\begin{pmatrix} B_{\mathrm{x}}^2 - \frac{1}{2}|B| & B_{\mathrm{x}}B_{\mathrm{y}} \\ B_{\mathrm{x}}B_{\mathrm{y}} & B_{\mathrm{y}}^2 - \frac{1}{2}|B| \end{pmatrix}}_{=:\sigma} \mathrm{d}S, \tag{3.43}$$

where σ is the Maxwell stress tensor matrix. In cylindrical coordinates this becomes

$$\boldsymbol{F}_{\mathrm{mx}}^{\mathrm{cyl}} = \begin{pmatrix} F_{\mathrm{mx},r} \\ F_{\mathrm{mx},\varphi} \end{pmatrix} = \frac{1}{\mu_0} \int\limits_{\partial\Omega} \begin{pmatrix} B_{\mathrm{n}}^2 - B_{\mathrm{t}}^2 \\ B_{\mathrm{n}}B_{\mathrm{t}} \end{pmatrix} \mathrm{d}S. \tag{3.44}$$

The convergence of force and torque is slower than for other field quantities [Sal95]. In this work, both virtual work and Maxwell forces are calculated using ANSYS Emag [ANS11]. It is ensured that they are in good agreement. In general, the virtual work forces are used for all further calculations.

3.5.1.2 Flux linkage, inductance, and magnetic energy

The phase flux linkages are needed for the system simulation models and control maps of the machines. For PMSMs, splitting the phase flux linkage into the PM flux linkage and a current-dependent part is optional as is the calculation of the (secant) inductances. For most cases, only the total flux linkage is required. Inductances are frequently needed for the controller configuration but estimates based on 2-D linearization of the d- and q-axis current dependent inductance are often sufficient. This linearization further delivers the PM flux linkage at zero current for integrator initialization in the machine model. Inductance calculation is done as described in [GO99] adding the fixed-permeability [BB98] method so that the secant rather than the differential inductances can be obtained. The non-linear model is solved and the saturation state of the iron elements is determined. The individual elements are then given linear magnetic permeabilities defined by their previous saturation state. Since the problem is now linear, differential and secant inductances are equal and calculation of the former delivers the latter as well.

Magnetic energy W_{mag} and co-energy $W_{\mathrm{mag}}^{'}$ are calculated for PMSMs so that the co-energy fluctuation related torque ripple component from equation (3.15) can be obtained. The stator current $\vec{i}_{\mathrm{s}}$ and rotor position θ_{m} dependence is preserved for all of the above quantities.

3.5.1.3 Field quantities

During the FE simulations, further field quantities, in particular the magnetic flux density, are exported for other purposes. The flux density in the iron and permanent magnets can be used for loss calculation. The flux density in the air-gap allows along with the Maxwell stress tensor allows for a further decomposition of the air-gap forces in terms of spatial flux density harmonics [vGRH09].

3.5.2 Simulation procedure for PMSMs

Section 3.4.1 has shown that the dq-current for IPMSMs lies in the second quadrant for motoring operation. The result quantities discussed above are therefore calculated for a grid

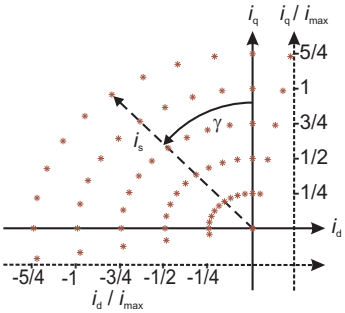

Figure 3.17: Typical simulation point distribution in the dq-current plane

of points in the second quadrant of the dq-current plane using an FE model forming a symmetry section of the machine. Figure 3.17 shows a typical operation point distribution. Each star represents one simulation. For the system simulation force models introduced in chapter 5, the simulation point distribution can by arbitrary. For the direct skew superposition without intermediate interpolation as discussed in section 4.4, a polar distribution with appropriate angular point distance is needed. For every simulation, the rotor is stepped in 1°el or 2°el until the results can be expanded due to symmetry which, for 3-phase machines, is usually 60°el. With such a simulation setup, the entire machine operating area can be simulated and analyzed. In case of eccentricity, the entire machine instead of a symmetry section has to be modeled. The rotor then needs to be stepped over 180°el for static eccentricity and over 360°mech in case of dynamic eccentricity.

Step width and aliasing

For the variable-step time-domain system simulations, we will discuss the need of low-pass filtering before sampling to prevent aliasing. The stepped FE simulation is also prone to aliasing, which cannot be prevented. Results with 2°el stepping angle have therefore been compared in the temporal frequency domain to those with 1°el step angle. It was ensured that for the relevant frequency components no significant deviation occurred.

3.5.2.1 Current or rotor alignment at simulation start

When starting an FE simulation, we have two choices how to align the current vector $\vec{i}_s$ with the rotor d-axis. We can either keep the rotor at the same starting position ($\theta_{start} = 0°$) and offset $\vec{i}_s$ in the phases by γ from the d-axis (current alignment) or keep the current vector in the same position with respect to the stator and move the rotor by $\theta_{start} = -\gamma$ away from $\vec{i}_s$ (rotor alignment). The advantage of *rotor alignment* is that skew superposition in the α-domain is readily possible (see section 4.4.1). In a machine with a skewed rotor, the skew segments have different orientations to the same current space vector $\vec{i}_s$. *Current alignment* is of interest when the force characteristics are evaluated graphically. This is used in figure 4.15 in section 4.4 where the force excitation characteristic of machine PM-C with a skewed and an unskewed rotor is compared. For use in system simulations, current aligned lookup tables are also required. If the control angle γ is changed, the current vector moves, not the rotor.

We assume rotor-aligned simulations below, yet current-aligned LUTs in the rest of the work, if not stated differently. Section 5.4.2.1 shows how shifting from one alignment to the other is achieved.

3.5.3 Simulation procedure for SRMs

As with most aspects – besides the question how to build a low-noise machine –, also the FE simulations are simpler for SRMs than they are for PMSMs. With current excitation in one phase, all current amplitudes from 0 the i_s^{max} and all rotor positions are simulated to obtain characteristic maps as those shown in figure 3.11. Due to symmetry, simulation from 0°el to 180°el is sufficient.

4 Air-gap force decomposition and analysis

This chapter is dedicated to the temporal and spatial decomposition as well as the analysis of air-gap forces in electrical machines. After a brief introduction into the decomposition of air-gap forces in electrical machines in section 4.1, formulas for the spatial and temporal composition of forces in PMSMs and SRMs are given in section 4.2. With these, the general acoustic characteristics of a certain machine are determined based on its configuration. The vibration synthesis process decouples the determination of force excitation and structural vibration responses based on a force response superposition approach. For this approach to be applicable, the force excitation needs to be decomposed in a manner which is on the one hand an as-close-as-possible approximation of the real force distribution in the machine and on the other hand allows to determine the structural responses for the individual force shapes. Three different approaches are presented and analyzed in section 4.3 and their advantages and limitations are discussed. The chapter closes with an application example analyzing the effectiveness of skew in a PMSM on reducing the shape 0 force excitation in section 4.4. Analytical transfer functions for the effect of continuous and discrete skew are given.

4.1 Air-gap force decomposition

We start the decomposition of the air-gap force with a visual impression of the force excitation. Figure 4.1 shows the (radial) air-gap force of the electrical machine PM-A at one moment in time. In addition to the curve of the air-gap force, spatial Fourier series components, the *force shapes*, are shown.

For the largest part, we will consider forces in 2-D as most machines are symmetric in the axial direction or can be approximated as piecewise constant in the third (axial) dimension (see the force model for skewed PMSM in section 5.4.2 or for axially segmented SRMs in section 5.4.3). The unit of the distributed lineic air-gap force, the force per unit length in the air-gap, is chosen as N/m.

Spatial decomposition

The force distribution $f_{d,U}(t,\alpha)$ in N/m along the air-gap is described in a Fourier series by the superposition of excitation modes ν up to the U^{th} spatial component as

$$f_{d,U}(t,\alpha) = \sum_{\nu=0}^{U} \left(f_{\cos,d,\nu}(t) \cos(\nu\alpha) + f_{\sin,d,\nu}(t) \sin(\nu\alpha) \right), \tag{4.1}$$

where α is the angular position in the air-gap. Index d denotes the direction, e.g., radial ('rad') or tangential ('tan'). At this point we know which shapes ν exist and can observe how their amplitudes $f_{\cos,d,\nu}(t)$ and $f_{\sin,d,\nu}(t)$ vary with time. Based on the observation that with increasing spatial order ν the vibration response of the machine to a force excitation shape decreases [Jor50], the Fourier series can eventually be truncated. This truncation is a corner

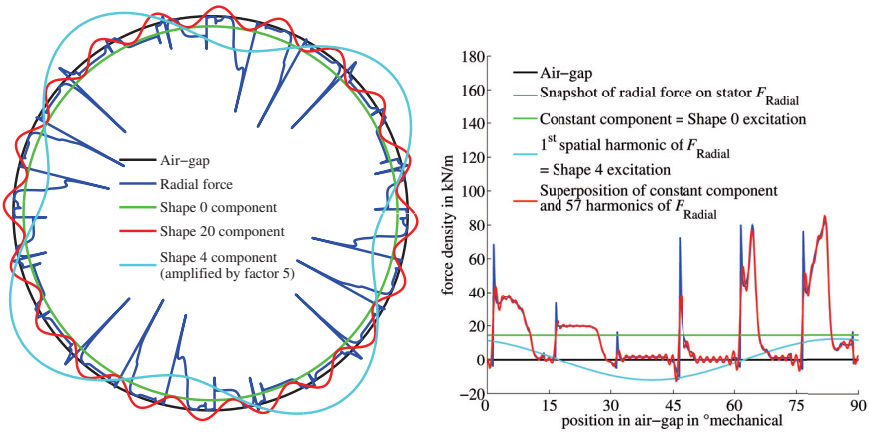

(a) Polar plot of the air-gap force

(b) xy-plot of a 1/4 symmetry section

Figure 4.1: Snapshot of the radial air-gap force in an electrical machine including spatial force harmonics (force shapes)

stone of the vibration synthesis process which only uses a finite number of forces shapes.

Recalling section 2.3.2, this type of Fourier series representation is not unique and the spatially decomposed forces will be analyzed using various Fourier series representations. The shapes in figure 4.1, for example, are a representation of the amplitude-phase notation. For the air-gap domain transformations to be introduced in section 4.3, the positive-negative sequence representation is used since this is the typical output from a Fast Fourier transform (FFT) and therefore best suited for mathematical operations. We will get back to the cosine-sine sequence representation for the time-domain simulation force models in chapter 5 where the coefficients $f_{\cos,d,\nu}$ and $f_{\sin,d,\nu}$ form the content of the lookup tables.

Temporal decomposition

For obtaining the temporal frequencies, i.e., the audible tones, the time dependent amplitude factors, $f_{\cos,d,\nu}(t)$ and $f_{\sin,d,\nu}(t)$, are decomposed into their complex frequency components,

$$f_{\cos,d,\nu}(t) \circ\!\!-\!\!\bullet F_{\cos,d,\nu}(f) \quad \text{and} \quad f_{\sin,d,\nu}(t) \circ\!\!-\!\!\bullet F_{\sin,d,\nu}(f). \tag{4.2}$$

Displaying $F_{\cos,d,\nu}(f)$ and $F_{\sin,d,\nu}(f)$ over the dq-current or torque-speed range allows, for example, to judge and compare the force excitation characteristics of PMSMs. This is used in section 4.4 for comparing the force excitation of machine PM-C with and without rotor skew.

4.2 Spatial and temporal composition of air-gap forces

In order to determine the orders of force shapes and its temporal frequencies, it is not necessary to calculate (by numerical or analytical means) and subsequently decompose the force exci-

tation of an electrical machine. The machine configuration determines the machine-inherent spatial shapes and the temporal frequency components of the air-gap forces. Therefore, the general acoustic characteristics are always known beforehand. Generic expressions for the machine-inherent components for both PMSMs and SRMs are given in the following. Further shapes (and related frequencies), arise, for instance, in case of eccentricity; further frequency components result, for example, from switching frequency components.

The *spatial* force shapes or orders ν are multiples of a base force shape ν_{base},

$$\nu \in \{0, \nu_{\text{base}}, 2\nu_{\text{base}}, \ldots\}\,. \tag{4.3}$$

The *temporal* frequency components for the spatial orders ν are defined by two machine configuration dependent frequencies, as all machine-inherent frequency components are multiples of the mechanical frequency f_{m}. The lowest frequency component $f_{0,\nu_{\text{base}}}$ in the machine is the fundamental frequency of the fundamental spatial order ν_{base}. It serves as an offset for determining the temporal frequencies f_ν of a spatial order ν. The fundamental frequency $f_{0,0}$ of the shape 0 force defines the frequency spreading. The frequencies f_ν are then defined as

$$f_\nu = \sigma(\nu)\,\frac{\nu}{\nu_{\text{base}}} f_{0,\nu_{\text{base}}} + \{\ldots, -f_{0,0}, 0, f_{0,0}, \ldots\}\,, \tag{4.4}$$

where $\sigma(\nu) \in \{1, -1\}$. The sign-function $\sigma(\nu)$ is only relevant if the rotation direction of the force waves is of interest. This will be the case when analyzing the frequency of stator and rotor forces in SRMs in section 5.3.4. For the determination of the audible tones it can be omitted. Below, the three machine configuration dependent constants ν_{base}, $f_{0,\nu_{\text{base}}}$, and $f_{0,0}$ as well as $\sigma(\nu)$ are determined for PMSMs and SRMs. For a detailed analysis of air-gap fields and forces in electrical machines, it is referred to the relevant literature [GWL06; Sei92; Jor50].

4.2.1 PMSM force composition

The force composition of a PMSM is determined by three parameters: the number of stator slots N_{s}, the number of pole pairs p, and the number of phases N_{phase}. As a dependent parameter, q, the number of slots per pole per phase, is also used below.

The fundamental *spatial* order ν_{base} (the base force shape) of the air-gap force is determined by the greatest common divider (GCD) of the number of stator slots N_{s} and the pole pair number p_0 of the fundamental air-gap field,

$$\nu_{\text{base}} = \gcd\left(\frac{N_{\text{s}}}{N_{\text{phase}}}, 2p\right). \tag{4.5}$$

If slotting is neglected, ν_{base} is twice the fundamental air-gap field order p_0. This is due to the fact that the force is approximately proportional to flux density squared, $F \propto B^2$. Higher orders arise because the air-gap field is never purely sinusoidal. A concentrated winding with $q = 0.5$ slots per pole per phase lowers the fundamental spatial order ν_{base}. In a 3-phase machine, the number of stator slots N_{s} is then $3p$, so that ν_{base} becomes p instead of $2p$. The latter is the case for machines with distributed windings where $q = 1$ or 2. The fundamental

pole pair number p_0 differs from the working harmonic's pole pair number p in fractional slot machines (e.g., the PM-A with $p_0 = 4$ and $p = 10$) where the working harmonic of the air-gap field is not the fundamental air-gap field harmonics. As for the concentrated winding, the fundamental air-gap force shape order is lowered.

The fundamental *temporal* frequency component $f_{0,\nu_{\text{base}}}$ is equal to the pole number $2p$, which is twice the electrical frequency f_{el}. The lowest shape $\nu = 0$ dependent frequency component is given by the quotient of N_s and q,

$$f_{0,\nu_{\text{base}}} = 2p \quad \text{and} \quad f_{0,0} = \frac{N_\text{s}}{q}. \tag{4.6}$$

For PMSMs, the sign function σ is not ν dependent. However, the author has not found a compact closed form expression for all cases of q. For $q = 1$ or 2, $\sigma = 1$. For $q = 0.5$, σ = -1. For $q = 0.4$, σ = -1. The latter is because the working harmonic is the 5^{th} harmonic of the air-gap field which is counter-rotating to the fundamental air-gap field harmonic.

4.2.2 SRM force composition

The force composition of an SRM with more than one phase is determined by two parameters: the number of stator teeth N_s and the number of rotor teeth N_r. $N_{\text{phase}} = {}^{N_\text{s}}/_{(N_\text{s}-N_\text{r})}$ then becomes a dependent parameter.

The fundamental *spatial* order ν_{base} is determined by the number of pole pairs p as:

$$\nu_{\text{base}} = 2p \quad \text{with} \quad 2p = \frac{N_\text{s}}{N_{\text{phase}}}. \tag{4.7}$$

A higher pole count leads to a higher fundamental spatial order. A high fundamental spatial order has a high eigenfrequency [Jor50], which is usually desirable from an acoustic point of view. With a given number of stator teeth N_s the trade-off comes in a lower number of phases which reduces the degrees of freedom for control – also regarding the acoustic behavior.

The fundamental *temporal* frequency $f_{0,\nu_{\text{base}}}$ is equal to the number of rotor teeth N_r. $f_{0,\nu_{\text{base}}}$ is equal to f_{el}. $f_{0,0}$ is the lowest common multiple (LCM) of the number stator slots N_s and rotor slots N_r.

$$f_{0,\nu_{\text{base}}} = N_\text{r} \quad , \quad f_{0,0} = \text{lcm}\,(N_\text{s}, N_\text{r})\,, \quad \text{and} \quad \sigma(\nu) = (-1)^{\left(\frac{\nu}{\nu_{\text{base}}}\right)}. \tag{4.8}$$

If the forces on the rotor are observed, N_r has to be replaced by N_s in equation (4.8).

Table 4.1 lists spatial orders and frequency components for common machine configurations.

4.2.3 Discussion of PMSM and SRM forces

In the following, the fundamental acoustic characteristics of PMSMs and SRMs for automotive traction applications with ratings between 10 kW (mild HEVs) and 150 kW (sportive or large/heavy EVs) and maximum rotational speeds of 8000-15 000 r/min are briefly compared.

shape	multiple of f_m						
0	0			30			60
10		10	20		40	50	
20		10	20		40	50	
30	0			30			60

(a) PMSM, $p = 6$, $m = 3$, $q = 2$ (PM-C)

shape	multiple of f_m						
0	0			60			120
4		20	40		80	100	
8		20	40		80	100	
12	0			60			120

(b) PMSM, $p = 10$, $m = 3$, $q = 0.4$ (PM-A)

shape	multiple of f_m						
0	0			24			48
4		8	16		32	40	
8		8	16		32	40	
12	0			24			48

(c) PMSM, $p = 4$, $m = 3$, $q = 0.5$ (PM-B) or SRM, $N_\mathrm{s} = 12$, $N_\mathrm{r} = 8$ ($m = 3$)

Table 4.1: Force component examples (signs have been omitted)

Spatial

Traction PMSMs often have 4-6 pole pairs p and $q = 2$ slots per pole per phase (i.e., $N_\mathrm{s} = 48$, 60, 72 stator slots). The resulting fundamental force shape is then 8, 10, or 12. For SRMs, typical stator-rotor tooth configurations for this application are $N_\mathrm{s}/N_\mathrm{r}$= 12/8 (3-phase) or 16/12 (4-phase). A machine of the latter type has been realized in the OKOFEH project [Vol+02; Ind02]. The fundamental force shape ν_base is then 4. Thus, the fundamental force shape for an SRM – in a conservative design – is lower by a factor of about 2, for both the 3- and the 4-phase configuration.

In parallel HEVs where the electric motor is placed between combustion engine and gearbox, PMSMs with concentrated windings are commonly used [Küs09]. For these "pie" type machines (large diameter, low stack length, and high pole count) concentrated windings are well suited due to their short winding heads. Their relatively low constant power range [Hon+97; SM94] and low high-speed efficiency does not come as a disadvantage as their main purpose is to support the engine at low speeds. For these machines, the above PMSM-vs-SRM fundamental force shape comparison no longer holds. The fundamental force shape is halved according to equation (4.5) and is then similar or equal to that of an SRM.

Temporal

For the above PMSMs, the fundamental frequency component f_{0,ν_base} is 8, 10, or 12. Due to the relatively high fundamental mode number (8, 10, or 12), the shape 0 related $f_{0,0}$ and in particular $2f_{0,0} = 48$, 60, or 72 tend to be the most prominent noise components.

Due to the lower spatial order (and along with the, so far not characterized, high excitation amplitudes) the shape $\nu_\mathrm{base} = 4$ related f_{0,ν_base} frequency components at multiples of the rotor tooth numbers of 8 (3-phase) or 12 (4-phase) make up the SRMs noise spectrum, along with the $\nu = 0$ related frequency components.

4.2.4 Further excitation shapes and tonal components

Various effects can lead to further excitation shapes and tonal components in the electromagnetically excited acoustic noise. Unbalanced excitation and switching harmonics are discussed below.

Unbalanced excitation

The consequence of an unbalanced excitation are additional force shapes and tonal components. Acoustically critical is in particular the excitation of lower orders, i.e., modes 1, 2, 3.... In case of dynamic eccentricity or equivalent fault conditions, modulation effects lead to additional frequency components. The form of the unbalance can be mechanical (eccentricity) or magnetic (phase faults). Analytical expressions for force shapes and frequencies in case of eccentricity are, for example, found in [GWL06]. Mechanical unbalance is not further analyzed in this work. Numerical simulation results of rotor dynamic eccentricity effects on synchronous machine vibrations have recently been presented by Pellerey et al. in [PLF12a]. In terms of the arising force shapes and frequency components, the magnetic unbalance investigated for machine SR-Y (SR-20/16or) is equivalent to dynamic eccentricity. The magnetic unbalance is investigated based on the reluctance network model from section 3.3.2.2. The force excitation under various fault conditions is modeled and the vibrations are synthesized (see section 7.5). In terms of the vibration synthesis process, unbalanced excitation requires a (preferably) system simulation force model which outputs the spatially decomposed air-gap forces.

Switching harmonics

Further tonal components arise due to switching harmonics in the stator currents located around multiples of the switching frequency f_{switch}. For space vector modulated PWM waveforms, the frequency content is analytically described in [BH90]. The system simulation based results in chapter 7 take into account switching harmonics. The switching frequency related frequency harmonics can dominate the acoustic noise if the switching frequency is comparatively low. This is shown in section 7.3.2.

4.3 Domains for air-gap force spatial decomposition

Letting aside the different Fourier series representations, section 4.1 lets assume that the way to decompose the air-gap force is unique. However, it is not. In this section, three different decomposition options are analyzed.

Force continuous in air-gap (sine)

The first option is the one chosen in figure 4.1 and equation (4.1). The spatial harmonics (force shapes) are determined for a domain spanning the entire air-gap. This decomposition option is called *sine* in the following. While the sine decomposition is readily achieved, it has one significant disadvantage: For the structural dynamics analysis, the force shapes need to be applied to a structural model of the machine and the main target is usually the stator. The stator, however, has slots and is therefore not continuous along the air-gap.

Force constant on teeth (tooth)

Another frequently used option is working with aggregate forces, i.e., one force per stator tooth. This is practical and according to Garvey et al. a valid approximation, because “the

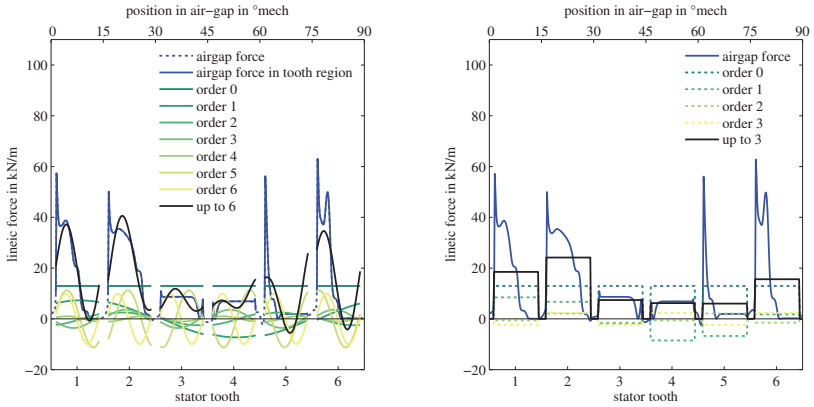

(a) tsine (b) tooth

Figure 4.2: Air-gap force and its tsine and tooth approximation at one point in time for PM-A

radial and tangential forces act predominantly at the tip of the tooth and that the tip is so small and stiff that these can be considered to be point forces" [Gar+97]. Tooth forces, also if this effect may be small in many cases, neglect the distribution of the force along the tooth surface and inherently lead to spatial aliasing. They are, however, easy to determine and to treat in system simulation models and they can be readily applied to structural models.

Force continuous on tooth surface (tsine)

The two approaches above have complementary advantages and disadvantages. The sine force can describe arbitrary air-gap forces but cannot be readily applied to structural models. The tooth force is compatible with structural models but can only approximate the air-gap force. Therefore, the *tsine* force is introduced to combine the advantages of both approaches. Since the air-gap force only acts on the tooth surface at the air-gap – the limitations of this assumption is discussed below –, the domain for force decomposition is chosen to encompass only the piecewise continuous stator tooth surface along the air-gap. This approach is compatible with structural models and can describe arbitrary force distributions along the stator teeth.

Graphical impression of tsine and tooth force

The mathematical transformation from sine to tsine or tooth force is derived in the next section. A first graphical impression of the tsine and tooth forces is given in figure 4.2 and figure 4.3. Figure 4.2 shows the air-gap force and its tsine (figure 4.2a) and tooth (figure 4.2b) approximation including the individual harmonics at one point in time for machine PM-A. This figure can be compared to figure 4.1b which shows a sine decomposition of the PM-A force. Figure 4.3 shows the same for machine PM-B. In both cases, the tsine Fourier series is truncated after $N_{\text{teeth}}+1$ elements, which is 6+1 or 3+1, respectively. The tooth force signal has only N_{teeth} values so that the complete Fourier series has floor($N_{\text{teeth}}/2$) + 1 elements in total.

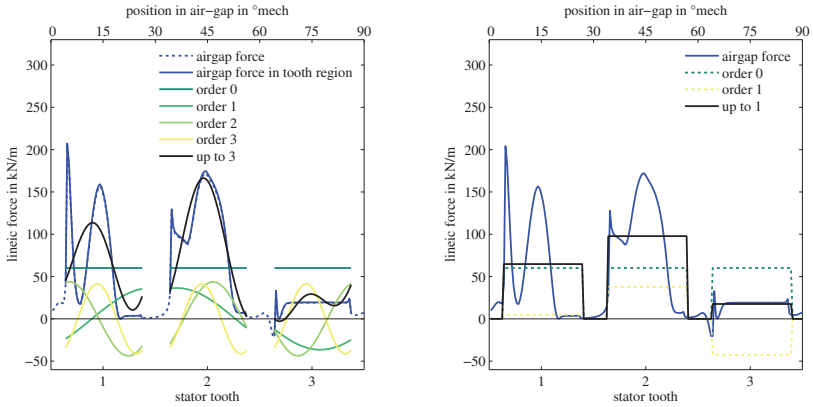

(a) tsine (b) tooth

Figure 4.3: Air-gap force and its tsine and tooth approximation at one point in time for PM-B

Remarks on sine and tooth forces

The sine force approach is in accordance with most analytic models (usually for rotating field machines). These start from a fundamental air-gap field and add harmonics for winding distribution and air-gap permeance. This approach is practical when paired with an analytical structural model as in [Le 08]. The sine force approach can further be used for continuous surfaces as, for example, the rotor of an interior permanent magnet machine. Sine forces can be applied to stators if not the tooth surface but the yoke is chosen as target. This, however, is an approximation as the "lever arm" of the teeth and their dynamics is not taken into account. Section 6.2.3.2 will show results for a simple simulation where tsine forces are successfully described by sine force. The same holds for tooth forces which can be described by both sine and tsine forces.

The tooth force approach was used by the author in [BSD11]. Acoustic models for SRMs also regularly use this approach [Ras99; Fie06]. On the commercial software side, the company ANSYS uses tooth forces when linking their Maxwell software with their ANSYS Structural software [AS12].

Conversion of the air-gap force

The 'default' force which is obtained in the FE simulations is the force in the air-gap. In the following, it is derived how the air-gap force is transformed into the continuous tooth force (tsine, section 4.3.1) and into the discrete tooth force (tooth).

When switching between the force distributions, the temporal frequency components stay the same, however their amplitudes change. Also, the spatial shapes remain the same, with the exemption that the tooth force limits them to $N_s/2+1$. The force can always be described by a Fourier series as introduced in equation (4.1) in section 4.1; only the coefficients and the domain which α describes change.

4.3.1 Converting the air-gap force (sine) to the continuous tooth force (tsine)

Geometric definitions

A stator tooth has the angular width τ_{tooth}, a slot (i.e., tooth plus slot opening) the width τ_{s}. The tooth width is lower than (or equal to) the slot width, $\tau_{\text{tooth}} \leq \tau_{\text{s}}$. The number of slots times the slot width spans the entire air-gap, $N_{\text{s}}\,\tau_{\text{s}} = 2\pi$. The ratio between tooth width and slot width is defined as $c_{\text{ratio}} = {}^{\tau_{\text{tooth}}}\!/_{\tau_{\text{s}}}$.

Concept

We derive in the following how the continuous tooth domain force shapes $\mathbf{F}_{\text{tsine}}(u)$ can be represented by the air-gap domain force shapes $\mathbf{F}(u)$. The spatially distributed force on the teeth $\mathbf{F}_{\text{tsine}}(u)$ is transformed into the (spatially distributed) air-gap force $\mathbf{F}(u)$ by $\mathbf{H}_{\text{tsine}}(u)$. This transform is bi-directional under the assumption that the force in the slot regions is zero. We will derive

$$\mathbf{F}(u) = \mathbf{H}_{\text{tsine}}(u) \cdot \mathbf{F}_{\text{tsine}}(u) \tag{4.9}$$

and eventually apply

$$\mathbf{F}_{\text{tsine}}(u) = \mathbf{H}_{\text{tsine}}(u)^{-1} \cdot \mathbf{F}(u) \tag{4.10}$$

to the air-gap force resulting from FE simulations.

$\mathbf{F}(u)$ and $\mathbf{F}_{\text{tsine}}(u)$ are $\mathbb{C}^{N_{\text{elem}} \times N_{\text{steps}}}$ matrices. N_{elem} is the number of sampling points along the air-gap, N_{steps} is the number of simulated time steps or rotor positions. The transforms derived here only affect the spatial frequency domain u, which is why all variables are only written as functions of u. The spatial transform is independent of the temporal domain so that the latter is not further denoted. $\mathbf{H}_{\text{tsine}}(u)$ is a $\mathbb{C}^{N_{\text{elem}} \times N_{\text{elem}}}$ matrix.

Derivation

For a normalized spatial harmonic ν, the (w.l.o.g. positive sequence) force distribution on the tooth surface is in the tooth domain $\tilde{\alpha}$ defined as

$$f_{\text{tsine},\nu}(\tilde{\alpha}) = \mathrm{e}^{\mathrm{j}\nu\tilde{\alpha}} \tag{4.11}$$

$$\updownarrow$$

$$F_{\text{tsine},\nu}(\tilde{u}) = \delta\left(\tilde{u} - \nu\right). \tag{4.12}$$

The air-gap force $f_\nu(\alpha)$ then describes the force seen in the air-gap if on the teeth this tooth force $f_{\text{tsine},\nu}(\tilde{\alpha})$ of order ν is applied. $f_\nu(\alpha)$ is the sum of the force on the individual teeth,

$$f_\nu(\alpha) = \sum_{n=0}^{N_\text{s}-1} f_{\nu,n}(\alpha) \tag{4.13}$$

$$\vdots$$

$$F_\nu(u) = \sum_{n=0}^{N_\text{s}-1} F_{\nu,n}(u) \tag{4.14}$$

In the air-gap domain α, the force $f_{\nu,n}(\alpha)$ on the n^{th} tooth is seen as

$$f_{\nu,n}(\alpha) = (h_{\text{cut},n}(\alpha) \cdot f_{\text{tsine},\nu}(\alpha)) \ * \ h_{\text{shift},n}(\alpha) \tag{4.15}$$

$$\vdots$$

$$F_{\nu,n}(u) = (H_{\text{cut},n}(u) * F_{\text{tooth},\nu}(u)) \ \cdot \ H_{\text{shift},n}(u). \tag{4.16}$$

$f_{\text{tsine},\nu}(\alpha)$ is the air-gap domain representation of the tooth domain force distribution $f_{\text{tsine},\nu}(\tilde{\alpha})$ of order ν,

$$f_{\text{tsine},\nu}(\alpha) = \mathrm{e}^{\mathrm{j}\left(\frac{\nu}{c_\text{ratio}}\alpha\right)} \tag{4.17}$$

$$\vdots$$

$$F_{\text{tsine},\nu}(u) = \delta\left(u - \frac{\nu}{c_\text{ratio}}\right), \tag{4.18}$$

with $\alpha = c_\text{ratio}\,\tilde{\alpha}$.

$h_{\text{cut},n}(\alpha)$ cuts out a segment of this continuous tooth force belonging to tooth n. It is defined as

$$h_{\text{cut},n}(\alpha) = \text{rect}\left(\frac{\alpha - n\,\tau_\text{tooth}}{\tau_\text{tooth}}\right) \tag{4.19}$$

$$\vdots$$

$$H_{\text{cut},n}(u) = \frac{\tau_\text{tooth}}{2\pi}\,\text{sinc}\left(\frac{\tau_\text{tooth}}{2\pi}u\right)\mathrm{e}^{-\mathrm{j}(n\tau_\text{tooth}u)}. \tag{4.20}$$

As the slot openings separate the teeth, this force segments needs to be moved to the correct position. $h_{\text{shift},n}(\alpha)$ therefore shifts the force segment to position in the air-gap where the respective force is located. $h_{\text{shift},n}(\alpha)$ is defined as

$$h_{\text{shift},n}(\alpha) = \delta\left(\alpha - n(\tau_\text{s} - \tau_\text{tooth})\right) \tag{4.21}$$

$$\vdots$$

$$H_{\text{shift},n}(u) = \mathrm{e}^{-\mathrm{j}n(\tau_\text{s}-\tau_\text{tooth})u}. \tag{4.22}$$

Combining the above gives us $F_\nu(u)$, the expression how ν^{th} force shape is seen in the

air-gap,

$$\Rightarrow F_\nu(u) = \frac{\tau_{\text{tooth}}}{2\pi} \operatorname{sinc}\left(\frac{1}{2\pi}\left(\tau_{\text{tooth}} u - \tau_{\text{s}} \nu\right)\right) \sum_{n=0}^{N_{\text{s}}-1} \mathrm{e}^{-\mathrm{j}2\pi \frac{n}{N_{\text{s}}}(u-\nu)}. \tag{4.23}$$

The spatial frequency u domain is discrete because the air-gap α domain is periodic with 2π. The above expression can therefore be simplified and we can write for the ν^{th} row in the transformation matrix $\mathbf{H}_{\text{tsine}}(u)$:

$$F_\nu(u) = \begin{cases} c_{\text{ratio}} \operatorname{sinc}\left(\frac{1}{2\pi}\left(\tau_{\text{tooth}} u - \tau_{\text{s}} \nu\right)\right) & \text{where} \quad u = \nu + k N_{\text{s}} (k \in \mathbb{Z}) \\ 0 & \text{otherwise} \end{cases}. \tag{4.24}$$

4.3.2 Converting the air-gap force (sine) to the constant tooth force (tooth)

We now derive how the discrete tooth domain force shapes $\mathbf{F}_{\text{tooth}}(u)$ can be represented by the air-gap domain force shapes $\mathbf{F}(u)$.

Concept

The constant force on the teeth $\mathbf{F}_{\text{tooth}}(u)$ is transformed into the (spatially distributed) air-gap force $\mathbf{F}(u)$ by $\mathbf{H}_{\text{tooth}}(u)$. This transform is bi-directional only under the assumption that the air-gap force is zero in the slot regions and constant over a stator tooth. In a real machine, this assumption cannot be met so that aliasing is inevitable. As for the tsine force above, we will derive

$$\mathbf{F}(u) = \mathbf{H}_{\text{tooth}}(u) \cdot \mathbf{F}_{\text{tooth}}(u) \tag{4.25}$$

and eventually apply

$$\mathbf{F}_{\text{tooth}}(u) = \mathbf{H}_{\text{tooth}}(u)^{+} \cdot \mathbf{F}(u) \tag{4.26}$$

to the air-gap force resulting from the FE simulations. $\mathbf{H}_{\text{tooth}}(u)^{+}$ is the (Moore-Penrose) pseudoinverse. $\mathbf{F}(u)$ is a $\mathbb{C}^{N_{\text{elem}} \times N_{\text{steps}}}$ and $\mathbf{F}_{\text{tooth}}(u)$ a $\mathbb{C}^{N_{\text{s}} \times N_{\text{steps}}}$ matrix. $\mathbf{H}_{\text{tooth}}(u)$ is a $\mathbb{C}^{N_{\text{elem}} \times N_{\text{s}}}$ matrix.

Derivation

For a spatial harmonic ν, the normalized discrete tooth force for tooth n is given as

$$f_{\text{tooth},\nu}(n) = \mathrm{e}^{\mathrm{j}\nu \frac{n}{N_{\text{s}}}}. \tag{4.27}$$

The continuous air-gap force $f_\nu(\alpha)$ then describes how this force is seen in the air-gap.

$$
\begin{aligned}
f_\nu(\alpha) &= \Big(\quad f_{\text{shape}}(\alpha) \quad \cdot \quad h_{\text{sample}}(\alpha) \qquad \Big) * \quad h_{\text{spread}}(\alpha) \\
&= \Big(\qquad \mathrm{e}^{\mathrm{j}\nu\alpha} \quad \cdot \quad \sum_{n=0}^{N_\text{s}-1} \delta\left(\alpha - n\tau_\text{s}\right) \Big) * \quad \text{rect}\left(\tfrac{\alpha}{\tau_\text{tooth}}\right) \\
&\quad \Big\downarrow \\
F_\nu(u) &= \Big(\quad \delta\left(u-\nu\right) \quad * \quad \sum_{n=0}^{N_\text{s}-1} \mathrm{e}^{-\mathrm{j}n\tau_\text{s}u} \qquad \Big) \cdot \quad \tfrac{\tau_\text{tooth}}{2\pi}\,\text{sinc}\left(\tfrac{\tau_\text{tooth}}{2\pi}u\right) \\
&= \qquad\qquad\qquad \sum_{n=0}^{N_\text{s}-1} \mathrm{e}^{-\mathrm{j}n\tau_\text{s}(u-\nu)} \quad \cdot \quad \tfrac{\tau_\text{tooth}}{2\pi}\,\text{sinc}\left(\tfrac{\tau_\text{tooth}}{2\pi}u\right)
\end{aligned}
$$

For the constant tooth force, the ν^{th} row in the transformation matrix $\mathbf{H}_{\text{tooth}}(u)$ is then formed by $F_\nu(u)$ as

$$
F_\nu(u) = \begin{cases} c_\text{ratio}\,\text{sinc}\left(\frac{1}{2\pi}\tau_\text{tooth}u\right) & \text{where} \quad u-\nu = kN_\text{s}(k\in\mathbb{Z}) \\ & \text{and} \quad \tilde{\nu} = \nu \bmod N_\text{s} \\ 0 & \text{otherwise} \end{cases} . \tag{4.28}
$$

4.3.3 Spatial transfer functions – how tsine and tooth are seen in the air-gap

A graphical impression of how the spatially decomposed continuous tooth force ('tsine') and the constant/discrete tooth force ('tooth') are seen in the air-gap is given by Figure 4.4. The figure shows the normalized $\mathbf{H}_{\text{tsine}}(u)$ and $\mathbf{H}_{\text{tooth}}(u)$ transfer functions which have been derived above. We recall that each row is $F_\nu(u)$ and shows how a spatial order ν of the tsine or tooth force is seen the u-domain of the air-gap. The example represents a 2-pole machine with 6 stator teeth and a c_ratio of 0.5.

A spatial order ν of both the tsine and the tooth force leads to an infinite number of air-gap force shapes with a sinc envelope. For the tsine force, the maximum is where the spatial air-gap frequency u is equal to the tsine force order ν. While an infinite number of tsine force shapes ν contributes to any air-gap force order u, the sinc envelope allows truncation in practical cases. Neglecting the sign of u, the transfer function for $\nu = 4$ has the same spatial components u as that of $\nu = 2$, $\nu = 5$ the same as $\nu = 1$, and $\nu = 6$ the same as $\nu = 0$ (thus the identical color).

For the tooth force, we see the aliasing effect. With $N_\text{s} = 6$, the spatial Nyquist frequency u_nyquist is 3 so that only 3+1 tooth force orders (0, 1, 2, 3) can be distinguished. From $\nu = 4$ on, the transfer function repeats with that of $\nu = 6$ being equal to that of $\nu = 0$. $\mathbf{H}_{\text{tooth}}(u = 4)$ is the mirror image of $\mathbf{H}_{\text{tooth}}(u = 2)$ and $\mathbf{H}_{\text{tooth}}(u = 5)$ that of $\mathbf{H}_{\text{tooth}}(u = 1)$. The repetition of the transfer function is only mathematical. Orders lager than $\nu = 3$ do not exist for the tooth force.

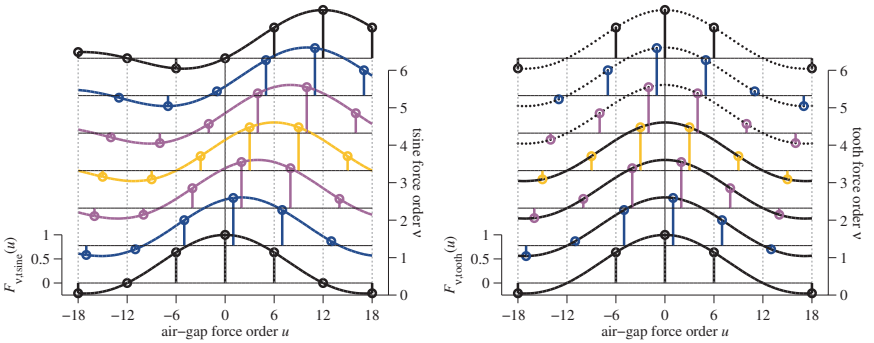

(a) Transfer function $\mathbf{H}_{\text{tsine}}(u)$ for the spatially decomposed tooth force ('tsine')

(b) Transfer function $\mathbf{H}_{\text{tooth}}(u)$ for the constant tooth force ('tooth')

Figure 4.4: Exemplary transfer functions for conversion of the sine force to tsine and tooth force

4.3.4 Comparing sine, tsine, and tooth forces over space and time

Section 4.3.1 and section 4.3.2 show strictly mathematically how the air-gap force is described by the tsine or the tooth force. This section adds further graphical examples (cf. figures 4.2 and 4.3 above) to visualize this process. Figure 4.5 shows the radial and figure 4.7 the tangential force in the air-gap for the various decomposition options. A segment of 6 teeth of machine PM-A is shown, which is the symmetry section after which the force repeats. In the time domain, 180°el are drawn, which is the temporal symmetry condition. The dq-current is kept constant. The underlying operating point is the corner point between base-speed range and field-weakening regime.

Radial forces

Figure 4.5a is the air-gap force as obtained in the FE analysis. The concentration of force at the tooth flanks can be seen.

Figure 4.5b is the representation of the air-gap force based on 6+1 tsine force shapes ν. This is a good approximation of the original air-gap force distribution. Using one more force shape for the vibrations synthesis than there are stator teeth in the machine's symmetry section has proven to be a good choice between complexity, accuracy, and transparency. In terms of complexity, the computational overhead for any additional force shapes is rather low. In terms of accuracy, even less force shapes are often sufficient. Transparency is achieved by this choice of shape number because the amplitude of the force shape with order $\nu = N_\text{s}$ is often rather high, its structural response, however, is low. Overall, the contribution of order $\nu = N_\text{s}$ to the acoustic noise is therefore usually small, yet – and that is what the terms transparency refers to – this is not readily apparent from the force.

Figure 4.5c is obtained if the air-gap force is converted to the constant tooth force. Apparently, this is an approximation which does not allow to preserve strong resemblence of the original air-gap force distribution. While therefore inferior to the tsine approach, it is still an

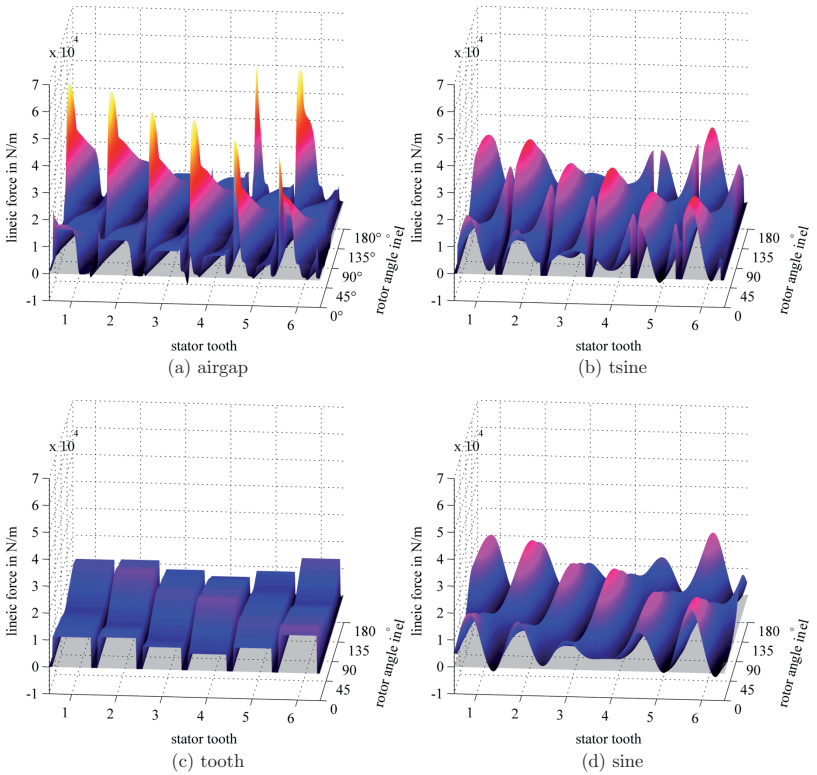

Figure 4.5: Radial air-gap force under various decomposition options over space and time for PM-A at the corner point

acceptable approach in most cases.

At last, figure 4.5d shows the air-gap force generated by 6+1 air-gap force orders. Using all $N_{\text{elem}}/2+1$ spatial orders leads to the original force from figure 4.5a.

Force leakage in finite element simulations

An SRM example is inserted to explain the effect of negative air-gap forces in the slot regions in figure 4.5a. Physically, magnetic forces can neither be negative nor can they act in the slot region where there is no (highly permeable) material. The negative force peaks in the air-gap (e.g., to the right of tooth 3) are a result of forces acting on the tooth flanks. This "edge effect" is also observed in [PLF12b] but not further considered. Figure 4.6 is used to explain this effect. It shows the force on an SRM stator in the unaligned position for two different cases of force calculation in the FE simulations.

Section 3.5.1.1 showed that the calculation of local electromagnetic forces in the FE simu-

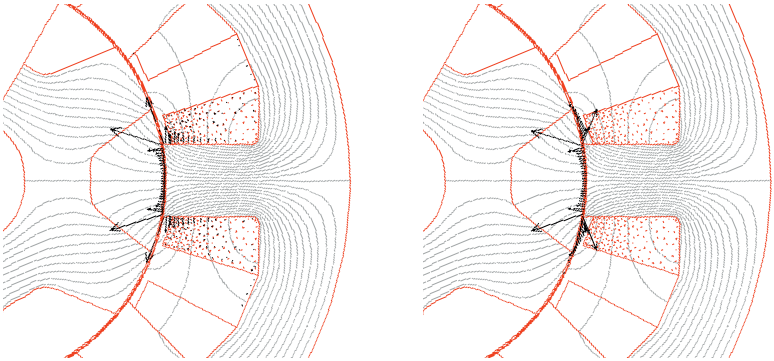

(a) stator iron as domain boundary (b) air-gap as domain bounday

Figure 4.6: Force distribution on an SRM stator in unaligned position depending on the domain for which force is calculated

lations requires the definition of regions for whose surrounding 'air' elements (materials with $\mu_r = 1$), electromagnetic forces are calculated. The results shown here have been obtained with ANSYS Emag [ANS12]. In figure 4.6a, the stator iron is the body for which the forces are calculated. The forces then act on the tooth tips and on the flanks of the stator, always at the interface between iron (high μ_r) and surrounding air or winding ($\mu_r = 1$). Letting aside that in case of saturation and a consequently gradual change of permeability, the forces acts inside the iron, too, this force distribution is physically valid. In figure 4.6b, the entire stator domain including the slot regions is used for force calculation. The interface at which the forces are calculated is now the air-gap. Forces now show in the slot region of the air-gap where they cannot exist physically, but where they are 'projected' to. We see that negative radial components appear as is also observed in figure 4.5a.

The example of forces in an SRM in the unaligned position is an extreme case. This is fortunately of little practical relevance as will be further discussed in section 5.3.3. In general, the leakage effect is compensated in two steps. First, the ratio c_{ratio} of tooth to total slot width for the tsine force calculation from section 4.3.1 is chosen slightly larger than the actual width of the tooth to preserve most of the overall energy. Second, some leakage force is then still not accounted for. It is mostly negative and affects in particular the shape 0 force. This force is mapped to the edge elements at the left and right hand side of the tooth. The tooth force is unaffected by the leakage effect as it can always be calculated between the midpoints of two slots[(i)].

Tangential forces

Figure 4.7 repeats the comparison from figure 4.5 for the tangential forces. The tangential force acts primarily at the left and right corners of the teeth. Thus, the 'leakage' effect is

[(i)] Equation (4.28) then changes. In the time domain, the tooth force by dividing by c_{ratio}. In the frequency domain, this means that that the rect function has τ_s in the denominator and c_{ratio} as factor up front. For the transfer function, this means that τ_{tooth} becomes τ_s in the sinc term.

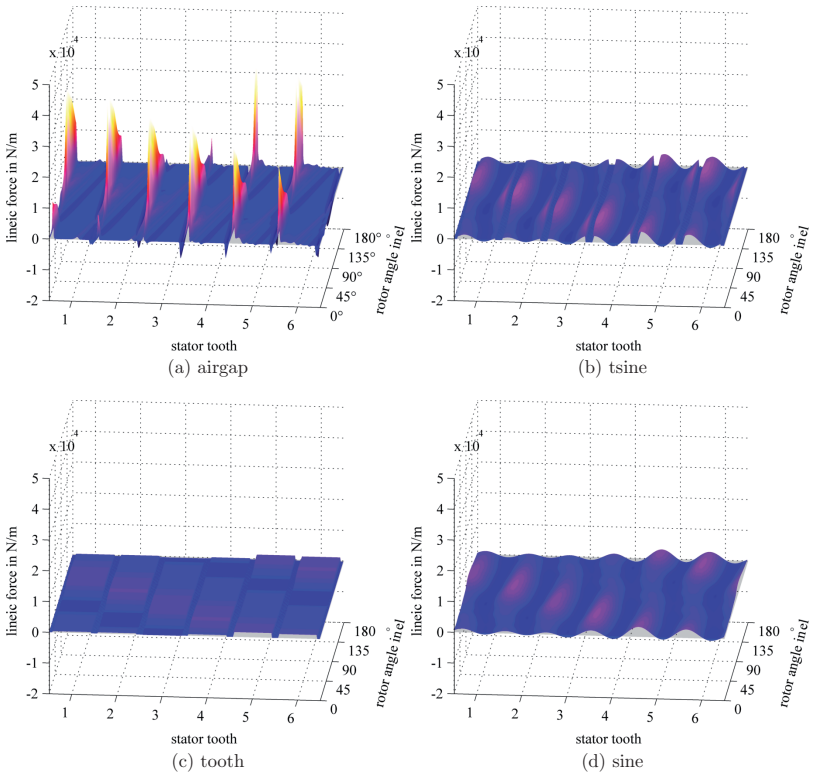

Figure 4.7: Tangential air-gap force under various decomposition options over space and time for PM-A at the corner point

particularly pronounced so that most of the force density appears in the air-gap. Due to the concentration of the forces on the tooth edges, higher spatial frequencies occur so that the tsine approximation of figure 4.7a in figure 4.7b with 6+1 shapes is not as close as that of figure 4.5a in figure 4.5b. However, anticipating the structural analysis results, these higher spatial force shapes are structurally and consequently acoustically not relevant.

4.3.5 Comparing the forces in the spatial frequency domain

Section 4.3.4 and in particular figure 4.5 and figure 4.7 provided a qualitative impression that tsine forces are a good approximation of the air-gap force. It could be easily concluded that the tsine force is a better match than the tooth force. It could, however, not be seen how well a particular spatial harmonic is met and in particular not whether – and that is what

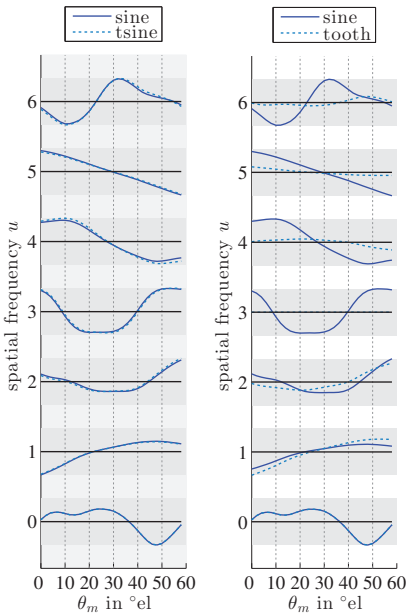

(a) tsine (b) tooth

Figure 4.8: Comparison of the time variation of the spatial orders of the original air-gap force to the air-gap force resulting from a tsine and a tooth approximation for PM-A machine

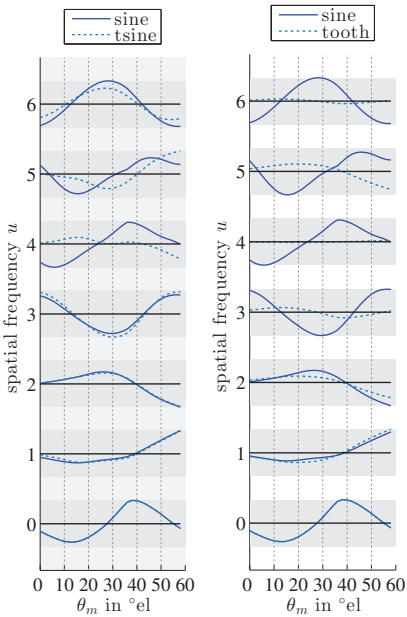

(a) tsine (b) tooth

Figure 4.9: Comparison of the time variation of the spatial orders of the original air-gap force to the air-gap force resulting from a tsine and a tooth approximation for PM-B machine

is acoustically relevant – the time variation is preserved. The above qualitative view is now further quantified. The air-gap force – in particular the time variation of the spatial orders – resulting from the tsine or tooth approximation is compared to the original air-gap force. Ideally, both are identical.

This is achieved with help of figure 4.8 and figure 4.9. There, normalized Fourier coefficients from the spatially decomposed radial air-gap force are compared. This allow to show whether time variation and amplitude are preserved. The comparisons are presented for a single dq-operating point but the comparison has been drawn for various operating points and the results stay similar.

The coefficients to be compared are obtained as follows. The sine, tsine, or tooth air-gap force over space and time (i.e., the content of figure 4.5 or what is shown for one time-instant in figure 4.2 and figure 4.3) is decomposed in space. Time t here is proportional to the rotor

position θ_m as machine speed is constant. The resulting Fourier series have the form

$$f_\mathrm{rad}(\theta_\mathrm{m},\alpha) = \sum_{\nu=0}^{6} \left(f_{\cos,\mathrm{rad},\nu}(\theta_\mathrm{m}) \cos(\nu\alpha) + f_{\sin,\mathrm{rad},\nu}(\theta_\mathrm{m}) \sin(\nu\alpha) \right), \tag{4.29}$$

as introduced in equation (4.1). The coefficients $f_{\cos,\mathrm{rad},\nu}(\theta_\mathrm{m})$ are normalized and compared. We skip the 'rad' index. Normalization of, for example, the tsine coefficient is done as

$$\tilde{f}^{\mathrm{tsine}}_{\cos,\nu}(\theta_\mathrm{m}) = \frac{f^{\mathrm{tsine}}_{\cos,\nu}(\theta_\mathrm{m})}{\min(f^{\mathrm{sine}}_{\cos,\nu}, f^{\mathrm{tsine}}_{\cos,\nu})} \tag{4.30}$$

so that the larger of the two curves is between -1 and 1. The normalized amplitudes can be compared because they are normalized to a common value.

It is seen in figure 4.8a for the PM-A that the tsine force is an almost perfect approximation for all 6+1 spatial orders shown. The spatial orders here refer to a symmetry section of 6 stator teeth representing $^1/_4{}^{\mathrm{th}}$ of the machine. Thus, $\nu = 1$ becomes $\nu = 4$ in the machine. Consequently, the shown orders cover in the machine the excitations up to shape $\nu = N_\mathrm{s} = 24$.

The spatial mean, the shape 0 component, is always preserved and therefore also matches for the tooth force in figure 4.8a. For $\nu = 1$, a deviation can already be seen. One may argue that this is still okay on a decibel (dB) scale. $\nu = 2$ is only a coarse approximation. $\nu = 4, 5, 6$ are too low. $\nu = 3$ is zero in $f_{\cos,\mathrm{rad},\nu}(\theta_\mathrm{m})$ for symmetry reasons (it exist in $f_{\sin,\mathrm{rad},\nu}(\theta_\mathrm{m})$). In figure 4.4b we see the sinc envelope. The higher orders can therefore be partially compensated by multiplying with the inverse envelope. The results for order higher than $\nu = 1$ remain unsatisfactory.

For machine PM-B in figure 4.9, the results are similar to PM-A above, except that for the tsine force a deviation is seen from $\nu = 4$ onwards. Comparison with a 6+1 Fourier series shows that this can only be partially attributed to the 3+1 instead of 6+1 Fourier elements used here. However, and that is key difference between tsine and tooth force: for the tsine force, additional spatial harmonics can be added until the difference between the original air-gap force and the tsine force lies only in the treatment of the leakage terms. The tooth force is limited by the Nyquist criterion with its spatial aliasing.

The above specifies the goal for system simulation force models. The models must provide the time variation of the fundamental spatial harmonics for the chosen force decomposition. Such models will be developed in chapter 5.

4.4 2-D analysis of shape 0 forces in skewed PMSMs

This chapter closes with an application example for the analysis of spatially decomposed forces in PMSMs. Focus is on the one force shape that, besides scaling, does not depend of the type of decomposition: the shape 0 force, the spatial mean of the air-gap force. The 'breathing' shape 0 force is acoustically most critical for many PMSM electric vehicle drives. Its tangential component is equal to torque ripple whose minimization is of interest in servo drives. Rotor skew is frequently used to reduce the shape 0 force ripple.

The force and torque fluctuations in highly utilized permanent magnet machines are strongly operating point dependent and therefore need to be determined for the full operating range.

Within this section, it is first shown how by suitable distribution of the operating points in the dq-current plane for the FE simulations introduced in section 3.5.2, (discrete) skew can be accounted for with negligible additional effort. An initial study on this is found in [BSD11]. An analytical expression for discrete skew is introduced, which describes its effect and the influence of the number of skew segments on the frequency composition of the shape 0 force excitation. Simulation results for machine PM-C show that while in the base speed range the analytical assumption is well met, the skew effect strongly deviates and the main force ripple component partially increases in the field-weakening regime. Skew eventually becomes counterproductive for force ripple reduction and acoustic noise increases. This is shown to result from a lack of phase shift between the forces on the skew segments so that they no longer cancel each other out. This ineffectiveness of skew at full load for machine PM-C will be confirmed in section 7.2.5 for synthesized vibrations based on a full structural model and forces from a system simulation run-up.

Within this work, skew is treated in 2-D and 3-D. 2-D skew refers to cases where the axial dimensions of the machine, i.e., the different z-axis positions of the slices are not important (e.g., integral quantities like torque, back-EMF, lumped parameters) or where, within limits, it can be disregarded (forces). 3-D skew refers to those cases where the 3-D nature of the force excitation is preserved and considered in the vibration synthesis. The results below are for a 2-D skew analysis or air-gap forces; results for a 3-D analysis of acoustic machine vibrations are shown in section 7.2.

4.4.1 Simulation procedure for skewed PMSMs

For PMSMs, skew is usually achieved by discrete skew of the rotor. The magnets in the rotor are segmented and different slices of the rotor stack are shifted against each other. In machine PM-C, the rotor is discretely skewed with 2 groups of $S = 3$ segments. Figure 4.10 shows a typical V-shape skew arrangement with 2 groups of $S = 3$ segments. Arranging the segments in 2 inverse groups prevents an axial net force on the rotor. One stator slot skew ($\theta_s = 30°\text{el}$) is the typical choice for reducing the shape 0 force excitation. In machines with concentrated coils, e.g., found in hybrid electric vehicles, one half slot skew would be the equivalent choice. However, this equals 60°el and the torque capability would suffer quite strongly so that this is usually not used. (Discretely) skewed machines are typically investigated using multi-slice methods in 2-D FE simulations [GVM01; DHW03; Hen06].

4.4.1.1 Distribution of the dq-current points allowing direct 2-D skew superposition

Without further consideration, the computational effort increases proportionally to the number of skew segments. Distributing the simulated operating points in the dq-current plane in a polar coordinate system (i.e., varying control angle γ and current amplitude $\hat{\imath}_\mathrm{s}$) allows to account for skewed machines with negligible additional effort. A suitable distribution for 3-segment 1-slot skew is shown in figure 4.11 which is equal to the exemplary operating point distribution from figure 3.17. Here, for the direct skew superposition, it is important that the angular distance γ between the different operating points is 10°el.

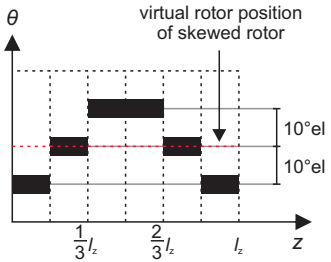

Figure 4.10: Schematic drawing of a skewed rotor

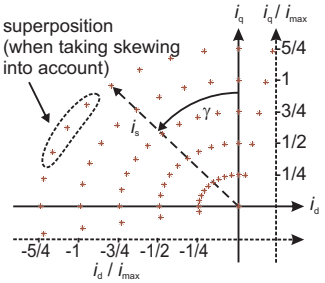

Figure 4.11: Simulation point distribution in the dq-current plane allowing for direct skew superposition

4.4.1.2 Result superposition to account for 2-D skew

Discrete 1-slot skew with 3 segments leads to a displacement of 10°el between the segments. In order to obtain the results for one operating point of the skewed machine, three simulations, as shown in figure 4.11, are superposed. The results are calculated from

$$\xi_{\text{results}} = \frac{\xi_{\gamma-10°\text{el}} + \xi_{\gamma} + \xi_{\gamma+10°\text{el}}}{3}, \tag{4.31}$$

with the control-angle γ and the result quantity ξ (e.g., force in air-gap, torque, back EMF). The second quadrant of the dq-current plane is typically analyzed. In this case due to skew, only the operating points at $\gamma = -10°\text{el}$ and $\gamma = 100°\text{el}$ in the first and third quadrant are simulated additionally to generate results for the skewed version of the machine.

4.4.2 Analytical description of discrete skew

Prior to evaluating simulation results, the effect of skew on the frequency composition of shape 0 forces is analytically approximated. For machine PM-C, the shape 0 force frequency components are at multiples of 30 times the mechanical frequency f_{m} with $60f_{\text{m}}$ as the strongest component (see section 4.2 and [BKD08]). Starting point of the analysis is the spatially decomposed air-gap force from equation (4.1),

$$f_{d,U}(t,\alpha) = \sum_{\nu=0}^{U} \left(f_{\cos,d,\nu}(t) \cos(\nu\alpha) + f_{\sin,d,\nu}(t) \sin(\nu\alpha) \right).$$

We focus on the spatially constant and thus only time-dependent radial shape 0 force, $f_{\text{rad},0}(t) = f_{\cos,\text{rad},0}(t)$, in the following. The frequency spectrum of $f_{\cos,\text{rad},0}(t)$ is written as $F_{\text{rad},0}(f)$[(ii)]. We make the idealizing assumption that the force on the superposed slices is identical except for phase shift. Then, a functional expression between the shape 0 forces

[(ii)] The 'cos' label is omitted since the sine term is zero for $\nu = 0$.

$f_{\mathrm{rad},0}^{\mathrm{skewed}}(t)$ in skewed machines and $f_{\mathrm{rad},0}^{\mathrm{unskewed}}(t)$ in unskewed machines can be expressed by the skew function $h_{\mathrm{skew}}(t)$ as

$$f_{\mathrm{rad},0}^{\mathrm{skewed}}(t) = h_{\mathrm{skew}}(t) * f_{\mathrm{rad},0}^{\mathrm{unskewed}}(t) \tag{4.32a}$$

$$\Updownarrow$$

$$F_{\mathrm{rad},0}^{\mathrm{skewed}}(f) = H_{\mathrm{skew}}(f) \cdot F_{\mathrm{rad},0}^{\mathrm{unskewed}}(f). \tag{4.32b}$$

Basically transforming the continuous expression, for example shown in [Han97], towards discrete skew with S slices (S odd here), $h_{\mathrm{skew,discrete}}(t)$ and $H_{\mathrm{skew,discrete}}(f)$ can be written as

$$h_{\mathrm{skew,discrete}}(t) = \frac{1}{S}\sum_{s=1}^{S}\delta\left(t - \frac{(S+1)T}{2S} + s\frac{T}{S}\right) \tag{4.33a}$$

$$\Updownarrow\ (S \text{ odd})$$

$$H_{\mathrm{skew,discrete}}(f) = \frac{1}{S} + \frac{2}{S}\sum_{k=1}^{(S-1)/2}\cos\left(2\pi f T\frac{s}{S}\right), \tag{4.33b}$$

where $T = {}^{1}\!/_{60f_{\mathrm{m}}}$, here.

Continuous skew (e.g., skewed rotor bars in induction machines) leads to the following skew functions in the time and frequency domain,

$$h_{\mathrm{skew,cont}}(t) = \frac{1\,\mathrm{s}}{T_{\mathrm{skew}}}\mathrm{rect}\left(\frac{t}{T_{\mathrm{skew}}}\right) \tag{4.34a}$$

$$\Updownarrow$$

$$H_{\mathrm{skew,cont}}(f) = \mathrm{sinc}(fT_{\mathrm{skew}}) \tag{4.34b}$$

with $T_{\mathrm{skew}} = {}^{\theta_{\mathrm{skew}}}\!/_{\omega_{\mathrm{m}}}$. Both skew functions have the form of moving average filters or – with time and frequency interchanged – ideal low-passes.

Figure 4.12 shows the continuous and discrete skew function in the time and frequency domain. For both continuous and discontinuous skew, $H_{\mathrm{skew}}(f)$ is zero at $60f_{\mathrm{m}}$ so that under the idealizing assumption made above, this main noise component would cancel out completely. In reality, a significant reduction is expected. In case of continuous skew, the envelope of the sinc function decreases with increasing frequency. For higher frequency components, the effect of skew therefore ideally increases regardless of whether the frequency is near a zero. This low-pass characteristic is already mentioned in [Han97]. This is not the case for continuous skew. Since being time discrete, the discrete skew function is periodic, with its periodicity depending on the number of skew slices.

4.4.3 Simulation results and analysis for a discretely skewed machine (PM-C)

Simulations results now show where the analytic description holds and where and why it deviates.

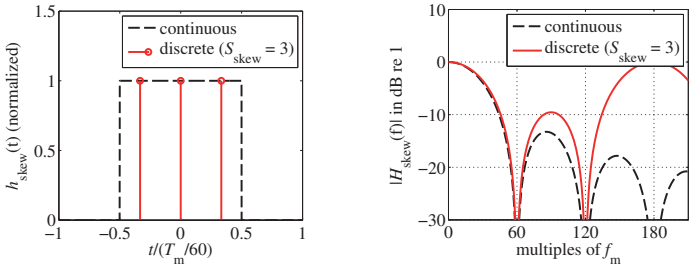

(a) time domain (b) frequency domain

Figure 4.12: Skew functions, continuous and discrete ($S_{skew} = 3$)

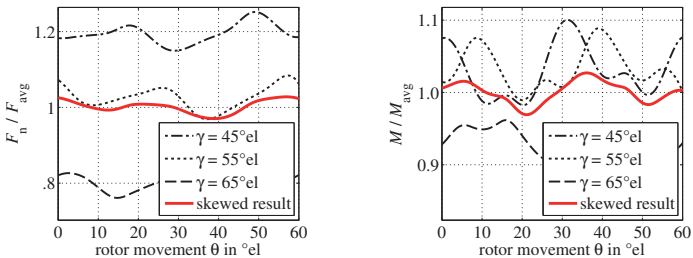

(a) radial force (b) torque

Figure 4.13: Effect of rotor skew on forces and torque in time domain, $i_s = i_s^{max}$, $\gamma = 55°$el

4.4.3.1 Force and torque in the time domain

Figure 4.13 shows radial force and torque in the time domain for a single operating point ($i_s = i_s^{max} = 400\,A$, $\gamma = 55°$el). The abscissa is spaced in electrical degrees so that its spacing is speed independent. The forces in the radial direction for the 3 slices are dashed/dotted (black). It is apparent from figure 4.13a that in contrast to the approximating assumption in section 4.4.2, they are not only phase shifted, in particular due to the DC offset. However, neglecting their DC offset, which does not contribute to force fluctuations, they are indeed similar and show the expected phase shift. The superposition of the operating points, solid (red) line, represents the skewed version of the machine. For the shown operation point, skew reduces the shape 0 force ripple and as a consequence reduces the noise emission of the machine compared to the unskewed version of the machine, dotted (black) line. The effectiveness for torque ripple reduction, figure 4.13b, is similar.

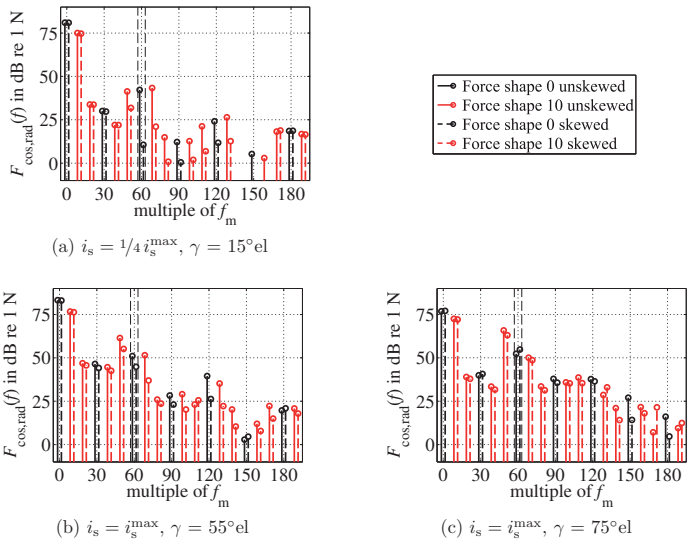

(a) $i_\mathrm{s} = 1/4\, i_\mathrm{s}^\mathrm{max}$, $\gamma = 15°\mathrm{el}$

(b) $i_\mathrm{s} = i_\mathrm{s}^\mathrm{max}$, $\gamma = 55°\mathrm{el}$

(c) $i_\mathrm{s} = i_\mathrm{s}^\mathrm{max}$, $\gamma = 75°\mathrm{el}$

Figure 4.14: Frequency composition of radial shape 0 and shape 10 force excitation for two exemplary operating points for the skewed and unskewed case

4.4.3.2 Force in the frequency domain

Figure 4.14 analyses the above operating point ($i_\mathrm{s} = i_\mathrm{s}^\mathrm{max}$, $\gamma = 55°\mathrm{el}$) along with two other operating points ($i_\mathrm{s} = 1/4\, i_\mathrm{s}^\mathrm{max}$, $\gamma = 15°\mathrm{el}$ and $i_\mathrm{s} = i_\mathrm{s}^\mathrm{max}$, $\gamma = 75°\mathrm{el}$) in the frequency domain. Shown is $F_{\mathrm{rad},0}(f)$, the frequency composition of the spatially constant 0 order force shape $f_{\mathrm{rad},0}(t)$ ($= f_{\mathrm{cosrad},0}(t)$), along with $F_{\mathrm{cos,rad},10}(f)$ of the first spatial force harmonic $f_{\mathrm{rad},10}(t)$ (shape 10). Shape 10 occurs due to the pole count of 10.

In accordance with $H_{\mathrm{skew,discrete}}(f)$ in figure 4.12b, 60 and $120 f_\mathrm{m}$ are well reduced in figure 4.14a and with lesser effect in figure 4.14b, while due to the periodicity of the skew function $180 f_\mathrm{m}$ is not damped. For 30 and $150 f_\mathrm{m}$, the skew function predicts little influence with stronger damping of $90 f_\mathrm{m}$ which can also be observed in figure 4.14a and figure 4.14b. In figure 4.14c, skew has no longer the force ripple reducing influence so that the acoustic characteristics of the skewed machine do not improve. The reason for this is eventually analyzed in section 4.4.3.5. The skew damping on the higher spatial harmonics, observable for shape 10 in figure 4.14a and figure 4.14b, is not further discussed here. Even though the amplitude of the shape 10 excitation is similar to that of shape 0, the structural response to this excitation is lower in the most part [BKD08]. All further results deal with shape 0 only.

4.4.3.3 Force excitation amplitudes over dq-current range

The strong frequency components 30, 60, and $120 f_\mathrm{m}$ of force shape 0 are further investigated. Their amplitude, which is only analyzed for three operating points above, is now shown in

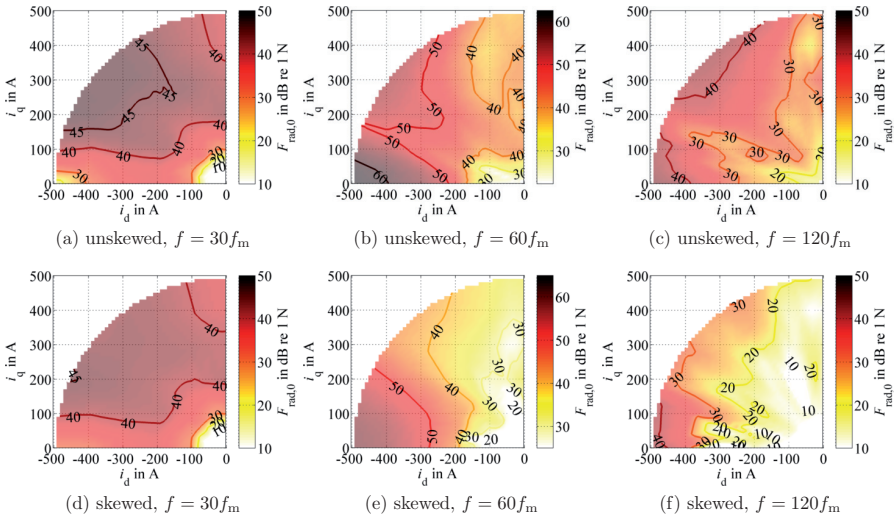

(a) unskewed, $f = 30f_m$ (b) unskewed, $f = 60f_m$ (c) unskewed, $f = 120f_m$

(d) skewed, $f = 30f_m$ (e) skewed, $f = 60f_m$ (f) skewed, $f = 120f_m$

Figure 4.15: Amplitudes of the most significant multiples of f_m for the shape 0 air-gap force for the unskewed and skewed machine

the entire second quadrant of the dq-current plane for both the unskewed and the skewed machine in figure 4.15.

Comparison of figure 4.15a and figure 4.15d shows that skew has only little influence on $30f_m$ as analytically predicted, regardless of the current. For $120f_m$, the analytical prediction of damping through skew generally holds (figure 4.15c vs. figure 4.15f); for the main frequency component $60f_m$ only as long as the machine is not driven significantly in the field-weakening regime, i.e., for small values of γ (figure 4.15b vs. figure 4.15e). For large values of γ the effect of skew decreases.

In the field-weakening range, the negative d-axis current leads to flux counteracting the PM flux. The overall strength (DC offset) of the shape 0 force, i.e., the attraction between stator and rotor, decreases. However, figure 4.15b and figure 4.15e show that this is not the case for the acoustically relevant force ripple at $60f_m$ whose amplitude even partially increases (compare, for example, the 50 dB contours). This is discussed further in section 4.4.3.4 below. This is in opposite to [JR04] where (at least under no load conditions) field-weakening is proposed as a means to decrease force ripple in PMSMs.

4.4.3.4 Effect of skew over the machine operating range

Enclosed in the maximum torque per ampere (MTPA), maximum current (MA), and maximum torque per flux (MTPF) contours, only a fraction of the above discussed dq-current range is used when the machine is operated (see section 3.4.1). The relevant dq-current range is covered by the black lines of constant torque shown in figure 4.16a. The figure itself displays

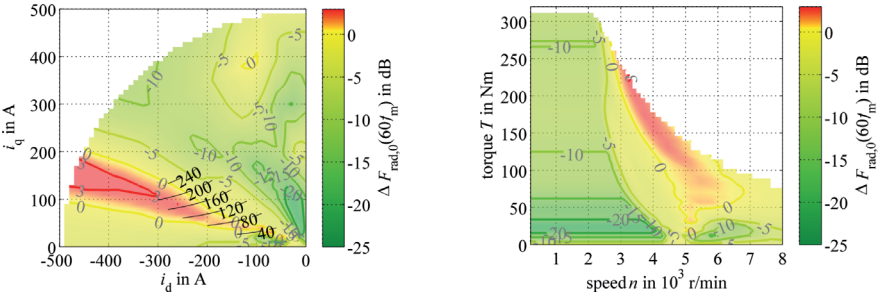

(a) over dq-current plane (b) over torque and speed

Figure 4.16: Radial force reduction due to skew for radial shape 0 force at $60f_m$

the difference in the force excitation between the skewed and the unskewed machine for radial shape 0 force excitation at $60f_m$. The difference is calculated in dB as

$$\Delta F_{rad,0}(f) = F_{rad,0}^{skewed}(f) - F_{rad,0}^{unskewed}(f) \tag{4.35}$$

for $f = 60f_m$. A negative result represents a reduction of the noise emission which is equivalent to a greenish color in figure 4.16.

Figure 4.16a shows for the dq-current plane that rotor skew reduces the radial force ripple in almost all operating points. Improvements of more than -20 dB can be achieved. However, for $66°\text{el} < \gamma < 72°\text{el}$ (red region in figure 4.16a) the force magnitude slightly increases when the rotor is skewed.

The same results mapped to the torque-speed plane based on the control strategy discussed in section 3.4.1 are shown in figure 4.16b. In the base-speed range (typical operating range for servo drives), significant improvements around -10 dB are visible at high loads. However, the acoustically most critical operating points for traction drives are typically along the constant power line in the field-weakening regime. There, the effect of skew is significantly lower. From 2000 r/min to 4000 r/min, rotor skew even increases the air-gap forces at high loads up to 3 dB.

4.4.3.5 Why skew partially deteriorates the acoustic performance in machine PM-C

The key assumption for the working principle of skew (also the basis of section 4.4.2) is that the forces between the segments are phase shifted. For one slot skew (30°el), the phase angle of the frequency component $60f_m$ is therefore expected to shift 360° over 30°el (i.e., 120° between two slices), while the amplitude remains constant. Figure 4.17a shows for different current amplitudes i_s the phase angle of $F_{rad,0}(60f_m)$ as a function of the control angle γ. If the slope of the phase angle is in parallel with the ideal line, the skew assumption for the phase relationship is met. The effectiveness of skew additionally depends on the change of the amplitude of $F_{rad,0}(60f_m)$ which ideally remains constant (and is desired to be as low as possible), cf. figure 4.17b.

It was shown in figure 4.16a that skew is particularly effective for low current amplitudes

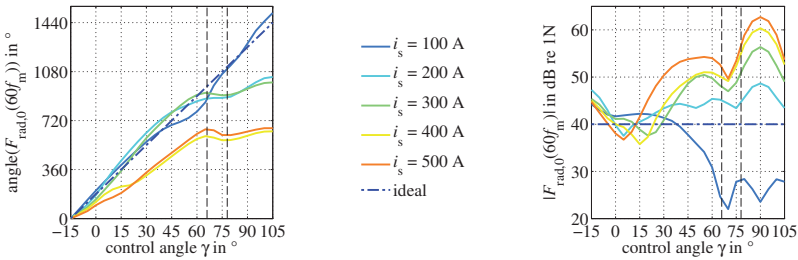

(a) angle (b) amplitude

Figure 4.17: Phase angle and amplitude of radial force shape 0 force at $60f_m$ as a function of the control angle γ

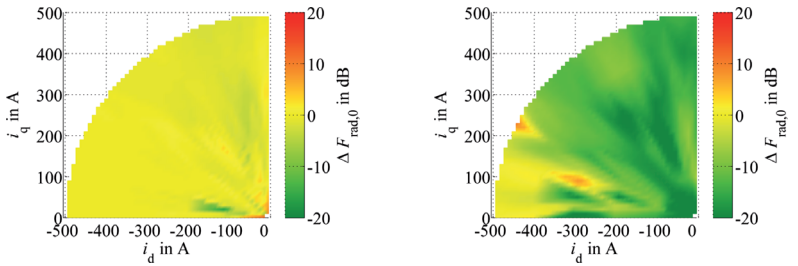

(a) $f = 60f_m$ (b) $f = 120f_m$

Figure 4.18: Difference in the radial shape 0 force excitation between 3-slice and 2-slice skew

and leads to deterioration for 66°el $< \gamma <$ 72°el. This effect can be understood with the help of figure 4.17. The lower the current, the more parallel is the angle to the ideal angle in figure 4.17a. For 66°el $< \gamma <$ 72°el and high current, the slopes become slightly negative and are fairly constant afterward. This means that no effective skew angle can be found there, regardless of the number of slices, their weights, or angular displacements.

4.4.3.6 Periodicity of the discrete skew function – comparing 3-slice vs. 2-slice skew

It is already observed in section 4.4.3.2 and attributed to the periodicity of the skew function that $180f_m$ is not reduced in figure 4.14b. To further confirm the periodicity, two 1-slot skew configurations are compared, namely 3-slice 10°el-per-segment skew and 2-slice 15°el-per-segment skew. Results are shown in figure 4.18. It can be seen that the force at $60f_m$ is almost equal (figure 4.18a). However, only 3-slice skew (figure 4.18b) is capable of reducing $120f_m$ – for 2-slice skew, the skew function is periodic with 120°el and does not dampen this frequency component.

4.4.4 Conclusion on the 2-D force analysis in skewed machines

It is shown that for assessing the effectiveness of a certain skew angle in highly utilized drives, the entire operating range needs to be investigated. Significant deviation from the analytically derived ideal effect occurs and force and torque ripple may even increase. This can be attributed to a change in the phase shift between the forces on the individual segments. It is shown that for machine PM-C operating points exist for which no skew combination has the desired force ripple reducing effect.

5 Force models for time domain simulations

Force models for use in time domain simulations are developed in this chapter. Permanent magnet and switched reluctance machines are considered including skewed PMSMs, stacked SRMs, and outer rotor machines. The models are lookup table based and parametrized with the coefficients of the spatially decomposed air-gap force. For these, the options sine, tsine, and tooth have been introduced in chapter 4. The force models complete the system simulation introduced in figure 3.1. Its force block is again shown below in figure 5.1. The vibration synthesis discussed in chapter 6 is then performed in the frequency domain based on the time domain force signals from the system simulation force models.

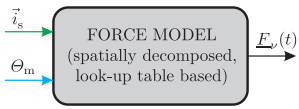

Figure 5.1: Generic force model block for the system simulation model

5.1 Force model for permanent magnet machines

The non-linear spatial-harmonic PMSM machine model from section 3.3.1, fed from a voltage-source inverter, is an efficient tool to determine the stator currents under arbitrary operating conditions taking into account external disturbances (switching frequency components) as well as internal effects (spatial harmonics). The force model allows to determine the corresponding electromagnetic air-gap forces in a system simulation. The force model for PMSMs has been introduced along with the spatial harmonics PMSM model from section 3.3.1 in [Boe+12].

5.1.1 Parametrization with the spatially decomposed air-gap force

In setting up the PMSM force model, we start again with the initial expression for the spatially decomposed air-gap force from equation (4.1) which is

$$f_{d,U}(t,\alpha) = \sum_{\nu=0}^{U} \left(f_{\cos,d,\nu}(t) \cos(\nu\alpha) + f_{\sin,d,\nu}(t) \sin(\nu\alpha) \right).$$

For simplicity, we omit the force direction index d in the following; the modeling procedure is identical for radial and tangential forces. The tangential shape 0 force from the force model has been used for the determination of T_LUT in figure 3.8c where the torque from the spatial harmonic machine model was validated against that from the force model. In the force model, the above time t dependence is expressed as a dependence on the stator current $\vec{i}_\mathrm{s}^{\,\mathrm{dq}}$ and the

rotor position θ_m, which themselves are functions of time. The two real valued Fourier series parameters a_ν and b_ν are combined to one complex coefficient $\underline{F}_\nu = a_\nu - \mathrm{j}b_\nu$. The above Fourier series for the spatially decomposed force is then rewritten as

$$f(\alpha)|_{\vec{i}_\mathrm{s}^\mathrm{dq},\theta_\mathrm{m}} = \sum_{\nu=0}^{U} \Re\left\{\underline{F}_\nu|_{\vec{i}_\mathrm{s}^\mathrm{dq},\theta_\mathrm{m}} \mathrm{e}^{\mathrm{j}\nu\alpha}\right\} \tag{5.1}$$

The structure of the force model block is shown in figure 5.2. Inputs to the model are the dq-current $\vec{i}_\mathrm{s}^\mathrm{dq}$ and the rotor position θ_m. Outputs are the time-dependent Fourier coefficients $\underline{F}_\nu(t)$ of the individual force shapes.

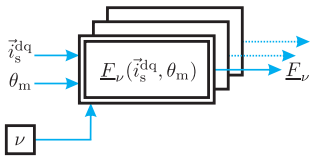

Figure 5.2: Element of the force model from figure 5.1. For each spatial force shape of order ν (both radial and tangential), a $\vec{i}_\mathrm{s}^\mathrm{dq}$ and θ_m dependent lookup table exists.

The air-gap force $f(\alpha)|_{\vec{i}_\mathrm{s}^\mathrm{dq},\theta_\mathrm{m}}$itself, for which in chapter 4 various snapshots were presented, is usually not explicitly re-synthesized according to equation (5.1). Instead, the time-dependent coefficients of the individual force shapes $\underline{F}_\nu|_{\vec{i}_\mathrm{s}^\mathrm{dq},\theta_\mathrm{m}}$ are analyzed. Examples are shown below.

For parametrization of the force model, the force distribution $f(\alpha)|_{\vec{i}_\mathrm{s}^\mathrm{dq},\theta_\mathrm{m}}$ in the air-gap is determined for a grid of current set-points in the dq-current plane as previously discussed in section 3.3.1.4. The grid points can be arbitrarily distributed in the dq-plane. It must only be ensured that the point distribution is fine enough to allow for interpolation. For the lookup tables, they are mapped onto a rectangular grid. For the spatial decomposition the options sine, tsine, and tooth can be used as introduced in chapter 4.

5.1.2 Time-domain interpolation of the air-gap force

The above coefficients $\underline{F}_\nu|_{\vec{i}_\mathrm{s}^\mathrm{dq},\theta_\mathrm{m}}$ form the basis of the force model shown in figure 5.2. It merely consists of complex-valued, three-dimensional lookup tables for each force shape ν, with input variables real and imaginary part of for $\vec{i}_\mathrm{s}^\mathrm{dq}$ and θ_m. By contrast, the $\vec{i}_\mathrm{s}^\mathrm{dq}(\vec{\psi}_\mathrm{s}^\mathrm{dq},\theta_\mathrm{m})$-block for the machine model with spatial harmonics was further decomposed into tables for the coefficients of individual spatial current harmonics n (see equation equation (3.30)). Hence, θ_m became a multiplier instead of a lookup table dimension. While this approach is generally possible for $\underline{F}_\nu|_{\vec{i}_\mathrm{s}^\mathrm{dq},\theta_\mathrm{m}}$, too, this is less advantageous as the force tables are neither inverted nor fed back (so that stability is not an issue). The frequency content of the force is therefore not explicitly defined by an $\mathrm{e}^{\mathrm{j}k\theta_\mathrm{m}}$ multiplier but implicitly by the lookup table data.

The time dependent force excitation $\underline{F}_\nu(t)$ related to a given current $\vec{i}_\mathrm{s}^\mathrm{dq}(t)$ and $\theta_\mathrm{m}(t)$ is found by interpolation. Figure 5.3 shows the trajectory of the dq-current for an exemplary operating point at constant speed and constant average torque. Without spatial harmonics and switching frequency components and assuming an ideal controller, the dq current is

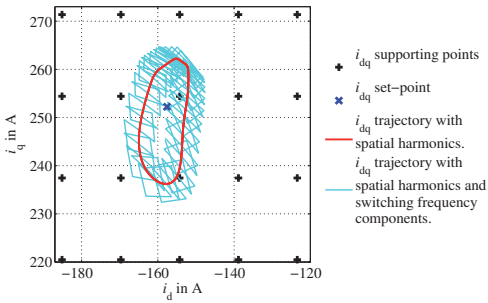

Figure 5.3: dq-current trajectory within an $\underline{F}_\nu|_{\vec{i}_s^{dq},\theta_m}$ lookup table from figure 5.2 for a stationary operating point.

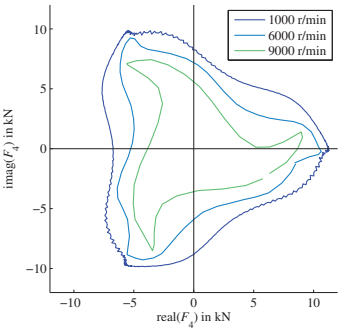

Figure 5.4: Space vector trajectory of $\underline{F}_4$ at different speeds

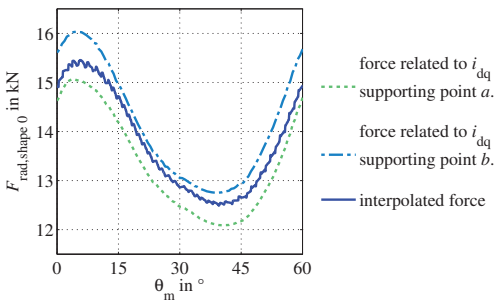

Figure 5.5: Example of an interpolated force (shape $\nu = 0$, radial) under the simplified assumption that only two supporting points contribute

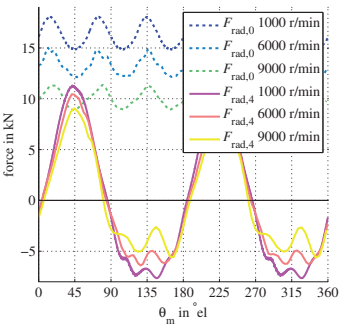

Figure 5.6: Time variation of $\underline{F}_0$ and the cosine shape of $\underline{F}_4$

not time-dependent and equal to the dq set-point ('×' marker). The resulting force can be determined from its supporting points ('+' markers) for which FE results exist. This can be done without the time domain simulations discussed in section 3.3.1.1 and is the case covered in [Boe+10], where purely sinusoidal currents are considered. Here, we deal with time dependent currents $\vec{i}_s^{dq}(t)$. The oval curve in figure 5.3 shows the $\vec{i}_s^{dq}(t)$ trajectory in case we take into account spatial harmonics without modulation, while the zig-zag curve is the trajectory in case of switching frequency components and spatial harmonics.

Exemplarily for force shape $\nu = 0$, figure 5.5 illustrates the interpolation of a force component. For simplicity, it is assumed that the current trajectory lies between only two supporting points (a and b). It can be noticed that the switching frequency ripple from the dq-current is present

in the force.

That all force shapes but 0 are rotating is visible in figure 5.4 for force shape 4 where the trajectory of $\underline{F}_4$ is shown at different speeds. The different rotational speeds and directions of the temporal orders cause the deformation of the trajectory. If there was only one temporal order, the trajectory would be a circle. Moreover, it makes clear why the force is also decomposed temporally after the initial spatial decomposition. Figure 5.6 shows the time variation of the cosine shapes (real part) of force shapes 0 and 4 at different speeds to give an impression of how the time signals on the model output look. The results in the above figures are based on a tsine force decomposition.

Upsampling the lookup table data in the θ_m dimension

The lookup table data from the FE simulations comes with 1°el or 2°el step width as discussed in section 3.5.2. For fast simulation times, the SIMULINK implementation of the force lookup uses linear interpolation in the time domain. Linear interpolation inevitably leads to artifacts in the spectrum. When validating the model by feeding the model with sinusoidal currents, the high-frequency content of the interpolated force tended to be higher than in the original force for some machines. This effect could be largely mitigated by upsampling the lookup table data. Alternatively spline interpolation as discussed for spatial PMSM models in section 3.3.1.9 may be investigated.

In figure 5.5, the grid in the dq-current plane is rather coarse which is usually not a problem as the tables are rather smooth in the dq-current domain. If the number of sampling points shall be increased (without additional FE simulations), then this cannot be done by upsampling since the functions are not periodic in the dq-current domain as they are in the θ_m dimension. Spline interpolation is used instead (cf. section 3.3.1.9).

5.1.3 Frequency domain evaluation of the air-gap force

Analogous to stator voltage and current in section 3.3.1.7, $\underline{F}_\nu(t)$ for the force shapes $\nu = 0$ and $\nu = 4$ are now evaluated for a run-up of machine PM-B. The analysis is again done in the frequency domain in the form of spectrograms (see figure 5.7) for the same run-up conditions from 0 r/min to 10 000 r/min at full load. In general, the frequency content can be compared to that of voltage and current: all frequency components of the force shapes change proportional to speed with the machine-inherent components starting from zero and the switching frequency components starting from $\pm f_\mathrm{switch}$. The latter are directly linked to the respective current components and do not exist if the modulator is left out. The machine-inherent components are a consequence of the machine configuration and also exist in case of sinusoidal currents. Their amplitude, however, is affected by the spatial-harmonic related current components. This is further analyzed in [Boe+12]. A brief analysis of how the machine current can suppress the shape 0 force excitation in PMSMs is performed in section 7.3.1.

$\underline{F}_\nu(t)$ are functions in time, since $\vec{i}_\mathrm{s}^{\,\mathrm{dq}}$ and θ_m are time dependent. $\underline{F}_\nu(t)$ is complex because it represents what can be seen as either two spatially orthogonal or counter-rotating force shapes of order ν. The latter interpretation is used in the following in accordance with the positive and negative sequence spectrograms. Positive frequency components rotate in one

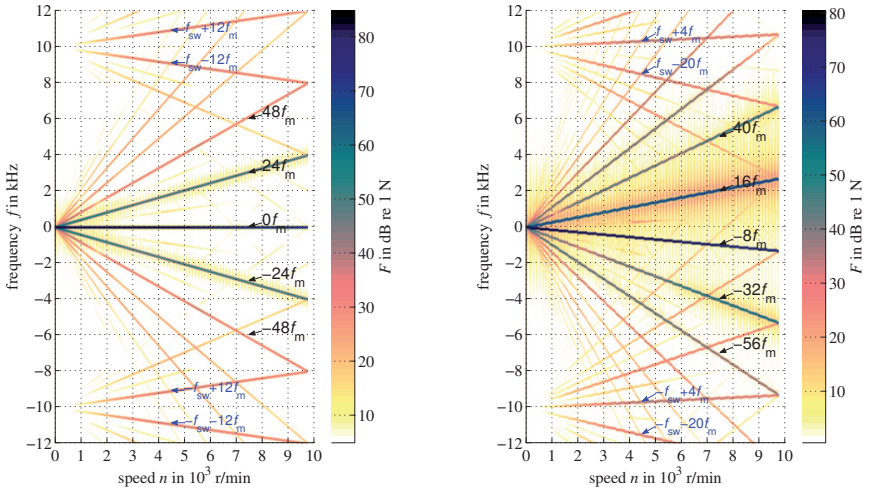

(a) Force shape 0

(b) Force shape 4

Figure 5.7: Force spectrogram for the two main excitation shapes $\nu = 0$ and $\nu = 4$ of machine PM-B during a run-up with full load. Based on an electromagnetic model with spatial harmonics and supplied from a PWM-SVM voltage source.

direction, negative ones in the other. $\underline{F}_\nu(t)$ can be written as

$$\underline{F}_\nu(t) = \sum_{k=-K}^{K} \underline{f}_k \mathrm{e}^{\mathrm{j}2\pi k f_\mathrm{m} t} \tag{5.2}$$

when taking into account only the machine inherent noise components. We can read the spatial and temporal composition of the air-gap force in machine PM-B from table 4.1c $\nu = 0$, k equals $0, \pm 24, \pm 48 \ldots f_\mathrm{m}$ (figure 5.7a) and for $\nu = 4$ k equals $-8, +16, -32, +40, \ldots f_\mathrm{m}$ (figure 5.7b). Comparing the spectrograms of shape $\nu = 0$ and $\nu = 4$, it can be seen that they are fact equal, except for a shift by $2f_\mathrm{el} = 2pf_\mathrm{m}$ due to the modulation by the rotating field/rotor. This also holds for the switching frequency components.

5.2 Forces in switched reluctance machines

This section deals with system simulation models for spatially decomposed SRM forces. First, SRM tooth forces are considered in section 5.2.1. Then they are spatially decomposed by a simple matrix multiplication. Subsequently, a universal SRM force model for time domain simulations is shown in section 5.2.2. This model allows interpolating the air-gap forces in SRM based on the sine, tsine, and tooth option for the spatial decomposition.

5.2.1 SRM tooth forces and their spatial decomposition

Obtaining tooth forces from FE simulations and modeling them in a system simulation is particularly simple for SRMs and can be seen as the standard approach in acoustic modeling of SRMs. In the electromagnetic SRM system simulation model in figure 3.10, the torque per phase is read from a lookup table. The torque is equal to the tangential force per tooth multiplied by the air-gap radius. For the radial tooth force, only an additional lookup table needs to be added. This modeling approach is used for example by Rasmussen in [Ras99] and by Fiedler in [Fie06].

Spatial decomposition of SRM tooth forces

Both, Rasmussen and Fiedler model the structural behavior based on analytically parametrized mass-spring-damper (MSD) models, where one MSD model describes one structural mode. Coupling matrices are introduced which link the excitation at the different teeth with a structural mode. These coupling matrices are the coefficients of a Fourier transform and can be used in complex notation to calculate the spatially decomposed tooth force.

The spatially decomposed tooth force can be transformed into the forces on the individual teeth via the generic coupling matrix $\mathbf{K}_{\text{coupling}}$ as

$$\boldsymbol{F}_{\text{tooth}} = \underbrace{\mathrm{e}^{\left(\frac{2\pi \mathrm{j}}{N}\,\boldsymbol{x}\boldsymbol{x}^{\mathrm{T}}\right)}}_{\mathbf{K}_{\text{coupling}}} \boldsymbol{F}_{\boldsymbol{\nu}}. \tag{5.3}$$

$\boldsymbol{F}_{\text{tooth}}$ is a vector containing the force on tooth 1 to N and $\boldsymbol{F}_{\boldsymbol{\nu}}$ is a vector containing the force shapes of orders ν in a positive-negative sequence form as $\nu \in [0{,}1,\ldots,{}^{N}/_{2}-1,-{}^{N}/_{2},-{}^{N}/_{2}+1,\ldots,-1]$. Both vectors have N_{teeth} elements. The coupling matrix $\mathbf{K}_{\text{coupling}}$ is square. The exponential function in equation (5.3) is not a matrix exponential but calculates the exponential of each element of its matrix argument. $\boldsymbol{x}$ is the vector

$$\boldsymbol{x} = [0{,}1,\ldots,N-1]^{\mathrm{T}}. \tag{5.4}$$

Likewise, the spatially decomposed tooth force can be obtained from the force on the individual teeth via the inverted coupling matrix as

$$\boldsymbol{F}_{\boldsymbol{\nu}} = \mathbf{K}_{\text{coupling}}^{-1}\,\boldsymbol{F}_{\text{tooth}}. \tag{5.5}$$

In a system simulation, only a multiplier parametrized with this inverse coupling matrix needs to be added for obtaining the spatially decomposed tooth force.

Temporal decomposition

The coupling functions can be further decomposed in time under the assumption that the machine is symmetrical, i.e., the forces on all stator teeth are equal and time shifted. The resulting transfer function then shows how much a frequency component in the tooth force is amplified or attenuated after the transform to a certain force shape. An example is given in section 5.3.4. The coupling matrix is further used in the acoustic simulation of the outer rotor machine SR-Y in section 7.5.

5.2.2 SRM force superposition and interpolation

Phase force superposition

The assumption in single-phase SRM models is that the phases are magnetically uncoupled. Based on this assumption, the forces resulting from the individual phases can be superposed. The air-gap force in an SRM is the sum of the forces resulting from the individual phases,

$$f(\alpha) = \sum_{n=1}^{N_{\text{phase}}} f_n(\alpha). \tag{5.6}$$

α is here in electrical degrees. This description assumes a symmetric machine where the force on every tooth belonging to the same phase is identical. In the general case, α is in mechanical degrees and N_{phase} is replaced by N_{s}. Superposition, however, is only valid as long as the above assumption of a magnetically uncoupled system is met. α is continuous in the air-gap only for the airgap force. It may also represent the piecewise constant tsine force or the discrete tooth force. The structure does not change.

$f_n(\alpha)$ depends on the phase current i_n and on the rotor position θ. For each phase, we take the same force base $f^0(\alpha)|_{i_n,\theta}$ center-aligned[(i)] at $\alpha = 0$ and shift it to the respective position in the air-gap,

$$f(\alpha) = \sum_{n=1}^{N_{\text{phase}}} f^0(\alpha)|_{i_n,\theta} * \delta\left(\alpha - 2\pi\frac{n-1}{N_{\text{phase}}}\right). \tag{5.7}$$

In the spatial frequency domain, this becomes

$$F(u) = \sum_{n=1}^{N_{\text{phase}}} \underline{F}^0(u)|_{i_n,\theta} \cdot \mathrm{e}^{\left(-\mathrm{j}2\pi\frac{n-1}{N_{\text{phase}}}u\right)}. \tag{5.8}$$

$\underline{F}^0(u)|_{i_n,\theta}$ is a lookup table for each spatial order ν with $\nu = u$. Besides this particular case of SRM force superposition, the above is applicable wherever forces need to be shifted in space.

Implementation of the time domain interpolation

A schematic of the SRM force-lookup is shown in figure 5.8. It is an implementation of equation (5.8). The difference between figure 5.8 and equation (5.8) lies in the fact that equation (5.8) is derived for a 1-pole model of the machine. For scaling to the full machine, the $\underline{F}^0(u)|_{i_n,\theta}$-LUT is scaled by $2p$ (this is done implicitly) and the spatial order ν of the force shape is scaled. One $\underline{F}^0(u)|_{i_n,\theta}$-LUT exists for each spatial order ν and phase. Inputs are phase currents and rotor position. Afterward, the forces are low-pass filtered, sampled, and written to the workspace[(ii)] .

Remarks on the tooth force

For the tooth force, the result is identical to the above direct-tooth-force-lookup and coupling-function based decomposition. Compared to this, the implementation here is more complex.

[(i)] 'Center aligned' means that the $\alpha = 0$ lies in the middle of the active tooth.

[(ii)] Within Simulink, implementation of this block as well as the PMSM force look-up process becomes very compact and generic in terms of number of phases when using n-dimensional (n-D) interpolation with Pre-Lookup- and For-Each-blocks for multiple input signals.

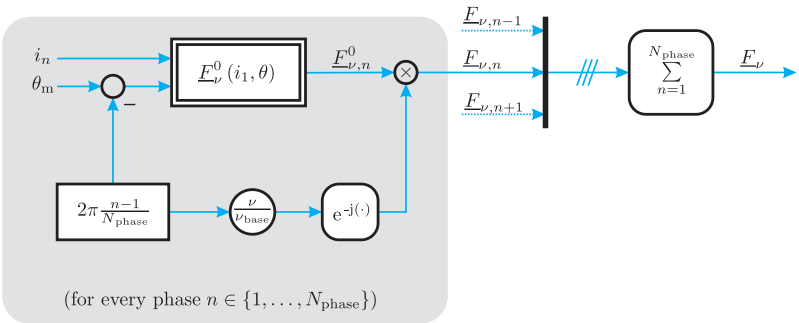

Figure 5.8: Schematic of the force interpolation for one spatial order ν in an SRM

However, its advantage is that it cannot only model the tooth force but also be parametrized with sine and tsine forces. Once it has been implemented, the internal complexity can be made transparent for the user.

5.3 Rotor forces – in particular for modeling outer rotor machines

The discussion of air-gap forces in this work has so far only considered forces acting on the stator of a machine and has neglected forces acting on the rotor. Below, the relationship between stator and rotor forces is discussed for PMSMs and SRMs.

For inner rotor machines, the net radial force on the rotor is zero in most cases. The air-gap force is balanced and does not dislocate the rotor. An unbalanced force perpendicular to the axis of rotation (shape $\nu = 1$ excitation) occurs in case of mechanical unbalance (eccentricity) or magnetic unbalance (phase faults for machine SR-Y, see section 7.5 or machines with diametrically asymmetric phase windings [Zhu+07]). Skew may lead to forces acting in the axial direction. The rotor and accordingly the forces acting on it are omitted in the inner-rotor-machine structural examples in this work. The synthesis process presented in chapter 6 allows for simultaneous consideration of rotor and stator forces, however, correct modeling of the bearings and the effect of rotation is outside of the scope of this work. The author hopes that other researches contribute to these aspects.

For outer rotor machines, the forces on the rotor are of primary acoustic interest rather than those on the stator and must not be omitted. One of the machines to which the acoustic vibration synthesis process is exemplarily applied is the outer rotor machine SR-Y from [Hen11]. Figure 5.9a shows the machine on the test bench and figure 5.9b a close-up of the machine with its integrated inverter.

5.3.1 Forces on PMSM rotors

If we assume the air-gap to be infinitely thin, the force distribution on the rotor is a mirror image of the force distribution on the stator. For rotating field machines with small air-gaps,

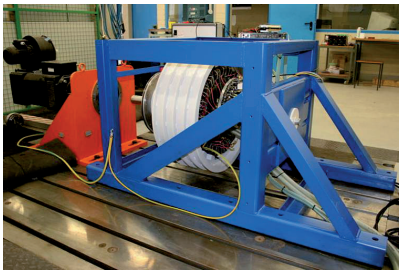

(a) Test bench assembly

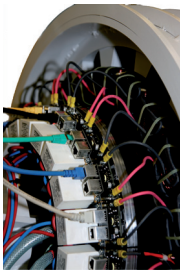

(b) Detail view of the machine with inverter

Figure 5.9: Outer rotor machine SR-Y [Hen11]

this a fair assumption. The rotor forces can be determined from the stator forces by shifting the reference system. In practical FE examples, the force can be directly obtained from the air-gap elements adjacent to the rotor. Decomposing the force for use with structural simulations can be done as for the stator. For most PMSMs, the iron-to-air interface of the rotor is continuous and smooth towards the air-gap so that the rotor provides a continuous surface to which the forces can be applied in the structural FE simulations. In this case, the sine decomposition can be used.

5.3.1.1 Change of the reference system – shift in space

In section 5.2.2, we have already seen a shift of the SRM forces in the air-gap, i.e., in the spatial domain. A similar shift in space occurs if force is shifted between two reference systems, e.g., from the stator-fixed $\alpha\beta$ to the rotor-fixed dq system. Let us assume we have two paths on which we calculate the force; one path fixed to the surface of the stator ($\alpha\beta$), one fixed to the surface of the rotor (dq). The corresponding shift expression is:

$$f^{\alpha\beta}(\alpha) = f^{\mathrm{dq}}(\alpha) * \delta\left(\alpha + \theta_{\mathrm{m}}\right), \tag{5.9a}$$

$$\underline{F}^{\alpha\beta}(u) = \underline{F}^{\mathrm{dq}}(u) \cdot \mathrm{e}^{\mathrm{j}\theta_{\mathrm{m}}u}. \tag{5.9b}$$

This transformation is the coordinate system transformation which is also at the center of the IRTF-based PMSM machine models from section 3.3.1.

5.3.2 Spatially distributed forces on SRM rotors

Spatially decomposing forces on SRM rotors poses more challenges than with SRM stators or with rotors and stators of typical rotating field machines. The force decomposition approaches from section 4.3 are based on a (piecewise) continuous straight or circular interface along which the forces act. It was discussed in section 4.3.4 that this ideal condition can never be

met in SRMs, as, for example, stator teeth see forces on their flanks. However, these effects are usually small and still allow the force to be mapped to the tooth surface.

Figure 5.10a shows that the problem seems to be more severe for SRM rotors. In the unaligned position, forces act entirely on the flanks of the rotor teeth; almost no force acts at the air-gap. Figure 5.10b, however, allows to explain why this problem is less grave than figure 5.10a suggests. When rotor and stator teeth overlap, the force starts to concentrate at the air-gap and only then the force reaches high levels. The vector arrows are not drawn to scale between the two figures; they are about 50 times higher in the overlapping case in figure 5.10b than in the unaligned position in figure 5.10a. The current is the same in both cases (50% rated current). For most operating points, the current is zero in the unaligned position. Some SR drives use the continuous conduction mode as boost mode at high speeds [IK04]. The current is then lower in the unaligned position compared to the aligned position but not zero.

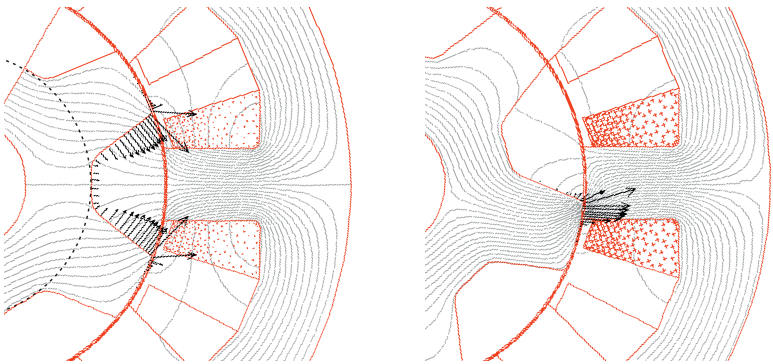

(a) unaligned position (b) partially aligned position

Figure 5.10: Force distribution on SRM rotor. Force arrows are not equally scaled in these figures. Force are about 50 times stronger in the partially aligned position.

It is concluded that despite the force distribution on the tooth flanks in the unaligned position, the error remains low when mapping the forces to the air-gap side of the teeth. The rotor forces are therefore treated like the stator forces and forces on the tooth flanks are mapped to the edge of a tooth. Tsine or tooth force can be used. Another option to cope with this effect is mapping the force to the rotor yoke (black dashed line) and to use "sine" forces, applying the forces directly onto the rotor yoke. This, however, prohibits that any tooth rocking effect is taken into account (cf. section 7.1.6.1).

5.3.3 Determining SRM rotor tooth forces from stator tooth forces

It was shown above that for PMSMs, the rotor forces can be determined from the stator forces by a coordinate system transformation. In SRMs with a phase count different from 1, the number of stator teeth N_s is different from the number of rotor teeth N_r. N_s is chosen larger

than N_r in most designs. When a rotor tooth passes a stator tooth, the respective phase on the stator is excited. Therefore, in case case of $N_s > N_r$, each of the N_s stator teeth is excited N_r times per revolution. On the rotor, more force pulses per tooth and revolution (N_s to N_r) occur on less teeth (N_r to N_s). This lower number of excitations, i.e., the lower fundamental electrical frequency, is the reason for choosing $N_s > N_r$ in the first place. As a consequence of the different pulse count, tsine or tooth forces cannot be mapped from the rotor to the stator side by a simple shift expression.

It is explained below how the rotor tooth forces can be determined from stator tooth forces. For acoustic modeling of the outer rotor machine SR-Y, rotor forces need to be known. In the reluctance-network based system simulation (cf. section 3.3.2.2) of machine SR-Y, fluxes linked with (and consequently forces acting on) the rotor teeth are not explicitly calculated. Yet, for the outer rotor machine SR-Y, the N_r forces $\boldsymbol{F}^{r}_{tooth}$ on the rotor teeth need to be known. They are calculated from the N_s stator tooth forces $\boldsymbol{F}^{s}_{tooth}$ via the rotor-position-dependent stator-to-rotor coupling matrix as

$$\boldsymbol{F}^{r}_{tooth} = \mathbf{K}_{stator\text{-}to\text{-}rotor}(\Theta_m)\, \boldsymbol{F}^{s}_{tooth}, \tag{5.10}$$

where $\mathbf{K}_{stator\text{-}to\text{-}rotor}$ is a $N_r \times N_s$ matrix. The entries in $\mathbf{K}_{stator\text{-}to\text{-}rotor}$ are determined as follows. We assume $N_r < N_s$. If a phase is in the aligned position, a rotor tooth is directly underneath a stator and both forces are equal (matrix entry equals 1). If a phase is in the unaligned position, the stator tooth force is split equally between two rotor teeth (matrix entry equals 1/2). The unaligned position is the middle of an overlap region approximated as 20% of an electrical cycle, where the force on a rotor tooth from a respective stator tooth is either ramped up from 0 to 1 or back down from 1 to 0.

5.3.4 Frequency composition of SRM stator and rotor tooth forces

The transformation from stator to rotor forces leads to a change in the frequency spectrum of the forces due to the change in reference system. Table 5.1a gives an overview of the spatial and temporal frequency spectrum of the air-gap force in machine SR-Y (SR-20/16or) in case of normal operation without faulty phases based on the definitions for the frequency composition according to section 4.2.2. For the rotor force tables, N_s and N_r are exchanged in the formulas in section 4.2.2.

The frequency composition of the shape 0 force is equal on stator and rotor if referred to the same base frequency. This is because its shape is position-independent so that its frequency composition is independent from the reference system from which it is observed. For force shape 4 and 8, the temporal frequency composition of stator and rotor forces differs. However, a frequency component of the stator force spectrum can be easily converted to one of the rotor forces and vice versa via

$$f^{r} = f^{s} + \sigma(\nu)\,\nu, \tag{5.11}$$

where $\sigma(\nu)$ is the sign-function from equation (4.8).

The fundamental frequency f_s of the stator forces is the so-called electrical frequency f_{el} with $f_{el} = N_r\, f_m$. Every stator tooth sees N_r rotor teeth passing per mechanical revolution so that the electrical cycle repeats N_r times. For the rotor, f_r is correspondingly defined as $f_r = N_s f_m$.

shape	multiples of $f_m (= 1/16 f_{el})$									
0	0				±80					±160
4		−16				+64		−96				+144	
8			+32	−48					+112	−128			

(a) stator

shape	multiples of $f_m (= 1/20 f_r)$								
0	0				±80				±160
4		−20				+60		−100				+140	
8				±40					±120				

(b) rotor

Table 5.1: SRM, $N_s = 20$, $N_r = 16$ ($m = 5$) (machine SR-Y)

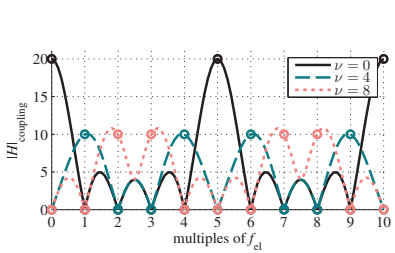

(a) stator, cosine

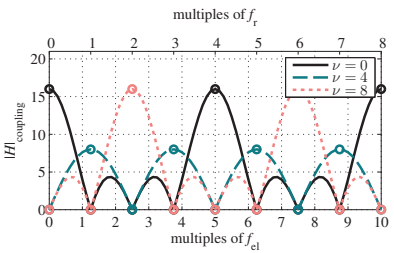

(b) rotor, cosine

Figure 5.11: Coupling functions in the spatial frequency domain

In section 5.2.1, it was already said that the coupling functions can be further decomposed in time under the assumption that the forces on all stator teeth are equal and only time shifted. Figure 5.11 shows the temporal frequency domain representation of the coupling functions from section 5.2.1 for the 20/16 machine SR-Y for both stator and rotor. For conciseness, only the cosine shapes (real part of the result) are shown. The bottom abscissa (x-axis) is in all cases labeled in multiples of f_{el} (i.e., f_s). For the rotor figure, a second abscissa is added on top labeled in multiples of f_r. In terms of the frequency composition of the force shapes, the information is equal to that of table 5.1 taking into account that for machine SR-Y $16 f_{el}$ equals $20 f_r$. The curves are normalized to the force on one tooth from which, based on the periodicity, the entire spectrum is calculated. For the DC component of the shape 0 force in figure 5.11a, it is easily understood that all $N_s = 20$ teeth contribute, so that the amplitude of the coupling function is 20 at that point. The spectral composition of force shapes $\nu = 0, 4, 8$ is of course equal to that from table 5.1.

The vibration spectrum of machine SR-Y is discussed in detail in section 7.5. At this point we content ourselves with confirming the above discussed frequency composition based on figure 5.12. Figure 5.12 shows the measured airborne sound during a run-up test from

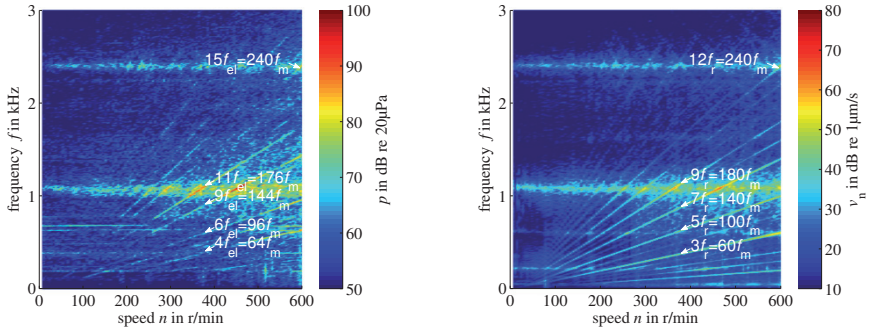

(a) Airborne sound in stationary reference system (A-weighted)

(b) Surface velocity in rotating reference system (A-weighted)

Figure 5.12: Frequency composition depending on reference system

0 r/min to 600 r/min. The measurement microphone is standing next to the machine and therefore in the stationary stator reference system. The frequency multiples 4, 6, 9, 11f_{el} are marked in figure 5.12a. The surface velocity in figure 5.12b is measured in the rotating rotor reference system. If the surface velocity was measured with a laser vibrometer the measured vibration spectrum would have the same frequency composition as the air-gap force due to the observation from the stationary reference system.

5.4 Forces in the third dimension

Most electrical machines are "flat" in the sense that their flux paths are in a plane perpendicular to the shaft. Up to here, we have only considered air-gap forces in 2-D. They act in either the radial or the tangential direction and are constant along the axial direction. We now take into account forces which vary in the axial direction (section 5.4.1–5.4.2) and forces that act in the axial direction (section 5.4.4).

5.4.1 Forces depending on the axial position

Two examples are used to discuss machines where forces vary in the axial direction: machines with skewed rotors and axially segmented machines. Rotor skew is frequently used for synchronous and induction machines for smoothing the air-gap field, i.e., to counteract the slotting-effects [Han97]. For PMSMs, the rotor is usually discretely skewed (see also section 4.4). Axial segmentation is proposed for switched reluctance machines, for example for acoustic reasons or for creating slim SRMs [Bra12]. For acoustic reasons, single-phase axial-air-gap transversal-flux switched-reluctance machines are stacked in a common housing on the same shaft in both, [UK74] (figure 5.13a) and [Hil99] (figure 5.13b); the latter machine is in principle the outer rotor version of the former.

With sine, tsine, and tooth, section 4.3 discussed various options for the decomposition

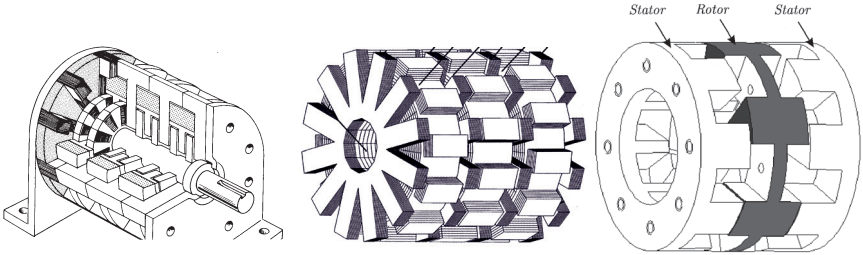

(a) Disc motor cross section from [UK74]

(b) Axially segmented outer rotor SRM [Hil99]

(c) 8/6 switched reluctance axial flux (SRAF) example from [PP98]

Figure 5.13: Examples of switched reluctance machines with axial and/or axial-position-dependent forces

and superposition of forces in the circumferential direction (i.e., radial and tangential forces). For axial position dependent forces we resort to the most basic approach: treat every skew segment (PMSM example) or single-phase machine (SRM example) separately (or model it as piecewise constant when continuous).

5.4.2 Modeling skewed PMSMs

In section 4.4, the effect of skew on the shape 0 force excitation of PMSMs has already been discussed comprehensively by both analytical and numerical means. There, the skew superposition was achieved using a superposition process where the FE results were directly superposed. Here, a force model is developed with which skewed PMSMs can be treated in a system just like non-skewed PMSM were treated in section 5.1. Due to an intermediate interpolation when forming the lookup tables, an arbitrary FE simulation point distribution in the dq-current planes can serve for the LUT data (cf. figure 3.17). Any skew setup in terms of the number of skew segments S and the skew angle θ_s can subsequently be modeled. Simulations results for skewed PMSMs based on the below developed model are presented in section 7.2.

5.4.2.1 Change of lookup table alignment – shift in time

In section 3.5.2.1, current alignment and rotor alignment were discussed as sorting options for the force (and all other) LUTs. Prior to commencing with the skew lookup table discussion, the transformation from one alignment to the other is presented here. By now, the spatial domain representation of the force shapes has been established and the alignment transformation is needed below. A spatial reference-system shift of the air-gap forces for PMSM was already used in section 5.3.1.1 for the transformation between rotor and stator forces.

The air-gap force usually repeats after 180°el so that $f(\theta_\mathrm{m})$ is periodic with $f(\theta_\mathrm{m}) = f(\theta_\mathrm{m}+\pi)$. The current-aligned force $f^\mathrm{c}(\theta_\mathrm{m})$ is transformed into the rotor-aligned force $f^\mathrm{r}(\theta_\mathrm{m})$

via the expression:

$$f^{\mathrm{r}}(\theta_{\mathrm{m}}) = f^{\mathrm{c}}(\theta_{\mathrm{m}}) \ast \delta\left(\theta_{\mathrm{m}} + \gamma\right), \tag{5.12a}$$

$$\downarrow$$

$$\underline{F}^{\mathrm{r}}(f) = \underline{F}^{\mathrm{c}}(f) \cdot \mathrm{e}^{\mathrm{j}\gamma 2\pi f}. \tag{5.12b}$$

5.4.2.2 Force lookup for the skew segments – shift force base in time, current vector in space

The explicit 2-D skew superposition in section 4.4.1 required both a certain alignment (rotor alignment, to be exact) and a polar coordinate distribution of the dq-current simulation points. The latter requirement is dropped for the lookup tables. Based on the force lookup table for a non-skewed PMSM, two steps need to be taken to create the data for each skew segment of a skewed synchronous machine.

First, a skew segment s which is displaced from the d-axis by the angle θ_s (cf. figure 4.10) sees a virtually different dq-axis current, namely,

$$\vec{i}^{\,\mathrm{dq}}_{\mathrm{s},s} = \vec{i}^{\,\mathrm{dq}}_{\mathrm{s}}\, \mathrm{e}^{-\mathrm{j}\theta_s}. \tag{5.13}$$

Second, the different rotor alignment of the slices needs to be taken into account. This is done like the transform between rotor- and current-aligned force above. The force $f_s(\theta_{\mathrm{m}})$ of slice s is obtained by shifting the reference force $f(\theta_{\mathrm{m}})$ via the expression:

$$f_s(\theta_{\mathrm{m}}) = f(\theta_{\mathrm{m}}) \ast \delta\left(\theta_{\mathrm{m}} + \theta_s\right), \tag{5.14a}$$

$$\downarrow$$

$$\underline{F}_s(f) = \underline{F}(f) \cdot \mathrm{e}^{\mathrm{j}\theta_s 2\pi f}. \tag{5.14b}$$

5.4.2.3 System simulation force model for skewed PMSMs

A block diagram for the skew implementation in a system simulation is shown in figure 5.14. The lookup table entries are the same as those used in the simulation of the unskewed PMSM (see figure 5.2). Skew is accounted for by modifying current and rotor position as discussed above. The number of force shapes on the output of the model increases proportional to the number of skew segments S. Instead of U time series $\underline{F}_\nu$ (with radial, tangential, and possibly axial component each) for the U spatial harmonics ν, $S \times U$ time series $\underline{F}_{\nu,s}$ are now generated.

5.4.2.4 Machine model parametrization for skewed PMSMs

The above described skew model makes the direct skew superposition according to equation (4.31) obsolete for PMSM forces in system simulations. However, this approach is still used when parametrizing the electromagnetic model from section 3.3.1. ξ_{results} in equation (4.31) was said to describe an arbitrary result quantity. As such this can also be flux linkage, inductance, or magnetic energy or co-energy needed for parametrizing the electromagnetic model.

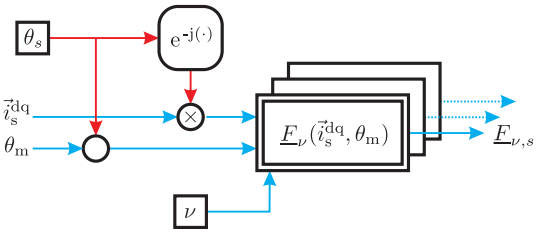

Figure 5.14: Lookup table based force model for skewed PMSMs

5.4.3 Modeling axially segmented SRMs

In principle, all single-phase segments of the shown axial flux switched reluctance machines (the disc motor in figure 5.13a from [UK74] or the axially segmented outer rotor SRM in figure 5.13b from [Hil99]) can be modeled identically. Differences exist in the shifting operations. Our primary focus are the forces on the housing of the machines which for the disc motor contains the stator and for outer rotor SRM the rotor. For both machines, the single-phase stators are inline whereas the rotors are displaced in the circumferential direction. The latter has to be taken into account for the outer rotor machine when determining the structural responses.

For skewed PMSMs, the forces on the segments were determined based on the same dq-current. The forces on a segment of the axially segmented single-phase SRM are only dependent on the current in that particular segment. Thus, they are treated like N_{phase} independent machines[(iii)]. The determination of the rotor force for the outer rotor machine is here simpler than for machine SR-Y in section 5.3.3. Because of the single-phase nature, N_s equals N_r and the two can be considered to be equal (keeping in mind the force leakage phenomena discussed in section 5.3.2). In case the axial forces at the two air-gaps are not equal (for example due to rotor misalignment), we resort to the discussion in the next section. For axially segmented SRMs, results are not presented in this thesis. This machine type has recently been investigated in [Har12].

5.4.4 Forces acting in the axial direction

A machine where the main air-gap flux path is in the axial direction is the switched reluctance axial flux (SRAF) machine shown in figure 5.13c and discussed in [PP98]. The machine concept is based on [UK74] which was discussed in section 5.4.3. Despite the axial instead of radial flux path, modeling the SRAF does not differ from modeling an equivalent 8/6 radial flux SRM. The only difference is that radial forces become axial forces which for the structural FE force response simulations is a minor modification.

[(iii)] The stators of adjacent phases may share the same yoke so that saturation can lead to mutual coupling. If this was the case, electromagnetic and force model would need to be adjusted. Since the dB-scale nature of acoustic phenomena is rather robust against small changes this would still be more of an issue for an in-depth electromagnetic design analysis than for acoustic modeling.

6 Structural response calculation and vibration synthesis

The two preceding chapters have discussed how the air-gap force in an electrical machine can be decomposed in a manner suitable for determining the corresponding structural response (chapter 4) and how the coefficients of the force shapes are determined in system simulations (chapter 5). We now focus on calculating the corresponding structural responses and on the subsequently performed vibration synthesis. Structural response calculation (offline, no user-interaction) and vibration synthesis (online, user-interactive) are separate steps (cf. - figure 1.2) but they share the same formalism. Parts of the structural response superposition are furthermore performed online in the vibration synthesis process. Structural response calculation and vibration synthesis are therefore combined in this chapter.

Section 6.1 delivers the formal basis for structural response calculation and vibration synthesis. Modal analysis and harmonic response analysis as well as material parameters and damping are discussed. Of particular importance is the representation of the vibration by a scaled superposition of eigenshapes. This formalism is presented to the degree required for understanding and implementing response calculation and vibration synthesis. Section 6.2 then deals with the force response calculation. Exemplary results on test bodies are given for the previously introduced sine, tsine, and tooth forces. The vibration synthesis process is discussed on a formal basis in section 6.3. Alternative methods and future extension are referred to in section 6.4. Real-life application examples will eventually be presented in chapter 7.

6.1 Fundamentals of structural analysis and vibration synthesis

The electromagnetic simulations and the derived electromagnetic and force models are nonlinear due to the saturation of the iron at high flux densities. The structural displacements of the mechanical structure are small with respect to the structure's dimension. The structure behaves – or is assumed to behave – linearly. A *linear* problem allows to solve the problem in the *frequency domain.* In machine acoustics in general, the transfer path from exciting force to radiated sound is modeled as a linear transfer path [GWL06]. A *modal analysis* is used to show how the structure can vibrate. By means of a *harmonic response analysis* it can be seen how the structure does vibrate.

The mathematical formulation of the modal analysis and the harmonic response analysis is introduced here. The structure is assumed to behave as a linear, time-invariant system described by a partial differential equation in time and space. The equation of motion of the finite element model is an approximation using a (finite) set of coupled linear ordinary differential equations with constant coefficients. The modal analysis solves the homogeneous problem (no excitation, free vibrations) while the harmonic analysis solves the inhomogeneous problem (with excitation, forced vibrations). Different methods for the harmonic response

analysis exist. Here, the *mode-superposition method* is applied which makes use of the results obtained by the modal analysis. This method is key to the response superposition process as the determination of additional force excitations comes at little costs once the modal base has been determined.

The objective of this work is to describe the acoustic vibration behavior of an electric motor assembly in a given operating range. In some mechanical engineering problems, it is sufficient to determine only eigenfrequencies by a modal analysis. This, for examples, assures that the frequencies of the exciting forces do not coincide with eigenfrequencies. Examples are bridges and turbine blades. Another example is the rotor shaft of a turbo generator which needs to rotate safely at constant speed between or above critical eigenfrequencies. For speed-variable electrical machines and drives, the situation is different. Many eigenfrequencies lie in the range of the exciting forces and several of them are usually significantly excited by the force distribution in the machine. The harmonic response analysis allows to determine operating point dependent vibration amplitudes and links these to the force excitation which can be used as an optimization criterion in the machine design. The mathematical representations of modal analysis and harmonic response analysis are based on [SGM02; ANS12; Dos88]. For further reading it is referred to these sources.

6.1.1 Modal analysis – eigenfrequencies and eigenshapes

The modal analysis forms the basis of the subsequent harmonic analyses and helps to familiarize with eigenfrequencies and eigenshapes. The objective of the modal analysis is to find the structure's *eigenvalues* or *eigenfrequencies* and the corresponding *eigenvectors* which are the *mode shapes* or *eigenshapes*. An assumption for the modal analysis is that damping is low, which leads to the fact that the eigenfrequencies are independent of the damping coefficient. This assumption holds for the low damping values that typically occur in electrical machines [Yan81]. Without damping and additional boundary conditions (e.g., applied forces, displacements, or the like), the equation of motion for a structure represented by finite elements is that of a set of coupled, undamped mass-spring systems. In matrix notation,

$$\mathbf{M}\,\ddot{\boldsymbol{u}}(t) + \mathbf{K}\,\boldsymbol{u}(t) = 0 \tag{6.1a}$$

$$\Downarrow$$

$$-\omega^2 \mathbf{M}\,\boldsymbol{u}(\omega) + \mathbf{K}\,\boldsymbol{u}(\omega) = 0, \tag{6.1b}$$

where $\boldsymbol{u}$ is the vector of the body's degree of freedom (DOF) in terms of displacement, $\mathbf{M}$ is the inertia matrix, and $\mathbf{K}$ the stiffness matrix. In a system with N degrees of freedom, this leads to an N-dimensional set of homogeneous linear and time-invariant ordinary differential equations (with constant coefficients). Free vibrations will be harmonic of the form

$$\boldsymbol{u}(t) = \boldsymbol{\phi}_m \cos(\omega_{0,m} t + \phi), \tag{6.2}$$

where $\omega_{0,m}$ is one of the N eigenfrequencies. $\boldsymbol{\phi}_m$ is the shape function of the m^{th} mode of vibration of the system which is – and this is key to the vibration synthesis process – location-dependent but not time-dependent. $\boldsymbol{\phi}_m$ is a vector of dimension N. It is also called *nodal translation* because the mode shape is described by a translation of the N nodes in the FE model. Mathematically, this represents a product ansatz of a location-dependent and a

time-dependent function. 6.1a has non-trivial solutions only if the determinant is zero:

$$\det[\mathbf{K} - \lambda\mathbf{M}] = 0, \tag{6.3}$$

where $\lambda = \omega_0^2$. The determinant gives the characteristic polynomial which is an N degree polynomial whose roots are the N eigenvalues λ_m of the system[(i)]. The angular eigenfrequencies $\omega_{0,m}$ are given by

$$\omega_{0,m} = \sqrt{\lambda_m}. \tag{6.4}$$

In practical cases, only M ($M < N$) eigenfrequencies are evaluated where ω_M is the largest eigenfrequency in the frequency range of interest. ω_M is typically set 1.5 to 2 times higher than the maximum frequency evaluated in the subsequent harmonic response analysis. Once the eigenvalues are found, the mode shape of the corresponding vibration can be found from equations 6.1a and 6.2. The eigenshapes are normalized to the mass matrix so that

$$\mathbf{\Phi}^{\mathrm{T}}\,\mathbf{M}\,\mathbf{\Phi} = \mathbf{1} \tag{6.5a}$$

$$\mathbf{\Phi}^{\mathrm{T}}\,\mathbf{K}\,\mathbf{\Phi} = \mathrm{diag}\left(\omega_{0,m}^2\right), \tag{6.5b}$$

where $\mathbf{1}$ is the identity matrix.

If the structure has symmetries, repeated roots occur. Then, more than one mode shape exists for a given eigenvalue. One example is an electrical machine with rotational symmetry which is flange mounted so that the mounting is also rotational symmetric. In this case, circumferential modes would always come in pairs at the same eigenfrequency. Where the one has a nodal point the other has an anti-node, so that the two are still orthogonal (just like sine and cosine). This is for example a necessary precondition in order to be able to speak of "the" mode 2 eigenfrequency. In any real machine structural asymmetries are present. There will always be two circumferential mode 2 shapes at different eigenfrequencies. This can, for example, be seen in the measurements and simulations by Kasper in [Kas10] for machine SR-X. It is consequently also found in the synthesized run-up vibration spectrograms presented in section 7.4. However, since such two eigenfrequencies are usually rather close, they still show as one resonance when looking at the entire spectrum.

6.1.2 Harmonic response analysis – structural transfer functions from force to vibration

The harmonic analysis delivers the structural transfer functions which link the force excitation to the vibrations. In a harmonic analysis, the *stationary response* of the structure to *stationary loads* is investigated. At first, this seems to contradict our assumption of *arbitrary* – and as such non-stationary – loads. However, from an acoustic point of view, loads (torque and speed) usually change rather slowly so that the excitation is quasi-stationary and periodic. We assume an electrical machine to be rotating at constant speed (stationary operation). The force excitation is then periodic. In a harmonic response analysis, these force components are applied to the structure as loads. The loads change sinusoidally with a given frequency and

[(i)] Finding the eigenvalues of a polynomial of a high degree is not a trivial problem. However, powerful algorithms like the Block-Lanczos method exist which are particularly suitable for the large sparse matrices of typical FE problems. These are implemented in the FE solvers and do not require user interaction.

phase shift. The stationary response of the structure to these loads is a function of frequency. Different spatial loads (different mode orders and different phase angles) can be considered simultaneously. However, the key concept behind the vibration synthesis process followed in this work is to apply normalized orthogonal force shapes individually and to subsequently superpose the results based on the operating point dependent excitation.

In the modal analysis described in section 6.1.1, the eigenvalues of the fundamental equation of motion are calculated neglecting damping. Equation 6.1a is set to zero. Here, the left part of equation 6.6a equals the external force $\boldsymbol{\mathcal{F}}(t)$. Additionally, damping is considered by the damping matrix $\mathbf{C}$.

$$\mathbf{M}\,\ddot{\boldsymbol{u}} + \mathbf{C}\,\dot{\boldsymbol{u}} + \mathbf{K}\,\boldsymbol{u} = \boldsymbol{\mathcal{F}}(t) \tag{6.6a}$$

$$\circ\!\!\bullet$$

$$(-\omega^2\,\mathbf{M} + \mathrm{j}\omega\,\mathbf{C} + \mathbf{K})\,\boldsymbol{u}(\omega) = \boldsymbol{\mathcal{F}}(\omega) \tag{6.6b}$$

In the frequency domain, equation (6.6a) is written as equation (6.6b). As the matrices $\mathbf{M}$, $\mathbf{C}$, and $\mathbf{K}$ are constant, an equivalent stiffness matrix can be formed,

$$\mathbf{K}_{\mathrm{eq}}(\omega) = -\omega^2\,\mathbf{M} + \mathrm{j}\omega\,\mathbf{C} + \mathbf{K}. \tag{6.7}$$

This yields a linear system of complex equations for the unknown displacements,

$$\mathbf{K}_{\mathrm{eq}}(\omega)\,\boldsymbol{u}(\omega) = \boldsymbol{\mathcal{F}}(\omega). \tag{6.8}$$

In structural dynamics simulations for acoustic purposes, (surface) velocities are typically calculated which are the derivative of the displacement,

$$\boldsymbol{v}(t) = \dot{\boldsymbol{u}}(t) \quad \circ\!\!\bullet \quad \boldsymbol{v}(\omega) = \mathrm{j}\omega\,\boldsymbol{u}(\omega). \tag{6.9}$$

Equation (6.6b) can be written as

$$\boldsymbol{v}(\omega) = \mathbf{H}_{\mathrm{struc}} \cdot \boldsymbol{\mathcal{F}}(\omega), \tag{6.10}$$

where the transfer function $\mathbf{H}_{\mathrm{struc}}$ is defined as

$$\mathbf{H}_{\mathrm{struc}} = \mathrm{j}\omega\,(\mathbf{K} + j\omega\,\mathbf{C} - \omega^2\,\mathbf{M})^{-1} \tag{6.11}$$

$$= \mathrm{j}\omega\,\mathbf{K}_{\mathrm{eq}}^{-1}. \tag{6.12}$$

All subsequent results will be described in such a transfer function form.

6.1.3 Modal superposition harmonic analysis – decoupling the system

Using the above representation of the harmonic analysis, the frequency dependent system matrix $\mathbf{K}_{\mathrm{eq}}(\omega)$ from equation (6.8) has to be solved for every frequency of interest using the same wavefront solver that is used for a static analysis, except that it is done using complex arithmetic. In this section, the method of *modal superposition* for solving the equation of motion in a harmonic analysis is described. This method is based on the modal analysis and

is utilized in this work. Advantages are a significant reduction of computational costs, the contribution of individual mode shapes to the overall vibrations can be analyzed, and solutions can be clustered around eigenfrequencies. It imposes the restrictions that non-zero imposed harmonic displacements are not allowed and that there is no material dependent damping. The former is generally no drawback, as the applied loads are forces and not displacements. The latter is further discussed in section 6.1.4.

The modal superposition method utilizes the fact that the dynamic behavior of a structure in a given frequency range can be modeled as a set of individual modes of vibration. The transformation of the coupled system of equations into the decoupled system is again done by means of a product ansatz,

$$\boldsymbol{u}(t) = \sum_{m=1}^{N} \boldsymbol{\phi}_m \cdot y_m(t). \tag{6.13}$$

The location-dependence is expressed by the eigenvectors (nodal translation) $\boldsymbol{\phi}_m$ obtained in a prior modal analysis as discussed above. The time-dependence is expressed by the unknown function $y_m(t)$, called *modal coordinates*. The modal coordinate describes how strong a certain mode shape contributes to the overall vibration. We will repeatedly use this combination of a time- (or frequency-) dependent and a location-dependent function in the vibration synthesis in section 6.3. As discussed for the modal analysis, in practical cases, a reduced ansatz with only M ($M < N$) eigenforms is used as an approximation since higher eigenforms can usually be neglected. In matrix notation:

$$\boldsymbol{u}(t) = \boldsymbol{\Phi}\, \boldsymbol{y}(t), \tag{6.14}$$

where $\boldsymbol{\Phi}$ is a $N \times M$ matrix and $\boldsymbol{y}(t)$ a vector of length M.

Inserting this expression in equation 6.6a and multiplying with $\boldsymbol{\Phi}^{\mathrm{T}}$ yields:

$$\mathbf{M}\, \ddot{\boldsymbol{u}} + \mathbf{C}\, \dot{\boldsymbol{u}} + \mathbf{K}\, \boldsymbol{u} = \boldsymbol{\mathcal{F}}(t) \tag{6.15a}$$

$$\Rightarrow \underbrace{\boldsymbol{\Phi}^{\mathrm{T}} \mathbf{M}\, \boldsymbol{\Phi}}_{=:\mathbf{m}}\, \ddot{\boldsymbol{y}} + \underbrace{\boldsymbol{\Phi}^{\mathrm{T}} \mathbf{C}\, \boldsymbol{\Phi}}_{=:\mathbf{c}}\, \dot{\boldsymbol{y}} + \underbrace{\boldsymbol{\Phi}^{\mathrm{T}} \mathbf{K}\, \boldsymbol{\Phi}}_{=:\mathbf{k}}\, \boldsymbol{y} = \underbrace{\boldsymbol{\Phi}^{\mathrm{T}}\, \boldsymbol{\mathcal{F}}(t)}_{=:\boldsymbol{f}(t)} \tag{6.15b}$$

$$\Leftrightarrow \mathbf{m} \cdot \ddot{\boldsymbol{y}} + \mathbf{c} \cdot \dot{\boldsymbol{y}} + \mathbf{k} \cdot \boldsymbol{y} = \boldsymbol{f}(t) \tag{6.15c}$$

The modal mass matrix $\mathbf{m} = \mathrm{diag}\,(m_m)$ (with $m_m = 1$ if normalized according to equation (6.5b)) and the modal stiffness matrix $\mathbf{k} = \mathrm{diag}\,(k_m)$ have non-zero entries only on the main diagonal. In case of modal damping or Rayleigh damping (see section 6.1.4) also the damping matrix $\mathbf{c}$ has entries only on the main diagonal. The system of equations is therefore decoupled. Each row of the above equation can be solved individually,

$$m_m \ddot{y}_m(t) + c_m \dot{y}_m(t) + k_m y_m(t) = f_m(t). \tag{6.16}$$

The *coupled* system from equation (6.6a) is now *decoupled* as it has been transformed to (orthogonal) modal coordinates. Dividing equation (6.16) by m_m and applying the following

substitutions

$$\omega_{0,m}^2 = \frac{k_m}{m_m}, \qquad \zeta_m = \frac{c_m}{2m_m\omega_{0,m}}, \qquad \gamma_m = \frac{f_m(t)}{m_m}, \tag{6.17}$$

where $\omega_{0,m}$, ζ_m, and f_m are the eigenfrequency, damping ratio, and modal force for the m^{th} mode, this results in the familiar equation for *a single DOF mass-spring-damper system*,

$$\ddot{y}_m(t) + 2\zeta_m\omega_{0,m}\dot{y}_m(t) + \omega_{0,m}^2 y_m(t) = f_m(t), \tag{6.18a}$$

$$\downarrow$$

$$\left(-\omega^2 + 2\mathrm{j}\omega\zeta_m\omega_{0,m} + \omega_{0,m}^2\right) y_m(\omega) = f_m(\omega). \tag{6.18b}$$

The general transfer or frequency response function between applied force excitation and resulting velocity was given in equation 6.10 as

$$\boldsymbol{v}(\omega) = \mathbf{H}_{\text{struc}}(\omega) \cdot \boldsymbol{\mathcal{F}}(\omega).$$

In section 6.1.1, the transfer function $\mathbf{H}_{\text{struc}}(\omega)$ is described by a *spatial model* which is found by assembling the FE matrices,

$$\mathbf{H}_{\text{struc}}(\omega) = \mathrm{j}\omega(\mathbf{K} + \mathrm{j}\omega\mathbf{C} - \omega^2\mathbf{M})^{-1}. \tag{6.19}$$

By means of the modal superposition technique it is then transformed into a *modal model*,

$$\mathbf{H}_{\text{struc}}(\omega) = \mathrm{j}\omega \sum_{m=1}^{M} \frac{\boldsymbol{\phi}_m}{\omega_{0,m}^2 + 2\mathrm{j}\zeta_m\omega_{0,m}\omega - \omega^2}\boldsymbol{\phi}_m^{\mathrm{T}}. \tag{6.20}$$

6.1.4 Damping in a modal superposition harmonic analysis

In a modal superposition harmonic analysis, three damping types can be used.

1. *Constant damping ratio* ζ: The damping is proportional to the velocity (viscous damping) and constant over the entire frequency range.

   $$\zeta = \frac{c}{c_{\text{critical}}}, \tag{6.21}$$

   where c_{critical} is the damping that provides the quickest approach to zero for a damped mass-spring-damper system. In the mode superposition method, c is used directly as the modal damping ratio in equation 6.18a. It is identical for all modes.

2. *Modal damping*: For every mode m, a damping ratio ζ_m as described in equation (6.17) can be assumed. This is useful, if these parameters have been obtained from tests. Modes with higher eigenfrequencies are typically more strongly damped than those with

low eigenfrequencies. Also, a vibrating winding head sees due to the insulation more damping than, for example, a metal cover vibrating at the same frequency.

3. *Rayleigh damping*: Together with α-damping, β-damping forms the so-called Rayleigh damping. Rayleigh damping is based on the assumption that the mass and stiffness distribution is a measure for the damping distribution. The damping is found as

$$\mathbf{C} = \alpha\mathbf{M} + \beta\mathbf{K}, \tag{6.22}$$

where α and β are the proportionality factors. In many cases, only β-damping is used so that the damping is proportional to the stiffness

$$\mathbf{C} = \beta\mathbf{K}. \tag{6.23}$$

The damping ratio for equation 6.18a is then found as

$$\zeta_m = \frac{c_m}{c_{\text{critical},m}} = \frac{\beta k_m}{2\omega_{0,m} m_m} = \frac{\beta}{2\omega_{0,m}}\omega_{0,m}^2 = \frac{\beta\omega_{0,m}}{2}. \tag{6.24}$$

β-damping increases with frequency which tends to dampen the effect of higher frequencies. It is in units of time.

The damping values for a machine assembly can unfortunately not be readily determined from material and assembly data sheets. Some publications try to take into account the influence of the stator lamination [Gar89] or the windings on the damping [SWV90]. An influence on the damping can be shown but general parameters cannot be derived. Therefore, it is not a drawback at this point that material dependent damping cannot be used in the modal superposition harmonic analysis discussed in section 6.1.3. The amplitude at resonance directly dependents on a certain damping values but the overall vibration response does not strongly depend on the damping if kept in a typical range. The results in chapter 7 all use constant damping so that damping is estimated by a global parameter. If the damping parameters are measured for more refined models, modal damping parameters can be obtained.

6.1.5 Linear elastic materials – mass and stiffness

The system's damping is defined above. Now mass and stiffness still need to be determined. These are material dependent parameters and used to parametrize the structural model.

Mass

The system's mass is defined via the materials' mass densities ρ.

Stiffness

Two different kinds of linear elastic materials are modeled, *isotropic* and *transverse isotropic* materials. The latter is applied to model the stator stacks which consist of metal sheets.

Hooke's law links the strain tensor $\boldsymbol{\epsilon}$ and stress tensor $\boldsymbol{\sigma}$ via the elasticity matrix $\mathbf{H}$,

$$\boldsymbol{\epsilon} = \mathbf{H}\,\boldsymbol{\sigma}. \tag{6.25}$$

The elastic behavior of *isotropic* materials is defined by two parameters, Young's modulus E and Poisson's ratio ν,

$$\begin{bmatrix} \epsilon_{xx} \\ \epsilon_{yy} \\ \epsilon_{zz} \\ \gamma_{xy} \\ \gamma_{yz} \\ \gamma_{zx} \end{bmatrix} = \begin{bmatrix} \frac{1}{E} & -\frac{\nu}{E} & -\frac{\nu}{E} & 0 & 0 & 0 \\ & \frac{1}{E} & -\frac{\nu}{E} & 0 & 0 & 0 \\ & & \frac{1}{E} & 0 & 0 & 0 \\ & & & \frac{2(1+\nu)}{E} & 0 & 0 \\ & \text{symm.} & & & \frac{2(1+\nu)}{E} & 0 \\ & & & & & \frac{2(1+\nu)}{E} \end{bmatrix} \begin{bmatrix} \sigma_{xx} \\ \sigma_{yy} \\ \sigma_{zz} \\ \sigma_{xy} \\ \sigma_{yz} \\ \sigma_{zx} \end{bmatrix}. \tag{6.26}$$

Both E and ν are independent of the direction. ϵ_{xx}, ϵ_{yy}, and ϵ_{zz} are strains and σ_{xx}, σ_{yy}, σ_{zz} stresses in the x-, y-, and z-direction. γ_{xy}, γ_{yz}, and γ_{zx} are (engineering) shear strains and σ_{xy}, σ_{yz}, and σ_{zx} are stresses in the plane of the first index pointing into the direction of the second index (and vice versa due to symmetry).

Transverse isotropic materials are symmetric about an axis (z) normal to a plane p (xy-plane) in which they are isotropic. Five parameters describe their elastic behavior (E_p, E_z, ν_p, ν_{zp}, ν_{zp}, G_{zp}),

$$\begin{bmatrix} \epsilon_{xx} \\ \epsilon_{yy} \\ \epsilon_{zz} \\ \gamma_{xy} \\ \gamma_{yz} \\ \gamma_{zx} \end{bmatrix} = \begin{bmatrix} \frac{1}{E_p} & -\frac{\nu_p}{E_p} & -\frac{\nu_{zp}}{E_z} & 0 & 0 & 0 \\ & \frac{1}{E_p} & -\frac{\nu_{zp}}{E_z} & 0 & 0 & 0 \\ & & \frac{1}{E_z} & 0 & 0 & 0 \\ & & & \frac{2(1+\nu_p)}{E_p} & 0 & 0 \\ & \text{symm.} & & & \frac{1}{G_{zp}} & 0 \\ & & & & & \frac{1}{G_{zp}} \end{bmatrix} \begin{bmatrix} \sigma_{xx} \\ \sigma_{yy} \\ \sigma_{zz} \\ \sigma_{xy} \\ \sigma_{yz} \\ \sigma_{zx} \end{bmatrix} \tag{6.27}$$

E_p is Young's modulus in the x- and y-direction, E_z that for the z-direction. ν_p is Poisson's ratio in the x-direction for stresses in the y-plane and vice versa. ν_{zp} is Poisson's ratio in the x-direction for stresses in the z-plane. G_{zp} is the shear modulus in the z-direction for the yz- and zx-plane.

Hooke's law equation (6.25) is linked to the equation of motion 6.1a with the strain $\boldsymbol{\epsilon}$ being the derivative of the displacement vector $\boldsymbol{u}$,

$$\boldsymbol{\epsilon} = \mathbf{D}\,\boldsymbol{u} \quad \text{where} \quad \mathbf{D} = \begin{bmatrix} \frac{\partial}{\partial x} & 0 & 0 \\ 0 & \frac{\partial}{\partial y} & 0 \\ 0 & 0 & \frac{\partial}{\partial z} \\ \frac{\partial}{\partial y} & \frac{\partial}{\partial x} & 0 \\ 0 & \frac{\partial}{\partial z} & \frac{\partial}{\partial y} \\ \frac{\partial}{\partial z} & 0 & \frac{\partial}{\partial x} \end{bmatrix}. \tag{6.28}$$

6.2 Force responses – characteristic structural transfer functions

The above presented structural analysis methods and in particular the modal superposition harmonic analysis form the basis of the below discussed *force response calculation* and the

subsequently introduced *vibration synthesis* (section 6.3). Chapter 4 has shown how the air-gap force in an electrical machine can be decomposed into a series of force shapes. In chapter 5, time-domain simulation models have been introduced which provide the time-signals of the force shape amplitudes under arbitrary operating conditions in a system simulation environment. Means to determine the force excitation have therefore been established. What is unknown is how the machine structure reacts to this excitation and what vibrations this causes. It will be shown in this section how the response of the machine structure to a certain force shape is obtained. The force responses are the second foundation of the vibration synthesis process which follows in section 6.3. The force excitation from the system simulation will be combined in the vibration synthesis with the force responses obtained here to form the operating vibrations.

6.2.1 Formalism of the force response calculation

A force excitation $\boldsymbol{\mathcal{F}}_j$, where j represents one of J force excitations, is defined by its spatial distribution $\mathcal{F}_j$ and its complex amplitude $\underline{F}_j$ as

$$\boldsymbol{\mathcal{F}}_j(\omega) = \mathcal{F}_j \, \underline{F}_j(\omega). \tag{6.29}$$

The spatial force distribution $\mathcal{F}_j$ is the FE representation of a force shape (sine, tsine, tooth) as discussed in section 4.3. The complex force amplitude $\underline{F}_j$ is the output of the force models discussed in chapter 5.

Applying the definition from equation (6.15b) for the modal force vector ($\boldsymbol{f} = \boldsymbol{\Phi}^{\mathrm{T}} \boldsymbol{\mathcal{F}}$) and equation (6.16) for the modal coordinates $y_m(\omega)$ to the modal model from equation (6.20), the vibration response $\boldsymbol{v}(\omega)$ to a force excitation $\boldsymbol{\mathcal{F}}(\omega)$ from equation (6.10) can be written as

$$\boldsymbol{v}_j(\omega) = \mathbf{H}_{v_{\mathrm{unit}},j}(\omega) \, \underline{F}_j(\omega), \tag{6.30}$$

with

$$\mathbf{H}_{v_{\mathrm{unit}},j}(\omega) = \mathrm{j}\omega \sum_{m=1}^{M} \boldsymbol{\phi}_m \, y_{m,j}(\omega). \tag{6.31}$$

The index v_{unit} is chosen because $\mathbf{H}_{v_{\mathrm{unit}},j}(\omega)$ is the velocity response to a unit force, i.e., a 1 N force. Compared to equation (6.10), the transfer function term has changed from a matrix to a vector and the force term from a vector to a scalar. Expression (6.31) for the transfer function (from unit force excitation to velocity) is similar to the product ansatz for the deflection from equation (6.13), except that here velocity instead of deflection is the resulting quantity.

Normalizing the excitation

The *unit force* characteristic is achieved by normalization of a force shape $\mathcal{F}_j$. When a force shape j is applied in the structural FE model, this is done as a pressure normal to or in parallel with the surface S. It holds:

$$\max(|p_j|) \, S = 1\,\mathrm{N}. \tag{6.32}$$

By $\max(|p_j|)$, both the positive/negative sequence and the cosine/sine representation are accounted for (see below). The force excitation amplitudes from the force models are scaled to a Newton basis to be in accordance with this normalization. Over a Newton-per-meter basis, the Newton basis has the advantage that electromagnetic force model and structural vibration model are further decoupled. If, for example, the teeth are wider in the electromagnetic model than they are in the force model (because the pole shoes are only modeled in the former case), then the Newton scaling takes this automatically into account. However, it must be kept in mind that the spatial air-gap force spectrum changes when the ratio c_{ratio} between tooth width and total slot width changes (see equation (4.24) for the tsine force and equation (4.28) for the tooth force).

Cosine/sine vs. positive/negative sequence representation
The dualism between a cosine/sine or positive/negative sequence representation also exists in the way the force shapes are applied to an FE model. In the positive/negative sequence representation, all elements of S see the same pressure ($p_j = 1\mathrm{N}/s$) but a different phase angle whereas in the cosine/sine representation, the phase is constant (zero) but the local pressure varies sinusoidally with an amplitude of ($\hat{p}_j = 1\mathrm{N}/s$). Eventually, it does not matter which representation is used. Both have been implemented and tested. For analyzing transfer functions and for measurement comparison, the cosine/sine representation seems a little bit more useful. Between cosine and sine, the amplitude distribution of the excitation differs, which also leads different magnitudes of the transfer functions, especially for non rotationally symmetric machine assemblies. Double-zeros (symmetric modes) hardly exist in real-life structure (cf. the vibration behavior of SR-X in section 7.4). For the positive/negative sequence excitation in contrast, the response only differs in phase. However, the results from one representation can be converted to the other at any time.

Storing the response
The approach is efficient in terms of computational effort and data storage. The frequency- and excitation-independent eigenshape vectors $\boldsymbol{\phi}_m$ from the modal analysis are calculated and stored only once (modal analysis). Every force response just adds M complex vectors $y_{m,j}(\omega)$ per force shape j (modal superposition harmonic analysis).

6.2.2 Implementation of the force response calculation

The force responses are obtained in an automated manner via an FE software (which here is ANSYS along with custom ANSYS parametric design language (APDL) scripts). The basic structure is shown in figure 6.1. An FE model is built from a computer-aided design (CAD) model. In the CAD or FE software, those surfaces or bodies are labeled onto which the force is applied or for which results shall be evaluated. The model is parametrized and meshed and boundary conditions are applied. The FE model is then written to a file. The force responses for the individual force shapes are found in a batch run. Parameters are, among others, the frequency range for the harmonic analysis, damping coefficients, the force shapes to be calculated and the type of force excitation, and, where applicable, the number of skew slice segments. In the solution process, first the model, then the modal model (eigenfrequencies and eigenshapes $\boldsymbol{\phi}_m$), and finally the modal coordinates representing the force responses for J force excitations are exported. The results are imported into MATLAB where the vibration synthesis is performed.

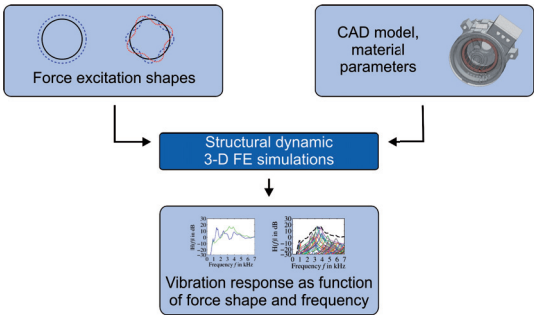

Figure 6.1: Determination of the force responses

Performance

The duration of a batch-run is in the "a-couple-of-hours" range on a quad-core PC with 16 GB RAM for the models used in this thesis. The calculation time of the modal analysis is below 1 h for problems with around 10^5-elements, if sufficient memory is available to perform it in-core (i.e., in the main memory (RAM)). 10^5 elements seemed to be the limit on a PC with 16 GB of RAM. A significant amount of time is currently spent on storing the nodal translations, which form the largest chunk of data. The implemented universal-file-format parser writes line based to text files so that a speed up is possible when, for example, switching to a binary format. The J harmonic analyses for the J force shapes then take a few minutes each. Their number varies. A lower limit could be 2 or 4 if only the radial component of 1 or 2 force shapes (cos/sin or pos/neg each) is taken into account. The upper limit in this thesis is 156 for the skewed PMSM in section 7.2.

6.2.3 Force response results for sine, tsine, and tooth force on test models

Three basic FE test models are used to characterize the force response for sine, tsine, and tooth excitation: First, in figure 6.2a, a 2-D ring as the numerical counterpart to an analytical cylindrical ring model. Second, in figure 6.2b, a 2-D, 6-teeth stator as a basic machine (3-phase, q=1 PMSM or 6/4 SRM). Third, in figure 6.2c, the 2-D stator extruded to 3-D with a length of 250 mm and fixed on one end as basic machine-flange-mounted-on-test-bench model. For all models, the outer radius R_s is 100 mm and the yoke height h_yoke is 20 mm. The air-gap radius R_airgap of the stator models equals 53.7 mm and the ratio between tooth width and slot width c_ratio is 50% so that the graphical $\mathbf{H}_\mathrm{tsine}(u)$ and $\mathbf{H}_\mathrm{tooth}(u)$ example from section 4.3.3 holds for these models. Damping is set to 3% constant.

Figures 6.3 to 6.5 illustrate in the following for the different models and several excitation conditions the unit-force to mean-square surface normal velocity transfer function[(ii)]. These are used to discuss characteristics of the different force excitation and influence of the model detail. In all cases, cosine force shapes 0 to 6 are applied.

[(ii)] The algorithm for the calculation of the mean-square surface normal velocity $\overline{|v_\mathrm{n}|^2}$ will eventually be explained in section 6.3.4.

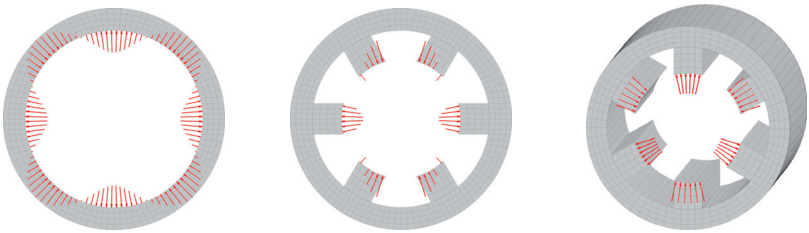

(a) 2-D ring (with shape 4 sine force) (b) 2-D stator (with shape 2 tsine force) (c) 3-D stator (with shape 3 tooth force, shown only at front edge)

Figure 6.2: FE models used for unit-force response study.

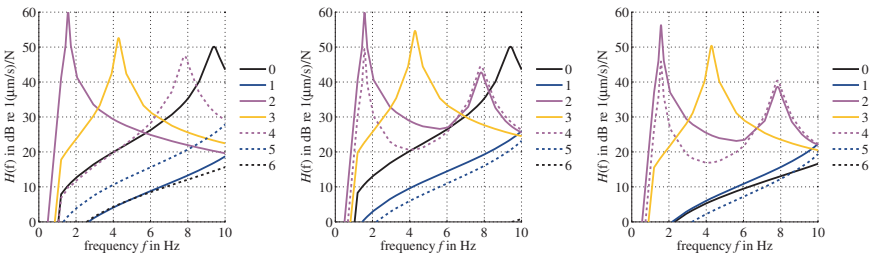

(a) Sine forces, radial. (b) Tsine forces, radial. (c) Tsine force, tangential.

Figure 6.3: *2-D ring model*, unit-force to mean-square surface normal velocity transfer function.

2-D ring

Figures 6.3 depicts results for the 2-D ring model. In figure 6.3a, radial sine forces are applied. Every force shape excites one eigenfrequency. The response is simply that of a second order system and every transfer functions has one resonant peak. With increasing order, the eigenfrequency of the bending modes rises and the peak amplitude decreases. This first result can also be obtained with the analytical ring model from [Jor50] which still serves regularly as vibration model for electrical machines [Fie06; Le 08].

In figure 6.3b, the force excitation changes from sine to tsine. The force is applied to the ring model where in the stator model the teeth connect to the yoke (giving a c_{ratio} of $1/3$). In the vibration response, it can be observed that the tsine force shape 4 also excites the mode 2 eigenfrequency at 1600 Hz and that shape 2 excites mode 4 near 8000 Hz. This was expressed in section 4.3.1 by the $\mathbf{H}_{\text{tsine}}(u)$ transfer function.

Next, the excitation is still tsine but now tangential instead of radial. The result is shown in figure 6.3c. The amplitudes of the structural response for tangential excitation are comparable to radial response for the bending modes (all modes but zero)[(iii)].

[(iii)] Deflection shapes are not presented here so that only a remark is made that an interesting dualism between

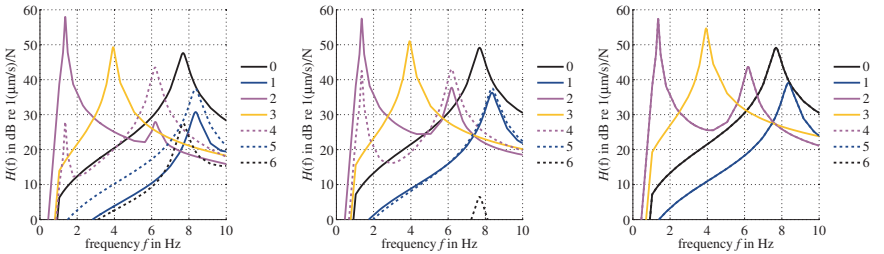

(a) Sine force, radial. (b) Tsine force, radial. (c) Tooth force, radial.

Figure 6.4: *2-D stator model*, unit-force to mean-square surface normal velocity transfer function.

2-D stator

Figure 6.4 illustrates vibration responses for the 2-D stator model. A sine excitation of the ring leads only to a vibration in a corresponding sine shape (see figure 6.3a). In contrast, we see in figure 6.4a that due to structural asymmetries from the stator teeth the sine excitation leads to an additional mode 2 (4) vibration in case of a shape 4 (2) excitation. Also for models with stator, the sine force is applied to the yoke as shown in figure 6.2a.

In figure 6.4b, the force excitation is again changed from sine to tsine. The shape 2 force excitation can be seen in figure 6.2b. $\mathbf{H}_{\text{tsine}}(u)$ in figure 4.4 predicts the quantitative difference between the mode 2 vibration from shape 2 and 4 to be 14 dB and that of mode 4 from shape 4 and 2 to to 6 dB. This is confirmed in figure 6.4b. Shape 6 is here able to excite a mode 0 with a response that is about 40 dB lower than that from shape 0. Based on $\mathbf{H}_{\text{tsine}}(u)$, shape 6 would ideally not excite mode 0 and it also does not in the ring model. However, here the structural asymmetry due to the teeth is present. This phenomenon needs to be further investigated because the force shape N_{teeth} has usually a relatively high amplitude and it needs to be ensured that this excitation is neither omitted nor overrated due to, for example, discretization errors.

Figure 6.4c is now the first result with tooth force excitation. For the tooth force, excitation shapes higher than the Nyquist frequency $f_{\text{nyquist}} = {}^{N_s}/_2 = 3$ do not exist. An alleged shape 4 excitation is merely the shape 2 excitation. Shapes higher than 3 mirror in the below Nyquist ones due to aliasing. This is why the color order was chosen symmetric around $\nu = 3$.

3-D stator

Figure 6.5a depicts the sine excitation results for the 3-D stator model. The more complex model leads to a more complex response with additional resonances. The general characteristics, however, are preserved. The fixed/free boundary condition allows a mode 1 vibration at 1595 Hz near the mode 2 vibration at 1695 Hz.

radial and tangential tsine force was regularly observed, also on realistic machine models. The deflection from a radial cosine-shape would look like that of a tangential sine-shape (sine in terms of cosine/sine not sine/tsine) excitation and vice versa. This does, of course, not hold for shape 0 which does not have a sine-shape.

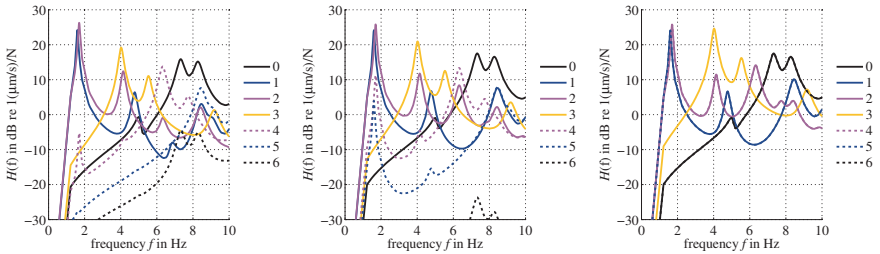

(a) Sine force, radial. (b) Tsine force, radial. (c) Tooth force, radial.

Figure 6.5: *3-D fixed-free stator model*, unit-force to mean-square surface normal velocity transfer function.

Figure 6.5b with tsine excitation and figure 6.5c for the tooth excitation confirm the results of the 2-D stator above for the 3-D stator.

6.2.3.1 Influence of the mesh density on the force response

The FE meshes for the test models in figure 6.2 have deliberately been chosen rather coarse. The objective is making models not more detailed than excitation and response require. Below, the 2-D stator model is shown with two mesh densities where the finer model has about 10 times more elements than the coarser one.

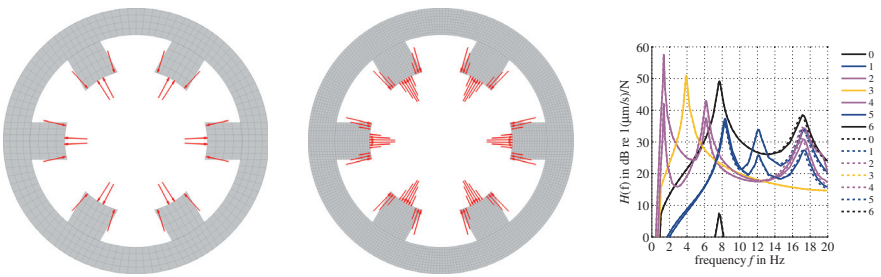

(a) Coarse mesh (b) Fine mesh (c) Response comparison

Figure 6.6: 2-D stator FE models with different mesh densities and a tsine shape 6 radial cosine force applied (a, b) and the vibration response (c)

In figure 6.6a, 6 elements are used along a stator tooth for applying the force. The fine-mesh example in figure 6.6b uses 14 elements. The above examples use force shapes up to order N_s for the tsine force, which means one wavelength per stator tooth. Using 6 elements then follows the minimum-6-points-per-wavelength rule-of-thumb. Figure 6.6c plots the force-to-mean-square-surface/velocity function for both cases. It can be observed that a difference between

the two cases can hardly be observed. Tests with 4 elements have also led to satisfactory results. It is concluded that meshing the tooth surface with 4-6 elements in the circumferential direction is sufficient for representing tsine force up to order N_s. Despite the good results based on few elements and piecewise constant force per element, the force mapping could gain from a continuous mapping based on the element shape functions as used in [vGie11].

6.2.3.2 Representing the tsine by the sine force

Equation (4.10) tells us that any tsine force can be represented by a superposition of sine forces. In figure 6.7a, a tsine shape 2 force acting on the tooth surface is shown. Figure 6.7b illustrates the representation of this force by sine force orders up to shape 12, which according to figure 4.4a means shape orders 2, 4, 8, and 10. Furthermore, the force is applied to the yoke rather than to the tooth surface because only there a continuous surface is found as required by the sine force.

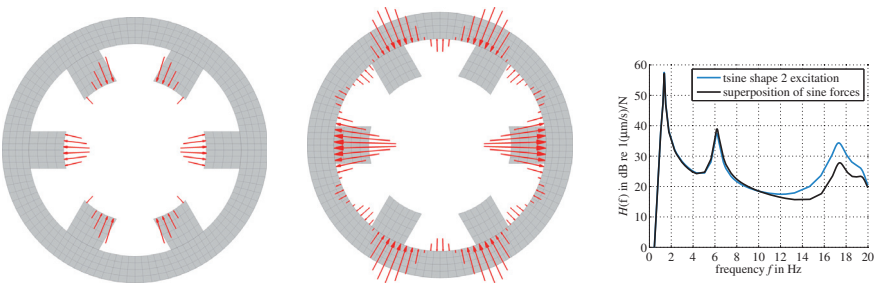

(a) Tsine force

(b) Sine force approximation of tsine force

(c) Response comparison

Figure 6.7: 2-D stator FE model with shape 2 tsine force shape and its sine force approximation.

We see from figure 6.7c that the responses are almost identical up to 10 kHz. A significant deviation can only be observed at higher frequencies. This observation also holds for the other investigated excitation shapes. It is not suggested to use this routinely in real-life applications. The test models here are rather stiff and have relatively high eigenfrequencies. Windings are not taken into account. It is expected that in real cases the limit of validity is lower. Furthermore, the force-on-yoke distribution is less intuitive for the user than applying the forces on the teeth where they in reality predominantly act.

V. d. Giet suggest in [vGie11] to apply air-gap forces (i.e., sine forces) to both, tooth and slot ground (i.e., the stator yoke surface between the stator teeth). He notes that this would require a node selection algorithm for stator structures more complex than his example with pie shaped teeth. Already for the example here, it seems to be difficult to select the proper next node or element when moving in the angular direction from tooth surface to slot ground. As these methods are approximations anyway, the force-on-yoke approach presented above may be a more convenient solution due to the simple implementation.

6.3 Vibration synthesis – the result superposition

The vibration synthesis process is the central element of the acoustic modeling process. It combines the force excitation from the system simulations with the force responses from the structural simulations. An overview of the acoustic modeling process has been given in the introduction in chapter 1 (cf. figure 1.2). The system simulation and the vibration synthesis are the two user-interactive online processes. For the system simulations, electromagnetic FE simulations provide the input data. The vibration synthesis combines the time dependence of the force shapes from the system simulation with the offline/determined force responses introduced above. This combination is shown in figure 6.8. Below, the formalism of the vibration synthesis process and its implementation are discussed.

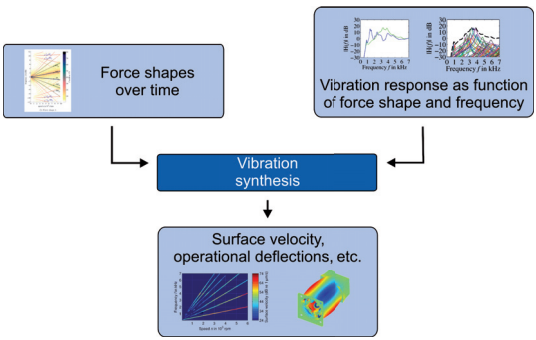

Figure 6.8: Overview of the vibration synthesis process

6.3.1 Basic concept of the response superposition

With an orthogonal set of force shapes $\mathcal{F}_j$, the force in the machine can be approximated by J force shapes as

$$\boldsymbol{\mathcal{F}}(\omega) = \sum_{j=1}^{J} \mathcal{F}_j \, \underline{F}_j(\omega). \tag{6.33}$$

The series of J forces is a general expression for arbitrary forces. These are eventually further broken down to radial, tangential, and axial forces. Furthermore, forces can act on different segments of the machine as in skewed PMSMs (see section 5.4.2) or axially segmented SRMs (see section 5.4.3). In the vibration synthesis, the response of the structure to these force shapes is synthesized. They encompass the structurally relevant portion of the force excitation in the machine.

6.3.2 Synthesizing the operational deflections – looking at the machine vibrations at a certain operating point

We will first describe how the *nodal* velocity is synthesized. This is typically of interest in two cases:

a) to see the (animated) shape of the vibrations of the (entire) structure at one certain operating point and frequency. This is called the *operational deflection*.

b) to analyze the velocity (in a certain direction) at a limited number of nodes over, for example, a run-up.

This is done as follows. For consistency, we will derive all expression for the velocity v which may be converted to displacement u where necessary as, for example, in case a).

Combining expression (6.33) for the decomposed force with the above equation (6.31) for the vibration response to a force excitation $\underline{F}_j$, $\boldsymbol{v}$ is given by

$$\boldsymbol{v}(\omega) = \sum_{j=1}^{J} \mathbf{H}_{v_{\mathrm{unit},j}}(\omega)\, \underline{F}_j(\omega) \tag{6.34}$$

with

$$\mathbf{H}_{v_{\mathrm{unit},j}}(\omega) = \mathrm{j}\omega \sum_{m=1}^{M} \boldsymbol{\phi}_m\, y_{m,j}(\omega)$$

as introduced in equation (6.31). $\boldsymbol{v}(\omega)$ is here described by a force-scaled-by-transfer-function expression. This transfer function consists of a location- and a time-dependent part. Explicit calculation of $\mathbf{H}_{v_{\mathrm{unit},j}}(\omega)$ in this form, in particular when performed for a large number of nodes, is computationally not efficient. Yet, it is given for consistency with the next two sections. A more efficient implementation is

$$\boldsymbol{v}(\omega) = \mathrm{j}\omega \sum_{m=1}^{M} \boldsymbol{\phi}_m \underline{F}_m(\omega) \tag{6.35}$$

with

$$\underline{F}_m(\omega) = \mathrm{j}\omega \sum_{j=1}^{J} y_{m,j}(\omega)\, \underline{F}_j(\omega), \tag{6.36}$$

where the summations over j and m are interchanged. Both operations above, the summation over the J excitations per mode m and the scaling and summation of the M mode shapes, are post-processing operations. They are performed online, i.e., upon user request, from the offline data when the operational deflection at a certain torque-speed operating point and vibration frequency is sought. In $\underline{F}_m$, different ω sampling points for $y_m(\omega)$ and $\underline{F}_j(\omega)$ have to be taken into account by interpolation. The frequencies of $y_m(\omega)$ are typically clustered around the eigenfrequencies. $\underline{F}_j(\omega)$ has equidistant frequencies if formed by a FFT from a regularly-sampled time signal.

6.3.3 Synthesizing the element dependent surface normal velocity

The next synthesis case is the *element-dependent* surface normal velocity. This is again of interest in two cases

a) to show the (animated) surface normal velocity of the (entire) structure at one certain torque-speed operating point and vibration frequency.

b) to determine the surface normal velocity $v_\mathrm{n}(t)$ over, for example, a run-up at a limited number of elements at the positions where vibration sensors are placed in measurements. The resulting time signals can be auralized.

With the surface normal velocity as defined in equation (2.9), we can write

$$\boldsymbol{v}_\mathrm{n}(\omega) = \sum_{j=1}^{J} \mathbf{H}_{v_\mathrm{n,unit},j}(\omega)\, \underline{F}_j(\omega) \tag{6.37}$$

with a transfer function consisting of a position- and a time-dependent part,

$$\mathbf{H}_{v_\mathrm{n,unit},j}(\omega) = \mathrm{j}\omega \sum_{m=1}^{M} \boldsymbol{\Phi}_m y_{m,j}(\omega), \tag{6.38}$$

and the vector of the element normal displacement,

$$\boldsymbol{\Phi}_m = (\boldsymbol{\phi}_m \boldsymbol{n})\,. \tag{6.39}$$

The calculation of $\boldsymbol{v}_\mathrm{n}(t)$ is again an online post-processing operation.

6.3.4 Synthesizing the mean-square surface normal velocity

While the nodal velocity and the element-dependent surface normal velocity are spatially distributed values, the mean-square surface normal velocity $\overline{|v_\mathrm{n}|^2}$ is a scalar (with a real-valued frequency domain function due to the square operation). Again in two (related) cases, the mean-square surface normal velocity is determined:

a) for the entire outside surface of the machine or parts of it as an estimate for the radiated sound power. (This is used in this work for all run-up spectrograms which are not compared with measurements.)

b) for a set of points on the surface for comparison with vibration sensor measurements. (This is used in this work for all run-up spectrograms validated against measurements.)

The mean-square surface normal velocity is readily derived by inserting the expression for the nodal velocity $\boldsymbol{v}(\omega)$ from equation (6.34) with the transfer function $\mathbf{H}_{v_\mathrm{unit},j}(\omega)$ from equation (6.3.2) into the definition of the mean-square surface normal velocity $\overline{|v_\mathrm{n}|^2}$ in equation (2.9). The result then becomes:

$$\overline{|v_\mathrm{n}|^2}(\omega) = \sum_{j=1}^{J} \sum_{i=1}^{J} \overline{\mathbf{H}_{v_\mathrm{n,unit},j,i}}(\omega)\, \underline{F}_j(\omega)\, \underline{F}_i^*(\omega) \tag{6.40}$$

with

$$\overline{\mathbf{H}_{v_\mathrm{n,unit},j,i}}(\omega) = \omega^2 \sum_{m=1}^{M} \sum_{n=1}^{M} \overline{\mathbf{\Phi}_{m,n}}\, y_{m,j}(\omega)\, y_{n,i}^*(\omega) \tag{6.41}$$

and

$$\overline{\mathbf{\Phi}_{m,n}} = \frac{1}{S} \iint_S (\boldsymbol{\phi}_m \boldsymbol{n})\, (\boldsymbol{\phi}_n \boldsymbol{n})\, \mathrm{d}S. \tag{6.42}$$

Again, the concept of scaling a transfer function by a force excitation amplitude (equation (6.40)) and a transfer function (equation (6.41)) consisting of position-dependent (equation (6.42)) and a time-dependent term is maintained. As $\boldsymbol{\phi}_m \boldsymbol{n}$ is the only space dependent term, only this is affected by the suface integral in the expression for the mean-square surface normal velocity.

$\overline{\mathbf{H}_{v_\mathrm{n,unit},j,i}}(\omega)$ and $\overline{\mathbf{\Phi}_{m,n}}$ are excitation amplitude independent so that they can be calculated offline. They have to be recalculated if the model is changed (e.g., if only a subset of nodes/element of the response surface or only a subset of modes is used). $\overline{\mathbf{H}_{v_\mathrm{n,unit},j,i}}(\omega)$ has to be recalculated additionally if the excitations (only a subset of excitation, e.g., only radial) are changed.

Torsional vibrations

The calculation of the mean-square surface velocity has been observed to deliver incorrect results in case of torsional vibrations in [Har12]. If a cylindrical body performs a torsional vibration around its axis, some surface elements see a (compared to the total velocity) small positive normal velocity component while others still see a small negative component. This is because the elements are never ideally parallel to the trajectory of the vibration. The average surface velocity is near zero, but not the mean square surface velocity. A finer discretization does not alleviate the problem significantly. Since the overall rotational velocity of a torsional vibration is at times rather large, a small normal portion may not be so small compared the normal component of other vibration shapes. Therefore, the respective torsional eigenfrequency shows in the mean-square surface normal velocity spectrogram. If the operational deflection shape is animated at the respective frequency, the normal velocity on the body looks checkered. In [Har12], a workaround was deleting the respective modes from the modal base. A general solution to this issue is still open. For the machines investigated in this thesis, this problem was not observed.

6.3.5 Implementation of the vibration synthesis process

Two implementations of the vibration synthesis process have been developed. The main focus in this work is on the universal *system-simulation-based* version, which takes the amplitudes

of the air-gap force shapes over time from a, hence the name, system simulation. It is applicable to all machine types and geometries. This approach has been the motivation for the system simulation in chapter 3 and the corresponding force models in chapter 5. A second implementation is a *direct* version for PMSMs, which maps the force from the dq-current plane to the torque-speed range without time-domain simulations. The offline calculations for the electromagnetic and structural results are identical in both cases. The two approaches differ in the representation of the force excitation and therefore in the implementation of the vibration synthesis. Figure 6.9 gives an overview on how the force excitation is determined for the two implementations. The entire process vibration synthesis process has been implemented in the software MATLAB.

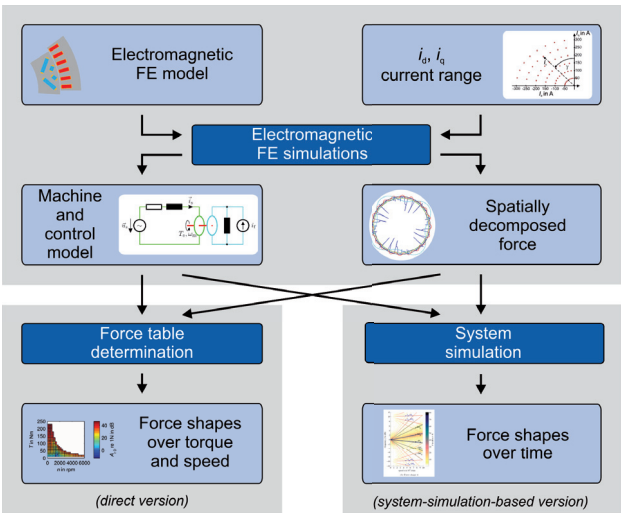

Figure 6.9: Direct and system-simulation-based version of the determination of the force excitation for the vibration synthesis

6.3.5.1 System-simulation-based implementation for arbitrary machines

The system-simulation-based approach is suitable for all types and geometric configurations of machines. The only prerequisite is a system level simulation model with force lookup. Models for PMSMs and SRMs have been developed in chapter 5. Use in combination with an induction machine model as the analytic model in [Le 08] is also readily possible. The approach builds on a system simulation as introduced in figure 3.1.

The system simulation is performed in the time domain. Controller and load influences are taken into account. In contrast to the direct approach, this approach does not directly deliver results for the entire operating range but provides force trajectories (e.g., a full-load run-up) in the torque speed plane. Multiple runs combined, however, allow characterizing the entire operating range. The output time signals can directly be auralized.

6.3.5.2 Direct implementation for PMSM

The basic idea behind the direct version is that in a PMSM, every torque-speed operating point leads to a certain dq-current as given by the control strategy (see section 3.4.1). If the force excitation is calculated for a range of operating points as in section 3.5.2, it can be mapped to the torque-speed plane. Since the force excitation is linked with the dq-current plane, the force excitation and consequently also the structural response can then be mapped to any torque-speed trajectory. The first implementation of the stationary version was introduced in [Boe+09; Boe+10] and further analyzed in [BD10; BD12]. The direct version has been reimplemented and extended for this thesis. It is now more modular and scales well for large models. Support for skewed machines was added. PWM switching frequency harmonics were taken into account and auralization was shown in a diploma thesis by Nießen [Nie11].

6.3.5.3 Discussion of the two implementations

The direct and system-simulation-based approach have been largely harmonized regarding the underlying functions. The direct implementation may appeal to the machine designer as it gives a broader insight into the relationships between feeding current, force excitation, and structural response. The system-simulation-based implementation is overall more flexible and easier to handle. While the direct approach focuses on the main noise components, the system-simulation-based approach also takes into account further harmonics and sidebands. The system-simulation-based approach is predominantly used now. All spectrograms in chapter 7 are based on this approach.

6.3.6 Comparing the vibration synthesis process with literature

The key element in the vibration synthesis process is the decomposition of the force excitation into force shapes and the subsequent scaled superposition of normalized force responses in a manner that converges against the full direct response.

Analytical structural models [Ras99; Fie06; Le 08] share the decomposition approach. They model individual structural modes via mass spring dampers excited by a certain force shape. However, they can only roughly approximate the structural response of a system or are limited to structures with a simple structural responses. The vibration of these structure must be strongly dominated by individual modes.

Numerical approaches tend not to decompose but to map the distributed air-gap force directly from the electromagnetic model to the structural model [WLA04; vRie+05; PLF12a]. The simulation path is then identical with the causal path of generation of acoustic noise (cf. figure 1.1). While this approach can deliver good results, it is numerically expensive because varying operating conditions require to go through the entire simulation change again. These approaches are therefore usually applied to investigate constant speed operating points [WLA04; vRie+05] or assume a force excitation whose amplitudes do not change with speed [PLF12a].

A decomposition of the force excitation not into air-gap force shapes but into the modal force $f_m(t)$ form equation (6.18a) is introduced in [VBG93; VB94]. A modally decomposed structural model is combined with an electromagnetic FE model. The modal force is determined from the change in flux linkage in an electromagnetic FE model deformed according to

a certain mode shape. Motivation for this approach was to improve accuracy by not having to determine the air-gap force explicitly. Structural and electromagnetic simulations are no longer decoupled. This approach does not seem to have found further application in recent years.

A numerical approach which also determines the machine vibrations by superposing force responses is that by Roivainen in [Roi09] and the remaining discussing here deals with this approach. A brief comparison has already been drawn in [BD10]. Differences between the synthesis process above (first introduced by the author in [Boe+09]) and the approach presented in [Roi09] are highlighted below. There are two main advantages of the approach presented in this thesis for modeling machine vibrations numerically.

First, Roivainen focuses on squared responses and describes direct responses (e.g., the above nodal velocity, section 6.3.2, and the element dependent normal velocity, section 6.3.3) as "not so tempting" because many unit-wave responses per DOF would need to be stored. This is because [Roi09] refers to storing the full $\mathbf{H}_{v_{\mathrm{unit},j}}(\omega)$-vector from equation (6.3.2). It has been discussed above that this is indeed inefficient, particularly in terms of memory usage, which is why the form in equation (6.35) is used performing the modal superposition approach online. The approach presented here has therefore the advantage that, for example, operational deflections can be obtained.

Second, with regard to squared responses like the mean-square surface normal velocity, Roivainen's approach builds on the assumption of week correlation between the force waves. This means that the squared responses for individual force excitations $\underline{F}_j$ can be added. For equation (6.40) this means that in the double-sum only the entries with $j = \mathrm{i}$ are taken into account (sparse form). This assumption indeed holds in cases where one force shape dominates a tonal component. Section 7.4 will show an example including the additional possibility of reducing the modal base to only few mode shapes. Yet, there is no disadvantage in routinely using the full form. Furthermore, there are cases which require the full approach. These are, for instance, skewed machines for which results will be presented in section 7.2. Skew builds on a phase shift between forces as has been discussed for the skewed force analysis in section 5.4.2. This phase shift is lost in the sparse formulation. A skewed machine would then behave like an unskewed machine. In [vGie11], the approach from [Roi09] is extended by considering the unit forces to be complex as in [Boe+09].

This work focuses on simulating the structural response. Roivainen, besides simulation, also aims at measuring the force responses. There, the assumption of weak correlation facilitates the determination of measured transfer functions.

6.4 Alternatives and future extensions

The interface between electromagnetic force excitation and structural dynamics response on the basis of force excitation shapes is flexible. Any type of model (FE, analytical, etc.) and simulation (2-D or 3-D, direct or system-simulation-based, etc.) can be used. Furthermore, the simulation can be extended by radiation or transfer path analyses. Some modifications and extensions are discussed below.

6.4.1 Force calculation

Analytical force calculation may be used as by Le Besnerais et al. for induction machines in [Le +09]. Eccentricity can be accounted for explicitly in the electromagnetic FE model by creating a full 2-D model of the machine. Alternatively, eccentricity can be applied analytically to the FE results by scaling the results for the air-gap quantities in accordance with the air-gap length variation due to eccentricity. Both approaches deliver the additional eccentricity related frequency components. In the explicit FE analyses, their amplitudes are more exact.

6.4.2 Refining the structural models

The structural FE models used in this work are rather simple. Extensive verification and parameter optimization have not been performed. However, the modular simulation approach is also chosen so that models built by structural dynamics experts can be used within the simulation process. A more elaborate structural model is, for example, found in [PLF12a].

6.4.3 Measuring transfer functions

A modal model does not necessarily have to be derived from an FE model. A method to analyze the vibration response of a structure by measurements is *modal testing*, also known as *experimental modal analysis* [Her05; Ewi00; Ewi00]. It is also applicable to verify and update the FE model. For an N DOF FE model, the frequency response function (FRF) $\mathbf{H}(\omega)$ is an $N \times N$-matrix. According to [Ewi00] it can be shown that "a single row or column of the FRF matrix, $\boldsymbol{H}(\omega)$, is capable of containing all the information which is present in the modal model and thus that such a set of FRFs is all that needs to be measured in a test designed to elicit the modal properties from measurements of responses". This means that if sufficient measurements (at sufficient excitation points and/or sufficient measurement points) are performed, a structural model can be derived from measurements alone. The FRFs are estimated from the measured auto- and cross-spectra of and between inputs and outputs. In mechanical engineering, modal testing is an advanced technique and powerful tools exist that allow to update the FE model automatically (e.g., curve-fitting, updating the stiffness matrix, etc.).

Instead of using a shaker or impact hammer, the electromagnetic excitation of the electrical machine itself can be used for measuring transfer functions. An advantage is that while a point excitation will excite a large number or modes, the machine itself will excite those modes that also occur under normal operation. Roivainen measures unit-wave responses for induction machines in [Roi09]. Franck et al. measure transfer functions of a PMSM in [FH12]. Kasper et al. use the electromagnetic excitation of an SRM for experimental modal analysis in [Kas+08].

6.4.4 Analytical structural models

Yet another approach for model building is to use analytical models as in [Le 08] for analyzing the vibration of induction machines for traction drives in trains or switched reluctance machines in [Ras99; Fie06]. Technically, these also use a spatial model. The number of modes that are considered is low (1 or 2), the machine structure is strongly simplified, and the calculation

of the mass-spring-damper parameters relies on analytical formulations. If, however, for a given system these parameters can be obtained, they allow straightforward investigation of optimization potential.

6.4.5 Extension to radiation

Extension to radiation is readily achieved by taking into account the radiation characteristics of the machine structure. It is discussed below how existing numerical approaches can be interfaced with the vibration synthesis process so that radiated sound power or sound pressure at distance from the drive can be obtained. For radiation into free-field, the perfectly matched layer (PML) approach, as a general numerical FE based method, appears to be a convenient option. The concept of acoustic transfer vectors (ATVs) building on the boundary element method (BEM) or on the PML interfaces well with the numerical approach used for the vibration synthesis. Last but not least, reference to analytical radiation models is made.

6.4.5.1 Sound by means of the perfectly matched layer method (FEM PML)

The perfectly matched layer concept was originally introduced by Berenger in [Ber94] for electromagnetic waves. The company LMS has integrated this technique into their software Virtual.Lab for acoustic problems [BT09; SV12]. The FE domain is encased by a so-called perfectly matched layer. *Perfectly matched* means that no sound reflects back into the FE domain and that the Sommerfeld radiation condition[(iv)] is therefore met. This method can be used for calculating the radiated sound power or to calculate sound pressure at points outside the PML.

6.4.5.2 Sound at field points via acoustic transfer vectors (BEM ATV)

The acoustic transfer vector concept is described in [Gér+02; MTG02]. Some of the authors are with the company LMS and the respective product incorporating the functionality is SYSNOISE. An implementation concerning electrical machines deriving "Simulated Transfer Functions for the Auralization of Electrical Machines" is found in [Mül+10].

ATVs form a relationship between the surface normal velocity of a vibrating body and the sound pressure level at a specific field point. They can be seen as a set of transfer functions from the surface elements to a single point in space (field point) or microphone position. For obtaining the sound pressure at a field point, the surface normal velocity on the structure (e.g., from an FE model or the respective mapping to a "softer" and coarser BEM mesh) is multiplied by a so-called *acoustic transfer vector* $\mathrm{ATV}(\omega)$,

$$p(\omega) = \mathrm{ATV}^{\mathrm{T}}(\omega)\boldsymbol{v}_{\mathrm{n}}(\omega). \tag{6.43}$$

The acoustic transfer vectors are determined via the boundary element method or from the PML. Once the ATVs have been determined, they allow for quick radiation calculations for arbitrary surface vibrations.

[(iv)] Sommerfeld defined that "the sources must be sources, not sinks of energy. The energy which is radiated from the sources must scatter to infinity; no energy may be radiated from infinity into [...] the field" [Som49].

In combination with a modally decomposed structural model, modal acoustic transfer vectors (MATVs) can be defined. These describe the sound pressure contribution of a certain mode shape. They have only a frequency dimension when describing a single field point. Equation (6.38) is extended by the acoustic transfer vector forming the MATV. Instead of the unit velocity transfer function $\mathbf{H}_{v_{\mathrm{unit},j}}(\omega)$, the unit sound pressure transfer function $H_{p_{\mathrm{unit},j}}(\omega)$ for the j^{th} force shape is found as,

$$H_{p_{\mathrm{unit},j}}(\omega) = \sum_{m=1}^{M} \underbrace{\mathrm{ATV}_m^{\mathrm{T}}(\omega)\boldsymbol{\Phi}_m}_{=:\mathrm{MATV}_m(\omega)} y_{m,j}(\omega), \tag{6.44}$$

where $\mathrm{MATV}_m(\omega)$ is introduced as the modal acoustic transfer vector for the m^{th} mode of vibration. The velocity transfer functions in the previous sections have all been split into a position- and time-dependent term. The modal acoustic transfer vector $\mathrm{MATV}_m(\omega)$, however, is frequency- (that is, time-) dependent. It is further position-dependent as it is defined for one or more field points (then as a matrix).

The sound pressure p is then synthesized as

$$p(\omega) = \sum_{j=1}^{J} H_{p_{\mathrm{unit},j}}(\omega)\, \underline{F}_j(\omega). \tag{6.45}$$

Based on ATVs, the sound power can be obtained by evaluating the sound pressure over number of field points following the procedures defined in the EN ISO 3744:2010 [CEN10].

One idea behind the vibration synthesis process is that the different parts should be independent. The electromagnetic forces can be obtained independently of the structural model. For the determination of the structural force responses, the actual force values do not need to be known. This can also be maintained for the radiation problem. The acoustic transfer vectors are independent of the mode shapes. They can therefore be determined independently as pointed out in [Gér+02]. The only prerequisite is that the outside geometry of the structural model does not change. This does not pose a limitation in most cases. Determination of the modal acoustic transfer vector from the acoustic transfer vectors is not computationally expensive and done prior to the sound pressure synthesis process when all results are available.

6.4.5.3 Sound power and pressure with analytical models

An alternative to the above numerical models are analytical radiation models. The radiating sphere model [CHP10] is, for example, used by Timar et al. in [TL94] and by Le Besnerais in [Le 08]. An infinite length cylinder model is used by Fiedler in [Fie06]. A finite-length cylinder model is used, for example, by Wang et al. in [WL00]. In the works listed above, the analytical models are used to determine the radiation efficiency, i.e., radiated sound power. Radiation characteristics are investigated by Kasper et al. in [Kas+07] based on a multipole model found in [KFC00]. The radiation characteristics of an induction machine including the auralized sound in a factory hall are obtained by Blum et al. in [Blu+11] and v. d. Giet in [vGie11] based on a finite-length cylinder model.

7 Application of the acoustic modeling process

The acoustic modeling process presented in this work was developed with the goal to be readily and routinely applicable in practice, to provide insight into the vibration characteristics of a drive, and to deliver real-life results. The application examples in this chapter underline that this goal is met. Section 7.1 starts off with a PMSM traction drive example for which the vibrations during a run-up of the machine are modeled and validated against their measured counterparts. In section 7.2, skewed PMSMs are modeled. Different skew setups are analyzed and the efficiency of skew on the acoustic characteristics is analyzed. Two application studies of the vibration synthesis process for noise mitigation via the feeding currents and for the acoustic assessment of different switching frequencies and modulation strategies are performed in section 7.3. Then, the switch from PMSMs to SRMs is made. Section 7.4 models the vibrations of a small SRM used as auxiliary drive for a weaving machine. The investigation of an outer-rotor direct-drive SRM for a railway traction application including the operation under various fault conditions closes this application chapter in section 7.5.

7.1 Permanent magnet synchronous machine

A permanent magnet machine is modeled acoustically in this section. The acoustic modeling process is applied to machine PM-A, which has already been the object of study in [Boe+09]. While the original investigation was based on the direct form of the vibration synthesis process, the system-simulation-based implementation is here primarily used. It is confirmed that the system-simulation-based vibration synthesis process can readily cope with spatial and switching harmonics in the currents and perform the synthesis based on realistic time-domain signals. Results which agree well with measurements are obtained.

7.1.1 Simulation and measurement setup

The individual modeling steps introduced in the previous chapters are now brought together.

System simulation

The transient simulation of the force excitation is based on the system simulation model from figure 3.1. The spatial harmonics machine model from section 3.3.1.4 is used as machine model. The controller is implemented as described in section 3.4.1. The parameters for the electromagnetic model, the force model, and the controller are obtained by FE simulations as described in section 3.5. For time-domain interpolation of the air-gap force, the force model from section 5.1 is used.

Structural model

The structural model is built from the CAD model of the machine, which has been simplified for the vibration analysis. Figure 7.1 shows the CAD model of the machine assembly used for vibration synthesis. The housing is made from aluminum alloy. The material parameters of

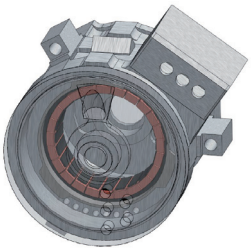

Figure 7.1: CAD model of machine PM-A as used for vibration synthesis

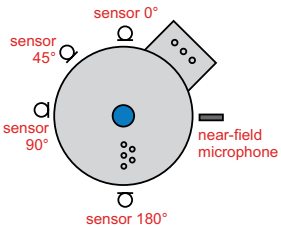

Figure 7.2: Locations of vibration sensors and near-field microphone position on machine PM-A

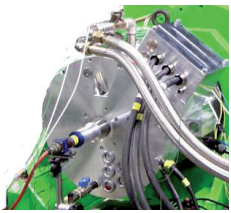

Figure 7.3: Machine PM-A on test-bench

laminations and windings are based on [Kas10]. The force responses are obtained as described in section 6.2. Damping is set to 2% constant.

Vibration synthesis
The vibration synthesis is finally performed as introduced in section 6.3.

Measurements
The machine vibrations were measured with 4 vibrations sensors placed on the circumference of the machine as shown in figure 7.2. Sound pressure was obtained with a near-field and a far-field microphone. However, focusing on machine vibrations, these signals are not evaluated here. One phase current was measured with a current probe. A picture of the test-bench setup is given in figure 7.3.

In the following, we will investigate currents, forces, mean-square surface normal velocity, and operational deflections for a run-up from 0 r/min to 6000 r/min. The maximum torque is set to $T_{\mathrm{m}}^{\mathrm{max}}$= 100 Nm. The machine's power limit is approximately $P_{\mathrm{m}}^{\mathrm{max}}$= 12 kW (cf. -table A.1).

7.1.2 Currents

The simulated currents obtained from the system simulation include spatial harmonics and switching frequency components. Figure 7.4 compares measured to simulated phase currents, with measurement on the left and simulation on the right. The spectral compositions are, aside from minor sidebands in the measurements, identical and the amplitudes agree well.

When the measurements were taken, the system-simulation-based modeling approach was not yet considered and only one phase current was measured. Otherwise, a two-sided spectrum as shown for the $\vec{i}_{\mathrm{s}}^{\,\alpha\beta}$-current simulation results in figure 3.9b taking into account the harmonics rotation direction could have been obtained. Paired with a position signal, this would further allow to draw the dq-trajectory in the dq-plane.

Spatial harmonic current components
Two pairs of spatial harmonic current components are labeled in both figures, the $5^{\mathrm{th}}/7^{\mathrm{th}}$ and the $11^{\mathrm{th}}/13^{\mathrm{th}}$ multiples of f_{el}. The amplitude ranges as well as their relative strengths are

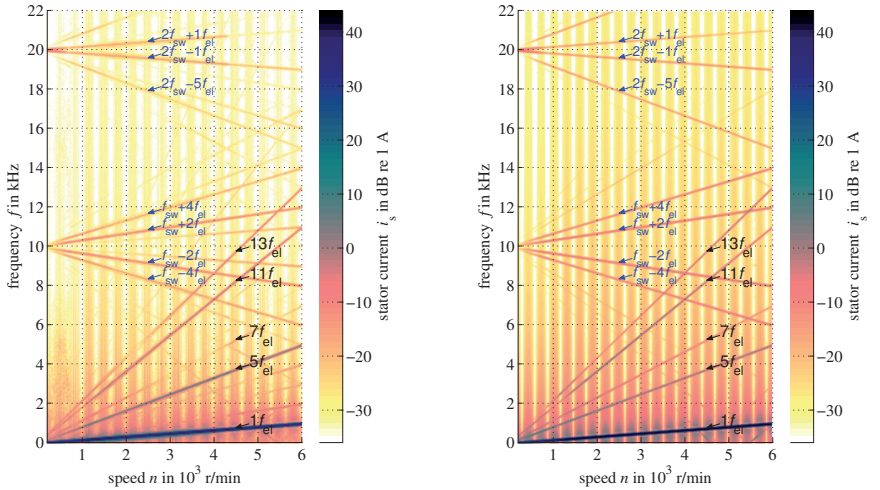

(a) Measured (b) Simulated

Figure 7.4: Measured and simulated current during run-up of machine PM-A from 0-6000 r/min ($T_{\mathrm{m}}^{\max}$= 100 Nm, $P_{\mathrm{m}}^{\max}$= 12 kW)

well preserved. In both, simulation and measurement, the 5$^{\text{th}}$ is, for example, higher than the 7$^{\text{th}}$ and the 11$^{\text{th}}$ higher than the 13$^{\text{th}}$. The amplitudes differ partially between simulation and measurement. The 7$^{\text{th}}$ is, for example, stronger in the simulation than in the measurement. Overall, the results are credible. With full knowledge of control and material parameters of the real machine, further improvement is expected.

We see that also in the measured current, spatial harmonics above the 13$^{\text{th}}$ are virtually not present despite them being an infinite series in theory. When introducing the spatial harmonics machine model in section 3.3.1.4 it was said that usually 2 or 3 (pairs of) spatial harmonics are taken into account. With the model residing in the dq reference frame, the first two spatial harmonics refer to the $\pm$6$^{\text{th}}$ and the $\pm$12$^{\text{th}}$. These are equivalent with the -5$^{\text{th}}$/+7$^{\text{th}}$ and -11$^{\text{th}}$/+13$^{\text{th}}$ in the $\alpha\beta$ reference frame. For the simulations shown, 2 pairs of spatial harmonics have been considered. The example here justifies the approach of taking into account only a limited number of harmonics.

Switching frequency related current components

The machine is operated with a PWM frequency of $f_{\mathrm{switch}} = 10\,\mathrm{kHz}$. In figure 7.4, the switching frequency related frequency components are marked at $f_{\mathrm{switch}} \pm 2f_{\mathrm{el}}$ and $f_{\mathrm{switch}} \pm 4f_{\mathrm{el}}$ and at $2f_{\mathrm{switch}} \pm 1f_{\mathrm{el}}$ and $2f_{\mathrm{switch}} - 5f_{\mathrm{el}}$ which conforms to the SVM frequency composition described in [Ued+91]. The relative agreement is again very good. Overall, the switching frequency related components tend to be higher in the simulation than in the measurement. Transient effects like eddy currents which are not taken into account in the model may be a reason for this. However, in the $> 10\,\mathrm{kHz}$ range, the structural model is much more of a challenge than

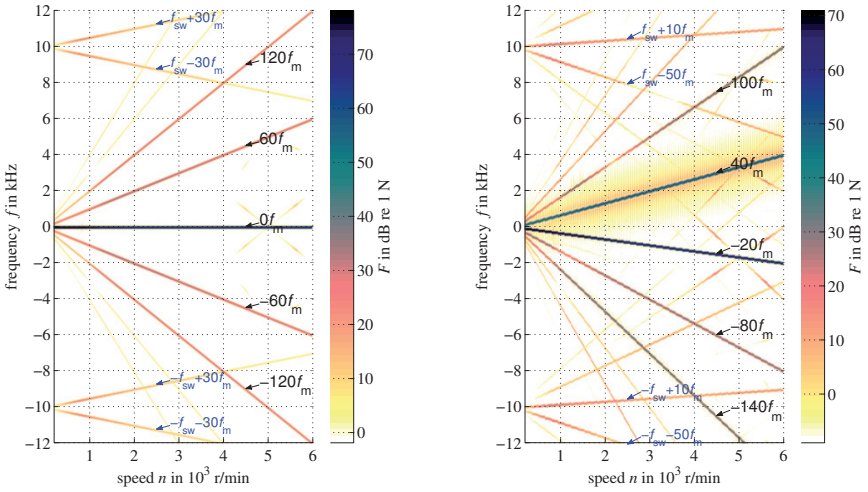

(a) Force shape 0 radial

(b) Force shape 4 radial

Figure 7.5: Force spectrogram for the two main excitation shapes during run-up of machine PM-A from 0-6000 r/min ($T_\mathrm{m}^\mathrm{max}$= 100 Nm, $P_\mathrm{m}^\mathrm{max}$= 12 kW)

modeling current or force are from the viewpoint of acoustic simulations.

7.1.3 Force excitation

From the currents, we now move on to the spatially decomposed forces which are the output of the force model presented in figure 5.2. The computed radial shape 0 force $\underline{F}_0$ is shown in figure 7.5a, the radial shape 4 force $\underline{F}_4$ in figure 7.5b in two-sided spectrograms for the complex-valued time signals. Frequency components are from now on labeled in multiples of f_m, with $f_\mathrm{m}= pf_\mathrm{el}$ and $p = 10$ pole pairs. The underlying force decomposition is tsine.

Preventing spectral leakage in spectrograms

In comparison with the current spectrograms from figure 7.4, the force spectrogram in figure 7.5 looks much cleaner. The smearing that spreads in figure 7.4 from the $1f_\mathrm{el}$ component over the entire figure is not found in figure 7.5a and only observed around the $40f_\mathrm{m}$ component in figure 7.5b. The reason is that for obtaining a spectrogram, the time signal is sliced. A time slice is then transformed into the frequency domain under the assumption that it was stationary. Since the speed changes, spectral leakage occurs. Its amplitude is relative to the strength of the respective frequency component. In figure 7.4, the fundamental current component $1f_\mathrm{el}$ is the by far strongest component and so its spectral leakage dominates the figure. In the force spectrograms in figures 7.5a and 7.5b, $0f_\mathrm{m}$ and -$20f_\mathrm{m}$, respectively, are the strongest components. While $0f_\mathrm{m}$ in figure 7.5a is always at $0f_\mathrm{m}$, figure 7.5b is transformed into a rotating reference system where $-20f_\mathrm{m}$ is stationary, i.e., at $0f_\mathrm{m}$, before forming the

spectrogram. Afterward, the spectrogram is rotated back. Spectral leakage is therefore seen for the second strongest component which is $40f_{\mathrm{m}}$ whose amplitude and consequently the spectral leakage is lower. This approach has already been used for the voltage and current spectrogram in figure 3.9 and force spectrograms in figure 5.7. It is explained here because of the comparison with figure 7.4.

Frequency composition

The speed-proportional frequency components at multiples of $20f_{\mathrm{m}}$ are the machine-inherent noise component defined by the machine design as explained in section 4.2.1 and listed in table 4.1b. The switching frequency related force harmonics start at $\pm f_{\mathrm{switch}}$. The shape 0 force is angular-position independent and does not rotate. All of its frequency components therefore exist in the positive as well as in the negative frequency range forming a standing wave. For the two main force shapes 0 and 4, the spectrum differs in both the fundamental as well as the switching frequency related harmonics, i.e., the shapes generate different tones. Shape 8 (except the sign) shares the spectrum of shape 4 and shape 12 that of shape 0, again as explained in section 4.2.1.

The spatial harmonics current components do not add additional tonal components but influence the existing ones as was already said in section 5.1.3 where machine PM-B's forces were shown. Machine PM-B has high spatial harmonic amplitudes. An influence on the force excitation was investigated in [Boe+12]. For machine PM-A, the spatial harmonics current components are lower and have only little influence on the force, which is not further investigated here.

Force excitation shapes

The synthesized vibrations following in section 7.1.5 are based on the tsine force decomposition introduced in section 4.3. With 24 stator teeth and shape 4 as fundamental force shape, a symmetry section of the machine for which the force decomposition is performed has 6 teeth. Almost perfect agreement up to the 6^{th} spatial air-gap order was seen in figure 4.8a between the original air-gap force and that from the tsine force when for the latter 6+1 force shapes were taken into account. The radial and tangential components of force shapes from 0 by 4 to 24 are consequently taken into account summing up to 26 excitations (6 force shapes with radial/tangential and cosine/sine excitation plus shape 0 with only the cosine shapes).

7.1.4 Structural response

The most important eigenshapes are the circumferential modes 0, 4, and 2. Modes 0 and 4 match with the main excitation shapes and mode 2 is excited by the strongest force shape 4 frequency component (as will be shown below).

Exemplary force responses

Figure 7.6 shows force responses (cf. section 6.2) for 2 of the 26 force excitations, namely for shape 0 and shape 4 excitation (radial, cosine). The shown transfer function (cf. - equation (6.40)) is from force excitation to mean-square surface normal velocity on the surface of the housing (except terminal box and front cover). The thick dashed line is the overall response while the thinner solid curves are the contributions of the individual modes.

Shape 0 and shape 4 response resemble each other. Section 7.1.6 will show that the vibration shapes, of course, differ. The response to both force shapes have their maximum just below

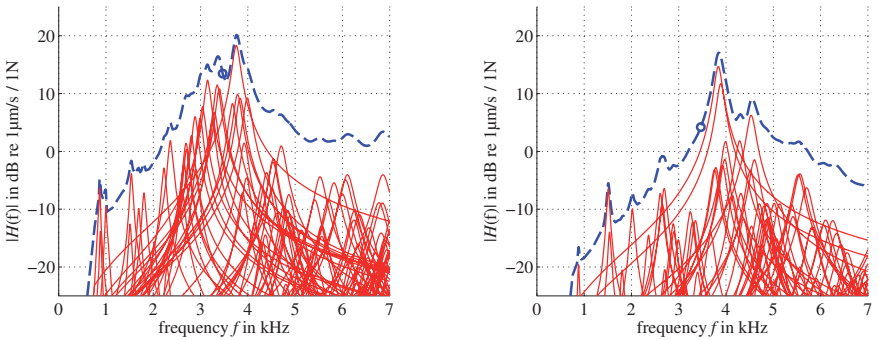

(a) Force shape 0, radial, cosine

(b) Force shape 4, radial, cosine

Figure 7.6: Force response for machine PM-A

4 kHz. In the frequency range below, local maxima stem from parasitically excited lower order modes. To what extent these show is strongly damping dependent.

We observe that the modal density becomes very high above 5 kHz. Individual peaks can no longer dominate the overall response. The harmonic response analyses are therefore only performed up to 7 kHz (with the modal base calculated to 1.5 times the maximum frequency). While going further is technically possible, the author expects the results to be no more than numerical noise. However, vibration spectrograms will be shown below up to 12 kHz to include the switching frequency components starting at 10 kHz. As a pragmatic solution for frequencies above 7 kHz, the 7 kHz response is used. This frequency range contributes little to the overall vibration level so that a quantitative agreement is of lesser importance. Yet the inclusion of these frequency components is important for the qualitative impression.

Frequency clustering and the low-frequency range

ANSYS allows either to define the frequencies for the harmonics analysis or to let the solver automatically cluster the frequency points around the eigenfrequencies. The latter option is used, and one negative side effect can be seen for the frequency range below the lowest eigenfrequency at 800 Hz. No further frequency points lie there except for one at 1 Hz leading to a sudden drop of the response below 800 Hz. This is not a problem for all results presented but taking more than 5 substeps per mode or defining the low-frequency range explicitly might be advantageous.

Eigenfrequencies

Simulated and measured eigenfrequencies are compared in table 7.1. For the simulated eigenfrequencies, two values are given where the two orthogonal shapes of the same circumferential order are at different frequencies. In the measurements, these frequencies cannot be identified clearly so that ranges are give instead. For modes 0, 4 and 2, the error is no more than 5%. Of minor importance are modes 3 and 1. Mode 1 is off by 50%, but it is a special case. For mode 1, the entire machines performs unbalanced vibrations with the entire structure moving,

e.g., up/down or left/right. Here, the stiffness of the mounting as well as the rotor play a decisive roll. Neglecting the rotor and assuming infinitely stiff mounting of the flange to the test bench leads to the higher eigenfrequency. This adds to the structural modeling aspects to be further investigated in the future as already said when discussing rotor force modeling in section 5.3. We we will be able to see mode 1 slightly in the measurements, while it is hardly excited in the simulation. Figure 7.6 shows small local maxima at 880 Hz but we will not really find this in the spectrograms.

Mode	Eigenfrequency	
	measured	simulated
0	3800 Hz	3782 Hz
4	3800–4000 Hz	3840&3940 Hz
3	2450–2500 Hz	2611&2692 Hz
2	1420–1500 Hz	1510&1540 Hz
1	560 Hz	880 Hz

Table 7.1: Eigenfrequencies, measured vs. simulated for machine PM-A

7.1.5 Vibrations

The acoustic modeling and vibration synthesis process is now brought together. Figure 7.7 presents a measured and a synthesized run-up spectrogram of the sensor-averaged mean-square surface normal velocity for machine PM-A. The characteristic frequency components are labeled and circles mark points for which the operational deflection will be discussed in the next section. Before going into detail, the general impression is that the agreement between measurement and simulation is very satisfactory. The machine-inherent as well as the switching-frequency-related frequency components are well represented in the simulation (for above 7 kHz we recall the constant structural response). The spectral composition has been discussed for the forces above. The vibration spectrograms as well as all following vibration spectrograms are A-weighted[(i)].

Resonances

Excited eigenfrequencies show in two ways. First, if a frequency component excites an eigenfrequency, the respective frequency component sees a (local) maximum when passing the eigenfrequency. Second, excited eigenfrequencies show continuously in a spectrogram as a horizontal band. In the measurement, we notice 4 bands, mode 1 around 500 Hz, mode 2 around 1500 Hz, mode 3 around 2500 Hz and the mode 4 and mode 0 band around 4000 Hz. In the simulation, the mode 1 band is not found. It is assumed that some degree of eccentricity exists in the machine which leads to a slightly unbalanced force which is not considered in the simulation. The mode 2, 3, and 4/0 bands are then also found in the simulated spectrogram with mode 3 being somewhat higher.

[(i)] A-weighting refers to a frequency weighting. Very low and high frequencies are attenuated in accordance with the lower sensitivity of the human ear for these frequencies. A-weighting is commonly used for environmental or industrial noise. It was originally intended for low-level noise only, with B-, C-, and D-weighting for higher levels.

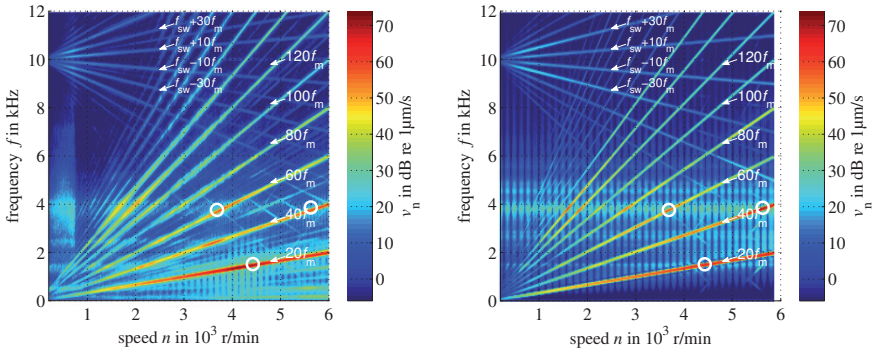

(a) Measured (b) Synthesized

Figure 7.7: Spectrogram comparison of measured and synthesized surface normal velocity during run-up of machine PM-A from 0-6000 r/min ($T_{\mathrm{m}}^{\max}$= 100 Nm, $P_{\mathrm{m}}^{\max}$= 12 kW)

Additional transversal modes in the simulation

Between 4500 Hz and 5000 Hz, the simulated spectrogram shows slightly excited resonances where in the measurements are none. The respective eigenshapes were found to be circumferential shapes 4 with a transversal shape 1. In figure 7.6b, such a mode leads to a local maxima at 4600 Hz. This phenomenon routinely occurs with the structural models used and is further investigated for the outer-rotor machine SR-Y in section 7.5.2.1.

Amplitudes

The overall amplitude agreement of the individual frequency components is considered to be good. For both measurement and simulation, $20f_{\mathrm{m}}$ is the strongest frequency multiple and reaches its peak amplitude when passing the mode 2 eigenfrequency near 1500 Hz. The shape 4 dominated frequency component $40f_{\mathrm{m}}$ as well as the shape 0 dominated frequency component $60f_{\mathrm{m}}$ see their maxima near 4000 Hz when passing the mode 4 or mode 0 eigenfrequency, respectively. For these above three points, the operational deflection is shown in section 7.1.6. Furthermore, well represented are $120f_{\mathrm{m}}$ and $140f_{\mathrm{m}}$ being the strongest components between 1500 r/min and 2000 r/min when passing the mode 0 or mode 4 resonance, respectively.

7.1.6 Operational deflections

Figure 7.8 depicts the operational deflection of machine PM-A for $20f_{\mathrm{m}}$ at 1514 Hz (4517 r/min, 25 Nm). The deflection is basically an elliptic mode 2, but with an superimposed rectangular shape due to the shape 4 excitation. It rotates clockwise.

For $40f_{\mathrm{m}}$ at 3857 Hz (5740 r/min, 14 Nm) in figure 7.9, the deflection shape is a mode 4 and it rotates counter-clockwise. That the fundamental vibration shape is mode 2 in the first case and mode 4 in this case becomes clearer with the help of figure 7.11a and figure 7.11b. There, two still frames (shifted 180° in time) of the outside of the housing are superposed for

the $20 f_{\mathrm{m}}$ and the $40 f_{\mathrm{m}}$ component.

The mode 0 vibration for $60 f_{\mathrm{m}}$ at 3760 Hz (3760 r/min, 32 Nm) can be easily examined in figure 7.10. Its overlay is found in figure 7.11c.

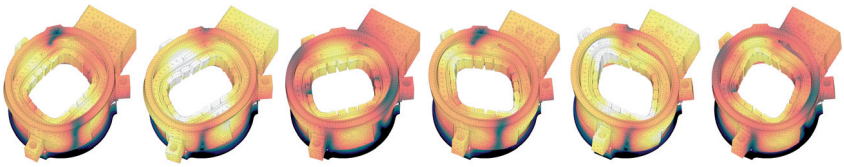

(a) 30° (b) 90° (c) 150° (d) 210° (e) 270° (f) 330°

Figure 7.8: Operational deflection of machine PM-A for $20 f_{\mathrm{m}}$ at 1514 Hz (4517 r/min, 25 Nm)

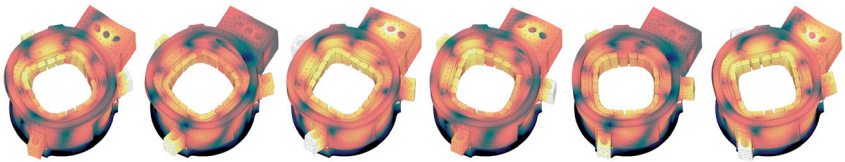

(a) 30° (b) 90° (c) 150° (d) 210° (e) 270° (f) 330°

Figure 7.9: Operational deflection of machine PM-A for $40 f_{\mathrm{m}}$ at 3857 Hz (5740 r/min, 14 Nm)

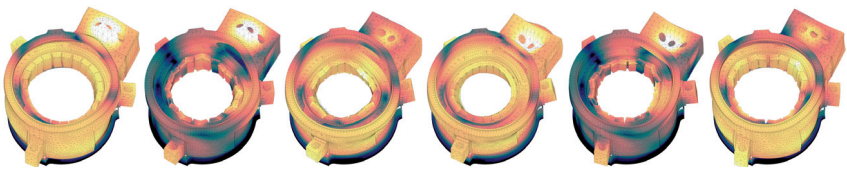

(a) 30° (b) 90° (c) 150° (d) 210° (e) 270° (f) 330°

Figure 7.10: Operational deflection of machine PM-A for $60 f_{\mathrm{m}}$ at 3760 Hz (3760 r/min, 32 Nm)

(a) Mode 2 at $20 f_{\mathrm{m}}$, 1514 Hz (b) Mode 4 at $40 f_{\mathrm{m}}$, 3857 Hz (c) Mode 0 at $60 f_{\mathrm{m}}$, 3760 Hz

Figure 7.11: Vibration shapes of the surface of the housing for the three characteristic points from figures 7.8-7.10

7.1.6.1 Mode $N_{\text{teeth}}/2$ and tooth rocking

The statement that with respect to acoustic modeling of drives further potential is seen in the structural modeling is repeatedly made in this thesis. It is here demonstrated that while the tsine force generally improves the air-gap force representation it also creates new challenges. One is tooth rocking which occurs at higher frequencies. If the cosine-shape of the radial shape $^{N_{\text{teeth}}}/_2$ tsine force is applied, the maximum (positive and negative) amplitudes of the force excitation lie in the centers of neighboring teeth (see figure 7.12a for a sketch). For the sine-shape of the $^{N_{\text{teeth}}}/_2$ tsine force, adjacent edges of two teeth see the maximum (positive or negative) amplitudes (see figure 7.12c). For the first case (which is much like the shape $^{N_{\text{teeth}}}/_2$ tooth force), the response is low over the entire modeled frequency range. For the latter case, the response rises towards higher frequencies and at 7 kHz exceeds the cosine response by 20 dB.

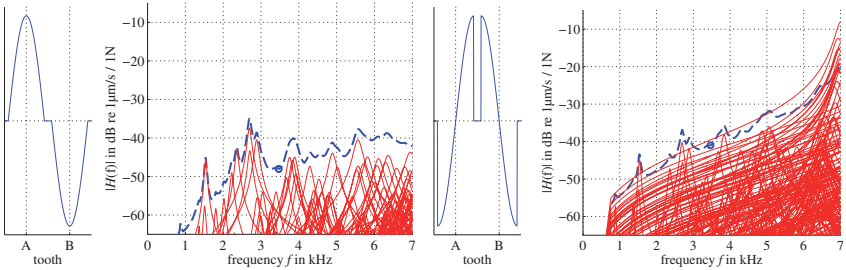

(a) force, cosine (b) response, cosine (c) force, sine (d) response, sine

Figure 7.12: Force shape 12, radial and its response for machine PM-A

(a) 30° (b) 90° (c) 150° (d) 210° (e) 270° (f) 330°

Figure 7.13: Tooth rocking of the stator teeth of machine PM-A for $80 f_{\text{m}}$ at 6885 Hz (5167 r/min, 17 Nm). Mainly caused by shape $^1/_2N_{\text{s}}$=12, sinus excitation.

The underlying vibration is presented in figure 7.13. The teeth start rocking against each other. The winding is included in the model but not shown here to better show the tooth

rocking. The assumption is that the model delivers incorrect results here. The 2% damping may well be too low at 7 kHz. Increasing global damping at high frequencies (via Raleigh damping; see section 6.1.4) does not solve the problem, though. For the results above, the influence of the radial shape 12 sine-shape in the tsine force is not yet very strong but this effect is supposed to repeat for other machines with relatively few stator teeth for a given size (e.g., q=0.5 PMSMs or SRMs).

7.2 Skewed permanent magnet synchronous machines

Permanent machines with rotor skew are modeled acoustically in this section. Both, the direct and the system-simulation-based synthesis process are used. Two example machines, machine PM-D (PM-N72p6) and machine PM-C (PM-N60p5), are investigated and exemplary results are obtained. It is confirmed that the vibration synthesis process can easily cope with skewed PMSMs with arbitrary rotor skew arrangements. For machine PM-D (PM-N72p6), the effectiveness of skew is confirmed and the dependence on the slice arrangement is analyzed. Skew was analyzed in the force domain in section 4.4. It was shown that for machine PM-C skew does partially not improve the acoustic characteristics. This is confirmed here in the structural domain.

7.2.1 Skew slice arrangements and simulation setup

In the following, the investigated rotor skew slice arrangements for machine PM-D as well as the system simulation for obtaining the force excitation in permanent magnet machines with rotor skew are described.

7.2.1.1 Rotor skew slice arrangements

Four rotor skew slice arrangements are investigated for machine PM-D. Figure 7.14 shows the angular displacements of the segments. The skew angle spans one slot, equaling 30°el. Without skew, all segments are aligned (figure 7.14a). In case of linear skew, the axial displacement increases linearly in 5°el steps (figure 7.14b). For V-skew, the skew segments from the linear skew arrangement are resorted in the axial direction placing one segment after another on the left-hand side and on the right-hand side (figure 7.14c). Mean skew refers to the case where the force superposition is not done in the structural domain but in the force domain. This case was discussed in section 4.4 for machine PM-C for which we will see structural results below. The gray bars in figure 7.14d depict that all segments see the mean of the forces otherwise acting on the different segments. This mean skew was performed in the 2-D force domain as described in section 4.4.2.

7.2.1.2 System simulations for obtaining the force excitation in skewed permanent magnet machines

The transient system simulation for skewed permanent magnet machines is analogous to the non-skewed case in in section 7.1.1. The force model, however, needs to incorporate skew. Therefore, the system simulation force model for skewed PMSMs from section 5.4.2.3 is used. The transient simulation is required for the system-simulation-based implementation of the

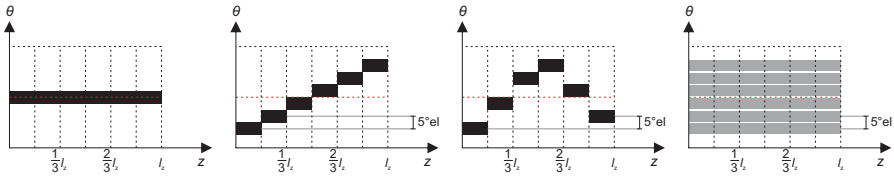

(a) no skew (b) linear skew (c) V-skew (d) mean skew

Figure 7.14: Schematic drawing of the skew slice arrangements investigated for machine PM-D

vibration synthesis process. In the direct implementation, the force lookup tables are shifted as described in section 5.4.2.2.

Simulation time affected by output filtering

The system simulation model includes by default 8+1 force shapes in both radial and tangential direction. With cosine and sine shape orientation, and 6 skew slices plus the output of the unskewed and the mean-skewed force, the number of output signals is $(8+1)\cdot 2\cdot 2\cdot(6+2)=288$ for the force alone[(ii)]. These signals are complemented by torque, speed, position, voltages, currents, and flux linkages. The force-lookup implementation remains compact and generic based on SIMULINK's Pre-Lookup- and For-Each-blocks, as mentioned in section 5.2.2. However, the simulation time is now strongly affected by the required output filtering. The simulation is run with variable time steps. Analog (continuous time) low-pass filters are therefore required on the output before sampling the output with a fixed sampling rate for further processing in the frequency domain. The simulation time for a 10 s run-up of a 6-slice skewed PMSM currently lies in the half-an-hour range in the Accelerator mode. It is desirable to speed up the simulation. The instant availability of arbitrary run-ups is currently an advantage of the direct implementation. However, switching and spatial harmonics are then not included.

Force examples in the time domain

With p=6 pole pairs, the fundamental force shape of machine PM-D is 12. Figure 7.15 shows as an example the radial force in the time domain for shape 0 and 12 of machine PM-D for the 6 skew segments and in addition the unskewed force and the skewed force from the mean of the slices. The degree values in the legend describe by what electrical angle a slice is shifted. The machine is running at 2000 r/min with 250 Nm. Also in the mean-skew case, the force is apparently far from flat. However, on a closer look the different frequency composition of unskewed and mean-skewed force can be seen. The periodicity is always 60°el. The mean-skewed force shows three distinct peaks per 180°el. With 6 pole pairs in machine PM-D, that is equivalent to a frequency of $36 f_\mathrm{m}$. For the unskewed case, three main and three lower peaks are visible. This indicates additional existence of a significant $72 f_\mathrm{m}$ component. This is exactly the frequency component which skew mainly aims at reducing and obviously achieves here.

A negative skew angle signifies a shift of the angular position of the segments against the

(ii) This is a default setting. Not all will be used in the synthesis below.

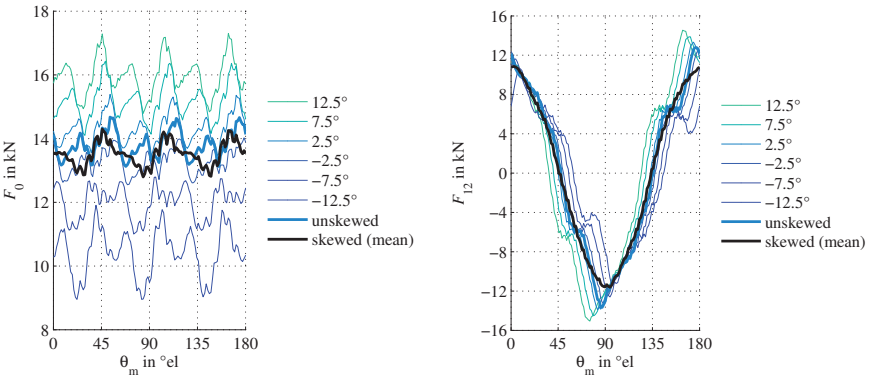

(a) Force shape 0

(b) Force shape 12 (cosine)

Figure 7.15: Force shapes 0 and 12 (radial, cosine) in the time domain for machine PM-D at 2000 r/min and 250 Nm

direction of rotation. In motoring mode, this means that the angular displacement between current space vector and the segments' d-axis increases. This is equivalent to a larger control angle, stronger field weakening, and consequently a lower overall force. However, as also discussed in section 4.4.3.3, the force ripple does not necessarily decrease but often even increases.

7.2.1.3 Vibration synthesis

The vibration synthesis is performed as introduced in section 6.3. Tsine is chosen as decomposition option and radial and tangential force shapes from 0 by 12 up to shape 72 (i.e., shape 6 in the 6-tooth, 1-pole symmetry section) are taken into account. Under equivalent conditions, 26 force excitations were taken into account for the non-skewed PMSM in section 7.1. This number is now up to 156 since it is multiplied by the number of slices. For incorporating skew it is now mandatory to preserve the phase relationship between the skew segments as well as to take into account the interaction between the response, i.e., to use the full $\overline{\mathbf{H}_{v_{\mathrm{n,unit}},j,i}}(\omega)$ matrix as discussed in section 6.3.6.

7.2.2 Influence of the skew arrangement on the effectiveness of skew for machine PM-D

It is analyzed in the following how the skew slice arrangement influences the effectiveness of skew on reducing the mean-square surface normal velocity.

7.2.2.1 Run-up spectrogram

Figure 7.16 shows simulated full-load run-up spectrograms ($T_\mathrm{m}^\mathrm{max}$= 260 Nm, $P_\mathrm{m}^\mathrm{max}$= 130 kW, cf. table A.4) for an unskewed and a V-skewed version of machine PM-D. The switching frequency is 10 kHz. The spectrograms are analyzed in detail below. The amplitudes of the main machine inherent noise components are mainly excited by shape 0 forces and are given in figure 7.17. The amplitude figures have been obtained by the direct implementation of the vibration synthesis process. The spatial harmonics content in the system-simulation currents is low so that direct and system-simulation results are equivalent for the main noise components.

General vibration characteristics

Machine PM-D as well as the subsequently investigated machine PM-C stand for typical automotive traction PMSMs as discussed in section 4.2.3. For these machines, the shape 0 related frequency components at multiples of $1/2 N_\mathrm{s} f_\mathrm{m}$ are usually prominent tonal components with $N_\mathrm{s} f_\mathrm{m}$ as strongest component. We first focus on the result for machine PM-D without skew in figure 7.16a. The shape 0 related frequencies at multiples of $36 f_\mathrm{m}$ are the strongest components. From the shape 12 related machine inherent noise components, $12 f_\mathrm{m}$ can be seen in the low and $60 f_\mathrm{m}$ in the high-frequency range[(iii)].

With shape 12, machine PM-D has a high fundamental spatial order compared to machine PM-A, for which it was 4 as discussed in section 7.1 above. For machine PM-A, the shape 4 frequency related frequency components exceeded the shape 0 related ones and dominated the spectrum. Therefore, skew is not an option for machine PM-A.

Influence of V-skew

The unskewed version of machine from PM-D figure 7.16a is now compared to the V-skewed machine in figure 7.16b. On a quick look, the two spectrograms appear rather similar. This impression is boosted by the chosen high dynamic rage. However, this dynamic range demonstrates the overall complexity of the resulting spectrogram with main and minor machine inherent noise components and additional switching frequency related components. The most important points are therefore marked and figure 7.17 helps to compare the amplitudes.

For the unskewed machine, $72 f_\mathrm{m}$ is the strongest noise component (see figure 7.16a and figure 7.17a) and it peaks around 3800 r/min and 4600 Hz. In figures 7.16b and 7.17b, we notice that 1-slot skew is generally effective in reducing this and higher shape 0 frequencies while $36 f_\mathrm{m}$ remains unaltered. This is in accordance with the theoretical analysis of discrete skew in section 4.4.2. What we see, though, in figures 7.16b and 7.17b is a new resonance peak for the $72 f_\mathrm{m}$ component of the V-skewed machine around 5400 r/min and 6400 Hz. The operational deflection is analyzed below in section 7.2.3. As before for machine PM-A, we will find a transversal vibration which is likely to be an artifact. But again, this will be further analyzed in section 7.5.2.1.

[(iii)] A $54 f_\mathrm{m}$ component is shape 0 related and can be noticed when passing the mode 0 eigenfrequency around 4600 Hz. This component is not part of the analytically predicted frequency spectrum from section 4.2 and does not occur in the direct implementation of the synthesis approach. Further analysis can clarify whether this is a valid component or, for example, an interpolation artifact.

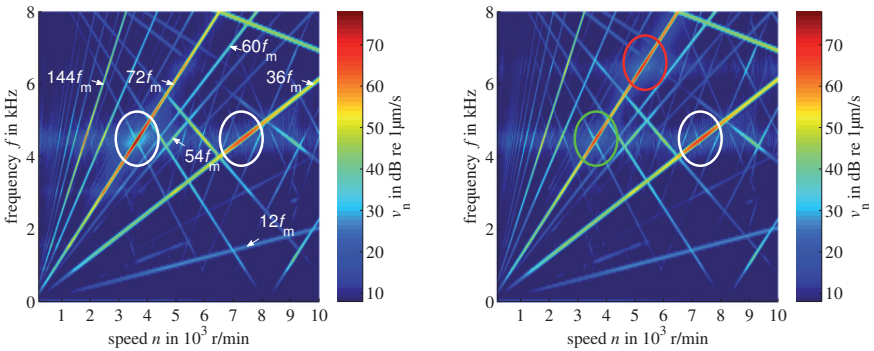

(a) no skew (b) V-skew

Figure 7.16: Simulated full-load run-up spectrograms for machine PM-D

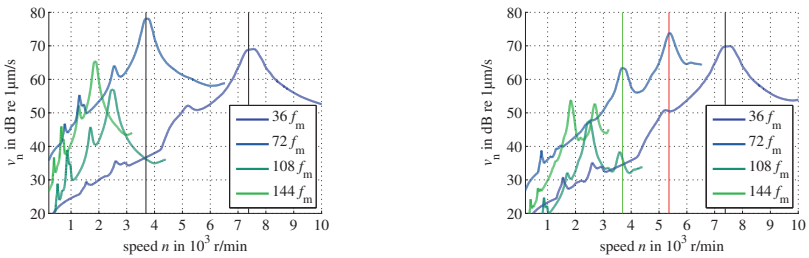

(a) no skew (b) V-skew

Figure 7.17: Amplitudes of shape 0 force related noise components of machine PM-D

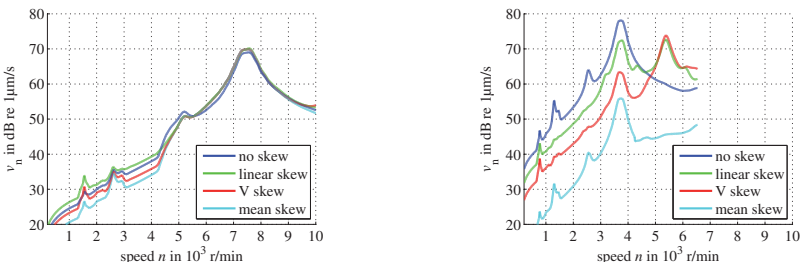

(a) $36f_m$ (b) $72f_m$

Figure 7.18: Influence of different skew slice arrangements for machine PM-D

Influence of different skew arrangements

So far, the unskewed machine has been compared to the V-skewed machine. With the help of figure 7.18, the influence of the different skew slice arrangements is analyzed regarding the effectiveness of skew on the mean-square surface normal velocity during a full-load run-up of machine PM-D. It is apparent from figure 7.18a that for all skew slice arrangements 30°el skew shows almost no influence on the $36f_{\mathrm{m}}$ frequency component, which is in accordance with the analytical description in section 4.4. From figure 7.18b we see that V-skew is almost 10 dB more effective than linear skew in reducing the $72f_{\mathrm{m}}$ frequency component below 5000 r/min. Above this speed, both excite an additional vibration mode shape as shown in figure 7.17 (again, this may be an artifact). The most effective form of skew is the only theoretical mean or 2-D skew where all skew segments see the mean of the force of the individual segments. The transversal mode at 5400 r/min is then furthermore not excited since the force does not change in the axial direction.

7.2.3 Operational deflections with and without skew

In the following, the operational deflections are analyzed. The stator and the outside of the housing are shown. Windings, flanges, etc. are incorporated in the model but not drawn here. For vibration shapes or modes, we have so far focused on circumferential modes. Now, the deflection along the transversal direction is additionally important. Modes or deflection shapes are in the following identified by two numbers from which the first characterizes the deflection in the axial direction and the second that along the circumferential direction. This naming scheme is chosen in accordance with literature, in particular the later discussed article [WW97]. For circumferential modes, the order represents the number of full sine waves (i.e., maximum and minimum). For transversal modes, the order identifies the number of half waves.

Figure 7.19 shows the operational deflection of machine PM-D without skew at the peak point from figure 7.17a, $72f_{\mathrm{m}}$ at 4637 Hz (3864 r/min, 250 Nm). The main excitation shape at $72f_{\mathrm{m}}$ is shape 0 and so it comes as no surprise that a mode (1,0) vibration dominates. Tangential forces do not contribute much to the overall vibration level but they cause the bending of the stator slots along axial direction. Without them, the vibration shape is rotationally symmetric.

Figure 7.20 depicts for the V-skewed machine the operational deflection at the same operating point as above. The above dominant mode shape (1,0) is suppressed as a result of skew. Mode (2,0) vibration shapes now dominate.

The deflection at the new resonant peak in case of V-skew is now presented in figure 7.21 for $72f_{\mathrm{m}}$ at 5364 Hz (6437 r/min, 210 Nm). Mode shape (3,0) is more strongly excited for V-skew than in the unskewed case and defeats a lot of the positive influence of V-skew. However, it is assumed that the simulation exaggerates this effect and furthermore, this type of vibration can be suppressed by stiffening rips which are left out on this simplified test housing.

7.2.4 Remarks on the vibration synthesis for machine PM-D

Force shape 36, with $36{=}{}^{1}\!/_{2}N_{\mathrm{s}}$, which caused tooth rocking at high frequencies for machine PM-A as analyzed in section 7.1.6.1 is here completely negligible in the investigated frequency

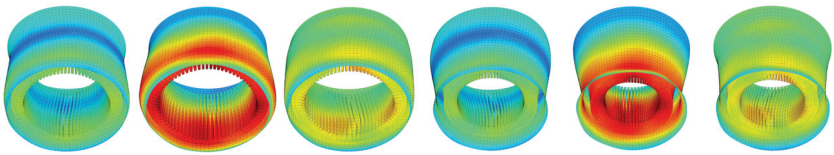

(a) 30° (b) 90° (c) 150° (d) 210° (e) 270° (f) 330°

Figure 7.19: No rotor skew – operational deflection in shape (1,0) for machine PM-D at peak point from figure 7.17a, $72f_{\mathrm{m}}$ at 4637 Hz (3864 r/min, 250 Nm)

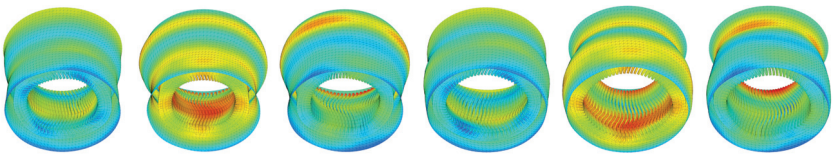

(a) 30° (b) 90° (c) 150° (d) 210° (e) 270° (f) 330°

Figure 7.20: V-skew – operational deflection in shape (2,0) at same operating point as above

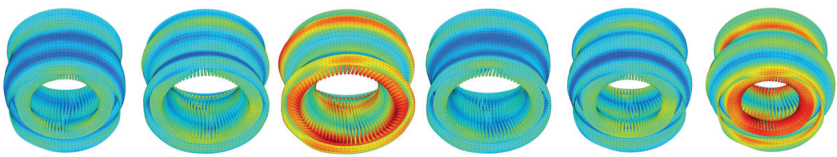

(a) 30° (b) 90° (c) 150° (d) 210° (e) 270° (f) 330°

Figure 7.21: V-skew – operational deflection at new peak in shape (3,0). $72f_{\mathrm{m}}$ at 5364 Hz (6437 r/min, 210 Nm)

range up to 8000 Hz. This supports the assumption that machines with relatively few stator teeth for a given size are more prone to this.

The air-gap force always sees a large shape N_{s} (72 here) force when decomposed as sine or tsine. This shape order cannot be represented with the tooth force (Nyquist criterion). Including shape 72 in the tsine synthesis, the spectrogram peaks at 76 dB, without it at 75 dB and shape 72 alone at 63 dB. Besides the lower amplitude, the response is similar to shape 0 which was also observed in the force response study in section 6.2.3 (figures 6.4b and figure 6.5b) and was put on the list of things to further investigate.

Influence of the number of force excitations

Figure 7.16 has been obtained based on 156 force excitations as discussed in section 7.2.1.2. If only shapes 0 and 12 and only the radial direction is taken into account, this number is reduced to 18. The result then looks only slightly different. For conciseness, the reduced result itself is not shown. A similar yet more drastic analysis will be presented in section 7.4.4 for

machine SR-X. The resemblance of the full and the reduced result is, of course, not surprising since the dominance of the fundamental excitation shapes as well as that of the radial force is well known. The – eventually obvious and also initially intended – conclusion drawn is that the vibration synthesis process does not set limits on the number of excitations that are considered but allows to reduce or increase this number as desired.

7.2.5 Ineffectiveness of skew at full load for machine PM-C

In section 4.4.3, the effectiveness of skew for machine PM-C has been investigated. The study was based on the force excitation alone and represents the case here called mean skew. It was found that skew partially deteriorates the acoustic characteristics. The result from figure 4.16b is repeated in figure 7.22a. What is shown is the difference in force excitation at $60f_\mathrm{m}$, i.e., the main shape 0 frequency for the 10-pole PM-C. Next to it in figure 7.22b, the difference in the mean-square surface normal velocity on the outside of the housing is now plotted. The underlying skew arrangement is the symmetric 6-slice V-skew from figure 4.10. For this study, the stator of machine PM-C was put into a similar simplified housing as that of machine PM-D above. We see that up to 5000 r/min the results for force excitation and vibration response are comparable. In the base speed range, skew is effective. We have already seen in figure 7.18b that the force-based mean skew overestimates the effectiveness of skew. Also here, the vibrational response is reduced less than the mean force excitation. The increase in force excitation at full load between 3000 r/min and 5000 r/min is confirmed by a similar increase in the mean-square surface normal velocity. Above 5000 r/min, the transversal mode is again excited consequently leading to a further deterioration of skew for this model.

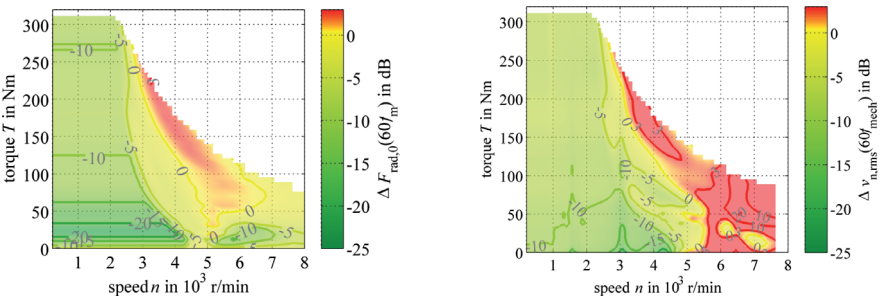

(a) Force (b) Vibration

Figure 7.22: Effectiveness of skew on reducing the $60f_\mathrm{m}$ component of machine PM-C over torque and speed for both force and vibration

Figure 7.23 finally compares the effectiveness of skew on reducing the $60f_\mathrm{m}$ noise component of machine PM-C for a run-up with full load and one with constant 38 Nm of torque. It is obvious that for full load, skew is only effective below 2500 r/min. Moreover, it is very effective at low loads below 4000 r/min. The reduction of the peak level is about 5 dB. Skew only deteriorates the response where the transversal mode is excited. The overall level, however, is about 20 dB lower in the low load case.

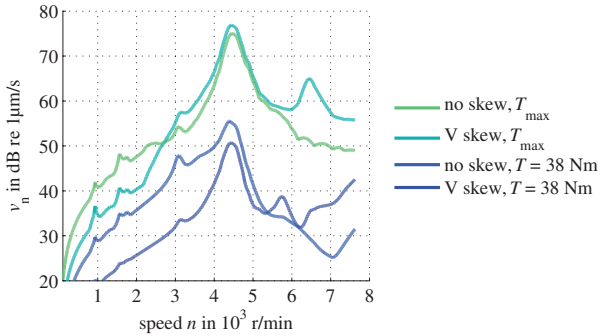

Figure 7.23: Effectiveness of skew on reducing the $60f_m$ noise component of machine PM-C for two run-ups with different load levels

7.2.6 Summary on the vibration synthesis for skewed PMSMs

It has been shown that the vibration synthesis process can efficiently model skewed permanent magnet machines. Skew slice arrangements have been investigated which indicate for machine PM-D best results for a V-skew arrangement. It could be seen that tangential forces have a notable influence on the shape of the operational deflections. The results of the 2-D analysis of shape 0 forces in skewed PMSMs from section 4.4 have been confirmed in the vibration synthesis. The transversal vibrations of the stator are an aspect which asks for further investigation. The skewed machines above are presented as numerical examples; it is expected that the approach works equally well for other types of machines.

7.3 PMSM application studies

Two application studies are presented below. Section 7.3.1 shows how the shape 0 force can be suppressed by harmonics in the feeding current. Section 7.3.2 is a brief investigation of different switching frequencies and modulation schemes.

7.3.1 Shape 0 force ripple mitigation via the feeding currents

Rotor skew has been analyzed above for force shape 0 ripple minimization in PMSMs as one option of acoustic optimization through electromagnetic design. Alternatively, shape 0 force ripple can be suppressed in most multiphase permanent magnet, induction, and switched reluctance machines via the feeding currents. Constraints for real-life applications regarding model quality, control method, sensors, and inverter hardware are put aside here for a brief simulation-based study using the current-fed PMSM force model. It shall be highlighted that with the PMSM force model an efficient force prediction model is at hand and that the vibration synthesis process allows to assess the effectiveness of the force ripple suppression. Control-based approaches are worthwhile topics for further investigation.

Ideal current control example for machine PM-C

A simulation model is built which assumes an ideal current controller. The current set-points from the controller are fed directly to the force model. For force ripple compensation, the shape 0 force ripple is fed back and added to the dq-set point via a proportional gain (P) controller. With only shape 0 radial to compensate and d- and q-axis currents as variables, this control problem is not fully determined. Generally, another criterion, e.g., torque ripple can also be minimized. Figure 7.24 shows the temporal mean of the shape 0 force and its dependence on the dq current. The black lines are lines of constant torque and cover the area used during operation. We see that for machine PM-C, the lines of constant force amplitude are fairly parallel to the q-axis. The force amplitude has a strong gradient in the q-axis and consequently the q-axis current is chosen for compensation.

A run-up from 0-1000 r/min is simulated with a maximum torque of 250 Nm and a maximum power of 45 kW. This is well within the operational limits of the machine so that it is generally realistic that this operating curve can provide headroom for a real current control. Figure 7.25 depicts the trajectory of the dq-current for the above run-up with and without force compensation by q-axis current.

Figure 7.26 shows the corresponding run-up spectrograms without compensation on the left and with compensation on the right. The difference is quite remarkable. The shape 0 related frequency components become almost constant and what remains is eventually only depending on the proportional gain of the controller. The highest amplitudes of the shape 0 excitation related frequency components $30f_{\mathrm{m}}$ and $60f_{\mathrm{m}}$ are now similar to the shape 10 force related $50f_{\mathrm{m}}$ component, which as a positive side effect is reduced as well. At least in the simulations, the transversal mode defeated the effectiveness of skew at high frequencies. Here, it is not excited since the force excitation shape is not changed but lowered altogether.

Further insight into force and currents is given with the help of figures 7.27–7.29. For different speeds, figure 7.27a shows the time variation of force shape 0 ($F_{\mathrm{r},0}$) and shape 10 ($F_{\mathrm{r},10}$). Without compensation, $F_{\mathrm{r},0}$ fluctuates around its mean amplitude, while it is constant with compensation. The corresponding currents are given below in figure 7.28. Without compensation, they are purely sinusoidal. The harmonic content introduced for compensating the force fluctuation is remarkably low. The corresponding spectra are shown in figure 7.29. For the general mathematical relationship between current harmonics and torque fluctuations in PMSM (which can be easily extended to radial force fluctuations), it is referred to [FCJ93]. In general, a pair of current harmonics acts on an infinite number of force harmonics and a force harmonic is influenced by an infinite number of current harmonics. However, in practice, a force harmonic is mainly influenced by current harmonics that have the same frequency in the dq system. The $\alpha\beta$-current harmonics 5 and 7 therefore suppress mainly $30f_{\mathrm{m}}$, while the 11^{th} and 13^{th} act on $60f_{\mathrm{m}}$ in the shape 0 force spectrum.

A model-based feed-forward implementation (i.e., without the feedback loop used above) is achieved when current harmonics are added to the current set point to cancel out the force excitation based on the tabulated data from the force model. For parametrization, the average force amplitude is differentiated in the operating point. As feed forward signal, the main current harmonic acting on particular force shape is scaled by dividing the force ripple amplitude by the negative derivative. A study using this technique has been performed for machine PM-B. However, all further investigations for PMSMs, as well as for other machines are left for future work.

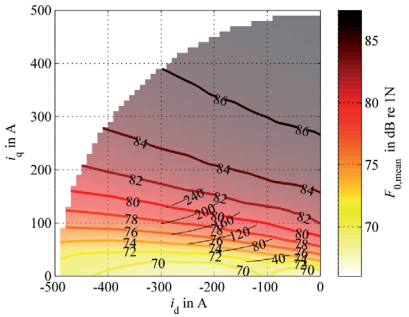

Figure 7.24: Amplitude of the shape 0 force over dq-current (mean value of the position dependence of the force shape)

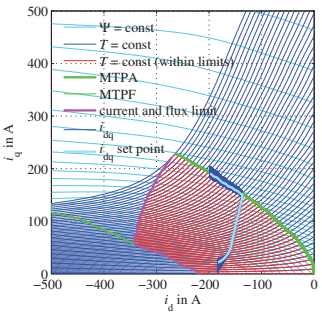

Figure 7.25: Trajectory of the dq-current for the run-up with force compensation by q-axis current

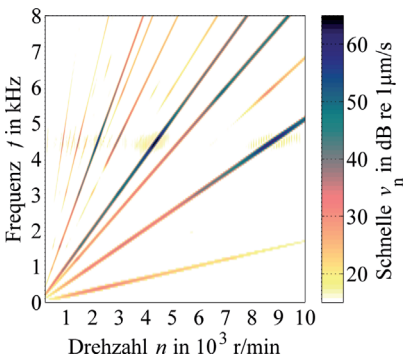

(a) no compensation – operation with sinusoidal currents

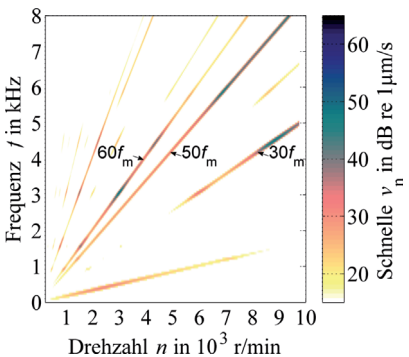

(b) compensation – current harmonics suppress force shape 0 ripple at multiples of $30 f_m$ by 20 dB and more

Figure 7.26: Current fed run-up spectrogram of the mean square surface normal vibration for machine PM-C without and with shape 0 force ripple compensation

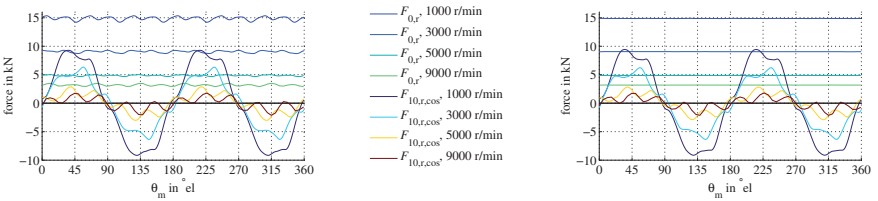

(a) no compensation – force shape 0 amplitudes vary

(b) compensation – force shape 0 amplitudes are constant

Figure 7.27: Force shape 0 and 10 over one electrical period with and without compensation

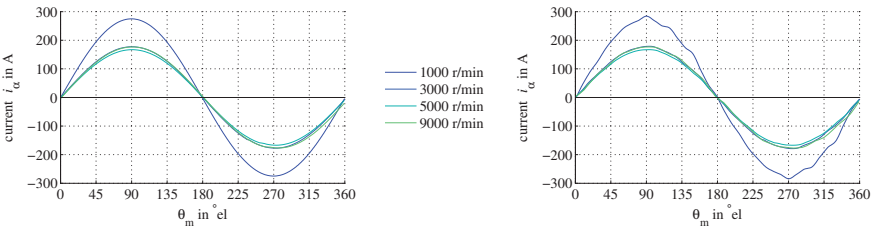

(a) no compensation – sinusoidal currents

(b) compensation – additional current harmonics

Figure 7.28: Current $i_{s\alpha}$ over one electrical period with and without compensation

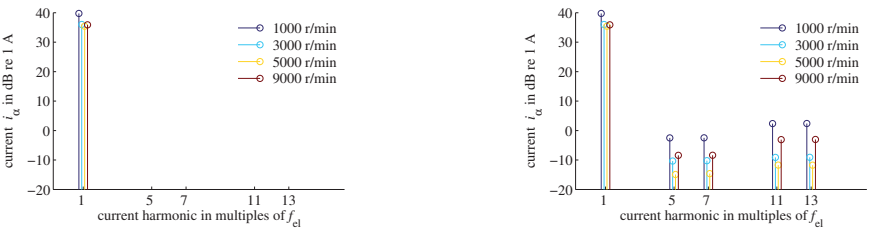

(a) no compensation – sinusoidal currents

(b) compensation – additional current harmonics

Figure 7.29: Current $i_{s\alpha}$ spectrum with and without compensation

7.3.2 Operation with different switching frequencies and modulators

The acoustics of railway traction drives has in recent years repeatedly been the object of study. One key element there is switching noise. A detailed acoustic analysis was conducted by Klemenz in [Kle05]. Le Besnerais models and optimizes in [Le 08] induction machines for railway traction with particular focus on PWM related noise. The automotive traction PMSMs investigated above are fairly small when compared to traction drives in trains or large industrial drives. Roughly speaking, the larger the drive, the larger the power electronics switches and the lower the switching frequency. For all results shown above, the switching frequency has been at 10 kHz. This may be perceived as distracting, but the switching noise components have little influence on the overall sound pressure or vibration level. In larger drives as in trains, switching frequencies around 2 kHz are common and these frequency components tend to dominate the acoustic emissions of the motors. Also for electric vehicle traction drives, lowering switching frequency can be advantageous in the low-speed range to reduce switching losses and thus increase the maximum current capability of the inverter.

Nießen has shown in [Nie11] that non-random switching frequency components, e.g., those from SVM can also be modeled in the direct version of the vibration synthesis process. Due to the general applicability also to random spectra, the system-simulation-based implementation is generally preferred when it comes to switching noise. Below, a run-up of machine PM-C from 0-2000 r/min is presented for three different switching frequencies schemes in figure 7.30. A snapshot of the vibration spectrum at 1100 r/min for the above switching schemes is shown in figure 7.31.

In figure 7.30a, space-vector modulation with a switching frequency of 10 kHz is used. The spectrogram is shown up to 10 kHz. The counter-rotating switching frequency components reach below 10 kHz. The acoustic spectrum is dominated by the machine inherent noise components. This differs if the switching frequency is reduced to 2 kHz (see figure 7.30b). The switching frequency related noise components strongly outweigh the machine inherent ones.

In figure 7.30c, the average switching frequency is still 2 kHz but white noise with ±300 Hz bandwidth is added. This allows to reduce the tonality and peak amplitudes. Around 4500 Hz, there lies the mode 0 eigenfrequency and the switching frequency components from the $2f_{\text{switch}}$ multiples excite this mode. Here, both lowering and increasing the switching frequency can reduce the noise. Changing the switching frequency to avoid resonances is exploited in [Le +10] where Le Besnerais et al. reduce the switching frequency in a railway-traction induction machine. This way, they avoid hitting an eigenfrequency and consequently reduce the acoustic noise level of the drive. The example here demonstrates how a drive engineer can easily conduct such investigations from within a system simulation environment based on the acoustic modeling and vibration synthesis process.

In figure 7.30d, a fixed switching frequency of 2 kHz is used up to 500 r/min. From then on, the switching frequency is synchronized to the electrical frequency. For the switching frequency, prime number multiples 43, 29, 17, and 11 of the electrical frequency are used. This type of modulation, which eventually ends in block commutation, with only one switching instant per electrical period is used when the ratio between switching frequency and fundamental frequency becomes low. Again, trains are a typical field of application.

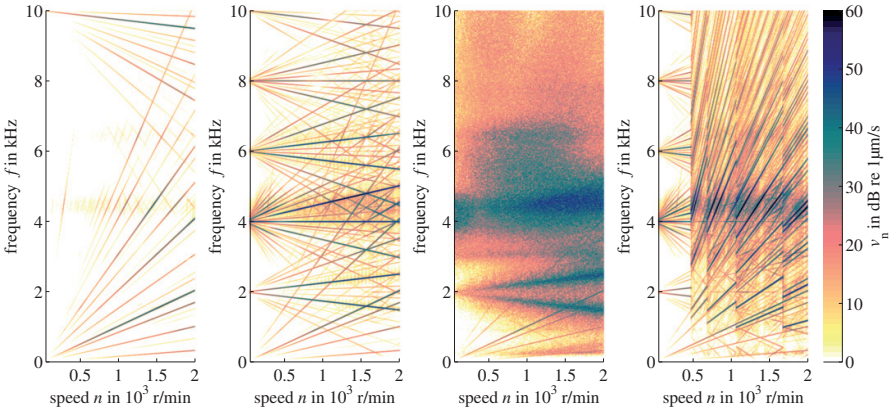

(a) $f_{\mathrm{switch}} = 10\,\mathrm{kHz}$ (b) $f_{\mathrm{switch}} = 2\,\mathrm{kHz}$ (c) $f_{\mathrm{switch}} = 2\,\mathrm{kHz} \pm 300\,\mathrm{Hz}$ white noise (d) constant $f_{\mathrm{switch}} = 2\,\mathrm{kHz}$ up to 500 r/min; then synchronous switching

Figure 7.30: Full-load run-up spectrogram up to 2000 r/min for machine PM-C with different switching schemes

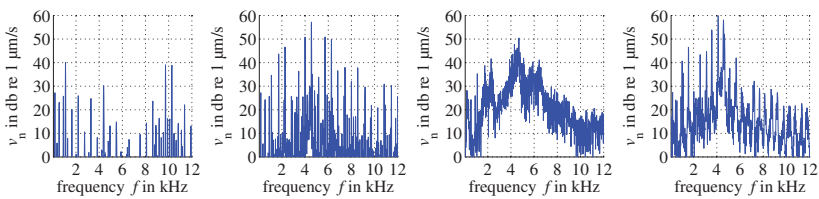

(a) $f_{\mathrm{switch}} = 10\,\mathrm{kHz}$ (b) $f_{\mathrm{switch}} = 2\,\mathrm{kHz}$ (c) $f_{\mathrm{switch}} = 2\,\mathrm{kHz} \pm 300\,\mathrm{Hz}$ white noise (d) synchronous switching

Figure 7.31: Snapshot of the vibration spectrum at 1100 r/min for the above switching schemes

7.4 Switched reluctance machine

The sections below cover acoustic modeling of standard *switched reluctance machines*. Object of this study is machine SR-X.

Background on SRM acoustics

Switched reluctance machines are generally given the positive attributes of being robust, inexpensive, high-speed capable, and efficient, in particular above base speed [VDE10]. Torque ripple resulting from simple current control strategies has been overcome with control strategies like DITC [Ind02] or PWM-DITC [Fue07]. The sometimes alleged higher converter complexity vanishes for mass-produced SRMs which allows custom power modules; the switch count for 3-phase SRMs and rotating field machines is eventually the same and the current ratings are similar to induction machines. What undoubtedly remains a challenge is acoustic noise.

Significant research effort has been put onto this topic. One early publication is [CLU92] by Cameron et al. on "The origin and reduction of acoustic noise in doubly salient variable-reluctance motors" from 1992, which is a good 40 years after Jordan's *Geräuscharme Elektromotoren - Lärmbildung und Lärmbeseitigung bei Elektromotoren* from [Jor50], a fundamental work on noise in electrical machines. Jordan's cylinder-ring models for the stator vibrations are still used in analytical models including SRMs. The general number of publications on SRMs started to rise steeply in the mid-eighties, culminating 20 years later, according to a statistic from the Brivit technical database [Fle]. When industrial research and development of automotive traction drives picked up speed roughly fifteen years ago following the success of Toyota's Prius, primary effort was spent on permanent magnet machines. Only in recent years has this trend shifted towards induction and also again to switched reluctance machines.

The acoustics behavior of SRMs continues to be a challenge. This thesis offers an acoustic modeling process which can comprehensively and effortlessly assess the acoustic characteristics of an SR drive system of any kind. It allows to judge the general suitability and rate optimization potential via control, design, and the like. With regard to traction SRMs publications on the acoustics of SRMs are scarce. The majority of research on acoustic noise of SRM has been performed in the lab on fairly small, mostly 2-pole, sometimes 4-pole, machines. Also the machine SR-X (SR-8/6) investigated below is of this type. For showing the applicability of the vibration synthesis process to SRMs, such a machine is suitable. However, that is not the case for assessing SRMs with respect to traction applications. Section 4.2.3 has discussed typical machine configurations for traction SRM and pointed out that a challenge is designing machines which combine a relatively high pole- and phase-count (see also [Fie06]). The investigations for PMSMs above have shown that with high pole count shape 0 eventually becomes the most critical yet generally controllable excitation. The same is expected for SRMs. The SR-X's 4 phases are appreciated. Its 2-pole design, however, is inevitable linked with a strong excitation of mode 2 with an eigenfrequency well in the acoustically particularly critical frequency range.

7.4.1 Simulation and measurement setup

The setup chosen for the acoustic modeling process is presented in the following.

System simulation

The structure of the system simulation model is again that from figure 3.1. Only the content of the individual blocks changes when now modeling an SRM instead of a PMSM. The single-phase inverse-magnetization model from section 3.3.2 is used as machine model. The controller uses a digital implementation of hysteresis bang-bang current control (HBCC) (see section 3.4.2). The general SRM force model from section 5.2.2 is used and configured to tooth forces.

Structural model

The structural dynamics behavior of machine SR-X has been investigated by Kasper in [Kas10] and the structural model is built based on this. Figure 7.32 shows a CAD model of the machine. Measured and simulated eigenfrequencies are listed in table 7.2. The notation for the mode shapes has been introduced in section 7.2.3. The letters a and b refer to the two orthogonal shapes which exist for each mode. Shape (1,2b) was not observed in the measurements. Measurement and simulation agree sufficiently well.

Mode	Eigenfrequency	
	measured	simulated
(0,2a)	2250 Hz	2295 Hz
(0,2b)	2370 Hz	2355 Hz
(1,2a)	2880 Hz	2863 Hz
(1,2b)	–	2907 Hz

Table 7.2: Eigenfrequencies, measured vs. simulated for machine SR-X

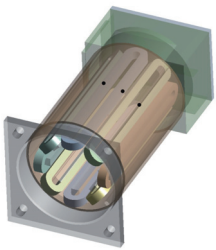

Figure 7.32: CAD model with sensor locations of machine SR-X

Figure 7.33: Measurement setup for machine SR-X

Vibration synthesis

The vibration synthesis is performed as introduced in section 6.3. The tooth decomposition of the force allows taking into account force shapes 0, 2, and 4, leading to a low complexity with regard to the force excitation.

Measurements

Measurements have been performed with 4 vibration sensors distributed around the housing of the machine in a similar manner as shown in figure 7.2. The measurement setup is shown in figure 7.33. A close look at figure 7.32 allows identifying three dots on top with 22.5° angular distance which mark sensor positions. A fourth sensor was positioned underneath the machine. The vibrations are synthesized for these sensor positions.

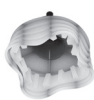

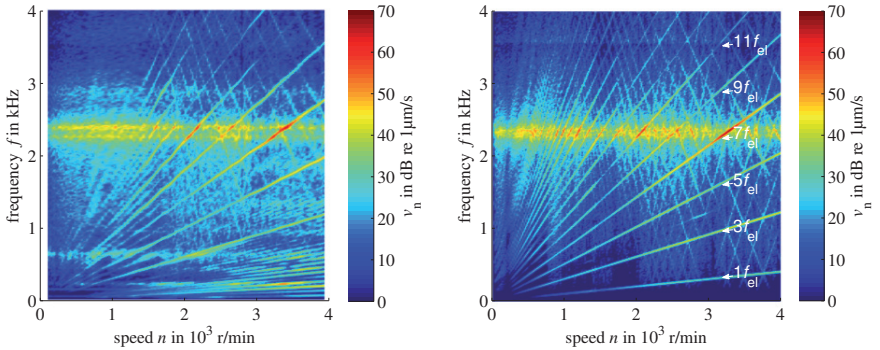

(a) Measured (b) Synthesized

Figure 7.34: Run-up spectrogram of machine SR-X. Circumferential mode 2 is excited.

7.4.2 Run-up spectrogram

Figure 7.34 presents measured and simulated spectrograms for machine SR-X for a run-up from 0-4000 r/min at 0.5 Nm of torque. The control angles for the hysteresis bang-bang controller are chosen based on the early single-pulse strategy (ESPS). We see that the spectral composition is well met for both the machine-inherent noise components as well as those resulting from the digital hysteresis bang-bang control with constant 10 kHz switching frequency. The temporal composition of the force shapes was explained in section 4.2.2. Here, only the odd multiples of the electrical frequency f_{el}, which are force shape 2 related, play a role acoustically. The shape 0 frequencies at multiples of $4f_{el}$ and the shape 4 frequencies at the remaining even multiples are virtually not found in measurements and simulations. We will get back to this in section 7.4.4. The vibration behavior is clearly dominated by the mode (0,2) vibrations around 2300 Hz. A difference between measurement and simulation is found in the frequency range below 800 Hz. First, an additional mode is excited in the measurement which is not accounted for in the simulation and second, we see additional frequency components in the measurement which are multiples of f_m. The flange has again been modeled infinitely stiff, which the test bench is not. This difference in combination with some mechanical unbalance in the real machine is expected to lead to the additional frequency components and to the excitation of what is presumably a mode 1 deflection.

Sound pressure level

Figure 7.35 compares the overall A-weighted sound pressure level. There is generally a very good agreement between simulation and measurement. Below 1500 r/min, the simulated level exceeds the measured level. We see in figure 7.34 that in this speed range high multiples of f_{el} pass the mode (0,2) eigenfrequency and that they are higher in the simulation than in the measurement. This should be further investigated. It was observed in section 5.1.2 for the PMSM force that based on the linear interpolation in the lookup tables, the high-frequency range was partially overestimated and that this could be eased by upsampling the data. The

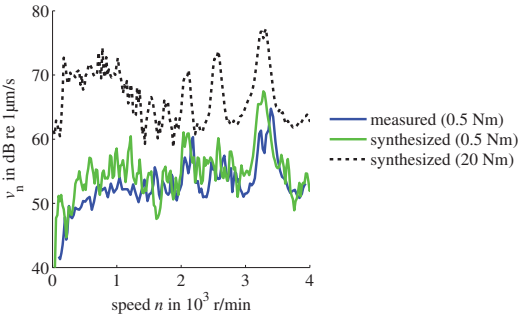

Figure 7.35: Simulated and measured vibration level during above run-up and additionally simulated full-load curve

same might be the case here. Transient effects, which are not taken into account in the static FE-based model, may also play a role.

Wu et al. have observed in [WP95] that the "largest vibrations are induced when the speed is such that an odd harmonic of the frequency of the exciting phase current coincides with the natural frequency of the stator". This can also be observed in figure 7.34 and figure 7.35. The simulated 20 Nm run-up level in figure 7.35 shows this behavior even more clearly. The three most prominent peaks are when $11 f_{\mathrm{el}}$ hits the resonance at 2090 r/min, $9 f_{\mathrm{el}}$ at 2555 r/min, and $7 f_{\mathrm{el}}$ at 3286 r/min. Furthermore, figure 7.35 shows the strong load dependence, which is generally the case for SRMs.

Auralization

The velocity signals from the vibration sensors can be auralized and the sound impression then resembles that of the near-field sound pressure, i.e., as if holding ones ear close to the machine. For machine SR-X, the similarity of simulated and measured sound is remarkable.

7.4.3 Operational deflections

The investigation of the operational deflection focuses on the vibration characteristics near the mode (0,2) vibrations around 2300 Hz. When a multiple of f_{el} passes either mode (0,2a) at 2295 Hz or mode (0,2b) at 2355 Hz, the resulting deflection is dominated by this mode. This is shown for mode (0,2a) in figure 7.36 and for mode (0,2b) in figure 7.37. The result is a stationary deflection dominated by one mode shape. This has been confirmed in [Kas10] by laser-vibrometer measurements. Below and above the eigenfrequency range, the two modes combine and form a rotating deflection shape as seen in figure 7.38.

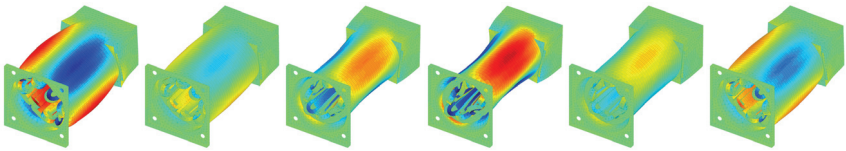

(a) 0° (b) 60° (c) 120° (d) 180° (e) 240° (f) 300°

Figure 7.36: Mode (0,2a) at resonance for $7f_{\mathrm{el}}$ at 2295 Hz and 3197 r/min

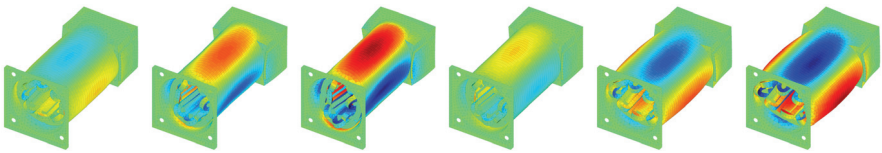

(a) 0° (b) 60° (c) 120° (d) 180° (e) 300° (f) 240°

Figure 7.37: Mode (0,2b) at resonance for $7f_{\mathrm{el}}$ at 2356 Hz and 3277 r/min

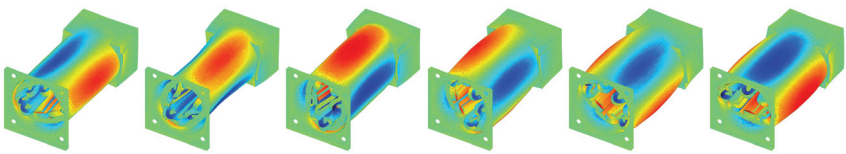

(a) 0° (b) 60° (c) 120° (d) 180° (e) 240° (f) 300°

Figure 7.38: Mode (0,2a) and (0,2b) combined form a rotating deflection above and below the resonance, here for $7f_{\mathrm{el}}$ at 2527 Hz and 3518 r/min

7.4.4 Reduced modal base and force excitation

The simulated run-up spectrogram in figure 7.34b is based on the default synthesis process taking into account all available forces on the excitation side and all modes on the structural side. These are the force shapes 0, 2, and 4 (i.e., 12 excitations) and 98 modes (in the frequency range up 8390 Hz which is already a fairly low number compared to the PMSM drives above). While generally only a limited number of force shapes and modes dominates the overall vibration response, the SR-X is a rather extreme example in this regard.

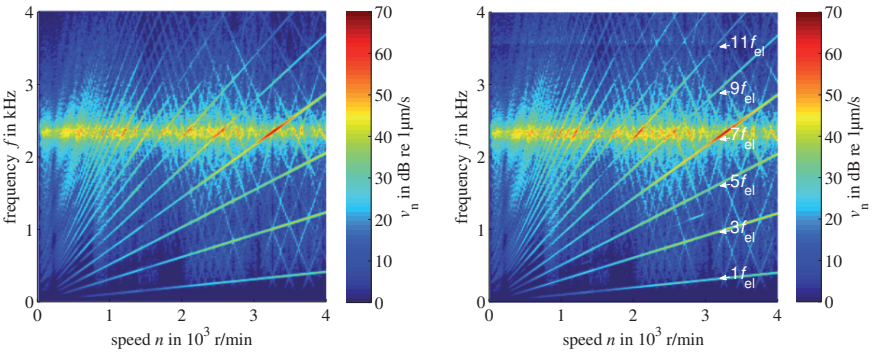

(a) Synthesis reduced to 2 force excitations and 2 modes

(b) Full synthesis

Figure 7.39: Showing the low vibrational complexity of machine SR-X

In section 7.2.3, reducing the number of force excitation shapes in the analysis has already been discussed. Here, the excitation is now reduced to two force shapes (shape 2 radial, leaving the cosine/sine or positive/negative sequence excitation). In addition, the structural response is reduced to two modes (the two mode 2 eigenshapes near 2300 Hz). The reduced synthesis result in figure 7.39a is hardly distinguishable from the full synthesis results from figure 7.39b (which is a reprint of figure 7.34b). The responses do not differ more than 1 or 2 dB.

The above comparison is drawn for the sensor positions on the circumference of the housing. For the vibrations of the clamping box, for example, additional modes should be taken into account. Nevertheless, the vibrational complexity of this drive is very low. It is a suitable drive for analytical models. It does not make use of the full potential of the vibration synthesis process. The low vibrational complexity is the reason why further studies were not performed on this drive and why, for example, the simulated 20 Nm run-up level is not accompanied by a measured counterpart in figure 7.35. Instead, the outer rotor machine SR-Y was investigated including various phase faults. This analysis follows in the next section.

7.5 Outer rotor switched reluctance machine

This section applies the vibration synthesis process to the outer rotor switched reluctance machine SR-Y (SR-20/16or). In [Hen11] and [HBD12], particular focus is on analyzing the redundancy of the machine and demonstrating its operational capabilities under fault conditions. Here, the acoustic characteristics under fault conditions are modeled. This section covers the modeling aspects *switched reluctance machines*, *outer rotor machines*, and *unbalanced excitation*.

7.5.1 Increased fault tolerance due to distributed inverter

Machine SR-Y is a 5-phase machine with 20 stator teeth and 16 rotor teeth in an outer rotor configuration. Each stator tooth carries a coil which is fed by its own dedicated inverter called pole module. A picture of machine and inverter was given in figure 5.9. Four coils with 90° angular displacement between two coils form one phase. As a consequence of the 4-pole configuration, the fundamental force shape ν_{base} is 4 (see section 4.2.2 where the spatial and temporal force composition for SRMs is derived). During normal operation, force shape 4 and force shape 0 are the acoustically most dominant force excitation shapes. Force shapes 1, 2, and 3 are the most important additional force shapes arising in case of phase faults.

The distributed inverter increases the redundancy of the machine. Most switched reluctance machines and also machine SR-Y carry a short-pitched winding[(iv)]. The asymmetric half-bridge is the most common inverter topology for SRMs [DPV11]. With short pitch and asymmetric half-bridge, the individual phases of an SRM are magnetically and electrically uncoupled. An SRM is therefore inherently fault tolerant. If one phase fails, the remaining phases are not influenced and can keep operating. About $1/N_{\text{phase}}$ of maximum average torque is lost. Below maximum torque and power, the remaining phases can partially compensate also the loss in instantaneous torque in machines with a phase number of 4 and higher by adjusting the conduction time. The distributed inverter of machine SR-Y now takes this redundancy a step further as also the individual coils of a phase are electrically uncoupled. In terms of torque production, loss of one phase module leads to loss of only $1/N_{\text{s}} = 1/20$ of maximum torque. However, if a single module fails, the magnetic excitation becomes unbalanced and the phases are no longer magnetically uncoupled. This requires the reluctance network approach from section 3.3.2.2 for efficient modeling. From an operational perspective, a drawback of a single pole module fault is that also the force excitation becomes unbalanced. Unbalanced forces strongly reduce the bearing lifetime and are also an acoustic issue. The latter is of interest here and makes machine SR-Y a welcome study case for acoustic modeling.

7.5.2 Simulation and measurement setup

For simulations and measurements of machine SR-Y, the following setup is used.

System simulations

The run-ups are performed from 0-600 r/min with 200 Nm of torque. The PWM frequency is 4900 Hz. The machine is controlled with PWM-DITC as introduced in section 3.4.2. The

[(iv)] For PMSMs, the term concentrated winding is used instead of short-pitched. A distributed winding is called fully-pitched [Mec93].

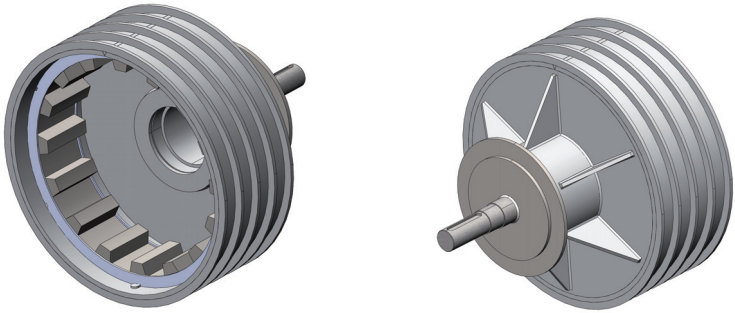

(a) front (b) back

Figure 7.40: CAD model of the rotor of machine SR-Y as used in the structural FE simulations

reluctance network from section 3.3.2.2 is integrated into the system simulation. In an outer rotor machine, the rotor is the main vibrating body so that determination of the forces on the rotor is required. Here, rotor tooth forces are determined from the stator tooth forces as described in section 5.3.3 since the reluctance network does currently not model the rotor forces explicitly. The spatial decomposition of the rotor forces is performed using the coupling matrix from section 5.2.1. The tonal spectrum of stator and rotor forces differs due to the different number of teeth. An analytical example for the frequency composition of machine SR-Y was given in section 5.3.4.

Structural model

Figure 7.40 shows the CAD model of the rotor which was used in the structural simulations. Table 7.3 lists the values for measured, simulated, and analytical eigenfrequencies of the rotor. The analytical eigenfrequencies are obtained based on [Jor50]. Due to the large diameter of the machine, the eigenfrequencies are comparatively low. As a consequence, the related electromagnetic noise also occurs at relatively low frequencies. Measurements and simulations are therefore only evaluated up to 3 kHz which covers all relevant effects and allows a good view on the frequency range below 1 kHz. This frequency range sees most changes when machine operation under fault conditions is investigated. The low frequency range is also the reason why using aggregated tooth forces rather than spatially distributed tsine forces is not a restriction.

Measurements

The measurements were obtained in a bachelor thesis by Wegmann [Weg10] by placing 4 accelerometers on the outside of the rotor with a distribution as in figure 7.2. Measured and synthesized vibrations are the RMS value of these 4 points.

Nomenclature

Simulated and measured run-up spectrograms under various fault conditions are investigated below. All faults or deactivated pole modules are in the same phase. All faults are open circuit faults. A deactivated pole module is identical with an open circuit fault. For identifying the

Mode	Eigenfrequency		
	measured	simulated	analytical
1	43 Hz	46 Hz	–
2	215 Hz	247 Hz	242 Hz
3	625 Hz	625 Hz	686 Hz
4	1077 Hz	1133 Hz	1320 Hz
5	1631 Hz	1700 Hz	2130 Hz
0	2412 Hz	2235 Hz	3190 Hz

Table 7.3: Eigenfrequencies, measured, simulated, and analytical for machine SR-Y

different operation cases, the following nomenclature from [Hen11] is used. A '1' signifies a functional pole module, a '0' a deactivated module or one with an open phase fault. The normal operation is therefore labeled (1111) since all 4 pole modules operate properly. One faulty module is (0111), two faulty and facing modules are (0101), and a deactivated phase is (0000).

7.5.2.1 The laminated rotor and modification of the modal base

In the following, transversal modes will be dealt with which occur in the simulations but not in the measurements.

We have seen for machine PM-A in the spectrogram in figure 7.7 in section 7.1.5 that in the higher frequency range between 4.5 kHz and 6 kHz modes appeared in the simulated spectrogram which were not found in the measurement. Likewise, transversal modes were excited for the skewed machine PM-D in section 7.2.2 and the skewed machine PM-C in section 7.2.5. This excitation of additional vibration shapes was generally plausible but the strength of the response was unexpected. For machine PM-D and machine PM-C, no comparative measurements were available but it was assumed that such vibrations would not show equally in measurements. The issue of transversal mode issue is now further analyzed.

The rotor laminations in machine SR-Y are not bonded. They are only kept from moving along the axial direction by welded rings on front and back and from rotation by a groove (see figure 7.40a). This leads to a vibration behavior which apparently differs strongly from homogeneous solids or bonded stacks. The latter are reported to have transverse isotropic material parameters but to be treatable as solids [LZH01; Kas10; vGie11].

Wang et al. investigate in [WW97] the effects of clamped laminations on the vibrational behavior of electrical machine stators experimentally. They compare the measured vibration shapes of a laminated stator stack to the analytically determined eigenshapes of a solid cylinder. A solid cylinder has in-plane modes (only 2-D) and transverse vibrational modes (3-D vibrations). For the laminated stack, they find that "as the number of laminations or the clamping pressure increases, the transverse vibrational modes start to disappear, but the in-plane vibrational modes are unaffected and finally the in-plane modes are the only modes that persist." This was observed for the laminated stator of a 4-pole, 550 V, 93 kW inner-rotor induction motor with an outside radius of 190 mm, which was composed of over 1000 stator laminations.

The stator assembly in [WW97] has free/free boundary conditions. The rotor of machine

SR-Y can be seen as free/clamped; free on the open side and clamped on the closed side. Thus, pure in-plane modes are not expected for machine SR-Y but those with a node on the flange side and a maximum on the open side. Apart from this, the same effect as in [WW97] is observed for the outer rotor machine SR-Y. In the structural FE simulations used here, the rotor was modeled as a solid. For vibrations with shape 0 and shape 4 in the circumferential direction additional transversal modes were found. In a (brief) analysis, no choice of material parameters could be identified with which these transversal modes would not exist or would not be exited. Regardless of whether the rotor stack was modeled as homogeneous material or with transverse isotropy as experimentally determined for bonded stacks in [Kas10; vGie11], transverse vibrational model were excited in the simulations. These modes, however, do not exist in the measurements. Machine SR-Y shows the same behavior as observed in [WW97]. As a pragmatic solution, the respective eigenshapes are removed from the modal base. While for modes 4, the identification of the alleged artifact modes was clear (see figure 7.41), the result for mode 0 was ambiguous. The mode at 2336 Hz (figure 7.42b) was removed (despite being closer to the measured eigenfrequency) and the mode at 2235 Hz (figure 7.42a) was kept[(v)]. Further tests in order to clarify this question could not be conducted on the machine. Figure 7.43 and figure 7.44 show the respective modes from a simple cylinder model for comparison. The issue of additional transversal modes adds to the points which are worthwhile investigating with respect to numerical structural modeling of electrical machines. After all, Garvey's conclusion from 1989 [Gar89] is still current in which he writes that "those who would attempt to make a full numerical examination of an electrical machine design with regard to vibration ought have data available to represent the laminated components".

[(v)] While the circumference shows a mode 6ish deflection, the overall deflection is a breathing mode zero. This mode 6 character shows less for the operational deflection in figure 7.48 below, which are dominated by this mode.

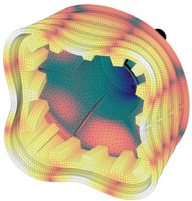

(a) in plane, 1133 Hz

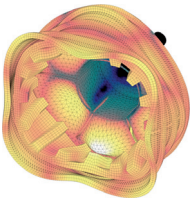

(b) transversal, 1610 Hz

Figure 7.41: Circumferential order 4 eigenshapes for machine SR-Y

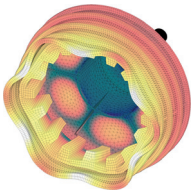

(a) (quasi) in plane, 2235 Hz

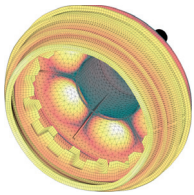

(b) transversal, 2336 Hz

Figure 7.42: Circumferential order 0 eigenshapes for machine SR-Y

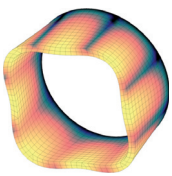

(a) (quasi) in plane

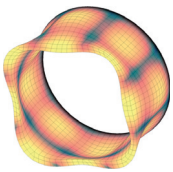

(b) transversal

Figure 7.43: Circumferential order 4 eigenshapes for solid cylinder

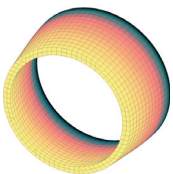

(a) (quasi) in plane

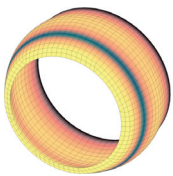

(b) transversal

Figure 7.44: Circumferential order 0 eigenshapes for solid cylinder

7.5.3 Normal operation (1111)

First, machine SR-Y is considered under normal operating conditions.

What the measurement shows

Under normal operating conditions, the acoustic noise spectrum of machine SR-Y is the one that is inherently linked with its stator/rotor configuration. The measured spectrogram in figure 7.45a confirms that during normal operation two main eigenfrequencies are excited, mode 4 at 1077 Hz and mode 0 at 2412 Hz. Where the respective equipment is available, the deflection shapes can also be measured. Here, the mode shape identification is made plausible by comparison to calculated eigenfrequencies as well as by the frequency composition. In section 5.3.4, we have seen that the rotor tooth forces of machine SR-Y have a shape 0 excitation at multiples of $4f_r$ as well as a shape 4 excitation at all odd and a shape 8 excitation at all remaining multiples of f_r. The resonance at 1077 Hz in figure 7.45a shows clearly the frequency composition of shape 4 with readily visible peaks in the frequency multiples 7, 9, 11, and $13f_r$. At 2412 Hz a closer look is required, but the respective frequency components at 12, 16, 20, $\ldots \times f_r$ can also be identified.

At 215 Hz and 625 Hz and very subtle at 1631 Hz additional resonances occur. They are mode 2, 3 and 5 related and result from some amount of structural and/or mechanical unbalance in the machine. The rotor bell is only mounted on one side and tends to bend down a little so that – with respect to the rotor – some degree of dynamic eccentricity is always present.

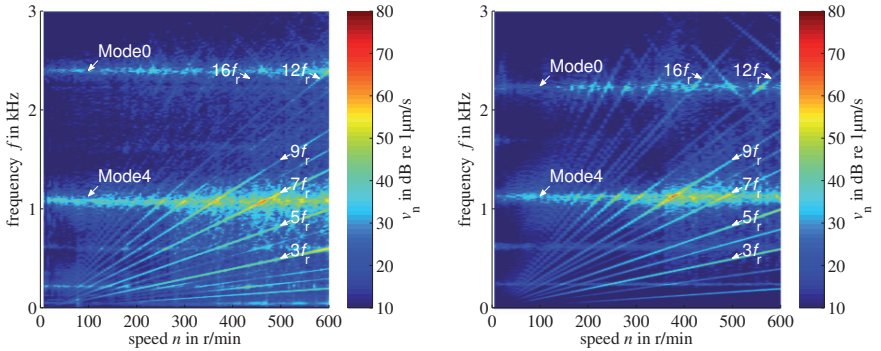

(a) Measured (b) Synthesized

Figure 7.45: Run-up spectrogram of machine SR-Y under normal operation (1111). Circumferential modes 4 and 0 are excited.

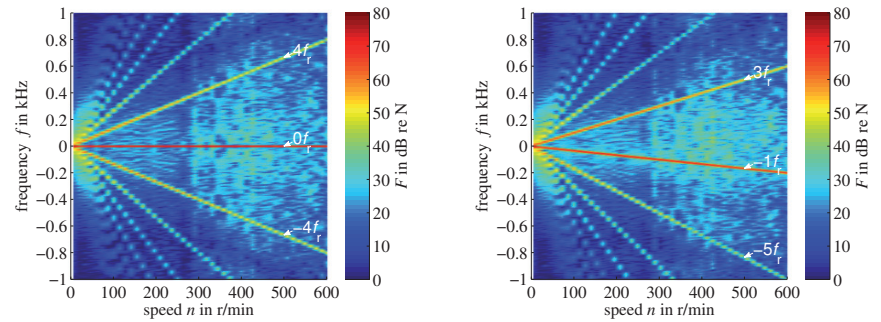

(a) Force shape 0 radial (b) Force shape 4 radial

Figure 7.46: Two-sided force spectrograms of shape 0 and 4

In general, rotation alters the dynamics of a system and influences the eigenfrequencies [ANS09]. However, it can be seen that for speeds up to 600 r/min, there is no relevant influence; the eigenfrequencies do not change with speed. No effort is made here to include rotation in the simulation.

How the simulation compares to it

Figure 7.45b shows the simulated run-up spectrograms. The frequency composition of the acoustic noise is well matched. This signifies that the force excitation is determined correctly. The two main resonances also appear clearly in the simulated spectrogram. This indicates the validity of the structural model after the modification discussed above. That the amplitudes agree well indicates quantitative agreement of force excitation amplitudes and structural

response.

The measurement shows naturally more (spread spectrum) noise than the simulation. At around 300 r/min the machine reaches the voltage limits. There, in both simulation and measurement, the broadband noise between 0 Hz and the mode 4 resonance increases. The overall level of this noise is higher in the measurements. Some Gaussian noise was added in the simulations to the current signals that are fed back to the controller. This is on the one hand generally physically correct because sensors are always subject to noise. On the other hand, this is a qualitative rather than a quantitative issue. The main noise components are not altered but the parasitic modes 1, 2, 3, and 5 are excited. The measurement signal noise is a source of electromagnetic unbalance with the same effect as structural unbalance that the rotor is subject to in the real machine. As such, this signal noise is also a graphical improvement because it eases interpretation of the spectrograms. Without this noise, only the mode 2 resonance, which in the measurement is found at 215 Hz between 0 r/min and 150 r/min, is found in the simulation besides mode 4 and 0. At last, also the switching frequency components running downwards from their 4900 Hz start point at 0 r/min appear similarly in measurement and simulation. Overall, these first results are very satisfactory.

Up to 2000 Hz, the spectrogram of machine SR-Y resembles that of machine SR-X up to 4000 Hz with here mode 4 taking the role of mode 2 and halved frequency – despite the higher spatial order – due to the significantly larger dimensions. However, for machine SR-X, the mode 0 eigenfrequency is further distant from the mode 2 resonance than mode 0 is from mode 4 here.

Force spectrograms

Two-sided force spectrograms of force shape 0 and 4 are presented in figure 7.46. It is confirmed that the shape 0 frequencies are at multiples of $4f_{\mathrm{el}}$ so that it is plausible that these (cf. 12 and 16 f_{m} in figure 7.45) peak around 2235 Hz when passing the mode 0 eigenfrequency. Likewise, it can be seen that the odd shape 4 related frequency components peak when passing the mode 4 eigenfrequency around 1100 Hz (cf. 3, 5, 7, and 9 f_{m} in figure 7.45).

Operational deflections

The operational deflections at the mode 4 and mode 0 eigenfrequencies show the expected shape. For the mode 4 resonance at 1128 Hz, the deflection shape is a rotating shape 4 at $9f_{\mathrm{m}}$ (376 r/min, 200 Nm) in figure 7.47. For the mode 0 resonance at 2240 Hz, $12f_{\mathrm{m}}$ causes the expected breathing mode 0 deflection (558 r/min, 200 Nm) in figure 7.48. As indicated above, the mode 6 deformation around the circumference is less pronounced for the operational deflection than it is for the sole eigenshape in figure 7.42a.

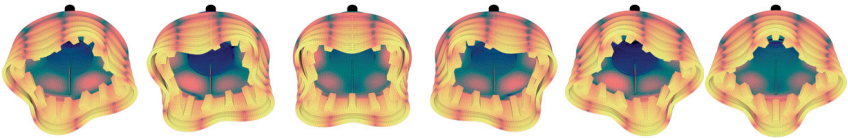

(a) 30° (b) 90° (c) 150° (d) 210° (e) 270° (f) 330°

Figure 7.47: Operational deflection of machine SR-Y in rotating mode shape 4 for $9f_{\mathrm{m}}$ at 1128 Hz (376 r/min, 200 Nm)

(a) 30° (b) 90° (c) 150° (d) 210° (e) 270° (f) 330°

Figure 7.48: Operational deflection of machine SR-Y as mode shape 0 for $12f_{\mathrm{m}}$ at 2240 Hz (558 r/min, 200 Nm)

7.5.4 Operation with module faults

In the following, operating under various fault conditions is investigated.

7.5.4.1 Operation with one faulty phase module (0111)

The first fault analyzed is operation with an open circuit fault in one pole module (0111).

Time domain analysis of force and torque

In one of the five phases, only 3 of 4 modules are active. Under normal conditions, the 4 modules of a phase receive the same PWM signals and build up the same flux linkage. In two facing modules the flux path points from stator to rotor and in the other two from rotor to stator. The sum of the fluxes is zero and the phases are consequently decoupled from each other (the yoke is designed not to saturate). If now one module fails, the flux sum over the pole modules of the faulty phase is no longer zero. Flux spreads over the remaining teeth and less flux passes through the stator tooth with the faulty pole module. Less flux means less force and a lower force at one point is equivalent to an unbalanced force excitation. Figure 7.49a shows a snapshot of the tooth force on the rotor in case of no-fault operation. If one phase is active, 4 forces pull simultaneously. When one module fails, its force disappears as can be seen in figure 7.49b. In figure 7.50a, the rotor force is shown over rotor position. At 72°el, only 3 rotor teeth see a force. The rotor tooth passing the faulty pole module experiences almost no radial force. The spatial force spectrum now contains a significant amount of all force shapes. The multiphase torque sharing algorithm within PWM-DITC, however, automatically compensates for the loss of one pole-module so that the torque remains fairly constant (see figure 7.50b).

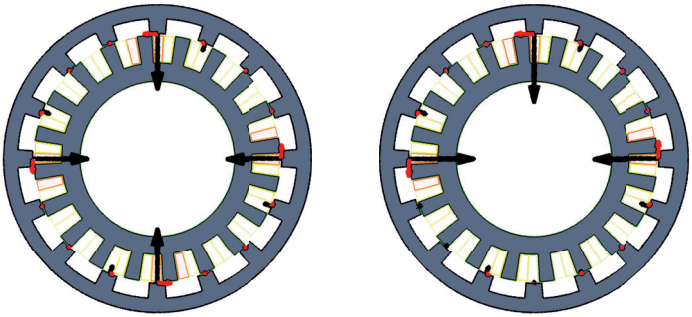

(a) no fault (1111) (b) one faulty phase module (0111)

Figure 7.49: Snapshot of tooth forces on the rotor of the outer rotor SRM [Hen11]

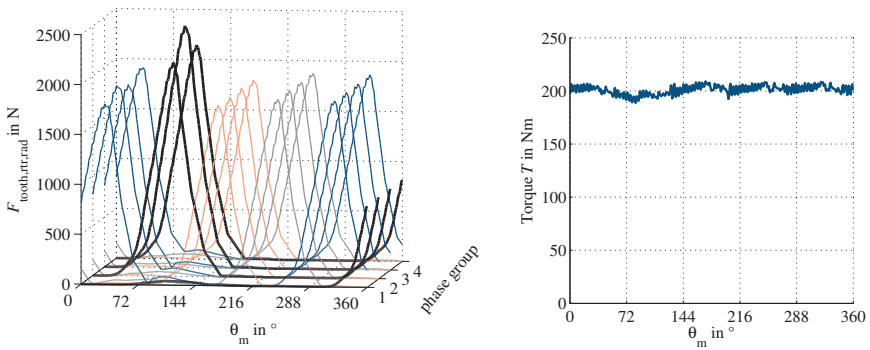

(a) Force (b) Torque

Figure 7.50: Torque and radial force over one electrical period in case of one faulty phase (0111)

Vibration spectrograms

The spectral composition of the vibrations can be seen in figure 7.51. It is clearly visible in figure 7.51a and figure 7.51b that modes 1, 2, 3 and 5 are now excited. In particular for modes 2 and 3, the vibration response is strong. Especially in the base speed range, the vibration response exceeds that of shape 4, the normally strongest resonance. The mode 1 eigenfrequency at 46 Hz is strongly attenuated in the plots due to the A-weighting. Without A-weighting it would have the highest amplitude. At least for a prolonged period of time, these operating conditions with unbalanced excitation are not desired.

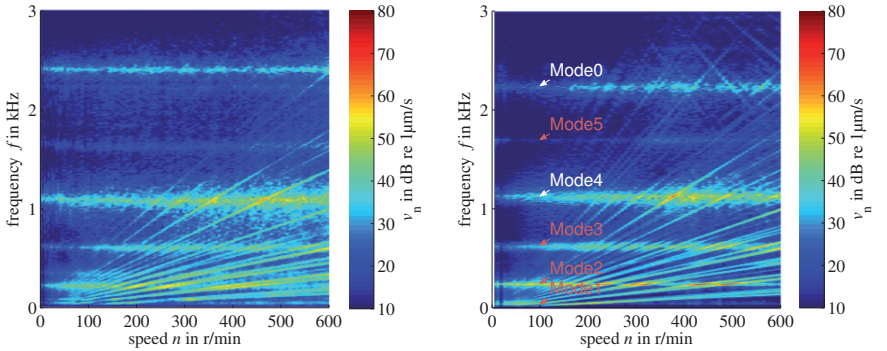

(a) Measured (b) Synthesized

Figure 7.51: Run-up spectrogram of machine SR-Y operating with one faulty module (0111). All circumferential modes (1, 2, 3, ...) are now excited.

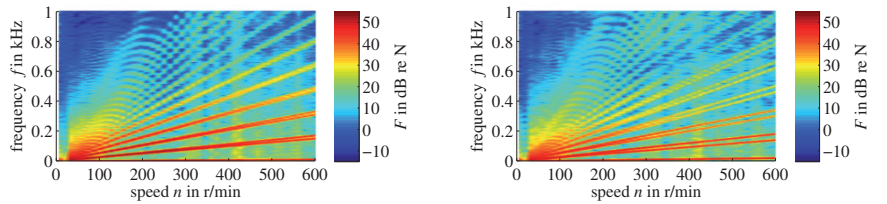

(a) Force shape 1 radial (b) Force shape 2 radial

Figure 7.52: One-sided force spectrograms for force shapes 1 and 2 in case of one faulty pole module (0111)

Force spectrograms

One-sided force spectrograms for force shape 1 and 2 are presented in figure 7.52a and figure 7.52b. It has been mentioned in section 4.2.4 that in terms of the arising force shapes and frequency components, the magnetic unbalance investigated for machine SR-Y is equivalent to dynamic eccentricity. The force spectrograms confirm this. In the stator domain, force shape 1 and 2 contain all multiples of $N_r f_m = 16 f_m$. In the rotor domain, these frequencies are shifted by $\pm\nu f_m$. For the stator force, fault (0111) is equivalent to a static eccentricity.

For normal operation (1111), spectrograms for force shape 0 and 4 have been shown in section 7.5.3. In case of fault (0111), the spectrograms contain all multiples of $N_r f_m = 16 f_m$. The strongest ones, however, are still those from figure 7.46, so that the vibration response to force shapes 0 and 4 hardly changes.

Operational deflections

Figure 7.47 and figure 7.48 have visualized the operational deflections where a mechanical multiple passes the eigenfrequency of mode 4 or 0, respectively. These deflection shapes are now supplemented by the operational deflection shapes at three further operating points. These are $1f_\mathrm{r}$ passing the mode 1 eigenfrequency at 59 Hz (202 r/min, 200 Nm) in figure 7.53, $2f_\mathrm{r}$ passing the mode 2 eigenfrequency at 242 Hz (425 r/min, 200 Nm) in figure 7.54, and $5f_\mathrm{r}$ passing the mode 3 eigenfrequency at 623 Hz (488 r/min, 200 Nm) in figure 7.55.

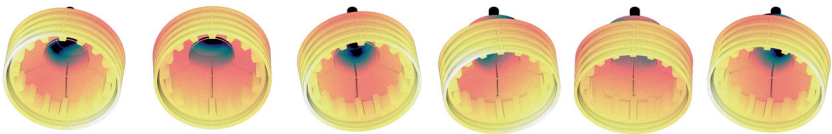

(a) 30° (b) 90° (c) 150° (d) 210° (e) 270° (f) 330°

Figure 7.53: Operational deflection of machine SR-Y in rotating mode shape 1 for $1f_\mathrm{r}$ at 59 Hz (202 r/min, 200 Nm)

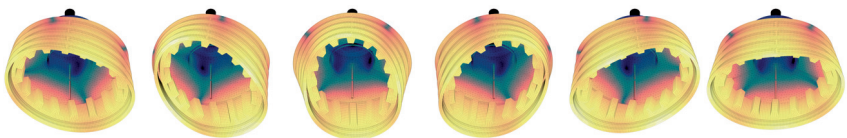

(a) 30° (b) 90° (c) 150° (d) 210° (e) 270° (f) 330°

Figure 7.54: Operational deflection of machine SR-Y in rotating mode shape 2 for $2f_\mathrm{r}$ at 242 Hz (425 r/min, 200 Nm)

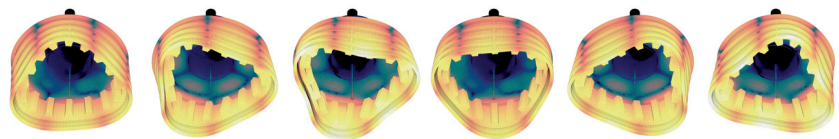

(a) 30° (b) 90° (c) 150° (d) 210° (e) 270° (f) 330°

Figure 7.55: Operational deflection of machine SR-Y in rotating mode shape 3 for $5f_\mathrm{r}$ at 623 Hz (488 r/min, 200 Nm)

Influence of the individual force shapes

How the individual force shapes contribute to the vibration spectrogram in case of a single module fault (0111) is demonstrated with help of figure 7.56.

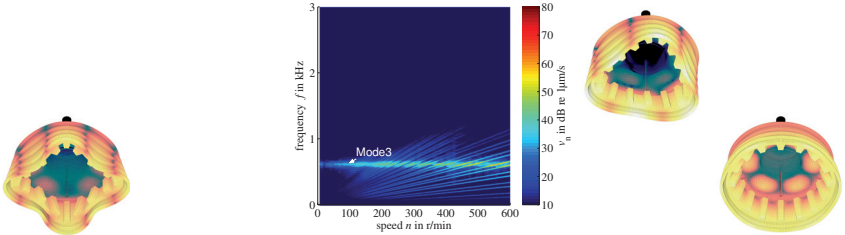

(a) Force shape 3

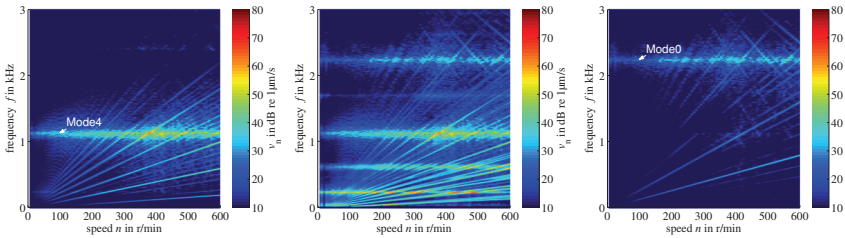

(b) Force shape 4 (c) All force shapes combined (d) Force shape 0

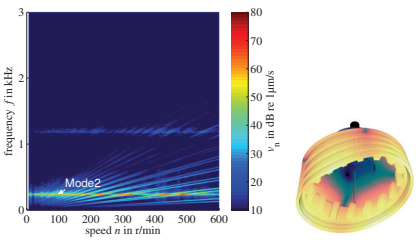

(e) Force shape 2

Figure 7.56: Contribution of the individual force shapes to the vibration spectrogram in case of fault (0111)

In the middle, the complete synthesized run-up spectrogram with all force shapes (from 0 by 1 to 8) from figure 7.51b is shown. It is surrounded by the 4 spectrograms which take into account only one force shape each. Their combination accounts for the largest part of the vibration in case of the single module fault. Stills from the operational deflection near the respective resonance are placed adjacent to the corresponding spectrograms. To the left and to the right from the center figure, there are the spectrograms of shapes 4 and 0 which make up most of the vibration response under normal operation (see figure 7.46b). Above

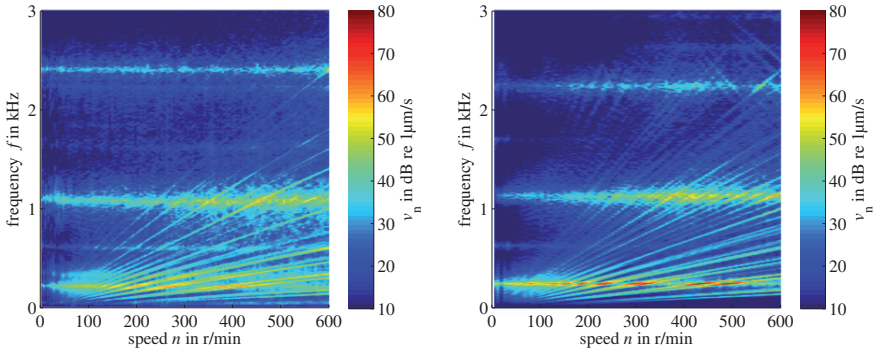

(a) Measured (b) Synthesized

Figure 7.57: Run-up spectrogram of machine SR-Y when two facing pole modules are inactive (0101)

and below, the vibration spectrograms for shapes 3 and 2 are placed. Figures for mode 1, important in the very low-frequency range, and mode 5 are left out.

7.5.4.2 Operation with two facing pole modules inactive (0101)

Operation with one open-circuit pole module (0111) lead to an unbalanced force excitation. The vibration contained all force shapes (ν=0, 1, 2, ...). Hennen has derived in [Hen11] that it is generally possible to compensate the loss of one pole module via torque and force sharing from the 19 remaining modules. However, he has also pointed out that implementation on the current hardware is not feasible. The simplest and most pragmatic solution for regaining a balanced force excitation is turning off the pole module opposite to the faulty module (0101). The excitation then becomes balanced again. This is depicted in figure 7.57. The fundamental force shape is now ν=2 so that strong mode 2 vibrations still occur. Their amplitudes are higher in the simulation (figure 7.57b) than they are in the measurements (figure 7.57a). Besides that, simulation and measurement show good agreement.

7.5.4.3 Operation with one deactivated phase (0000)

The mode 2 vibration is only prevented if the entire phase is deactivated (0000). The complete loss of a phase would be the general case if the inverter was not distributed. Here, the tradeoff is between either further loss of torque and partly increased torque ripple (0000) or a significant deterioration of the acoustic behavior (0111, 0101). The spatial spectrum of the force excitation under operation with one deactivated phase (0000) is equal to that under normal operation (1111) with shape 4 as fundamental spatial order. The difference, however, lies in the temporal composition of the force excitation. The frequency spectrum is now more dense with $^1/_{N_{\mathrm{phase}}} f_{\mathrm{r}}$ instead of f_{r} as fundamental frequency component which is shown in figure 7.58.

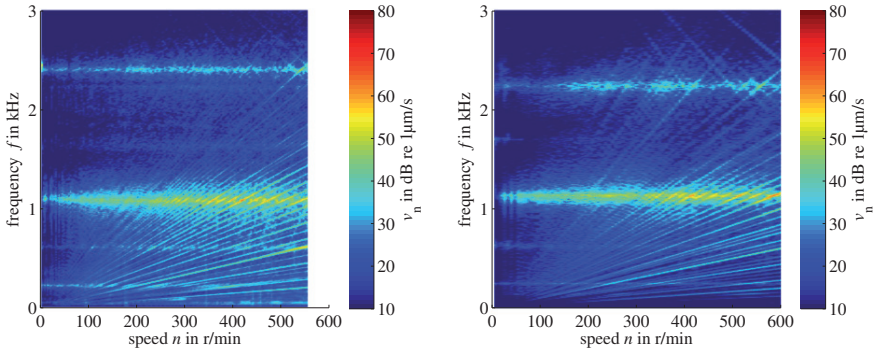

(a) Measured

(b) Synthesized

Figure 7.58: Run-up spectrogram of machine SR-Y with one phase entirely deactivated (0000)

7.5.5 Summary on the vibration synthesis for an outer rotor SRM

Above, vibration results for the outer rotor switched reluctance machine SR-Y have been presented and validated under normal operation and various fault conditions. The examples given confirm that the vibration synthesis process can readily cope with outer rotor machines. It was furthermore shown that unbalanced excitation, as it also occurs in case of eccentricity, can be taken into account. It can be concluded that the vibration synthesis process is suitable for non-conventional machine designs and special operation conditions.

8 Summary and conclusions

A comprehensive acoustic modeling process for electrical drives has been presented in this thesis.

Vibration synthesis for arbitrary machines based on force response superposition

At the core of this thesis is the vibration synthesis process. This process is readily applicable to any machine type and configuration. The methodology proposed in this thesis is based on the observation that from the spatially distributed force in the air-gap of an electrical machine, only a limited number of force shapes contributes noticeably to acoustic noise. Due to the linear nature of the machine vibrations for small excitations, normalized responses are determined which are later scaled and superposed. Benefits of this approach are that it decouples the force excitation and vibration response, that it is computationally efficient, and that it gives insight into the vibrations characteristics by showing how the individual parts of the force excitation influence the acoustic characteristics. Detailed structural FE models can be used while keeping the overall computational effort low. The structural vibration responses to the force excitations are furthermore determined offline and independently from the operating point dependent force excitation. This independence of structural response determination and force excitation facilitates application in practice where these modeling steps are often performed by different people. The computational efficiency allows to model the force excitation with a high degree of detail. By using modal superposition harmonic analyses in the structural simulations, additional force shapes come at a very low cost. Tangential forces, often left out in acoustic investigations altogether, are routinely taken into account. Skewed machines, where the number of force excitations grows proportional to the number of skew segments, are no challenge.

System simulation based acoustic modeling

The vibration synthesis process is computationally efficient and provides excellent results. However, it would only be of limited use if it were not readily applicable in practice, for example, for designers of machines, drive systems, and control algorithms. For this reason, the acoustic modeling process is integrated into a system simulation for electrical drives. Changes on any level can be accounted for in the acoustic model immediately. Converter, control, and switching harmonics influences show directly in the acoustic noise signature. Force models for use in system simulations have been developed for PMSMs including skewed PMSMs and SRMs. Based on the time waveforms of the machine currents and the rotor position, the force shapes are determined as functions of time. These shapes are used to scale and superpose the force responses within the vibration synthesis. The time-domain nature of the noise and vibration signals allows for direct auralization. Electromagnetic FE simulations provide the parameters for the force models. They are a second offline and operation point independent simulation step. Together with the force responses from structural simulations, these two form the offline basis of the acoustic modeling process.

Permanent magnet machine model with spatial harmonics

The force excitation depends on the currents in the machine. Realistic machine models are therefore required in the system simulation. An ideal rotating transformer (IRTF) based PMSM machine model with spatial harmonics has been developed for this purpose. IRTF models have generally a lean and physically based structure. The inverse magnetization nature further omits any derivatives in the model, adding to its numerical stability. For a spatial harmonics PMSM model based on numerical data, the model's individual treatment of the spatial harmonics is a unique feature. Model parameters in the lookup tables are not given an additional rotor position dimension. The rotor position dependence, i.e., the spatial harmonics, are instead represented as Fourier series coefficients. This reduces the overall model size and omits 3-D tables as well as the respective lookup operations. The Fourier series approach further allows to investigate the effect of individual spatial harmonics. The model is applicable as a general PMSM machine model in system simulations. The influence of spatial harmonics is, for example, also of interest for control or torque ripple related investigations.

Air-gap force decomposition

The interface between electromagnetic excitation and structural response is the air-gap force. Three different options for the decomposition of the air-gap force are presented. The straightforward approach is decomposing the force along a circle in the air-gap in the machine. This is not directly compatible with structural models with slotted stators. The force shapes are continuous along the air-gap while the stator is discontinuous due to slotting. A simple solution is working with tooth forces. From the air-gap force, the mean over a stator tooth is formed and the subsequent decomposition is then based on these tooth forces. Constant forces along the surface of a stator tooth are correspondingly applied in the structural model. This approach is particularly simple. Forming the mean of the force, however, inevitably leads to spatial aliasing. Despite this limitation, the tooth force concepts delivers satisfactory results in many practical cases. The limitations of the above two approaches are overcome if the stator tooth surface without the slot region is chosen as the domain for force decomposition. The resulting spatial Fourier series for the air-gap force then converges against the original force and the individual force shapes can be applied in the structural model. The functional relationship between the different force representations has been analyzed showing that a particularly good approximation of the original air-gap force is realized with the latter approach.

Skewed permanent magnet machines

The investigations on the acoustics of PMSMs in this work was mainly triggered through demand from the automotive industry. In recent years, predominantly PMSMs have been applied as traction drives for hybrid electric and electric vehicles. For PMSMs, skew is a common means for reducing force and torque ripple. Against this background skewed PMSMs are investigated quite prominently within this work. The skew effect and its limitations are described and analyzed analytically. Transfer functions for the effect of continuous and discrete skew are derived and analyzed in comparison with FE simulations. Skewed PMSMs have been integrated into system simulation force models and vibration synthesis. Within the application study, different skew arrangements are investigated.

Application examples for PMSMs and SRMs

The vibration synthesis process has finally been applied to PMSMs and SRMs. The example of an outer-rotor switched reluctance machine with integrated distributed inverter operating

under fault conditions underlines that the acoustic modeling approach is flexible enough to cope with off-standard applications. In general, surface vibrations are synthesized and represented in spectrograms which are validated against the measured counterparts. Operational deflections are analyzed. Further application studies investigate skew arrangements, switching frequency influences, and the mitigation of acoustic noise via harmonics in the stator currents.

Open issues and future work

Naturally, some aspects remain open and even more so, topics seeking further investigation have been brought up. Some of them are listed below.

Force models for induction and DC machines

While the vibration synthesis is readily applicable to all machine types, implementation of a system simulation force model for induction and DC machines is required for modeling these machines.

Structural modeling

Effects like high-frequency tooth rocking from higher order force shapes, incorrect mean-square surface normal velocity for torsional vibrations, or transversal vibrations found in simulations but not in measurements seek further investigation. The alleged ability of coping with more detailed structural models should be exploited and, for example, the rotor should be added to inner-rotor machine models.

Mitigation of acoustic noise via control

Control-based approaches for acoustic noise mitigation are a worthwhile topic for further investigation. The numerical example for a PMSM in the application chapter has shown that is is generally feasible to suppress acoustic noise via harmonics in the stator current. Possibilities and limitations of control strategies can now be derived and investigated further.

SRMs and electric vehicles

The initially promising relationship between SRMs and electric vehicles soon cooled off when it turned out the former was rather noisy while the latter asked for silent operation. Research has looked into the acoustics of SRMs quite extensively but has mostly focused on small machines. The characteristics of larger traction drives with higher pole counts along with the transmission paths from the drive into the cabin of the vehicle have only seen limited attention. The machine design may eventually leave little room for optimization but with advanced control methods a significant noise reduction is expected. The acoustic modeling process is an adequate starting ground for such investigations.

Application and implementation

The first step in future work is to apply what is already there. At ISEA, the acoustics characteristics are now routinely taken into account when designing PMSM or SRM drive systems. The author hopes that some of the presented aspects appeal to other researchers to implement or extend them.

The final word

Overall, the author is confident that this work improves the quality of acoustic models for electrical drives and makes acoustic modeling more accessible. With help of the presented acoustic modeling process, realistic acoustic models can be used routinely in the drive design process. Independent of the approach chosen, hope and expectation are that comprehensive acoustic modeling soon becomes a standard step in the overall design and assessment of electrical drive systems.

A Appendix

A.1 Investigated machines – parameters

The tables on the next pages list characteristic data for the machines investigated in this work.

Interior permanent magnet synchronous machine PM-A (PM-N24p10)

Application	HEV
Number of stator slots N_s	24
Number of pole pairs p	10
Number of phases m	3
Number of slots per pole per phase q	0.4
Maximum speed $n_\mathrm{m}^\mathrm{max}$	6000 r/min
Max. torque @ $n_\mathrm{m}^\mathrm{base}$	$\geq$ 250 Nm @ 450 r/min
Max. torque @ $n_\mathrm{m}^\mathrm{max}$	$\geq$ 20 Nm @ 6000 r/min
Max. power $P_\mathrm{m}^\mathrm{max}$	$\approx$ 12 kW
DC-link voltage u_dc	105 V
Stator outer-Ø	290 mm
Stack length l_stk	70 mm

Table A.1: Characteristic data for machine PM-A

Interior permanent magnet synchronous machine PM-B (PM-N12p4)

Application	HEV
Number of stator slots N_s	12
Number of pole pairs p	4
Number of phases m	3
Number of slots per pole per phase q	0.4
Base speed $n_\mathrm{m}^\mathrm{base}$	4700 r/min
Maximum speed $n_\mathrm{m}^\mathrm{max}$	10 000 r/min
Maximum torque $T_\mathrm{m}^\mathrm{max}$	150 Nm
Max. power $P_\mathrm{m}^\mathrm{max}$	$\approx$ 70 kW
DC-link voltage u_dc	400 V
Maximum current $i_\mathrm{s}^\mathrm{max}$	280 A
Stator outer-Ø	147 mm
Stack length l_stk	225 mm

Table A.2: Characteristic data for machine PM-B

Interior permanent magnet synchronous machine PM-C (PM-N60p5)

Application	EV
Number of stator slots N_s	60
Number of pole pairs p	5
Number of phases m	3
Number of slots per pole per phase q	2
Base speed $n_\mathrm{m}^\mathrm{base}$	2150 r/min
Maximum speed $n_\mathrm{m}^\mathrm{max}$	13 000 r/min
Maximum torque $T_\mathrm{m}^\mathrm{max}$	310 Nm
Max. power $P_\mathrm{m}^\mathrm{max}$	$\approx$ 70 kW
DC-link voltage u_dc	300 V
Maximum current $i_\mathrm{s}^\mathrm{max}$	400 A
Stator outer-Ø	210 mm
Stack length l_stk	100 mm

Table A.3: Characteristic data for machine PM-C

Interior permanent magnet synchronous machine PM-D (PM-N72p6)

Application	EV
Number of stator slots N_s	72
Number of pole pairs p	6
Number of phases m	3
Number of slots per pole per phase q	2
Base speed $n_\mathrm{m}^\mathrm{base}$	4950 r/min
Maximum speed $n_\mathrm{m}^\mathrm{max}$	12 000 r/min
Maximum torque $T_\mathrm{m}^\mathrm{max}$	260 Nm
Max. power $P_\mathrm{m}^\mathrm{max}$	$\approx$ 130 kW
DC-link voltage u_dc	350 V
Maximum current $i_\mathrm{s}^\mathrm{max}$	550 A
Stator outer-Ø	240 mm
Stack length l_stk	133 mm

Table A.4: Characteristic data for machine PM-D

Switched reluctance machine SR-X (SR-8/6)

Application	Auxiliary drive in weaving machine
Stator/rotor tooth configuration N_s/N_r	8/6
Number of phases m	4
Pole pair number p	1
Nominal speed n_m^{base} @ T_m^{nom}	1500 r/min
Max. speed n_m^{max}	4000 r/min
Nominal torque T_m^{nom}	10 Nm
Max. torque T_m^{max}	22 Nm
Max. power P_m^{max}	$\approx$ 3 kW
DC-link voltage	290 V
Stator outer-Ø	120 mm

Table A.5: Characteristic data for machine SR-X

Outer rotor switched reluctance machine SR-Y (SR-20/16or)

Application	Direct drive for railway traction application
Stator/rotor tooth configuration N_s/N_s	20/16
Number of phases m	5
Pole pair number p	4
Nominal torque T_m^{nom}	1800 Nm
Max. speed n_m^{max}	750 r/min
Nominal power P_m^{nom}	66 kW
DC-link voltage	300 V
Rotor outer-Ø	640 mm
Rotor inner-Ø	518 mm
Stator outer-Ø	515 mm
Stator inner-Ø	300 mm
Stack length l_{stk}	150 mm

Table A.6: Characteristic data for machine SR-Y

A.2 Space vector conventions

This work uses space vectors for machine modeling.

Space vectors vs. phasors
Following [DPV11], space vectors and phasors are notated differently to also set them apart visibly. Space vectors $\vec{X}$ are marked with a vector arrow. Phasors $\underline{X}$ are underlined. Besides the visible separation between space vectors and phasor, the vector notation of space vectors allows to consider them as 2-D or 3-D. The latter is, for example, needed when a zero-sequence system is taken into account or for machines where the axis of rotation changes as in the spherical motor in [Kah+04]. Within this work, however, the space vectors are in-plane. Zero-sequence components are not taken into account. Due to the space vectors' 2-D nature, complex number arithmetic can be used, which facilitates mathematical operations on space vector.

Complex number arithmetic
The multiplication of a space vector with the imaginary number is defined as,

$$\mathrm{j}\vec{x}^{\mathrm{dq}} = \mathrm{j}\begin{pmatrix} x_\mathrm{d} \\ x_\mathrm{q} \end{pmatrix} = \begin{pmatrix} -x_\mathrm{q} \\ x_\mathrm{d} \end{pmatrix}.$$

Multiplication with $\mathrm{e}^{\mathrm{j}\theta}$ is equivalent to multiplication with the rotation matrix,

$$\mathrm{e}^{\mathrm{j}\theta} = \begin{pmatrix} \cos(\theta) & -\sin(\theta) \\ \sin(\theta) & \cos(\theta) \end{pmatrix}.$$

Torque via exterior product
The IRTF torque equation (3.23) uses the cross-product ($\times$) notation. This is mathematically precise only in 3-D. The general case is the exterior product or wedge product ($\wedge$) [Wik]. However within this work, the notation introduced by Veltman et al. in [VvB91] is followed, where the cross-product notation is used also if the space vectors are 2-D,

$$T_\mathrm{el} = \vec{\psi}_\mathrm{s} \times \vec{i}_\mathrm{s} = \begin{pmatrix} \psi_\mathrm{sd} \\ \psi_\mathrm{sq} \end{pmatrix} \times \begin{pmatrix} i_\mathrm{sd} \\ i_\mathrm{sq} \end{pmatrix} = \psi_\mathrm{sd} i_\mathrm{sq} - \psi_\mathrm{sq} i_\mathrm{sd}.$$

In 2-D, the result of the exterior product is a scalar. For rotational movements, the axis of rotation is the perpendicular to the plane the space vectors lie in. The sign of the scalar determines the direction. In 3-D, the result is a vector, which defines the axis of rotation explicitly.

Acronyms

PM-D (PM-N72p6)	permanent magnet synchronous machine
PM-B (PM-N12p4)	permanent magnet synchronous machine
SR-Y (SR-20/16or)	20/16 outer rotor switched reluctance machine
PM-C (PM-N60p5)	permanent magnet synchronous machine
PM-A (PM-N24p10)	permanent magnet synchronous machine
SR-X (SR-8/6)	8/6 switched reluctance machine
1-D	1-dimensional
2-D	2-dimensional
3-D	3-dimensional
ANSOFT	ANSOFT, a subsidiary of ANSYS
ANSYS	ANSYS (ANalysis SYStem), finite element software
ANSYS EMAG	ANSYS Emag, ANSYS for electromagnetic problems
ANSYS Structural	ANSYS Structural, ANSYS for structural dynamics problems
APDL	ANSYS parametric design language
ATV	acoustic transfer vector
BEM	boundary element method
CAD	computer-aided design
dB	decibel
DC	direct current
DCM	DC machine
DITC	direct instantaneous torque control
DOF	degree of freedom
EMF	electromotive force
ESPS	early single-pulse strategy
EU	European Union
EV	electric vehicle
FE	finite element
FEM	finite element method
FFT	Fast Fourier transform
FRF	frequency response function
FT	Fourier transform

GCD	greatest common divider
HBCC	hysteresis bang-bang current control
HEV	hybrid electric vehicle
ICE	internal combustion engine
IM	induction machine
IPMSM	interior permanent magnet synchronous machine
IRTF	ideal rotating transformer
ISEA	Institute for Power Electronics and Electrical Drives, `http://www.isea.rwth-aachen.de`
JMAG	JMAG, simulation software for electromechanical design and development by JSOL
JSOL	JSOL Corporation develops, among others, the computer-aided engineering (CAE) software JMAG
LCM	lowest common multiple
LMS	LMS International, an engineering services and software company
LUT	lookup table
MA	maximum current
MATLAB	(MATLAB, matrix laboratory) numerical computing environment developed by MathWorks
MATV	modal acoustic transfer vector
Maxwell	Maxwell, electromagnetic field simulation software by ANSOFT for designing and analyzing 3-D and 2-D electromagnetic and electromechanical devices
MMF	magnetomotive force
MSD	mass-spring-damper
MTPA	maximum torque per ampere
MTPF	maximum torque per flux
n-D	n-dimensional
NHTSA	National Highway Traffic Safety Administration
OKOFEH	Optimierte KOmponenten Für Elektro- und Hybridfahrzeuge, research project funded by the Federal Ministry of Economics and Technology from 1999 to 2002, `http://tuvpt.de/188/`
P	proportional gain
PC	personal computer
PI	proportional-integral
PM	permanent magnet

PML	perfectly matched layer
PMSM	permanent magnet synchronous machine
PWM	pulse-width-modulated
PWM-DITC	pulse width modulation based predictive direct instantaneous torque control
RAM	random-access memory
RMS	root mean square
Simplorer	Simplorer, multi-domain simulation program by ANSOFT for simulation of power electronics and electrically controlled systems
Simulink	SIMULINK, graphical block diagramming tool for modeling, simulating, and analyzing multi-domain dynamic systems developed by MATHWORKS
SM	synchronous machine
SOC	state of charge
SR	switched reluctance
SRAF	switched reluctance axial flux
SRM	switched reluctance machine
SVM	space-vector modulation
SYNCHREL	synchronous reluctance motor
SYSNOISE	SYSNOISE, acoustic noise prediction software (using boundary element method). Predicts the vibro-acoustic performance at the softprototype stage.
US	United States
w.l.o.g.	without loss of generality

Symbols

Type

$\underline{X}$ complex number
$|X|$ absolute value
$\hat{X}$ amplitude
X^* complex conjugate
$\mathbf{X}^{-1}$ inverse of a matrix
$\underline{\mathbf{X}}$ matrix
$\overline{X}$ mean value
$\underline{X}$ phasor
$\mathbf{X}^+$ Moore-Penrose pseudoinverse of a matrix
$\vec{X}$ space vector
X^{T} transpose of a vector or matrix
$\boldsymbol{X}$ vector

Roman letters

A Fourier series coefficient (amplitude)
B (magnetic) flux density
C damping (matrix)
E Young's modulus
F force
G conductance
G shear modulus
H transfer function (in frequency domain)
H (magnetic) field strength
I intensity
J number of force excitations (in structural model)
K stiffness (matrix)
K maximum temporal order (e.g., from force)
L inductance
M mass, inertia (matrix)
M maximum mode number (in structural model)
N number of degrees of freedom
N number (e.g., Number of segments)
N maximum order of current harmonics (in spatial synchronous machine (SM) model)
P power
R radius
R reluctance
R resistance
S surface (area)
S number of skew segments or slices

T period
T torque
U maximum spatial order (e.g., from force)
W energy
Z impedance
a Fourier series coefficient (cosine)
a radius
b Fourier series coefficient (sine)
c Fourier series coefficient (complex)
c damping (matrix, model)
c speed of sound
d force direction (e.g., radial, tangential, axial))
e back EMF
f force
f frequency (temporal)
h height
h transfer function (in time domain)
i current
j force excitation counter (in structural model)
k factor (e.g., winding factor)
k stiffness (matrix, modal)
k temporal order (e.g., from force)
k wavenumber
l incremental inductance
l length
m mass
m mode number (in structural model)
m number of phases
n order of a current harmonic (in spatial SM model)
n speed
n tooth counter (e.g., in SRM)
p pole pair number
p pressure
p sound pressure
q number of slots per pole per phase
r radius
s direction in space (e.g., x, y, z)
s slice index (for rotor skew segments in SM)
t time
u displacement
u frequency (spatial)
u voltage
v velocity
x auxiliary variable
y modal coordinate

Greek letters

Ω region, domain
α angular position in air-gap
ϵ strain
γ control angle of a PMSM
γ modal force
γ (engineering) shear strain
λ eigenvalue
λ wavelength
μ permeability
ν Poisson's ratio
ν spatial order (e.g., force order)
ω angular frequency (temporal)
ω angular speed (in electrical degrees)
ψ (magnetic) flux linkage
ρ density
σ Maxwell stress tensor
σ radiation efficiency
σ stress
τ angular length or position (e.g., angular width of stator tooth)
θ angle (in electrical degrees)
Φ (magnetic) flux
φ potential (electric or magnetic)
ξ general result quantity from an FE simulation
ζ damping ratio
$\boldsymbol{\phi}$ eigenshape
Θ angle (in mechanical degrees)
$\partial\Omega$ surface of region Ω

Superscripts

X^0 free space (e.g., free-space permeability)
X^* reference (e.g., reference current)
$X^{\alpha\beta}$ stator fixed coordinates
X^{base} base value
X^{dq} field oriented coordinates
X^{free} free (e.g., free-wheeling angle)
X^{max} maximum (e.g., maximum current)
X^{min} minimum (e.g., minimum current)
X^{nom} nominal (e.g., nominal torque)
X^{off} off (e.g., turn-off angle)
X^{on} on (e.g., turn-on angle)
X^{xy} rotor-oriented coordinates

Subscripts

X_0 resonant (e.g., eigenfrequency); fundamental (fundamental air-gap field pole pair number)

X_{α} α-axis component of $\alpha\beta$-coordinates
X_{β} β-axis component of $\alpha\beta$-coordinates
X_{PM} permanent magnet (e.g., permanent magnet flux linkage)
X_{airgap} air-gap
X_{a} armature quantity
X_{critical} critical (e.g., critical damping)
X_{dc} direct current
X_{d} d-axis component of dq-coordinates
X_{elem} elements (e.g., number of elements in air-gap)
X_{el} electric (e.g., electrical frequency)
X_{eq} equivalent (e.g., equivalent stiffness)
X_{f} excitation (e.g., excitation flux linkage)
X_{in} input (e.g., input power)
X_{lin} linear
X_{l} inductive
X_{mag} magnetic (e.g., magnetic energy)
X_{mx} Maxwell (e.g., Maxwell forces)
X_{m} mechanical (e.g., mechanical position)
X_{nyquist} Nyquist (e.g., Nyquist frequency)
X_{n} negative (e.g., negative Fourier coefficients)
X_{n} normal (e.g., normal velocity)
X_{phase} phase (e.g., number of phase in an electrical machine)
X_{p} positive (e.g., positive Fourier coefficients)
X_{q} q-axis component of dq-coordinates
X_{rad} radial (e.g., radial force)
X_{r} relative (e.g., relative permeability)
X_{r} rotor teeth (e.g., number of rotor teeth in an SRM)
X_{r} rotor quantity
X_{sc} short circuit
X_{skew} skew
X_{start} start (e.g., starting position)
X_{steps} steps (e.g., number of time-steps in a finite element method (FEM) simulation)
X_{stk} stack (e.g., stack length)
X_{struc} structural (e.g., structural transfer function)
X_{switch} switching (e.g., switching frequency)
X_{s} slots (e.g., number of stator slots)
X_{s} stator teeth (e.g., number of stator teeth in an SRM)
X_{s} stator quantity
X_{tan} tangential (e.g., tangential flux density)
X_{teeth} teeth (e.g., number of teeth in an SRM)
X_{tooth} tooth (e.g., force constant on stator tooth)
X_{tsine} tsine (e.g., force decomposed on stator teeth)
X_{t} tangential (e.g., tangential flux density)
X_{unit} unit (e.g., force with unit amplitude)
X_{vw} virtual work (e.g., virtual work forces)
X_{yoke} yoke

Bibliography

[ANS09] ANSYS Inc. *Rotordynamic Analysis Guide, Release 12.1*. Nov. 2009 (cit. on p. 149).

[ANS11] ANSYS Inc. *ANSYS Mechanical APDL Theory Reference*. Release 14.0. Southpointe, 275 Technology Drive, Canonsburg, PA 15317, USA, Nov. 2011 (cit. on pp. 39, 40).

[ANS12] ANSYS Inc. *Release 14.0 Documentation for ANSYS*. HTML help-file. 2012 (cit. on pp. 57, 88).

[AS12] ANSYS Inc. and Solveson, M. *Electric Machines Considering Power Electronics*. Presentation slides. May 2012 (cit. on p. 50).

[Bae+03] Bae, B.-H., Patel, N., Schulz, S., and Sul, S.-K. "New field weakening technique for high saliency interior permanent magnet motor." In: *Conference Record of the Industry Applications Conference, 38th IAS Annual Meeting*. Vol. 2. Oct. 2003, pp. 898–905 (cit. on p. 37).

[Ber94] Berenger, J.-P. "A perfectly matched layer for the absorption of electromagnetic waves." In: *Journal of Computational Physics* 114.2 (1994), pp. 185–200. ISSN: 0021-9991. DOI: 10.1006/jcph.1994.1159 (cit. on p. 110).

[BT09] Beriot, H. and Tournour, M. "On the locally-conformal perfectlymatched layer implementation for helmholtz equation." In: *Proceeding of the conference on Noise and Vibration: Emerging Methods, NOVEM 2009*. Oxford, England, Apr. 2009 (cit. on p. 110).

[BA10] Bianchi, N. and Alberti, L. "MMF Harmonics Effect on the Embedded FE Analytical Computation of PM Motors." In: *Industry Applications, IEEE Transactions on* 46.2 (Mar. 2010), pp. 812–820. ISSN: 0093-9994. DOI: 10.1109/TIA.2010.2041098 (cit. on p. 27).

[BB98] Bianchi, N. and Bolognani, S. "Magnetic models of saturated interior permanent magnet motors based on finite element analysis." In: *Industry Applications Conference, 1998. Thirty-Third IAS Annual Meeting. The 1998 IEEE*. Vol. 1. Oct. 1998, pp. 27–34. DOI: 10.1109/IAS.1998.732255 (cit. on p. 40).

[Blu+11] Blum, J., Pollow, M., Müller-Trapet, M., v. d. Giet, M., Dietrich, P., Hameyer, K., and Vorländer, M. "Simulationskette zur Prädiktion der abgestrahlten Schallleistung elektrischer Maschinen." In: *37. Deutsche Jahrestagung für Akustik - DAGA*. Mar. 2011 (cit. on p. 111).

[BD10] Boesing, M. and De Doncker, R. "Exploring a vibration synthesis process for the acoustic characterization of electric drives." In: *Proceedings of the 19th International Conference on Electrical Machines (ICEM)*. Rome, Italy, Sept. 2010. DOI: 10.1109/ICELMACH.2010.5608187 (cit. on pp. 107, 108).

[BD12] Boesing, M. and De Doncker, R. "Exploring a Vibration Synthesis Process for the Acoustic Characterization of Electric Drives." In: *Industry Applications, IEEE Transactions on* 48.1 (Jan. 2012), pp. 70–78. ISSN: 0093-9994. DOI: 10.1109/TIA.2011.2175469 (cit. on p. 107).

[BKD08] Boesing, M., Kasper, K., and De Doncker, R. "Vibration Excitation in an Electric Traction Motor for a Hybrid Electric Vehicle." In: *Proceedings of the 37th International Congress and Exposition on Noise Control Engineering, INTER-NOISE 2008*. Shanghai, China, Nov. 2008 (cit. on pp. 11, 32, 62, 65).

[Boe+12] Boesing, M., Niessen, M., Lange, T., and De Doncker, R. "Modeling spatial harmonics and switching frequencies in PM synchronous machines and their electromagnetic forces." In: *Electrical Machines (ICEM), 2012 XXth International Conference on*. Sept. 2012, pp. 3001–3007. DOI: 10.1109/ICElMach.2012.6350315 (cit. on pp. 23, 71, 74, 117).

[Boe+10] Boesing, M., Schoenen, T., Kasper, K., and De Doncker, R. "Vibration Synthesis for Electrical Machines Based on Force Response Superposition." In: *IEEE Transactions on Magnetics* 46.8 (Aug. 2010), pp. 2986–2989. ISSN: 0018-9464. DOI: 10.1109/TMAG.2010.2042291 (cit. on pp. 23, 73, 107).

[BSD11] Boesing, M., Schniedertoens, T., and De Doncker, R. W. "Analysis of Electromagnetic Forces in Skewed Electric Drives in the Full Operating Range." In: *Compumag Conference*. July 2011 (cit. on pp. 50, 61).

[Boe+09] Boesing, M., Schoenen, T., Kasper, K. A., and De Doncker, R. W. "Vibration Synthesis for Electrical Machines based on Force Response Superposition." In: *Compumag Conference, Florianopolis, Brazil*. Nov. 2009 (cit. on pp. 23, 107, 108, 113).

[BD02] Bonet-Madurga, J. and Díez-González, A. "Modelling of permanent magnet synchronous motors with spatial harmonics." In: *European Transactions on Electrical Power* 12.5 (Sept. 2002), pp. 369–375. ISSN: 1546-3109. DOI: 10.1002/etep.4450120508. URL: http://dx.doi.org/10.1002/etep.4450120508 (cit. on p. 27).

[BH90] Boys, J. T. and Handley, P. G. "Harmonic analysis of space vector modulated PWM waveforms." In: *IEE Proceedings - Electric Power Applications*. Vol. 137. July 1990, pp. 197–204 (cit. on pp. 30, 48).

[Bra07] Brauer, H. J. "Torque Control Strategies for Switched Reluctance Machines." In: *7 minute oral presentation during the ISEA excursion to the SPEED laboratory at Glasgow University*. 2007 (cit. on p. 38).

[Bra12] Brauer, H. J. "Schnelldrehender Geschalteter Reluktanzantrieb mit extremem Längendurchmesserverhältnis." PhD thesis. RWTH Aachen University, Faculty of Electrical Engineering, Information Technology, Institute for Power Electronics, and Electrical Drives, 2012 (cit. on p. 83).

[BHD12] Brauer, H., Hennen, M., and De Doncker, R. "Control for Polyphase Switched Reluctance Machines to Minimize Torque Ripple and Decrease Ohmic Machine Losses." In: *Power Electronics, IEEE Transactions on* 27.1 (Jan. 2012), pp. 370–378. ISSN: 0885-8993. DOI: 10.1109/TPEL.2011.2161332 (cit. on p. 38).

[CLU92] Cameron, D., Lang, J., and Umans, S. "The origin and reduction of acoustic noise in doubly salient variable-reluctance motors." In: *Industry Applications, IEEE Transactions on* 28.6 (Nov. 1992), pp. 1250–1255. ISSN: 0093-9994. DOI: 10.1109/28.175275 (cit. on p. 138).

[CEN10] CEN - European Committee For Standardization. *Acoustics — Determination of sound power levels and sound energy levels of noise sources using sound pressure — Engineering methods for an essentially free field over a reflecting plane.* European Standard EN ISO 3744:2010. 2010 (cit. on p. 111).

[CED89] Chang, L., Eastham, A., and Dawson, G. "Permanent magnet synchronous motor: finite element torque calculations." In: *Industry Applications Society Annual Meeting, 1989., Conference Record of the 1989 IEEE.* Vol. 1. Oct. 1989, pp. 69–73. DOI: 10.1109/IAS.1989.96633 (cit. on p. 39).

[CM89] Corda, J. and Masic, S. "Computation of torque pulsations of switched reluctance drive." In: *Electrical Machines and Drives, 1989. Fourth International Conference on.* Sept. 1989, pp. 308–311 (cit. on pp. 31, 32).

[CM84] Coulomb, J. and Meunier, G. "Finite element implementation of virtual work principle for magnetic or electric force and torque computation." In: *Magnetics, IEEE Transactions on* 20.5 (Sept. 1984), pp. 1894–1896. ISSN: 0018-9464. DOI: 10.1109/TMAG.1984.1063232 (cit. on p. 39).

[CHP10] Cremer, L., Heckl, M., and Petersson, B. A. *Structure-Borne Sound: Structural Vibrations and Sound Radiation at Audio Frequencies.* Softcover reprint of hardcover 3rd ed. 2005. Springer, Oct. 2010. ISBN: 9783642061554 (cit. on pp. 11, 111).

[Daj06] Dajaku, G. "Electromagnetic and Thermal Modeling of Highly Utilized PM Machines." Dissertation. Universität der Bundeswehr München, Fakultät für Elektrotechnik und Informationstechnik, July 2006 (cit. on p. 25).

[DPV11] De Doncker, R., Pulle, D. W., and Veltman, A. *Advanced Electrical Drives - Analysis, Modeling, Control.* 1st ed. Springer Science+Business Media B.V., 2011, 462 p. (Cit. on pp. 18, 19, 25, 36, 144, 167).

[DHW03] De Gersem, H., Hameyer, K., and Weiland, T. "Skew interface conditions in 2-D finite-element machine models." In: *IEEE Transactions on Magnetics* 39.3 (May 2003), pp. 1452–1455. ISSN: 0018-9464. DOI: 10.1109/TMAG.2003.810543 (cit. on p. 61).

[Dos88] Dossing, O. *Structural Testing - Part II - Modal Analysis and Simulation.* Bruel & Kjær, Denmark., 1988 (cit. on p. 88).

[Eur11] European Commission. *Proposal For A Regulation Of The European Parliament And Of The Council On The Sound Level Of Motor Vehicles (COM(2011) 856 final 2011/0409 (COD)).* Dec. 2011 (cit. on p. 7).

[Ewi00] Ewins, D. J. "Basic and state-of-the-art modal testing." In: *Sadhana - Academy Proceedings in Engineering and Sciences, Indian Academy of Science* 25 (2000), pp. 207–220 (cit. on p. 109).

[FCJ93] Favre, E., Cardoletti, L., and Jufer, M. "Permanent-magnet synchronous motors: a comprehensive approach to cogging torque suppression." In: *Industry Applications, IEEE Transactions on* 29.6 (Nov. 1993), pp. 1141–1149. ISSN: 0093-9994. DOI: 10.1109/28.259725 (cit. on p. 133).

[Fie06] Fiedler, J. "Design of Low-Noise Switched Reluctance Drives." PhD thesis. RWTH Aachen University, Faculty of Electrical Engineering, Information Technology, Institute for Power Electronics, and Electrical Drives, 2006 (cit. on pp. 16, 50, 76, 98, 107, 109, 111, 138).

[FKD05] Fiedler, J., Kasper, K., and De Doncker, R. "Acoustic noise in switched reluctance drives: an aerodynamic problem?" In: *Electric Machines and Drives, 2005 IEEE International Conference on*. May 2005, pp. 1275–1280. DOI: 10.1109/IEMDC.2005.195886 (cit. on p. 9).

[Fin09] Fingerhuth, S. "Tonalness and consonance of technical sounds." PhD thesis. RWTH Aachen University, Faculty of Electrical Engineering and Information Technology, Institute for Technical Acoustics, 2009 (cit. on p. 16).

[Fle] Fleadh Electronics Limited. *Brivit database*. URL: http://www.fleadh.co.uk/srmbrivit.asp (cit. on p. 138).

[FH12] Franck, D. and Hameyer, K. "FEM2measurement transfer functions - denition of acoustic transfer functions of electrical drives." In: *Deutsche Jahrestagung für Akustik, DAGA 2012*. Darmstadt, Germany, Mar. 2012 (cit. on p. 109).

[Fue07] Fuengwarodsakul, N. "Predictive PWM-based Direct Instantaneous Torque Control for Switched Reluctance Machines." PhD thesis. RWTH Aachen University, Faculty of Electrical Engineering, Information Technology, Institute for Power Electronics, and Electrical Drives, 2007. ISBN: 978-3832262105 (cit. on pp. 37, 138).

[Gar89] Garvey, S. "The vibrational behaviour of laminated components in electrical machines." In: *Fourth International Conference on Electrical Machines and Drives*. Sept. 1989, pp. 226–231 (cit. on pp. 93, 147).

[Gar+97] Garvey, S., Penny, J., Friswell, M., and Glew, C. "Modelling the vibrational behaviour of stator cores of electrical machines with a view to successfully predicting machine noise." In: *Modeling the Performance of Electrical Machines (Digest No: 1997/166), IEE Colloquium on*. Apr. 1997, pp. 3/1–3/13. DOI: 10.1049/ic:19970897 (cit. on pp. 2, 9, 48, 49).

[Gér+02] Gérard, F., Tournour, M., Masri, N. E., Cremers, L., Felice, M., and Selmane, A. "Acoustic Transfer Vectors for Numerical Modeling of Engine Noise." In: *S.V. Sound and vibration* 36.7 (2002), pp. 20–25 (cit. on pp. 110, 111).

[GWL06] Gieras, J. F., Wang, C., and Lai, J. C. *Noise of Polyphase Electric Motors*. Taylor and Francis Group, 2006 (cit. on pp. 2, 45, 48, 87).

[GO99] Gyimesi, M. and Ostergaard, D. "Inductance computation by incremental finite element analysis." In: *Magnetics, IEEE Transactions on* 35.3 (May 1999), pp. 1119–1122. ISSN: 0018-9464. DOI: 10.1109/20.767144 (cit. on p. 40).

[GVM01] Gyselinck, J., Vandevelde, L., and Melkebeek, J. "Multi-slice FE modeling of electrical machines with skewed slots-the skew discretization error." In: *IEEE Transactions on Magnetics* 37.5 (Sept. 2001), pp. 3233–3237. ISSN: 0018-9464. DOI: 10.1109/20.952584 (cit. on p. 61).

[Han09] Hanna, R. *Incidence of Pedestrian and Bicyclist Crashes by Hybrid Electric Passenger Vehicles*. Tech. rep. DOT HS 811. U.S. Department of Transportation, National Highway Traffic Safety Administration, Sept. 2009 (cit. on p. 8).

[Han97] Hanselman, D. "Effect of skew, pole count and slot count on brushless motor radial force, cogging torque and back EMF." In: *IEE Proceedings - Electric Power Applications* 144.5 (Sept. 1997), pp. 325–330. ISSN: 1350-2352. DOI: 10.1049/ip-epa:19971205 (cit. on pp. 63, 83).

[Har12] Harries, M. "Vibrationsanalyse Geschalteter Reluktanzmaschinen verschiedener Bauformen für den automobilen Einsatz (Vibration Analysis of Different Switched Reluctance Type Machines for Automotive Applications)." Diplomarbeit (unpublished). RWTH Aachen University, Faculty of Electrical Engineering and Information Technology, Institute for Power Electronics and Electrical Drives, Aug. 2012 (cit. on pp. 86, 105).

[Hen11] Hennen, M. "Switched reluctance direct drive with integrated distributed inverter." PhD thesis. RWTH Aachen University, Faculty of Electrical Engineering, Information Technology, Institute for Power Electronics, and Electrical Drives, Oct. 2011 (cit. on pp. 16, 34, 35, 78, 79, 144, 146, 152, 156).

[HBD12] Hennen, M. D., Boesing, M., and De Doncker, R. W. "Analysis of the Fault Tolerance of a Switched Reluctance Machine with Distributed Inverter." In: *EVS26 – International Battery, Hybrid and Fuel Cell Electric Vehicle Symposium*. Los Angeles, California, USA, May 2012 (cit. on p. 144).

[Hen06] Henschel, M. "Berechnung und Optimierung permanenterregter Maschinen am Beispiel von Generatoren für Windkraftanlagen." PhD thesis. Technische Universität Darmstadt, 2006 (cit. on p. 61).

[Her05] Herlufson, H. *Modal Analysis using Multi-Reference and Multiple-Input Multiple-Output Techniques - Application Note Sheet*. Bruel & Kjær. Denmark, 2005 (cit. on p. 109).

[Her+11] Herold, T., Franck, D., Lange, E., and Hameyer, K. "Extension of a d-q model of a permanent magnet excited synchronous machine by including saturation, cross-coupling and slotting effects." In: *Electric Machines Drives Conference (IEMDC), 2011 IEEE International*. May 2011, pp. 1363–1367. DOI: 10.1109/IEMDC.2011.5994804 (cit. on pp. 31, 32).

[Hil99] Hill, W. "Transverse flux machine." German, English, French. EP 0 799 519 81 (Hengelhaupt, Jürgen, Dipl.-lng. et al, Patentanwälte, Gulde Hengelhaupt Ziebig, Lützowplatz 11-13, 10785 Berlin (DE)). June 16, 1999 (cit. on pp. 83, 84, 86).

[Hol12] Holbrook, E. "Electric Cars: The Silent Killer." In: *National Law Review* (May 2012) (cit. on p. 7).

[Hon+97] Honda, Y., Nakamura, T., Higaki, T., and Takeda, Y. "Motor design considerations and test results of an interior permanent magnet synchronous motor for electric vehicles." In: *Industry Applications Conference, 1997. Thirty-Second IAS Annual Meeting, IAS '97., Conference Record of the 1997 IEEE*. Vol. 1. Oct. 1997, pp. 75–82. DOI: 10.1109/IAS.1997.643011 (cit. on p. 47).

[ID03] Inderka, R. B. and De Doncker, R. W. A. A. "DITC-direct instantaneous torque control of switched reluctance drives." In: *IEEE Transactions on Industry Applications* 39.4 (July 2003), pp. 1046–1051. ISSN: 0093-9994. DOI: 10.1109/TIA.2003.814578 (cit. on p. 37).

[Ind02] Inderka, R. B. "Direkte Drehmomentregelung Geschalteter Reluktanzantriebe." PhD thesis. RWTH Aachen University, Faculty of Electrical Engineering, Information Technology, Institute for Power Electronics, and Electrical Drives, 2002 (cit. on pp. 37, 47, 138).

[IK04] Inderka, R. B. and Keppeler, S. "Extended Power by Boosting with Switched Reluctance Propulsion." In: *Proceedings of the 21th International Electric Vehicle Symposium EVS21*. 2004 (cit. on p. 80).

[JR04] Jiao, G. and Rahn, C. "Field weakening for radial force reduction in brushless permanent-magnet DC motors." In: *IEEE Transactions on Magnetics* 40.5 (Sept. 2004), pp. 3286–3292. ISSN: 0018-9464. DOI: 10.1109/TMAG.2004.832989 (cit. on p. 66).

[Jor50] Jordan, H. *Geräuscharme Elektromotoren - Lärmbildung und Lärmbeseitigung bei Elektromotoren*. Verlag W. Giradet, Essen., 1950 (cit. on pp. 2, 14, 43, 45, 46, 98, 138, 145).

[JSO10] JSOL Corporation. *Introducing JMAG-RT – Motor Models Furthering Model Based Design*. Presentation Slides. Aug. 2010 (cit. on p. 32).

[Kah+04] Kahlen, K., Voss, I., Priebe, C., and De Doncker, R. "Torque control of a spherical machine with variable pole pitch." In: *Power Electronics, IEEE Transactions on* 19.6 (Nov. 2004), pp. 1628–1634. ISSN: 0885-8993. DOI: 10.1109/TPEL.2004.836623 (cit. on p. 167).

[Kas+07] Kasper, K. A., Bosing, M., De Doncker, R., Fingerhuth, S., and Vorlander, M. "Noise Radiation of Switched Reluctance Drives." In: *7th International Conference on Power Electronics and Drive Systems*. Bangkok, Thailand, 2007, pp. 967–973 (cit. on p. 111).

[Kas10] Kasper, K. A. "Analysis and Control of the Acoustic Behavior of Switched Reluctance Drives." PhD thesis. RWTH Aachen University, Faculty of Electrical Engineering, Information Technology, Institute for Power Electronics, and Electrical Drives, 2010 (cit. on pp. 2, 16, 38, 89, 114, 139, 141, 146, 147).

[Kas+08] Kasper, K., De Doncker, R. W., Scharrer, R., Fingerhuth, S., and Vorländer, M. "Experimental Modal Analysis of Electrical Machines Using Electromagnetic Excitation." In: *Proceedings of the 37th International Congress and Exposition on Noise Control Engineering, INTER-NOISE 2008*. Shanghai, China, Nov. 2008 (cit. on p. 109).

[KFC00] Kinsler, L. E., Frey, A. R., and Coppens, A. B. *Fundamentals of Acoustics*. 4th ed. Wiley & Sons., 2000 (cit. on p. 111).

[Kle05] Klemenz, M. "Die Geräuschqualität bei der Anfahrt elektrischer Schienenfahrzeuge." PhD thesis. Aachen, Germany: RWTH Aachen University, Faculty of Electrical Engineering and Information Technology, Institute for Technical Acoustics, 2005 (cit. on p. 136).

[Kön07] König, W. "Wie laut sind unsere Autos wirklich?" In: *Auto Bild* 33 (Aug. 2007) (cit. on p. 8).

[Küs09] Küsell, M. "Bosch Parallel Hybrid before Start of Production." In: *18. Aachener Kolloquium Fahrzeug- und Motorentechnik*. Robert Bosch GmbH, Stuttgart, 2009 (cit. on p. 47).

[Le +10] Le Besnerais, J., Lanfranchi, V., Hecquet, M., and Brochet, P. "Characterization and Reduction of Audible Magnetic Noise Due to PWM Supply in Induction Machines." In: *Industrial Electronics, IEEE Transactions on* 57.4 (Apr. 2010), pp. 1288–1295. ISSN: 0278-0046. DOI: 10.1109/TIE.2009.2029529 (cit. on p. 136).

[Le +09] Le Besnerais, J., Lanfranchi, V., Hecquet, M., Lemaire, G., Augis, E., and Brochet, P. "Characterization and Reduction of Magnetic Noise Due to Saturation in Induction Machines." In: *IEEE Transactions on Magnetics* 45.4 (Apr. 2009), pp. 2003–2008. ISSN: 0018-9464. DOI: 10.1109/TMAG.2008.2012112 (cit. on p. 109).

[Le 08] Le Besnerais, J. "Reduction of magnetic noise in PWM-supplied induction machines – low-noise design rules and multi-objective optimisation." PhD thesis. Laboratoire d'Électricité et d'Électronique de Puissance de Lille; École Centrale de Lille, Nov. 2008 (cit. on pp. 2, 50, 98, 106, 107, 109, 111, 136).

[LZH01] Long, S. A., Zhu, Z. Q., and Howe, D. "Vibration behaviour of stators of switched reluctance motors." In: *IEE Proceedings - Electric Power Applications*. Vol. 148. May 2001, pp. 257–264. DOI: 10.1049/ip-epa:20010255 (cit. on p. 146).

[MTG02] McCulloch, C., Tournour, M., and Guisset, P. "Modal Acoustic Transfer Vectors Make Acoustic Radiation Models Practical for Engines and Rotating Machinery." In: *Proceedings of the International ANSYS Conference and Exposition*. Pittsburgh, Pennsylvania, USA, Apr. 2002 (cit. on p. 110).

[Mec93] Mecrow, B. "Fully pitched-winding switched-reluctance and stepping-motor arrangements." In: *Electric Power Applications, IEE Proceedings B* 140.1 (Jan. 1993), pp. 61–70. ISSN: 0143-7038 (cit. on p. 144).

[Mil95] Miller, T. "Faults and unbalance forces in the switched reluctance machine." In: *Industry Applications, IEEE Transactions on* 31.2 (Mar. 1995), pp. 319–328. ISSN: 0093-9994. DOI: 10.1109/28.370280 (cit. on p. 34).

[Mil+05] Miller, T., Popescu, M., Cossar, C., and McGilp, M. "Computation of the voltage-driven flux-MMF diagram for saturated PM brushless motors." In: *Industry Applications Conference, 2005. Fourtieth IAS Annual Meeting. Conference Record of the 2005.* Vol. 2. Oct. 2005, pp. 1023–1028. DOI: 10.1109/IAS.2005.1518479 (cit. on p. 31).

[Moh+12] Mohr, M., Bíró, O., Stermecki, A., and Diwoky, F. "An Improved Physical Phase Variable Model for Permanent Magnet Machines." In: *Proceedings of the 20th International Conference on Electrical Machines (ICEM'2012).* Marseille, France, Sept. 2012 (cit. on pp. 31, 32).

[Mül+10] Müller-Trapet, M., Dietrich, P., v. d. Giet, M., Blum, J., Vorländer, M., and Hameyer, K. "Simulated Transfer Functions for the Auralization of Electrical Machines." In: *EAA Euroregio Congress.* Ljubljana, Sept. 2010 (cit. on p. 110).

[Nie11] Nießen, M. "Akustische Bewertung umrichtergespeister Antriebe für Elektrofahrzeuge." Diplomarbeit (unpublished). RWTH Aachen University, Faculty of Electrical Engineering, Information Technology, Institute for Power Electronics, and Electrical Drives, July 2011 (cit. on pp. 107, 136).

[One10] One Hundred Eleventh Congress of the United States of America. *Pedestrian Safety Enhancement Act of 2010.* Apr. 2010. URL: http://www.govtrack.us/congress/bills/111/s841 (cit. on p. 8).

[PLF12a] Pellerey, P., Lanfranchi, V., and Friedrich, G. "Coupled Numerical Simulation Between Electromagnetic and Structural Models. Influence of the Supply Harmonics for Synchronous Machine Vibrations." In: *Magnetics, IEEE Transactions on* 48.2 (Feb. 2012), pp. 983–986. ISSN: 0018-9464. DOI: 10.1109/TMAG.2011.2175714 (cit. on pp. 48, 107, 109).

[PLF12b] Pellerey, P., Lanfranchi, V., and Friedrich, G. "Numerical simulations of rotor dynamic eccentricity effects on synchronous machine vibrations for full run up." In: *Electrical Machines (ICEM), 2012 XXth International Conference on.* 2012, pp. 3008–3014. DOI: 10.1109/ICElMach.2012.6350316 (cit. on p. 56).

[PL91] Preston, M. and Lyons, J. "A switched reluctance motor model with mutual coupling and multi-phase excitation." In: *Magnetics, IEEE Transactions on* 27.6 (Nov. 1991), pp. 5423–5425. ISSN: 0018-9464. DOI: 10.1109/20.278859 (cit. on p. 34).

[PP98] Pulle, D. and Petersen, I. "A unified approach to switched reluctance drive modeling: application to an axial flux (SRAF) motor." In: *Power Electronics Specialists Conference, 1998. PESC 98 Record. 29th Annual IEEE.* Vol. 2. May 1998, pp. 1681–1686. DOI: 10.1109/PESC.1998.703405 (cit. on pp. 22, 84, 86).

[Ram+09] Raminosoa, T., Farooq, J., Djerdir, A., and Miraoui, A. "Reluctance network modelling of surface permanent magnet motor considering iron nonlinearities." In: *Energy Conversion and Management* 50.5 (2009), pp. 1356–1361. ISSN: 0196-8904. DOI: 10.1016/j.enconman.2009.01.012 (cit. on p. 34).

[Ras99] Rasmussen, P. O. e. a. "Acoustic Noise Simulation for Switched Reluctance Motors with Audible Output." In: *European Power Electronics Conference EPE.* Lausanne, Switzerland, 1999 (cit. on pp. 50, 76, 107, 109).

[Roi09] Roivainen, J. "Unit-wave response-based modeling of electromechanical noise and vibration of electrical machines." PhD thesis. Department of Electrical Engineering, Helsinki University of Technology, 2009 (cit. on pp. 108, 109).

[Sal95] Salon, S. J. *Finite Element Analysis of Electrical Machines*. Kluwer Academic Publishers, 1995 (cit. on p. 40).

[SV12] Segaert, P. and Vansant, K. "Berechnung von Schallabstrahlung mit akustischen Finite Elemente : leistungsfähige Simulation mit dem PML/AML Verfahren." In: *Proceedings of the Deutschsprachige NAFEMS Konferenz: Berechnung und Simulation – Anwendungen, Entwicklungen, Trends,* Bamberg, Germany, May 2012 (cit. on p. 110).

[Sei92] Seinsch, H. O. *Oberfelderscheinungen in Drehfeldmaschinen*. Ed. by Hannover, U. B. G. Teubner, Stuttgart, 1992 (cit. on p. 45).

[SWV90] Singal, R. K., Williams, K., and Verma, S. P. "The effect of windings, frame and impregnation upon the resonant frequencies and vibrational behavior of an electrical machine stator." In: *Experimental Mechanics* 30.3 (Sept. 1990), pp. 270–280. ISSN: 0014-4851 (Print) 1741-2765 (Online). DOI: 10.1007/BF02322822 (cit. on p. 93).

[Som49] Sommerfeld, A. *Partial Differential Equations in Physics*. New York: Academic Press, 1949 (cit. on p. 110).

[SM94] Soong, W. and Miller, T. "Field-weakening performance of brushless synchronous AC motor drives." In: *Electric Power Applications, IEE Proceedings* - 141.6 (Nov. 1994), pp. 331–340. ISSN: 1350-2352. DOI: 10.1049/ip-epa:19941470 (cit. on p. 47).

[SLT09] Stanton, S., Lin, D., and Tang, Z. "Interior permanent magnet machine analysis using finite element based equivalent circuit model." In: *Vehicle Power and Propulsion Conference, 2009. VPPC '09. IEEE*. Sept. 2009, pp. 291–294. DOI: 10.1109/VPPC.2009.5289839 (cit. on pp. 31, 32).

[Sta+96] Staton, D., Deodhar, R., Soong, W., and Miller, T. "Torque prediction using the flux-MMF diagram in AC, DC, and reluctance motors." In: *Industry Applications, IEEE Transactions on* 32.1 (Jan. 1996), pp. 180–188. ISSN: 0093-9994. DOI: 10.1109/28.485830 (cit. on pp. 21, 28).

[SSM95] Staton, D., Soong, W., and Miller, T. "Unified theory of torque production in switched reluctance and synchronous reluctance motors." In: *Industry Applications, IEEE Transactions on* 31.2 (Mar. 1995), pp. 329–337. ISSN: 0093-9994. DOI: 10.1109/28.370281 (cit. on p. 21).

[SGM02] Stelzmann, U., Groth, C., and Mueller, G. *FEM Fuer Praktiker, Band 2, Strukturdynamik*. Expert-Verlag, 2002 (cit. on p. 88).

[SC79] Stephenson, J. and Corda, J. "Computation of torque and current in doubly salient reluctance motors from nonlinear magnetisation data." In: *Electrical Engineers, Proceedings of the Institution of* 126.5 (May 1979), pp. 393–396. ISSN: 0020-3270. DOI: 10.1049/piee.1979.0095 (cit. on pp. 31, 32).

[Tim+89] Timar, P. L., Fazekas, A., Kiss, J., Miklos, A., and Yang, S. J. *Noise and Vibration of Electrical Machines*. Ed. by Timar, P. L. Elsevier, 1989. ISBN: 0-444-98896-3 (cit. on p. 9).

[TL94] Timar, P. and Lai, J. "Acoustic noise of electromagnetic origin in an ideal frequency-converter-driven induction motor." In: *Electric Power Applications, IEE Proceedings* - 141.6 (Nov. 1994), pp. 341–346. ISSN: 1350-2352. DOI: 10.1049/ip-epa:19941342 (cit. on p. 111).

[Ued+91] Ueda, S., Honda, K., Ikimi, T., Hombu, M., and Ueda, A. "Magnetic noise reduction technique for an AC motor driven by a PWM inverter." In: *Power Electronics, IEEE Transactions on* 6.3 (July 1991), pp. 470–475. ISSN: 0885-8993. DOI: 10.1109/63.85897 (cit. on p. 115).

[UK74] Unnewehr, L. and Koch, W. "An Axial Air-AP Reluctance Motor for Variable Speed Applications." In: *Power Apparatus and Systems, IEEE Transactions on* PAS-93.1 (Jan. 1974), pp. 367–376. ISSN: 0018-9510. DOI: 10.1109/TPAS.1974.293956 (cit. on pp. 83, 84, 86).

[vGie11] V. d. Giet, M. "Analysis of electromagnetic acoustic noise excitations: A contribution to low-noise design and to the auralization of electrical machines." PhD thesis. RWTH Aachen University, Faculty of Electrical Engineering and Information Technology, Institute for Electrical Machines, Jan. 2011 (cit. on pp. 2, 101, 108, 111, 146, 147).

[vGRH09] V. d. Giet, M., Rothe, R., and Hameyer, K. "Asymptotic Fourier decomposition of tooth forces in terms of convolved air gap field harmonics for noise diagnosis of electrical machines." In: *COMPEL* 28.4 (2009), pp. 804–818. ISSN: 0332-1649. DOI: 10.1108/03321640910958937 (cit. on p. 40).

[vHoe+10] V. Hoek, H., Boesing, M., v. Treek, D., Schoenen, T., and De Doncker, R. "Power electronic architectures for electric vehicles." In: *Emobility - Electrical Power Train, 2010*. Nov. 2010, pp. 1–6. DOI: 10.1109/EMOBILITY.2010.5668048 (cit. on p. 37).

[vRie+05] V. Riesen, D., Henrotte, F., Schlensok, C., and Hameyer, K. "Coupled simulations in the design of electrical machines." In: *Internatial Conference on Computational Methods for Coupled Problems in Science and Engineering, Barcelona, Spain*. Ed. by Papadrakakis, M., Onate, E., and Schrefler, B. CIMNE. 2005 (cit. on p. 107).

[vTre11] V. Treek, D. "Position Sensorless Torque Control of Switched Reluctance Machines." PhD thesis. RWTH Aachen University, Faculty of Electrical Engineering, Information Technology, Institute for Power Electronics, and Electrical Drives, 2011 (cit. on p. 16).

[VDE10] VDE Verband der Elektrotechnik, Elektronik, Informationstechnik e.V. *Elektrofahrzeuge – Bedeutung, Stand der Technik, Handlungsbedarf*. Aug. 2010 (cit. on p. 138).

[VvB91] Veltman, A. and v. d. Bosch, P. "A universal method for modelling electrical machines." In: *Electrical Machines and Drives, 1991. Fifth International Conference on (Conf. Publ. No. 341)*. Sept. 1991, pp. 193–197 (cit. on pp. 23, 167).

[Vel+03] Veltman, A., v. d. Hulst, P., v. Gurp, J. P., and Jonker, M. C. "Sensorless Control of a 2.4 MW Linear Motor for launching roller-coasters." In: *EPE 2003 - 10th European Conference on Power Electronics and Applications*. ISBN: 90-75815-07-7. Toulouse, France, Sept. 2003 (cit. on p. 30).

[VBG93] Verdyck, D., Belmans, R., and Geysen, W. "An approach to modelling of magnetically excited forces in electrical machines." In: *Magnetics, IEEE Transactions on* 29.2 (Mar. 1993), pp. 2032–2035. ISSN: 0018-9464. DOI: 10.1109/20.250809 (cit. on p. 107).

[VB94] Verdyck, D. and Belmans, R. "An Acoustic Model for a Permanent Magnet Machine: Modal Shapes and Magnetic Forces." In: *Industry Applications, IEEE Transactions on* 30.6 (Nov. 1994), p. 1625. ISSN: 0093-9994. DOI: 10.1109/TIA.1994.350317 (cit. on pp. 2, 107).

[Vol+02] Volkswagen, Siemens, Voith Turbo Antriebstechnik, RWTH Aachen / ISEA, and Emotron Antriebstechnik. *OKOFEH - Optimierte Komponenten für Elektro- und Hybridfahrzeuge*. Bundesministeriums für Wirtschaft und Technologie (BMWI). 1999-2002. URL: http://www.tuvpt.de/index.php?id=188 (cit. on p. 47).

[WL00] Wang, C. and Lai, J. "The sound radiation efficiency of finite length acoustically thick circular cylindrical shells under mechanical excitation I: theoretical analysis." In: *Journal of Sound and Vibration* 232.2 (2000), pp. 431–447. ISSN: 0022-460X. DOI: 10.1006/jsvi.1999.2749 (cit. on p. 111).

[WLA04] Wang, C., Lai, J., and Astfalck, A. "Sound power radiated from an inverter driven induction motor II: Numerical analysis." In: *IEE Proceedings – Electric Power Applications* 151.3 (May 2004), pp. 341–348. ISSN: 1350-2352. DOI: 10.1049/ip-epa:20040120 (cit. on p. 107).

[WW97] Wang, H. and Williams, K. "Effects Of Laminations On The Vibrational Behaviour Of Electrical Machine Stators." In: *Journal of Sound and Vibration* 202.5 (1997), pp. 703–715. ISSN: 0022-460X. DOI: 10.1006/jsvi.1996.0845 (cit. on pp. 129, 146, 147).

[Weg10] Wegmann, R. "Development of a Telemetry System to Measure Vibration of an Electric Direct Drive." Bachelorarbeit (unpublished). RWTH Aachen University, Faculty of Electrical Engineering and Information Technology, Institute for Power Electronics and Electrical Drives, Oct. 2010 (cit. on p. 145).

[Wik] Wikipedia. *Exterior algebra*. URL: http://en.wikipedia.org/wiki/Exterior_algebra (cit. on p. 167).

[WP95] Wu, C.-Y. and Pollock, C. "Analysis and reduction of vibration and acoustic noise in the switched reluctance drive." In: *Industry Applications, IEEE Transactions on* 31.1 (Jan. 1995), pp. 91–98. ISSN: 0093-9994. DOI: 10.1109/28.363045 (cit. on p. 141).

[Yan81] Yang, S. *Low-noise electrical motors*. Monographs in electrical and electronic engineering. Clarendon Press, 1981. ISBN: 9780198593324 (cit. on p. 88).

[Zhu+07] Zhu, Z., Ishak, D., Howe, D., and Jintao, C. "Unbalanced Magnetic Forces in Permanent-Magnet Brushless Machines With Diametrically Asymmetric Phase Windings." In: *Industry Applications, IEEE Transactions on* 43.6 (Nov. 2007), pp. 1544–1553. ISSN: 0093-9994. DOI: 10.1109/TIA.2007.908158 (cit. on p. 78).

Curriculum Vitae

Matthias Bösing

Personal Information

Date of birth	14. April 1981
Place of birth	Duisburg, Germany
Nationality	German

Education

10/2000–02/2007	Studies in Electrical Engineering and Information Technology at RWTH Aachen University; Diploma degree
08/1997–01/1998	Semester abroad at Pacifica Marina High School in Garden Grove, CA, USA
07/1991–06/2000	Gymnasium Otto-Pankok-Schule in Mülheim an der Ruhr (high school)

Work Experience

10/2012–today	Development engineer in the advance development of power electronics for electric vehicle drives with Robert Bosch GmbH, Schwieberdingen, Germany
05/2007–08/2012	Research Associate at the Institute for Power Electronics and Electrical Drives (ISEA) of RWTH Aachen University under the supervision of Professor Rik W. De Doncker in the Research Group Electrical Drives
10/2005–03/2006	Internship in the R&D department of Siemens Medical Instruments, Singapore
04/2004–12/2004	Student worker at the Institute for Technical Acoustics, RWTH Aachen University, Professor Michael Vorländer
07/2001–08/2001 & 02/2002–03/2002	Summer job at Vodafone TeleCommerce GmbH, Ratingen
10/2000–07/2001	Social service in a day care center for children with special needs, Priesters Hof in Mülheim an der Ruhr

Aachener Beiträge des ISEA

ABISEA Band 1
Eßer, A.
Berührungslose, kombinierte Energie- und Informationsübertragung für bewegliche Systeme,
1. Auflage 1992, 130 Seiten;
ISBN 3-86073-046-0

ABISEA Band 2
Vogel, U.
Entwurf und Beurteilung von Verfahren zur Hochausnutzung des Rad-Schiene-Kraftschlusses durch Triebfahrzeuge,
1. Auflage 1992, 130 Seiten;
ISBN 3-86073-060-6

ABISEA Band 3
Reckhorn, Th.
Stromeinprägendes Antriebssystem mit fremderregter Synchronmaschine,
1. Auflage 1992, 130 Seiten
ISBN 3-86073-061-4

ABISEA Band 4
Ackva, A.
Spannungseinprägendes Antriebssystem mit Synchronmaschine und direkter Stromregelung,
1. Auflage 1992, 135 Seiten
ISBN 3-86073-062-2

ABISEA Band 5
Mertens, A.
Analyse des Oberschwingungsverhaltens von taktsynchronen Delta-Modulationsverfahren zur Steuerung von Pulsstromrichtern bei hoher Taktzahl,
1. Auflage 1992, 170 Seiten
ISBN 3-86073-069-X

ABISEA Band 6
Geuer, W.
Untersuchugen über das Alterungsverhalten von Bleiakkumulatoren,
1. Auflage 1993, 100 Seiten
ISBN 3-86073-097-5

ABISEA Band 7
Langheim, J.
Einzelradantrieb für Elektrostraßenfahrzeuge,
1. Auflage 1993, 215 Seiten
ISBN 3-86073-123-8
(vergriffen)

ABISEA Band 8
Fetz, J.
Fehlertolerante Regelung eines Asynchron-Doppelantriebes für ein Elektrospeicherfahrzeug,
1. Auflage 1993, 136 Seiten
ISBN 3-86073-124-6
(vergriffen)

ABISEA Band 9
Schülting, L.
Optimierte Auslegung induktiver Bauelemente für den Mittelfrequenzbereich,
1. Auflage 1993, 136 Seiten
ISBN 3-86073-174-2
(vergriffen)

ABISEA Band 10
Skudelny, H.-Ch.
Stromrichtertechnik,
4. Auflage 1997, 259 Seiten
ISBN 3-86073-189-0

ABISEA Band 11
Skudelny, Ch.
Elektrische Antriebe,
3. Auflage 1997, 124 Seiten
ISBN 3-86073-231-5

ABISEA Band 12
Schöpe, F.
Batterie-Management für Nickel-Cadmium Akkumulatoren,
1. Auflage 1994, 156 Seiten
ISBN 3-86073-232-3
(vergriffen)

ABISEA Band 13
v. d. Weem, J.
Schmalbandige aktive Filter für Schienentriebfahrzeuge am Gleichspannungsfahrdraht,
1. Auflage 1995, 125 Seiten
ISBN 3-86073-233-1

ABISEA Band 14
Backhaus, K.
Spannungseinprägendes Direkantriebssystem mit schnellaufender geschalteter Reluktanzmaschine,
1. Auflage 1995, 156 Seiten
ISBN 3-86073-234-X
(vergriffen)

ABISEA Band 15
Reinold, H.
Optimierung dreiphasiger Pulsdauermodulationsverfahren,
1. Auflage 1996, 116 Seiten
ISBN 3-86073-235-8

ABISEA Band 16
Köpken, H.-G.
Regelverfahren für Parallelschwingkreisumrichter,
1. Auflage 1996, 125 Seiten
ISBN 3-86073-236-6

ABISEA Band 17
Mauracher, P.
Modellbildung und Verbundoptimierung bei Elektrostraßenfahrzeugen,
1. Auflage 1996, 192 Seiten
ISBN 3-86073-237-4

ABISEA Band 18
Protiwa, F.-F.
Vergleich dreiphasiger Resonanz-Wechselrichter in Simulation und Messung,
1. Auflage 1997, 178 Seiten
ISBN 3-86073-238-2

ABISEA Band 19
Brockmeyer, A.
Dimensionierungswerkzeug für magnetische Bauelemente in Stromrichteranwendungen,
1. Auflage 1997, 182 Seiten
ISBN 3-86073-239-0

ABISEA Band 20
Apeldoorn, O.
Simulationsgestützte Bewertung von Steuerverfahren für netzgeführte Stromrichter mit verringerter Netzrückwirkung,
1. Auflage 1997, 132 Seiten
ISBN 3-86073-680-9

ABISEA Band 21
Lohner, A.
Batteriemanagement für verschlossene Blei-Batterien am Beispiel von Unterbrechungsfreien Stromversorgungen,
1. Auflage 1998, 144 Seiten
ISBN 3-86073-681-7

ABISEA Band 22
Reinert, J.
Optimierung der Betriebseigenschaften von Antrieben mit geschalteter Reluktanzmaschine,
1. Auflage 1998, 168 Seiten
ISBN 3-86073-682-5

ABISEA Band 23
Nagel, A.
Leitungsgebundene Störungen in der Leistungs¬elektronik: Entstehung, Ausbreitung und Filterung,
1. Auflage 1999, 160 Seiten
ISBN 3-86073-683-3

ABISEA Band 24
Menne, M.
Drehschwingungen im Antriebsstrang von Elektrostraßenfahrzeugen – Analyse und aktive Dämpfung,
1. Auflage 2001, 192 Seiten
ISBN 3-86073-684-1

ABISEA Band 25
von Bloh, J.
Multilevel-Umrichter zum Einsatz in Mittelspannungs-Gleichspannungs-Übertragungen
1. Auflage 2001, 152 Seiten
ISBN 3-86073-685-X

ABISEA Band 26
Karden, E.
Using low-frequency impedance spectroscopy for characterization, monitoring, and modeling of industrial batteries,
1. Auflage 2002, 154 Seiten
ISBN 3-8265-9766-4

ABISEA Band 27
Karipidis, C.-U.
A Versatile DSP/ FPGA Structure optimized for Rapid Prototyping and Digital Real-Time Simulation of Power Electronic and Electrical Drive Systems,
1. Auflage 2001, 164 Seiten
ISBN 3-8265-9738-9

ABISEA Band 28
Kahlen, K.
Regelungsstrategien für permanentmagnetische Direktantriebe mit mehreren Freiheitsgraden,
1. Auflage 2003, 158 Seiten
ISBN 3-8322-1222-1

ABISEA Band 29
Inderka, R.
Direkte Drehmomentregelung Geschalteter Reluktanzantriebe,
1. Auflage 2003, 190 Seiten
ISBN 3-8322-1175-6

ABISEA Band 30
Schröder, S.
Circuit-Simulation Models of High-Power Devices Based on Semiconductor Physics,
1. Auflage 2003, 124 Seiten
ISBN 3-8322-1250-7

ABISEA Band 31
Buller, S.
Impedance-Based Simulation Models for Energy Storage Devices in Advanced Automotive Power Systems,
1. Auflage 2003, 136 Seiten
ISBN 3-8322-1225-6

ABISEA Band 32
Schönknecht, A.
Topologien und Regelungsstrategien für das induktive Erwärmen mit hohen Frequenz-Leistungsprodukten,
1. Auflage 2004, 170 Seiten
ISBN 3-8322-2408-4

ABISEA Band 33
Tolle, T.
Konvertertopologien für ein aufwandsarmes, zweistufiges Schaltnetzteil zum Laden von Batterien aus dem Netz,
1. Auflage 2004, 150 Seiten
ISBN 3-8322-2676-1

ABISEA Band 34
Götting, G.
Dynamische Antriebsregelung von Elektro-straßenfahrzeugen unter Berücksichtigung eines schwingungsfähigen Antriebsstrangs,
1. Auflage 2004, 166 Seiten
ISBN 3-8322-2804-7

ABISEA Band 35
Dieckerhoff, S.
Transformatorlose Stromrichterschaltungen für Bahnfahrzeuge am 16 2/3Hz Netz,
1. Auflage 2004, 158 Seiten
ISBN 3-8322-3094-7

ABISEA Band 36
Hu, J.
Bewertung von DC-DC-Topologien und Optimierung eines DC-DC-Leistungsmoduls für das 42-V-Kfz-Bordnetz,
1. Auflage 2004, 156 Seiten
ISBN 3-8322-3201-X

ABISEA Band 37
Detjen, D.-O.
Characterization and Modeling of Si-Si Bonded Hydrophobic Interfaces for Novel High-Power BIMOS Devices,
1. Auflage 2004, 146 Seiten
ISBN 3-8322-2963-9

ABISEA Band 38
Walter, J.
Simulationsbasierte Zuverlässigkeitsanalyse in der modernen Leistungselektronik,
1. Auflage 2004, 134 Seiten
ISBN 3-8322-3481-0

ABISEA Band 39
Schwarzer, U.
IGBT versus GCT in der Mittelspannungsanwendung – ein experimenteller und simulativer Vergleich,
1. Auflage 2005, 184 Seiten
ISBN 3-8322-4489-1

ABISEA Band 40
Bartram, M.
IGBT-Umrichtersysteme für Windkraftanlagen: Analyse der Zyklenbelastung, Modellbildung, Optimierung und Lebensdauervorhersage
1. Auflage 2006, 195 Seiten
ISBN 3-8322-5039-5

ABISEA Band 41
Ponnaluri, S.
Generalized Design, Analysis and Control of
Grid side converters with integrated UPS or Islanding functionality,
1. Auflage 2006, 163 Seiten
ISBN 3-8322-5281-9

ABISEA Band 42
Jacobs, J.
Multi-Phase Series Resonant DC-to-DC Converters
1. Auflage 2006, 185 Seiten
ISBN 3-8322-5532-X

ABISEA Band 43
Linzen, D.
Impedance-Based Loss Calculation and Thermal Modeling of Electrochemical Energy Storage Devices for Design Considerations of Automotive Power Systems
1. Auflage 2006, 150 Seiten
ISBN 3-8322-5706-3

ABISEA Band 44
Fiedler, J.
Design of Low-Noise Switched Reluctance Drives,
1. Auflage 2007, 183 Seiten
ISBN 978-3-8322-5864-1

ABISEA Band 45
Fuengwarodsakul, N.
Predictive PWM-based Direct Instantaneous Torque Control for Switched Reluctance Machines,
1. Auflage 2007, 150 Seiten
ISBN 978-3-8322-6210-5

ABISEA Band 46
Meyer, C.
Key Components for Future Offshore DC Grids,
1. Auflage 2007, 196 Seiten
ISBN 978-3-8322-6571-7

ABISEA Band 47
Fujii, K.
Characterization and Opti-mization of Soft-Switched Multi-Level Converters for STATCOMs
1. Auflage 2008, 206 Seiten
ISBN 978-3-8322-6981-4

ABISEA Band 48
Carstensen, C.
Eddy Currents in Windings of Switched Reluctance Machines,
1. Auflage 2008, 190 Seiten
ISBN 978-3-8322-7118-3

ABISEA Band 49
Bohlen, O.
Impedance-based battery monitoring,
1. Auflage 2008, 200 Seiten
ISBN 978-3-8322-7606-5

ABISEA Band 50
Thele, M.
A contribution to the modelling of the charge acceptance of lead-acid batteries – using frequency and time domain based concepts,
1. Auflage 2008, 168 Seiten
ISBN 978-3-8322-7659-1

ABISEA Band 51
König, A.
High Temperature DC-to-DC Converters for Downhole Applications
1. Auflage 2009, 160 Seiten
ISBN 978-3-8322-8489-3

ABISEA Band 52
Dick, C. P.
Multi-Resonant Converters as Photovoltaic Module-Integrated Maximum Power Point Tracker
1. Auflage 2010, 192 Seiten
ISBN 978-3-8322-9199-0

ABISEA Band 53
Kowal, J.
Spatially-resolved impedance of nonlinear inhomogeneous devices – using the example of lead-acid batteries –
1.Auflage 2010, 214 Seiten
ISBN 978-3-8322-9483-0

ABISEA Band 54
Roscher, M.
Zustandserkennung von LiFePO4-Batterien für Hybrid- und Elektrofahrzeuge
1. Auflage 2011, 194 Seiten
ISBN 978-3-8322-9738-1

ABISEA Band 55
Hirschmann, D.
Highly Dynamic Piezoelectric Positioning
1. Auflage 2011, 156 Seiten
ISBN 978-3-8322-9746-6

ABISEA Band 56
Rigbers, K.
Highly Efficient Inverter Architectures for Three-Phase Grid Connection of Photovoltaic Generators
1. Auflage 2011, 254 Seiten
ISBN 978-3-8322-9816-9

ABISEA Band 57
Kasper, K.
Analysis and Control of the Acoustic Behavior of Switched Reluctance Drives
1. Auflage 2011, 214 Seiten
ISBN 978-3-8322-9869-2

ABISEA Band 58
Köllensperger, P.
The Internally Commutated Thyristor - Concept, Design and Application
1. Auflage 2011, 212 Seiten
ISBN 978-3-8322-9909-5

ABISEA Band 59
Schoenen, T.
Einsatz eines DC/DC-Wandlers zur Spannungs-anpassung zwischen Antrieb und Energiespeicher in Elektro- und Hybrid-fahrzeugen
1. Auflage 2011, 138 Seiten
ISBN 978-3-8440-0622-3

ABISEA Band 60
Hennen, M.
Switched Reluctance Direct Drive with Integrated Distributed Inverter
1. Auflage 2012, 150 Seiten
ISBN 978-3-8440-0731-2

ABISEA Band 61
van Treek, D.
Position Sensorless Torque Control of Switched Reluctance Machines
1. Auflage 2012, 144 Seiten
ISBN 978-3-8440-1014-5

ABISEA Band 62
Bragard, M.
The Integrated Emitter Turn-Off Thyristor. An Innovative MOS-Gated High-Power Device
1. Auflage 2012, 172 Seiten
ISBN 978-3-8440-1152-4

ABISEA Band 63
Gerschler, J. B.
Ortsaufgelöste Modellbildung von Lithium-Ionen-Systemen unter spezieller Berücksichtigung der Batteriealterung,
1. Auflage 2012, 350 Seiten
ISBN 978-3-8440-1307-8

ABISEA Band 64
Neuhaus, C.
Schaltstrategien für Geschaltete Reluktanzantriebe mit kleinem Zwischenkreis
1. Auflage 2012, 144 Seiten
ISBN 978-3-8440-1487-7

ABISEA Band 65
Butschen, T.
Dual-ICT - A Clever Way to Unite Conduction and Switching Optimized Properties in a Single Wafer
1. Auflage 2012, 178 Seiten
ISBN 978-3-8440-1771-7

ABISEA Band 66
Plum, T.
Design and Realization of High-Power MOS Turn-Off Thyristors
1. Auflage 2013, 130 Seiten
ISBN 978-3-8440-1884-4

ABISEA Band 67
Kiel, M.
Impedanzspektroskopie an Batterien unter besonderer Berücksichtigung von Batteriesensoren für den Feldeinsatz
1. Auflage 2013, 232 Seiten
ISBN 978-3-8440-1973-5

ABISEA Band 68
Brauer, H.
Schnelldrehender Geschalteter Reluktanzantrieb mit extremem Längendurchmesserverhältnis
1. Auflage 2013, 202 Seiten
ISBN 978-3-8440-2345-9

ABISEA Band 69
Thomas, S.
A Medium-Voltage Multi-Level DC/DC Converter with High Voltage Transformation Ratio
1. Auflage 2014, 236 Seiten
ISBN 978-3-8440-2605-4

ABISEA Band 70
Richter, S.
Digitale Regelung von PWM-Wechselrichtern mit niedrigen Trägerfrequenzen
1. Auflage 2014, 134 Seiten
ISBN 978-3-8440-2641-2

ABISEA Band 71
Bösing, M.
Acoustic Modeling of Electrical Drives – Noise and Vibration Synthesis based on Force Response Superposition
1. Auflage 2014, 208 Seiten
ISBN 978-3-8440-2752-5